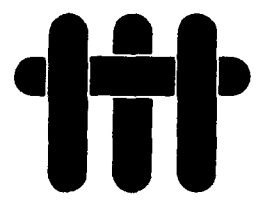


1

AD-A216 146

ANNUAL REPORT
University Research Initiative
Contract No.: N00014-86-K-0753
September 15, 1988-September 14, 1989



**The Processing and Mechanical
Properties of High Temperature/
High Performance Composites**

S DTIC
ELECTE
DEC 26 1989
D **D**

by

A. G. Evans & R. Mehrabian
University of California,
Santa Barbara

Arizona State University
Cambridge University
Harvard University
Stanford University
Washington State University
University of Wisconsin-Madison

DISTRIBUTION STATEMENT A
Approved for public release
Distribution Unlimited

Sponsored by: The Defense Advanced Research Projects Agency
Monitored by: Office of Naval Research

Book 6 of 6
Section 4: PROCESSING: Matrices and Composites
Part 2 of 2

89 12 31 037

SUMMARY
of
TABLE OF CONTENTS

EXECUTIVE SUMMARY

SECTION 1: COATINGS AND INTERFACES Book 1

SECTION 2: STRENGTH AND FRACTURE RESISTANCE

Part 1 Book 2

Part 2 Book 3

SECTION 3: FLOW AND CREEP STRENGTH Book 4

SECTION 4: PROCESSING: Matrices and Composites
--

Part 1	Book 5
--------	--------

Part 2	Book 6
--------	--------

Accession For	
NTIS CRAM	↓
DTIC TAB	□
Unannounced	□
Justification	
By <i>PCG</i>	
Distribution	
Availability Codes	
Dist	Avail and/or Special
<i>A1</i>	

BOOK 6

SECTION 4: PROCESSING: *Matrices and Composites*

Part 2 of 2

Intermetallics (con't.)

- | | | |
|-----|--|---|
| 62. | Densification of Rapidly Solidified Titanium Aluminide Powder during Hot Isostatic Pressing | B.W. Choi
Y-G. Deng
C. McCullough
B. Paden
R. Mehrabian |
| 63. | Experimental Verification of HIP Densification Models for TiAl Using In-Situ Sensing | B. Paden
B.W. Choi
J. Marschall
Y-G. Deng
C. McCullough
R. Mehrabian |
| 64. | Evolution of Boride Morphologies in Ti-Al-B Alloys | M.E. Hyman
C. McCullough
C.G. Levi
R. Mehrabian |
| 65. | Development of Ti-Al Intermetallic Matrix Composites by Solidification Processing | J.J. Valencia
C. McCullough
J. Rösler
C.G. Levi
R. Mehrabian |
| 66. | Numerical Modelling of the Planar Flow Melt-Spinning Process, and Experimental Investigation of the Solidification Puddle Dynamics | Z. Gong
P. Wilde
E.F. Matthys |

Ceramics

- | | | |
|-----|--|--------------------------------------|
| 67. | Densification Behavior of Al_2O_3 Powder
Containing ZrO_2 Inclusions | O. Sudre
D.C.C. Lam
F.F. Lange |
| 68. | Densification Behavior of Single Crystal
and Polycrystalline Spherical Particles of
ZrO_2 made by Electrostatic Atomization | E.B. Slamovich
F.F. Lange |
| 69. | Powder Processing and Densification of
Ceramic Composites | F.F. Lange
D.C.C. Lam
O. Sudre |

EXECUTIVE SUMMARY

The third annual report of the University Research Initiative project at UCSB on High-Temperature, High-Performance Composites consists of sections compiled in a total of six books. The first section in Book 1 is concerned with the properties and structure of bimaterial *interfaces* and the related problem of *coating* decohesion and cracking. The second section describes research on the *strengths and fracture resistance* of brittle matrix composites manufactured with fibers, whiskers and ductile phases. This information is presented in Books 2 and 3. The third section addresses the *flow and creep strength* of reinforced systems, with emphasis on effects of aspect ratio and the incidence of damage, and is offered in Book 4. The fourth section, Books 5 and 6, describes work on processing of intermetallic and ceramic matrices and composites, as well as numerical modelling of the melt-spinning process.

SECTION 4: PROCESSING: Matrices and Composites

INTERMETALLICS

PHASE EQUILIBRIA - The assessment of the binary TiAl phase diagram has been completed through combined efforts on thermodynamic modelling, differential thermal analysis and annealing experiments (Mishurda et al.), as well as high-temperature X-ray diffractometry and controlled solidification experiments (McCullough et al.). In particular, the liquid-solid equilibrium in the vicinity of the equiatomic composition and the boundaries of the high temperature α -(Ti) field are now well-established. The revised diagram and corollary thermodynamic

information has been instrumental not only in elucidating the microstructural evolution paths of binary Ti-Al intermetallic alloys, but also in permitting the systematic evaluation and computer calculation of related ternary systems, notably Ti-Al-Nb, Ti-Al-Ta and Ti-Al-B.

Substantial progress has been made on the Ti-Al-Nb ternary system. Extensive solidification experiments have been combined with the binary diagram information to define the approximate shape of the liquidus surface and the boundaries of the different primary phase fields (Jewett et al.). The α -(Ti) liquidus on the Ti-Al binary shrinks with the addition of Nb and is totally encroached by the β and γ -(TiAl) fields at ~ 18at%Nb. All other regions on the liquidus surface have temperatures that decrease from the Nb-Al binary toward the Ti-Al binary. Significant problems still exist in the vicinity of the Ti₂NbAl composition, where two ternary phases (T1 and T2) had been detected (Jewett et al., Boettinger et al.). Both phases have B2 structures at 1200°C and decompose upon cooling to rather complex microstructures involving α_2 , γ and a B8₂ phase.

Phase equilibria studies on the Ti-Al-Ta system have been initiated. Solidification work suggests that the shape of the liquidus surface in the vicinity of γ is quite similar to that reported for Ti-Al-Nb with the α -(Ti) field shrinking with Ta additions until it is encroached by the β -(Ti) and γ -(TiAl) fields (McCullough et al.), but the liquidus temperatures are generally higher than those for Nb additions. High temperature X-ray diffraction has been extensively used to study the phases present in the vicinity of the 50at%Al isoconcentrate (McCullough et al.). In addition, a preliminary isothermal section at 1100°C has been delineated based on the X-ray evidence combined with diffusion couples and isothermal annealing experiments developed under other DARPA sponsored programs.

SOLIDIFICATION - The fundamental understanding of the solidification of Ti-Al alloys developed in the previous funding period was systematically applied to elucidate the microstructure evolution of rapidly solidified powders produced by the industrial participants (McCullough et al., Jewett et al.). Microstructures of powders produced by containerless processing (PREP) were in general consistent with the trends established by the controlled solidification experiments, wherein β was found to be the kinetically preferred primary phase at high supercoolings, even in the composition range where α and/or γ are thermodynamically favored (45-55at%Al). In contrast, atomization processes involving graphite crucibles and/or nozzles (XSR) were found to yield powders with a large proportion of primary α -(Ti) phase, even at compositions where β is the equilibrium primary phase. This was ascribed to carbon contamination of the melt ($\sim 0.5\text{at}\%C$), which seems to shift the α/β liquidus boundary (McCullough et al.). Furthermore, the solidification behavior of dilute ($\geq 5\text{at}\%Nb$ or Ta) ternary alloys in the $\alpha_2 - \gamma$ range was found to proceed essentially as in the binary Ti-Al alloy of the same aluminum content (Jewett et al., McCullough et al.).

Studies on the effects of cooling rate after solidification using binary and dilute ($\geq 5\text{at}\%Nb$ or Ta) ternary alloys (McCullough et al., Jewett et al.), revealed that diffusion-controlled lath transformation is sensitive to quenching. Indeed, γ precipitation may be completely suppressed by decreasing the Al content or adding ternary elements (Nb or Ta) that exhibit strong partitioning between the α_2 and γ phases. It was also found that the $\alpha \rightarrow \alpha_2$ ordering is not suppressible by quenching.

The solidification of γ -TiAl base alloys containing 10 to 28at%Ta (McCullough et al.) revealed that primary β -(Ti) forms with γ segregates in the interdendritic spaces. The leaner alloys appear to go through the double peritectic cascade

previously reported for the binary system $L + \beta \rightarrow \alpha$ and $L + \alpha \rightarrow \gamma$, but the extent of α formation is reduced with increasing Ta content and most probably eliminated in the richer alloys. All these alloys exhibit strong partitioning of Ta toward the dendrite cores. This severe "coring" would require long homogenization treatments and its presence may lead to erroneous conclusions when mechanical and oxidation behavior studies are conducted on as-cast materials. Furthermore, the Ta-rich cores appear to follow a different transformation path in the solid state than the rest of the dendrites, substantially complicating the analysis of the phase sequencing and microstructure evolution during the post-solidification cooling. The scale of segregation can be refined by approximately one order of magnitude using melt-spinning or splat-quenching instead of arc melting. Homogenization has then been accomplished in a few hours.

CONSOLIDATION - HIP consolidation of titanium aluminide powders produced by Rapid Solidification Rate (RSR) and Rotating Electrode Process (REP) were studied (Choi et. al) and compared to computer model predictions (Ashby). In a corollary effort a high temperature sensor was developed (Paden et. al) for in-situ monitoring of the consolidation process. Characterization of the starting powders; RSR Ti-48%Al-2.5%Nb-0.3%Ta, and REP Ti-50%Al-2%Nb, showed dendrites with primarily hexagonal symmetry, indicative of α -phase formation from the liquid. These microstructures were consistent with solidification studies reported above - e.g. carbon contamination in the RSR process strongly favors the formation of primary α . Good agreement was obtained between the predicted HIP maps and the experimental data during later stages of densification (>85%) and longer times (4 and 16 hours). The power law creep mechanism predicted by the model is in best agreement with the experiments. However, discrepancies arise at the earlier stages. At lower temperatures, the model predicts much faster consolidation, indicating a

required adjustment to the model. At higher temperatures and short times (1 hour), the model predicts a slower densification. Direct in-situ sensing, using an eddy current sensor, provided an explanation for the latter discrepancy. It was found that significant consolidation occurred during the pressurization process which the model does not take into consideration.

COMPOSITES - The composite processing facet of this research has explored using alloying additions that develop reinforcements in titanium aluminides, through suitable control of the chemistry and solidification parameters. The compounds of most interest are those which exhibit strongly anisotropic growth from the melt, either because of their crystal structure and/or interfacial tension characteristics. Plate reinforcements have been readily grown in the Ti-Al-C system, where the phase in equilibrium with γ -TiAl is Ti_2AlC , a hexagonal structure with a rather complicated stacking sequence along the c-axis (Valencia et al.). Plates $\sim 1 \mu m$ thick with aspect ratios of ~ 20 and up to 12% by volume have been grown as primary phases in Ti-(48-51at%)Al-3at%C. Significant increases (20-60%) in creep strength were observed in these alloys when compared with unalloyed γ , but there are indications that some of the strengthening is due to dissolved C in the matrix.

Borides appear more promising as reinforcing phases for γ -TiAl; they offer flexibility for microstructural control and relatively straightforward processing conditions. The structures of interest are all based on the trigonal prismatic coordination of 6 metal atoms around each B, which may be arranged in close-packed (TiB_2), columnar (TiB) or lamellar (TaB,NbB) arrays. The boride in equilibrium with the binary γ -TiAl is TiB_2 , which forms a mixture of plates, needles and highly convoluted flakes when solidifying as a secondary phase. Major progress has been made in the understanding of these different morphologies and their dependence on alloy composition and solidification rate (Hyman et al.), but

TiB₂ may not lend itself to the production of appreciable volume fractions of reinforcements with the desirable morphologies. However, controlled additions of Ta or Nb change the structure of the stable primary boride to TiB, with Ta or Nb partially substituting for Ti. These borides grow as rods ~ 1 to 5 μm in diameter with aspect ratios of 20 or larger, as expected from crystallographic considerations, and have been produced in volume fractions up to 15% (Valencia et al.). Current studies are focused on optimizing the scale and distribution of these reinforcements, as well as on exploring alloy compositions which may produce platelike phases based on the structure of TaB.

PLANAR FLOW CASTING - High-speed, high-magnification video techniques were used to investigate the geometry and stability of the puddle during planar flow casting of aluminum alloys. Puddle oscillations and surface instabilities are correlated to macroscopic defects in the ribbon. The process was modelled numerically using fluid mechanics and heat transfer to establish thermal profiles in the solidifying puddle. Although not specifically reported herein, the system has been upgraded and used to produce ribbons of titanium aluminides for some of the solidification studies in this report.

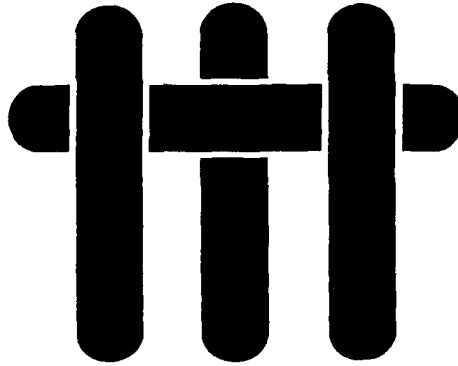
CERAMICS

Pressureless densification of ceramic powders containing reinforcements has been emphasized as needed to understand processing limitations and to develop new methods for processing ceramic composites. Two major problems have been studied: the forming of powder compacts containing reinforcements and the constrained densification of the matrix powder. It has been shown that pressure filtration can be used to pack powder within a fiber preform provided: a) repulsive forces exist between particles and between the reinforcement and particles and b) the

particle size to fiber diameter ratio is ≤ 0.01 . The latter requirement not only provides for the flow of particles through preform channels, but also for high packing density within the preform. Densification of the powder matrix is constrained by the reinforcement. Studies of this problem have emphasized powders containing a non-connected network of inert particles, viz., Al_2O_3 -SiC plates and Al_2O_3 - ZrO_2 inclusions. Shrinkage measurements, mercury porosimetry, and microstructural observations illustrate the sequential events: sintering and shrinkage occurs until an interconnected dense network forms that surrounds lower density regions. Coarsening of grains within the lower density regions causes voids within these regions to grow and dissipate the sintering potential. *Higher particle packing density results in less differential shrinkage and higher composite density.*

Studies concerning sintering via vapor phase transport have been initiated with the goal of strengthening the powder matrix without the shrinkage associated with other modes of material transport. Studies have also been initiated in which precursor ZrO_2 fibers are incorporated into powders which also shrink, either more or less than the powder, depending on their prior heat treatment.

M A T E R I A L S



DENSIFICATION OF RAPIDLY SOLIDIFIED

TITANIUM ALUMINIDE POWDERS

DURING HOT ISOSTATIC PRESSING

by

B.W. Choi, Y.G. Deng, C. McCullough, B. Paden and R. Mehrabian

Materials Department
College of Engineering
University of California
Santa Barbara, California 93106

ABSTRACT

Rapidly solidified γ -titanium aluminide powders were characterized and subjected to consolidation by hot isostatic pressing (HIP). Primary solidification of hcp α -phase followed by formation of interdendritic γ -segregate prevails in both REP (Ti-50%Al-1.8%Nb) and RSR (Ti-48%Al-2.4%Nb-0.3%Ta) powders, except for a minor fraction of fine powders that form bcc β -phase from the liquid. The evolution of these microstructures and their subsequent solid state transformations are in line with previous observations on binary titanium aluminide droplets solidified with and without supercooling. In the consolidation experiments, the influences of time, temperature and pressure on final densification were experimentally determined and compared with predicted HIP maps using best estimates of input data on material properties. Experimentally it was found that the densification rate is independent of average mean particle diameter. Best agreement between predictions and experiments were obtained for power law creep as the dominant consolidation mechanism at high pressure, i.e. 182MPa. Modifications of the model are suggested for the low temperature creep regime, including consolidation during the pressurization and dynamic recrystallization.

1. INTRODUCTION

Recent emphasis on the development of a new class of lightweight, oxidation-resistant, high-temperature titanium alloys for aerospace applications has generated renewed interest in the titanium aluminide intermetallics. Binary and higher order titanium alloys with aluminum contents close to 50%* with γ ($L1_0$) as the predominant phase possess superior high temperature moduli, tensile and creep strengths. However, the $L1_0$ phase is brittle and results in serious cracking problems when processed by conventional ingot metallurgy and shape casting techniques. Powder processing, on the other hand, can overcome this problem in some γ -alloys, and offers the opportunity of near-net shape fabrication through HIP consolidation.

A number of recent developments have significantly improved the potential application of γ -titanium aluminides. Firstly, studies on the Ti-Al phase diagram and solidification of near- γ alloys provide the basis for predicting the evolution of microstructures during both rapid solidification and subsequent solid-state transformations [1-3]. These include phase stability studies using high temperature X-rays. Secondly, it has been shown that compositing of γ -titanium aluminide powders with other more ductile powders (phases) can result in improved room temperature toughness [4-6]. Thirdly, a HIP map (diagram) generation computer program has been developed that becomes predictive when combined with experimental data [7]. Availability of a HIP map should permit optimization of temperature, pressure and time to achieve full density, and yet, prevent undue coarsening of the rapidly solidified microstructures (e.g. second phase dispersoids), and permit control of interface interactions between γ -matrices and the ductilizing

* all figures are given in atomic percent

phases.

The HIP computer program [7] is for monolithic materials. It is based on models [8-10] that predict densification rates, and permits the establishment of dominant densification mechanisms for various combinations of temperature, pressure and time. The program assumes that densification of mono-size powders occurs at a rate that is the sum of individual contributions from several possible mechanisms, i.e. plastic flow, power law creep, volume and boundary diffusion, and Nabarro-Herring creep. The program integrates contributions from each densification rate equation (mechanism) to give density as a function of process variables and input parameters based on material properties. The results are then plotted as relative density as a function of temperature at constant pressure, or vice versa, in the form of constant time contours. The "field of dominance" of each densification mechanism is graphically displayed on the HIP diagram.

In the present study a thorough examination of γ -alloy powders produced by two atomization processes was conducted. The genesis of their rapidly solidified microstructures was established based on previous phase diagram and solidification studies [1-3]. The powders were subsequently consolidated under a range of processing conditions. The data thus generated was compared to HIP maps to both identify the mechanisms responsible for densification and to provide a basis for the development of future HIP cycles and predictive models for γ -matrix composites.

2. EXPERIMENTAL

2.1 Powders

Two powder compositions, Ti-48%Al-2.4%Nb-0.3%Ta and Ti-50.3%Al-1.8%Nb, were used in this study. Compositions of minor elements are given in Table I. The first composition was produced by a centrifugal atomization technique, the Rapid Solidification Rate process (RSR), and the second by the Rotating Electrode Process (REP). It should be noted that the earlier version of the RSR process used for the production of these powders caused some carbon contamination since the molten alloy was in contact with a graphite crucible prior to atomization. The carbon alters the solidification "path" of the atomized powder [3]. The as-received powders were sieved into different size fractions to determine their size distribution, shown in Fig. 1. A single size distribution was used for the REP powder, ranging between 60-300 μ m, and two size distributions were used for the RSR powder, (i) up to 300 μ m (-50 mesh) and (ii) up to 106 μ m (-140 mesh); the latter permitting the effect of particle size on consolidation to be studied. The powders were also characterized by optical microscopy, X-ray diffraction and SEM, and then consolidated in the HIP as described below.

2.2 X-Ray

Room and high temperature X-ray diffraction was performed to elucidate the high temperature phase equilibria in a consolidated billet of the Ti-48%Al-2.4%Nb-0.3%Ta alloy, (Table I). This was provided by Pratt & Whitney as a hot forged billet, consolidated at 1339K for 3 hours at 225MPa. Thin slices were cut from the billet, 8mm x 8mm, and ground to 300-400 μ m thickness. Any surface deformation due to grinding was removed via electropolishing, and hydrogen pick-up and hydride

formation was minimized by chemical cleaning [11]. These slices were then used for high temperature X-ray diffraction experiments in the manner described by McCullough et. al [1, 2]. The sample was heated through a series of temperatures, with diffraction spectra taken after 5-10 minutes at each temperature to allow for thermal equilibration. Microstructures were examined both before and after the experiments, and the compositions checked by EDS in a SEM using standards to monitor possible aluminum evaporation.

2.3 HIPing

The RSR -140 and -50 mesh powders were provided in sealed commercial purity titanium tubes (12.7mm OD by 1.27mm wall thickness by 100mm long) by Pratt and Whitney. The REP powder was carefully "canned" in our laboratory as follows. First, a length of commercial purity titanium tubing (12.7mm OD by 0.70mm wall thickness) was crimped and TIG (tungsten inert gas) welded to seal one end. Next, in a glove box (argon gas environment), the powder was poured into the tube and a valve with a powder-restraining filter was fitted to the open end. The resulting assembly was removed from the glove box, evacuated, and the open end was crimped twice to seal the loosely packed powder in the tube. This end was also TIG welded to ensure a reliable seal.

Following the canning, the samples were HIPed in an ASEA QIH-3 hot isostatic press using a molybdenum furnace and ultra-high-purity argon. The cylindrical furnace sample chamber is 100mm in diameter and 125mm high with a single heater coil located at its base. The localization of the heating motivated the use of two thermocouples to assure uniform temperature distribution within the sample chamber. Both thermocouples are on the side of the chamber--one 50mm from the bottom and the other at the top. At typical HIPing pressures (182MPa) the reading from the upper thermocouple was somewhat lower (~15K) than that from

the lower thermocouple. Thermal conduction in the sample should further reduce this temperature gradient. During the HIP cycle the lower thermocouple was used for the feedback control of the furnace temperature.

A total of forty-one HIP experiments were carried out to establish the effects of starting material, HIPing time, pressure and temperature on the final density and microstructure, see Tables II, III, and IV. Typical temperature and pressure trajectories for a HIP cycle are shown in Figure 2. The important features to note are: i) the sample is heated to the desired temperature and soaked for 20 minutes prior to pressurization, ii) the pressurization is not instantaneous due to limited capacity of the high-pressure pump, iii) the HIPing time (t_{hip}) is measured from the time the desired pressure is attained to the time venting begins - t_{hip} is a slight underestimate of the effective HIPing time.

2.4 Relative Density Measurements

The relative densities of the consolidated powders were measured using an automatic image analysis system. The relationship Area Fraction equals Volume Fraction was used to estimate the relative density of the samples from visible porosity on polished sample surfaces. Repeated measurements were made on both horizontal and vertical cross sections to assure accuracy. This method produced excellent data at high relative density and compared well to repeated measurements made with a water immersion technique at low relative density (the water immersion technique fails at high relative density due to the large fraction of closed pores in the sample).

The REP powders contain no internal voids (Fig. 3b) and the measured interparticle void fraction was directly translated to relative density for the different HIPing temperature/pressure/time cycles, see Table II. On the other hand, the RSR powders contain significant internal porosity (Fig. 3a) and measurements were

made to separate these from interparticle porosity for each HIPing cycle. The measured relative density based on interparticle porosity is given in Table II along with the REP data. The relative density calculated based on measured internal porosity, interparticle porosity and total porosity (internal plus interparticle) for the two size ranges, -140 and -50 mesh, are given in Tables III and IV, respectively.

3. RESULTS

Results are described under two major headings. The first deals with microstructure characterization of both the starting and the consolidated materials. In the second, the results of densification experiments are presented and compared to predictive models.

3.1 Microstructures

The microstructural results are divided into three sections. The first deals with the microstructure of the starting powder, together with a description of its evolution during rapid solidification. Next, results of high temperature X-ray experiments on Ti-48%Al-2.4%Nb-0.3%Ta are presented which elucidate the phase equilibria at elevated temperatures. Finally, microstructures of the consolidated material are described and the effect of HIPing on grain size and matrix cracking are explored.

3.1.1 Powder Microstructures

A striking difference between the RSR and REP powders may be seen in Fig. 3, which shows comparable size fractions from each. RSR powders (Fig. 3a), while primarily spheroidal, contain numerous internal voids produced by gas entrapment during atomization. In contrast, all the REP powders (Fig. 3b) are fully dense

spheres.

Microstructurally, both the RSR and REP powders exhibit dendrite characteristics with hexagonal symmetry, indicative of the formation of hcp- α as the primary phase from the liquid. These structures were seen in 95% of the RSR powders (Fig. 4a), while the remaining 5% showed martensitic relief (Fig. 4b). The latter structure is evidence of the formation of the bcc- β phase from the liquid, which then transforms martensitically to α' . Similar structures were observed for the REP powders (Figs. 4c, d), but the proportion that were martensitic dropped to ~1%. In all cases, the martensitic structures were only associated with the smallest particle size ranges, i.e. $<30\mu\text{m}$.

Previous studies of microstructure evolution in supercooled droplets of binary Ti-Al alloys [3, 12] proposed that when β is the equilibrium phase (up to 49%Al), it forms at all supercoolings. However, when α is the equilibrium phase, this may be superseded by β at higher supercoolings (80-100K in Ti-50%Al) - almost as soon as the formation of β is thermodynamically possible. This is because β is kinetically favored over α , even though solidification of α may have a higher thermodynamic driving force. The effect of ~1.8 to 2.4%Nb in both the REP and RSR alloys and 0.3%Ta in the RSR alloy on the $\beta \rightarrow \alpha$ peritectic transformation composition is not known. However, high temperature X-ray data on the RSR alloy, described below, does not show discernable differences in high temperature phase stability from its binary alloy counterpart [2]. Hence, for the REP powder (Ti-50.3%Al-1.8%Nb), it is expected that α forms at low supercoolings (large powders) and β forms at large supercoolings (small powders). However, in the RSR powders (Ti-48%Al-2.4%Nb-0.3%Ta) primary β should form at all supercoolings, and hence at all powder sizes. This clearly is not the case. The reason lies in the carbon contamination of the melt in the RSR process (see Table I). Carbon is known to alter the phase selection strongly in favor of α , as reported for the case of binary Ti-48%Al

with 0.1-0.2% carbon contamination, [3]. Hence, α is also seen as the primary phase in a majority of the RSR powders.

X-ray diffraction of the powders showed they contained only the phases γ and α_2 . The α_2 is contained within the primary dendrites as a result of ordering of the α during solid state cooling, and the γ is present both as an interdendritic segregate phase and as a fine lamellar precipitate within the transformed dendrites of α_2 [3, 12].

3.1.2 X-ray Diffraction

As previously noted, the starting material for the high temperature studies was a billet forged at 1339K from the RSR powders. TEM examination showed two distinct structural regions. The first was a fine grained γ microstructure, $\sim 2\mu\text{m}$ diameter (Fig. 5a), containing small Al_2O_3 inclusions. A diffraction pattern in Fig. 5b from one γ grain shows a $[101]_\gamma$ zone axis. The second area contained striations which were mainly twins of the γ , but occasionally contained some α_2 laths (Fig. 5c). The diffraction pattern from this region shows two twin related $[\bar{1}\bar{1}0]_\gamma$ zones and a faint $[\bar{1}\bar{2}10]_{\alpha_2}$ zone (Fig. 5d).

At 298K, the X-ray spectrum (Fig. 6) contained only peaks of the γ -phase, the dominant peaks being $\{111\}_\gamma$, $\{002\}_\gamma$ and $\{200\}_\gamma$ at 39° , 45° and 46° , respectively. This is consistent with a starting material of single phase γ , because the small fraction of α_2 noted in the TEM is well below the detection limit of the diffractometer. The first sign of change in the spectra occurred at 1623K with the appearance of two small α -peaks; one near 40° , which is the dominant $\{01\bar{1}1\}_\alpha$ signal in the α -spectrum, and the other at 77.5° due to a $\{11\bar{2}2\}_\alpha$ signal. Furthermore, the $\{201\}_\gamma$ and $\{112\}_\gamma$ peaks, seen at 51° and 56° at 298K, disappeared at 1623K. This shows that at 1623K, the material enters a two-phase ($\gamma + \alpha$) field, although it still contains γ as its main constituent.

Further heating to 1673K, caused the disappearance of all the γ peaks except for the small $\{111\}_\gamma$ peak at 39° . The $\{01\bar{1}1\}_\alpha$ near 40° was much stronger, and many new α -signals appeared with particularly strong $\{01\bar{1}0\}_\alpha$ and $\{01\bar{1}2\}_\alpha$ signals at 36° and 53° , respectively. This indicates that between 1623K and 1673K, the material transformed almost entirely to α . Upon heating to 1703K, only α -peaks were observed, with a particularly strong texture along $\{01\bar{1}1\}_\alpha$ at 40° due to preferential growth of this orientation at high temperature. Hence, at 1703K, the material was in the single-phase α -field. Further heating to 1723K, resulted only in the sharpening of the $\{01\bar{1}1\}_\alpha$ texture.

Cooling to room temperature, resulted in the disappearance of all the α -signals and the re-emergence of only γ peaks (not shown). Subsequent microstructural examination showed a typical $\alpha_2 + \gamma$ lath structure, with a small fraction of α_2 , previously observed in binary Ti-48.3%Al alloy [2]. The alloy composition, after the X-ray cycle, measured by EDS in the SEM was Ti-47.6%Al-2.3%Nb-0.25%Ta. This suggests a slight Al loss of 0.4% which is within the EDS experimental error. The transformations noted are nearly identical to those described in binary Ti-48.3 to 50at%Al alloys [2].

3.1.3 Consolidated Material

The effect of HIPing on matrix microstructure, including grain size and cracking, was studied. Completely consolidated (1339K/182MPa/4hrs--see Table II) microstructures of both REP and RSR materials were examined in the TEM. The REP microstructure is single phase γ with a fine grain size of ~ 7 to $10\mu\text{m}$, Fig. 7a. Note that the small grain size is unique to the region shown, on average the grain size of this specimen was $\sim 28\mu\text{m}$, Fig. 9d. Only γ patterns were noted by electron diffraction, e.g. $\{101\}_\gamma$ in Fig. 7b. Also, a low dislocation density suggests complete recrystallization at this consolidation temperature and pressure. Distributed

through the microstructure were small particles (~500nm in diameter), which gave a strong aluminum signal upon EDS analysis. These were situated principally on grain-boundaries, especially prior powder boundaries, and were assumed to be alumina formed on the powder surface. Two distinct microstructural regions were observed in the RSR material. The first is a fine grained, 1-2 μm , γ phase region with occasionally small grains of α_2 (Figs. 8a, b). The second contains larger grains, up to 20 μm , and consists of $\alpha_2 + \gamma$ laths, Fig. 8c. Electron diffraction from this region (Fig. 8d) produced two twin related $[1\bar{1}0]_\gamma$ zones and a $[1\bar{2}10]_{\alpha_2}$ zone. Note the similarity between these microstructures and those of vacuum forged material shown in Fig. 5. Thus, the major difference between the RSR and REP materials is that the former is close to the $\alpha_2 + \gamma/\gamma$ boundary line at 1339K, but still in the two phase field, while the latter, due to its higher Al content is probably in a single phase γ field at the same temperature.

Grain size - During HIPing the grain size changes due to recrystallization and grain growth. To study these changes, REP powders HIPed for 4 hours at 182MPa and various temperatures were examined. Wherever possible, the grain size was measured using the mean linear intercept method. Up to 1123K (Fig. 9a) no new grains were observed, and the powders retained their solidification microstructure. The mean REP powder particle diameter is ~150 μm (Fig. 1), and each particle contains several (4 to 6) grains in the as-solidified condition (Fig. 4c). First sign of recrystallization was noted in the specimen consolidated at 1173K (Fig. 9b) although these grains were very small and difficult to distinguish from the matrix. New grains, ~12 μm , were clearly noted at the 1223K HIPing temperature (Fig. 9c) and their size increased with temperature, up to averages of ~28 μm at 1339K (Fig. 9d).

Figure 10 shows the microstructure of the REP powder after HIPing at 1339K and 182MPa for only 1 hour. The residual porosity was ~0.3%. The micrograph

shows two large spheroidal particles containing coarser grains than the surrounding matrix. The different grain size is attributable to different degrees of deformation in the particles - with larger particles experiencing reduced relative deformation. On the other hand, the surrounding matrix, presumably consisting of smaller particles, undergoes dynamic recrystallization. Similar observations have been reported in HIP consolidation of a nickel-based superalloy [13].

Matrix Cracking - Small microcracks were observed in the REP material consolidated at high temperatures. Microcracking increased with increasing temperature from 1173K to 1339K. Fig. 11a shows an extensive network of microcracks in material consolidated at 1339K and 182MPa for 4 hours. Careful control of the cooling cycle, using a 0.03K/s cooling rate or cooling with the pressure removed, failed to eliminate the microcracks. Low pressure (34.5MPa) experiments, samples #36 and #39 in Table II, also failed to improve this condition. However, virtually no microcracking was observed in the RSR material consolidated under any of the conditions listed in Table II. Fig. 11b shows the microstructure of the RSR sample #35 consolidated at 1339K and 182MPa for 4 hours. As previously noted, the lower Al content of the RSR material results in a consolidated γ microstructure with minor amounts of α_2 , whereas the REP material is all γ , Figs. 7 and 8. It is well recognized that α_2 improves the ductility of γ titanium aluminides and is probably the primary factor in accommodating the cooling stresses in the RSR material.

3.2 Consolidation

Experimental results of the HIP densification studies on both REP and RSR powders are presented first, and then compared to HIP maps to identify the rate-controlling mechanisms.

3.2.1 REP Powder

The relative density data versus temperature at a constant pressure of 182MPa from Table II is plotted in Figure 12. The time contours are for 1, 4 and 16 hours, with higher relative densities achieved at shorter times at higher temperatures. For example, full density is reached at only 4 hours at 1339K, but takes 16 hours at 1223K. Figure 13 illustrates the effect of temperature on consolidation at constant pressure and time, 182MPa and 4 hours. At the lowest temperature, 1023K (Fig. 13a), densification is dominated by establishing points of contact between particles. With increasing temperature densification occurs by both increased number of contacts between particles and growth of the contact areas. The porosity is still interconnected at 1123K (Fig. 13c), but becomes isolated at 1173K (Fig. 13d). Thereafter, the individual pores shrink and disappear with increasing temperature.

Some deductions on densification mechanisms are possible even from this limited data. The cusped porosity in Figs. 13a to c is a good indication that densification is occurring by particle deformation. Some curvature is noted in Figure 13d, however, it is not very clear especially since the remaining porosity at a higher temperature 1223K (Fig. 13e) is still relatively angular. SEM and optical views of microstructures consolidated at 182MPa and 1173K for 1 hour are shown in Fig. 14. The density of this sample is 88.6%. Firstly, it is noted that the porosity is still interconnected, Fig. 14a. Secondly, the fractured compact in Figs 14a and b shows the development of flat contact facets between the particles deformed during HIP. The cusped porosity (angular pores) in Fig. 14c is further evidence that the operative densification mechanism involves particle deformation rather than interparticle diffusion. Furthermore, in the absence of fine grains in Fig. 14c, the primary densification mechanism is probably power law creep. Fig. 10 shows a duplex grain structure of the consolidated powder under the same conditions of pressure and time, 182MPa/1 hour, but at a higher temperature, 1339K. The

remaining porosity is still angular, but recrystallization has occurred in the smaller particles. Thus, from this evidence alone densification by Nabarro-Herring creep cannot be ruled out.

3.2.2 RSR Powder

Two important variances, in starting material and experimental conditions, between this and the REP powder should be noted. One is that the RSR powder contains internal voids which do not densify as rapidly as the interparticle porosity, Tables III and IV. The other is that two size distributions, Fig. 1, were used to study the effect of particle size.

The experimental data in the form of relative density (interparticle and total porosity) as a function of temperature at 182MPa for consolidation times of 1, 4 and 16 hours are shown in Figs. 15a to c. The curves in Fig. 15a are for the coarse powder, -50 mesh, and denote the differences attributable to internal porosity. The shape of all the curves is similar to the REP powder, with both total and interparticle porosity decreasing with increasing temperature and time. Fig. 15b shows similar data plotted for the finer powder, -140 mesh. In both Figs. 15a and b, the interparticle porosity differs from total porosity by 1 to 7%, depending on temperature and time, until close to full densification, suggesting that internal voids behave similar to isolated interparticle voids. Furthermore, their final closure, at least on the magnification scale examined, occurs at a slower rate than the interparticle porosity. When the results of the two powder sizes are compared, Fig. 15c, there is little difference between the data for total porosity except for the lowest temperatures where initial packing density may have played a role.

Fig. 16 shows the effect of temperature and time at 182MPa on the consolidated microstructures. At the lowest temperature, 1123K, the specimens consolidated for both 1 and 4 hours contain small angular interparticle porosity and

large spherical voids inside the particles. With increasing temperature, i.e. 1223K, all the voids decrease in size, but the internal voids now contribute much more significantly to the total porosity, e.g. Fig. 16e. At the highest HIP temperature, 1339K, the total remaining porosity after 1 hour is ~0.5% to 0.7%, Tables III and IV, compared to ~0.3% for the REP powder, Table II. Finally, no porosity is detectable after 4 hours at 182MPa at this temperature, Fig. 16f.

3.2.3 Comparison of Experiment with Theory

The experimental data for both the RSR and the REP powders consolidated at 182MPa are presented in Fig. 17 and compared to a HIP map generated using Ashby's computer program [7]. For the RSR powder both size fractions are included, however, only the interparticle porosity is considered in order to facilitate a direct comparison with the REP powder. All the experimental data is suitably represented by the three constant time contours, suggesting the mechanisms involved in removing interparticle porosity are essentially independent of powder type and the size distributions studied. There is some scatter in the data, but it is probably due to differences in initial packing density and experimental error in differentiating between all the internal and interparticle voids in the RSR powder.

As previously noted, the calculated HIP map is based on rate equations derived for various densification mechanisms [7-10]. Each densification mechanism is described by two sets of equations: one for the stage where relative density is $< \sim 0.9$ to 0.95 and pores are interconnected, and the second for relative density $> \sim 0.95$ where the pores are isolated. The computer program sums-up the densification rate contributions from each mechanism and integrates over time, with due consideration for a smooth transition between the two sets of equations for each mechanism, to get final relative density. As the body densifies, the mechanisms may change, and these are also considered in the computation. The "fields of

dominance" are displayed on the HIP map, Fig. 17, e.g. PL-CRP1 denotes stage 1 power-law creep is the dominant mechanism.

The predictions are critically dependent on the material properties (parameters) used in the densification-rate equations. Those used in this study are presented in Table V. Some of the γ -titanium aluminide material parameters are not available, especially the values of coefficients and activation energies in the diffusion equations. When input data is not available the program uses algorithms to estimate data from correlations established from other published data. The experimental HIP data was also used to further refine these parameters to get closer agreement with the predicted contours. The specific references used in deducing the input parameters are noted in Table V. In addition to the material properties, the powder particle size and grain size are important inputs for the calculations. The particle radius used in the calculation was $70\mu\text{m}$, close to the average size of the coarsest powder (REP), see Fig. 1. The grain size within the particles was approximated at $30\mu\text{m}$.

The calculated HIP map in Fig. 17 shows five regions where specific mechanisms or stages dominate the densification rate. On the left are the Nabarro-Herring creep regimes (stages 1 and 2), on the right the power-law creep regimes (stages 1 and 2), and the bottom denotes the instantaneous plastic yield region. The prediction shows that at 182MPa power-law creep is the dominant mechanism throughout most of the densification process. There is good agreement between the map and the experimental data during later stages of densification (85%) and longer HIPing times (4 and 16 hours). However, discrepancies arise at earlier stages of densification. At low temperatures, the model predicts much faster consolidation, indicating a required adjustment in the model. At higher temperatures and short time (1 hour), the model predicts a slower densification. These will be discussed later.

Effect of Pressure- The role of pressure was investigated by performing a limited series of experiments at 34.5MPa for 4 hours at 1223K and 1339K (Tables II to IV). Data for the two pressures, 34.5 and 182MPa, are plotted for each temperature in Figs. 18a and b. Experimental data at 182MPa and 1339K for 1 hour, and 1223K for 1 and 16 hours are also incorporated in these plots. As expected, at a given temperature, higher pressures lead to higher densities. The calculated maps are also superimposed in Figs. 18a, b, and the "fields of dominance" are specified. Note that a new mechanism, volume diffusion, appears at lower pressures and longer times to facilitate final densification. Agreement between experiment and prediction using the input parameters of Table V is very good for the 1339K map. On the other hand, the experimental data for relative density based on interparticle porosity at low pressure and temperature, 34.5MPa and 1223K, ranges between 0.69 and 0.836. However, the predicted curve for 4 hours is in agreement with the average of the three measurements. Again, we ascribe some uncertainty to low density measurements in the RSR powders because of difficulty in differentiating between interparticle and internal voids. It is clear from the predictions that the densification mechanism shifts from power-law creep to Nabarro-Herring creep with decreasing pressure, especially in early times. Finally, Fig. 19 shows the microstructure of REP powder consolidated at 1339K and low pressure (34.5MPa) for 4 hours. The specimen density is 89.2%, Table II, and the porosity has the distinctive feature denoting creep consolidation. Increasing the pressure to 182MPa leads to complete consolidation, Fig. 13f.

4. DISCUSSION

The above experiments and predictions have shown the strength of this approach for development of predictive HIPing maps for titanium aluminides, as

well as needed modifications to the present models for densification. The experimental data plotted on axes of relative density and temperature, at constant pressure, give well behaved constant time contour maps e.g. Fig. 12. This information combined with the study of consolidated microstructures, e.g. cusped interparticle porosity (angular with sharp points) at 182MPa permit inference of creep as the primary mechanism for densification. Furthermore, the densification rate is independent of particle radius for the range of sizes studied. The mean particle radii for the three size distributions, shown in Fig. 1, are 33 μm and 54 μm for the RSR powders and 70 μm for the REP powder. This is consistent with equations describing densification by both power-law creep and Nabarro-Herring creep, whereas, diffusion mechanisms are particle size dependent with smaller particles sintering faster than the large ones. On the other hand, at the lower pressure (34.5MPa) the few experimental data points are not conclusive enough to draw such an inference, especially near the end of densification where predictions suggest a role for volume diffusion.

It is clear, from both the microstructures and the HIP maps, that densification is occurring by creep-deformation. On the other hand, if the grain size is much smaller than the particle size, Nabarro-Herring diffusional creep-deformation of the particles can make a significant contribution. The predictions in Fig. 17 are based on a grain size of 30 μm . Earlier data presented on recrystallization during HIPing showed that grain size is both a function of temperature and particle deformation, Figs. 9 and 10. The computer model does not incorporate grain size changes. When a smaller grain size, e.g. 10 μm , is used as an input parameter the "field of dominance" shifts to Nabarro-Herring creep, but the predicted time contours are no longer in reasonable agreement with the experimental data in Figs. 12 or 17. This may require further fine tuning of other input parameters to bring together the predictions and the experimental findings. The same input data, including grain

size, was used for the predictions in Figs. 18a and b. The "field of dominance" is now primarily Nabarro-Herring. The fact that one set of input data closely predicts both constant temperature and constant pressure plots, lends credence to these predictions.

As previously noted, there is discrepancy between predictions at low temperature, low density (<85%), and at high temperature/short time (1 hour). The latter is ascribed to the fact that the theory assumes consolidation begins only when the system reaches the pre-programmed HIPing pressure. There is no consideration for consolidation during the pressure ramp-up shown in Fig. 2. Experiments incorporating an on-line sensor have shown that significant consolidation does occur during pressurization [20]. The discrepancy at low density is probably due to the fact that both activation energy and creep exponent are very different at low temperature and allowance needs to be made for this in the model. A relatively low initial relative density of 0.52 was used to reduce predicted early densification in Fig. 17 for better agreement with experiment. However, this did not prove to be very satisfactory.

While the solidification microstructures of the powders were primarily hexagonal-dendritic, and nearly identical, the centrifugally atomized RSR powders contained extensive internal voids with entrapped inert gas (helium) used in the atomization process. In the absence of diffusion out of the pores, the gas is compressed during consolidation until the internal pore pressure is balanced by the externally applied pressure. From a modelling perspective, this is similar to consolidation of isolated interparticle porosity (with an initial gas content) at the later stages of consolidation, relative density >0.95. The equation predicting the ultimate limiting relative density, Δ_{ult} , achievable by the HIPing pressure has been derived by Ashby [10]:

$$\Delta_{ult} = \frac{P \Delta_c}{P \Delta_c + P_i (1 - \Delta_c)} \quad (1)$$

where P is applied pressure, P_i is the initial entrapped gas pressure in the powder, and Δ_c is relative density at which pores are isolated in interparticle space (~0.95). The later is a reasonable estimate of the internal pore contribution to the relative density of the RSR powder, Fig. 15. For an initial pore pressure $P_i = 0.1\text{MPa}$ and an applied pressure $P = 182\text{MPa}$, the ultimate density from equation (1) is 0.99997 - which is clearly beyond the detection limit of the image analyzer.

In order to verify that internal gas porosity was retained in the specimens RSR samples #34 and #35 were reheated to 1339K under 0.1MPa pressure for 1 hour. The gas compressed in the pores under the HIP pressure expanded and fine porosity became visible throughout the specimens, Fig. 20. The measured density of both specimens after the reheat treatment was ~99.3%.

5. CONCLUSIONS

Significant progress has been made in elucidating the evolution of rapidly solidified microstructures in γ -titanium aluminide powders. Correlation with high temperature xXray data, to establish phase fields and boundaries, and supercooled droplets permits plausible explanations based on particle size, composition and impurity content. HIP experiments on REP and RSR powders have demonstrated the importance of modest composition differences, presence of α_2 in the consolidated microstructures, in producing crack-free titanium aluminides. Based on available and estimated input data, HIP maps were constructed to predict the densification mechanisms in these materials, and good agreement between the models and extensive experimental data was obtained. The computer software needs to be modified to account for consolidation during initial pressurization,

microstructure (grain size) changes, and a low temperature power-law creep regime. There is sufficient experimental data in this study to also permit further fine-tuning of the input data. Once these are done, the model should have significant predictive capability to permit selection of optimum consolidation "paths", pressure/temperature/time, to retain microstructure (second phase) refinement conferred by rapid solidification and/or control interface interactions with ductilizing phases.

ACKNOWLEDGEMENTS

This work was sponsored by the Defense Advanced Research Projects Agency under a University Research Initiative Grant N00014-86-K-0753, supervised by Dr. Ben Wilcox and monitored by Dr. Steven Fishman of the Office of Naval Research. The authors are grateful to Dr. Martin Blackburn and Ralph E. Anderson of Pratt and Whitney for providing the REP and RSR powders. Discussions with Prof. Mike F. Ashby and the availability of his computer program is gratefully acknowledged.

REFERENCES

1. C. McCullough, J.J. Valencia, C.G. Levi and R. Mehrabian, *Scripta Metall.*, 22, 1117-1136, (1988).
2. C. McCullough, J.J. Valencia, C.G. Levi and R. Mehrabian, *Acta Metall.*, 37, 1321-1336, (1989).
3. C. McCullough, J.J. Valencia, C.G. Levi and R. Mehrabian, accepted for publication in *Mat. Sci. and Eng.*, (1989) (in press).
4. C. K. Elliott, G.R. Odette, G.E. Lucas and J.W. Sheckard, *High Temperature, High Performance Composites* (edited by Lemkey et. al), MRS Proceedings, Vol. 120, 95, (1988).
5. H.C. Cao, B.J. Dalgleish, C. Elliott, H.E. Deve, A.G. Evans, G.R. Odette and R. Mehrabian, *Acta Metall.*, (in press).
6. H.E. Deve, A.G. Evans, G.R. Odette, R. Mehrabian, M.L. Emiliani and R.J. Hecht, submitted to *Acta Metall.*
7. M.F. Ashby, *Operating manual for HIP487*, Cambridge University, England, (1987).
8. M.F. Ashby, *Acta Metall.*, 22, 275, (1975).
9. A.S. Helle, K.D. Easterling and M.F. Ashby, *Acta Metall.*, 33, 2163, (1985).
10. M.F. Ashby, in "Proc. Lulea Conf. on HIPing", University of Lulea, Sweden, (1987).
11. H. Hu and R.S. Cline, *Trans. A.I.M.E.*, 242, 1013, (1968).
12. J.J. Valencia, C. McCullough, C.G. Levi and R. Mehrabian, *Acta Metall.*, 37, 2517-2530, (1989).
13. N.A. Kaysser, M. Aslan, E. Arzt, M. Mitkov and G. Petzour, *Powder Metallurgy*, 31 No. 1, 63, (1988).
14. R.E. Schafrik, *Met. Trans. A.*, 8A, 1003, (1977).
15. Pratt and Whitney Aircraft, private communication.

16. S.C. Huang, *Scripta Metall.*, 22, 1885, (1988).
17. Ken-ichiro Ouchi, Y. Iijima, Ken-ichi Hirano, *Proceedings of the Fourth International Conference on Titanium, Book #1*, (edited by H. Kimura and O. Izumi), 559, (1980).
18. P.L. Martin, M.G. Mendiratta, H.A. Lipsitt, *Met. Trans. A.*, 14A, 2170, (1983).
19. J.J. Valencia, C. McCullough, J. Rosler, C.G. Levi, R. Mehrabian, *Proc. Conf., TMS, Indianapolis*, (1989).
20. B.W. Choi, J. Marschall, Y.G. Deng, C. McCullough, B. Paden, R. Mehrabian, to be published.

TABLE I

Compositions of materials *

<i>Powders</i>	Al	Nb	Ta	C	O	N
RSR	48	2.4	0.3	0.33	0.29	0.008
REP	50.3	1.8	-	-	0.2	-
 <i>Billet</i>						
Vacuum Hot Forged	48	2.4	0.3	0.25	0.04	-

* all figures in atomic percent.

TABLE II

Measured Relative Density Data Versus Consolidation Conditions
 for
 Ti-50.3at%Al-1.8at%Nb Alloy Powders Produced by REP
 and
 Ti-48at%Al-2.4at%Nb-0.3at%Ta Alloy Powders Produced by RSR
 P= 182 MPa

Sample #	Temp(K)	Time(hr)	Total Relative Density	Relative Density (interparticle porosity)	Relative Density (interparticle porosity)
			REP	RSR-140	RSR-50
1	1023	4	0.643		
2	" "	16	0.727		
3	1073	4	0.755		
4	" "	16	0.881		
5	" "	16		0.880	
6	" "	16			0.832
7	1123	1	0.764		
8	" "	1		0.733	
9	" "	1			0.789
10	" "	4	0.890		
11	" "	4		0.871	
12	" "	4			0.884
13	" "	16	0.945		
14	" "	16		0.947	
15	" "	16			0.948
16	1173	1	0.886		
17	" "	4	0.976		
18	" "	16	0.990		
19	" "	16		0.998	
20	" "	16			0.997
21	1223	1	0.967		
22	" "	1		0.969	
23	" "	1			0.964

TABLE III

Measured Relative Density Data Versus Consolidation Conditions
for
Ti-48at%Al-2.4at%Nb-0.3at%Ta Alloy Powders Produced
by RSR

-140 Mesh Powder

P= 182 MPa

Sample #	Temp(K)	Time(hr)	Relative Density (internal porosity)	Relative Density (interparticle porosity)	Total Relative Density
5	1073	16	0.947	0.880	0.827
8	1123	1	0.947	0.733	0.680
11	" "	4	0.947	0.871	0.817
14	" "	16	0.945	0.947	0.892
19	1173	16	0.977	0.998	0.975
22	1223	1	0.962	0.969	0.931
25	" "	4	0.991	0.993	0.984
31	1339	1	0.994	0.998	0.993
34	" "	4	1.000	1.000	1.000

P= 34.5 MPa

37	1223	4	0.939	0.765	0.704
40	1339	4	0.972	0.930	0.902

P= 182 MPa

continued

Sample #	Temp(K)	Time(hr)	Total Relative Density REP	Relative Density (interparticle porosity) RSR-140	Relative Density (interparticle porosity) RSR-50
24	" "	4	0.987		
25	" "	4		0.993	
26	" "	4			0.991
27	" "	16	1.000		
28	1273	4	0.997*		
29	" "	16	1.000		
30	1339	1	0.997		
31	" "	1		0.998	
32	" "	1			0.997
33	" "	4	1.000		
34	" "	4		1.000	
35	" "	4			1.000

* * Average of two runs

P=34.5 MPa

36	1223	4	0.836		
37	" "	4		0.765	
38	" "	4			0.690
39	1339	4	0.892		
40	" "	4		0.930	
41	" "	4			0.904

TABLE IV

Measured Relative Density Data Versus Consolidation Conditions
for
Ti-48at%Al-2.4at%Nb-0.3at%Ta Alloy Powders Produced
by RSR

-50 Mesh Powder
P= 182 MPa

Sample #	Temp(K)	Time(hr)	Relative Density (internal porosity)	Relative Density (interparticle porosity)	Total Relative Density
6	1073	16	0.914	0.832	0.746
9	1123	1	0.930	0.789	0.719
12	" "	4	0.909	0.884	0.793
15	" "	16	0.956	0.948	0.904
20	1173	16	0.992	0.997	0.989
23	1223	1	0.973	0.964	0.938
26	" "	4	0.992	0.991	0.983
32	1339	1	0.998	0.997	0.995
35		4	1.000	1.000	1.000

P= 34.5 MPa

38	1223	4	0.881	0.690	0.571
41	1339	4	0.919	0.904	0.823

TABLE V

Input Parameters for HIP Maps

<u>Input Parameter</u>	<u>Value</u>	<u>Reference</u>
1. Melting point (K)	1730	[2]
2. Surface energy (J/m ²)	1.76	[***]
3. Young's modulus (GPa)	168	[14,15]
4. T-dependence of modulus, $-T_M/E(dE/dT)$	0.313	[14,15]
5. Yield stress (MPa)	981	[15,16,*]
6. T-dependence of yield stress, $-T_M/\sigma_y(d\sigma_y/dT)$	0.775	[15,*]
7. Atomic volume (m ³)	1.63×10^{-29}	[**]
8. Pre-exp. vol. diffusion (m ² /s)	8.30×10^{-7}	[17]
9. Activ. energy, vol diff. (kJ/mol)	200	[17,*]
10. Pre-exp. bdry. diff. (m ³ /s)	7.60×10^{-13}	[***]
11. Activ. energy. bdry. diff. (kJ/mol)	180	[***]
12. Pre-exp. surface diff. (m ³ /s)	7.60×10^{-9}	[***]
13. Activ. energy surf. diff. (kJ/mol)	150	[***]
14. Power law creep exponent	3.00	[18,19,*]
15. Reference stress, P-L creep (MPa)	2350	[*]
16. Activ. energy for P-L creep (kJ/mol)	320	[18,*]
17. Solid density (kg/m ³)	4.00×10^3	[**]
18. Particle radius (m)	7.03×10^{-5}	[**]
19. Initial relative density	0.52	[*]
20. Initial pore pressure (MPa)	0.1	[**]
21. Grain diameter in particle (m)	3.00×10^{-5}	[**]

* Extrapolated to produce appropriate (measured) values at consolidation temperature or to get better agreement with experimental data in this study.

** Measured or calculated.

*** Estimated from published data on other materials.

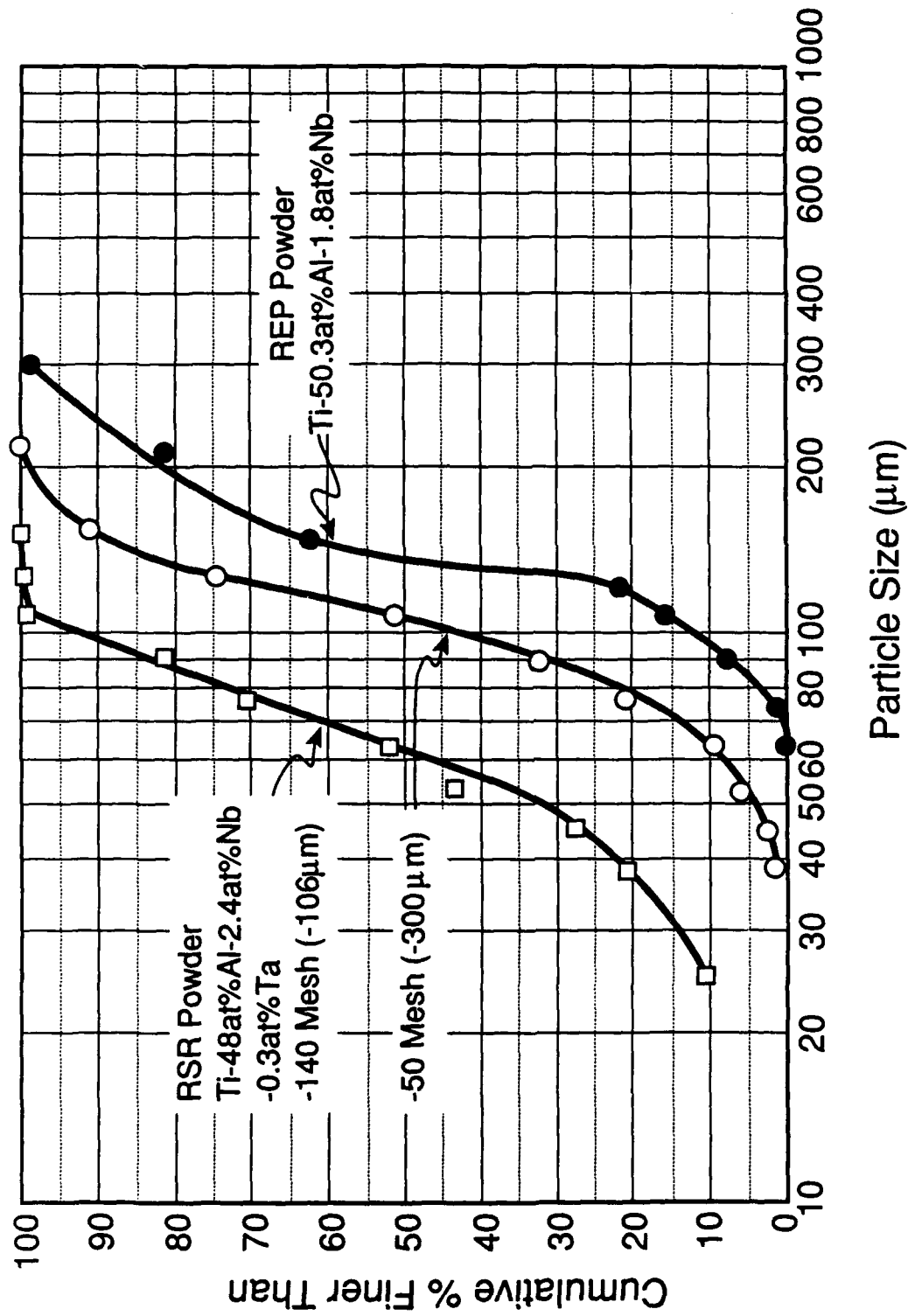


Figure 1. Particle size distribution for the REP and RSR powders.

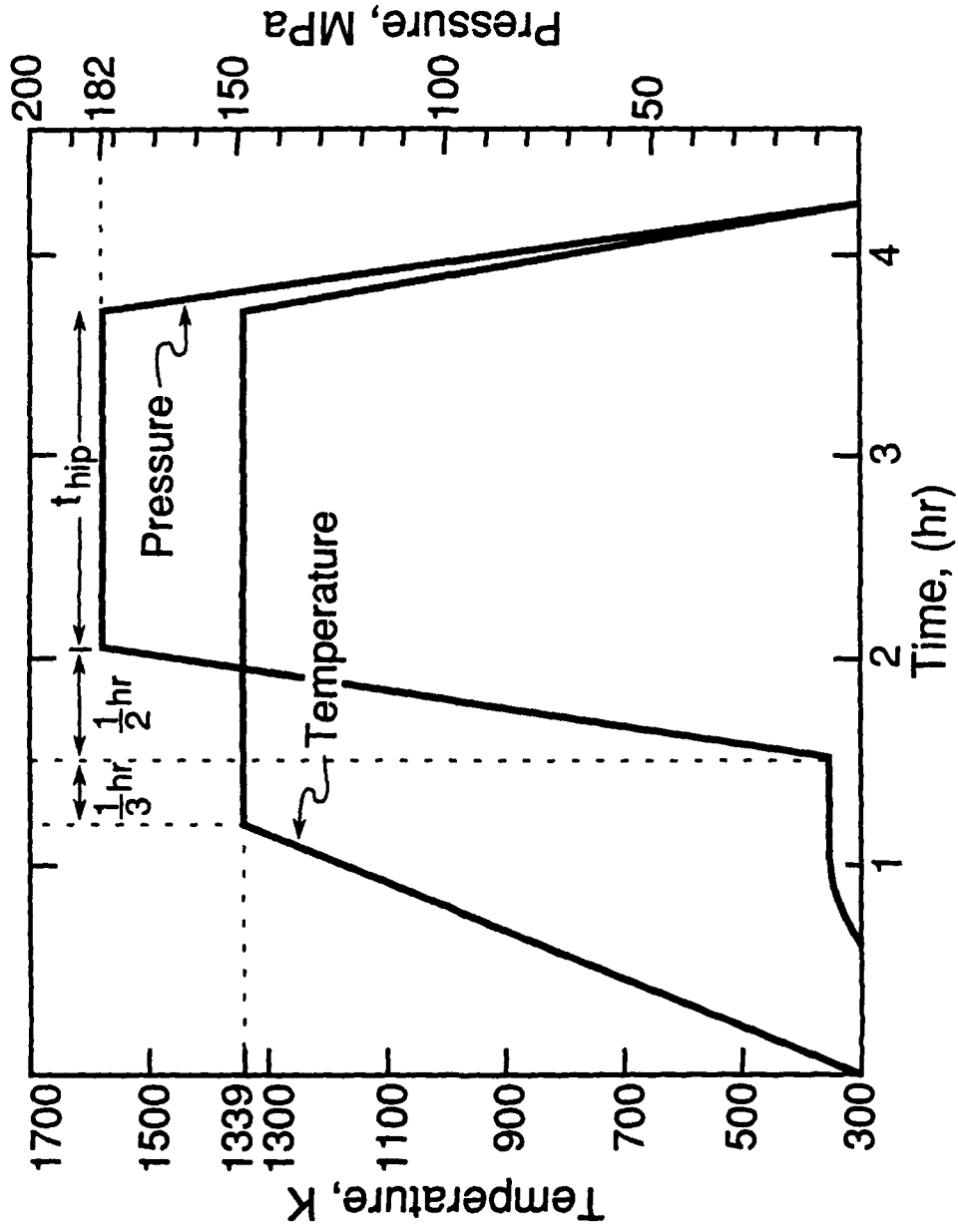


Figure 2. Typical temperature and pressure trajectories for a HIPing cycle.

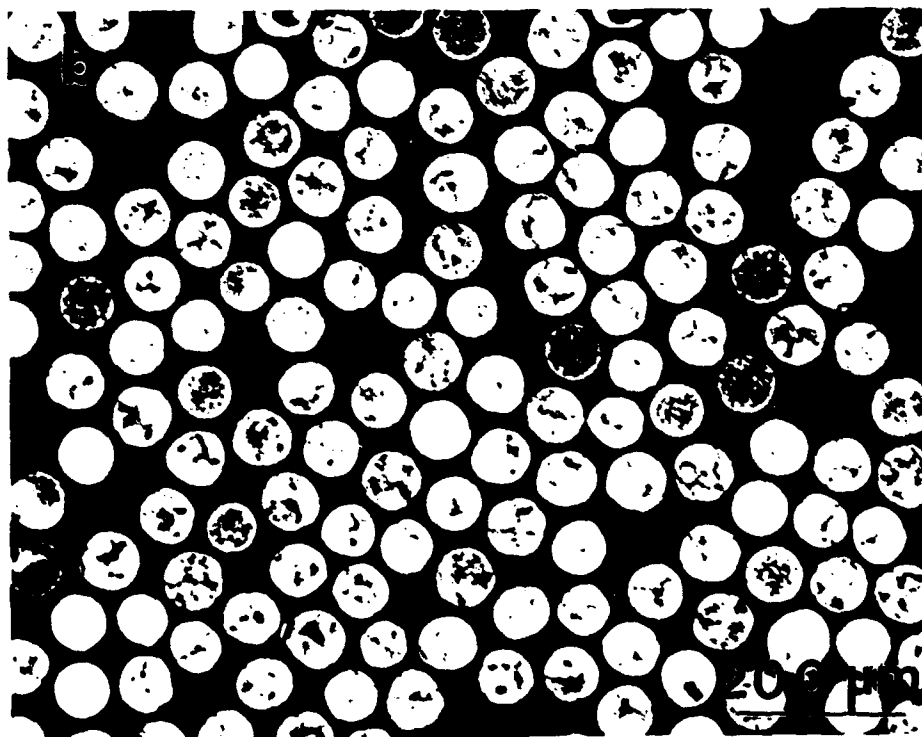
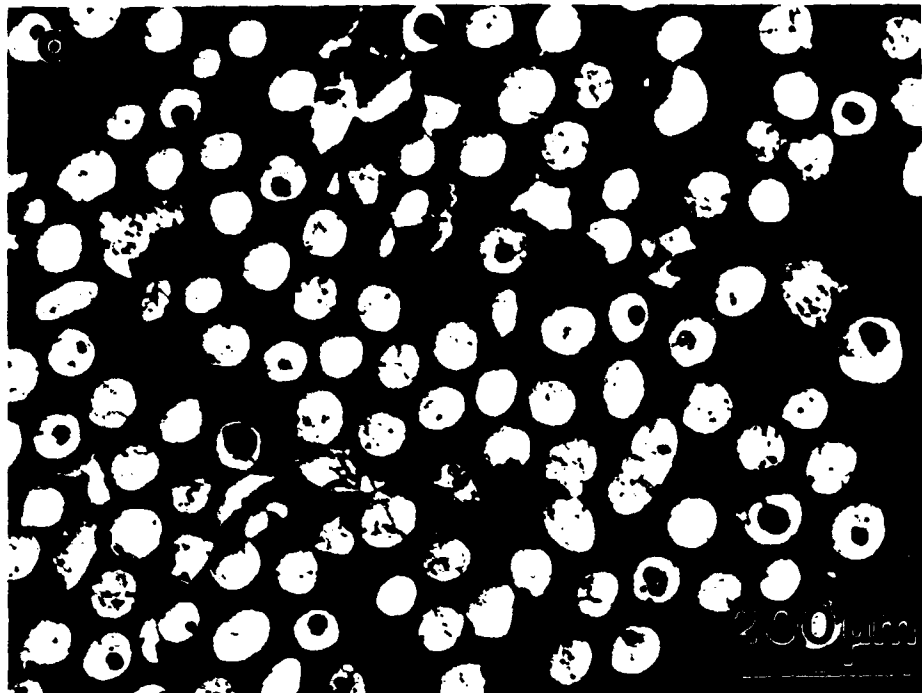


Figure 3. Cross sections of 63 μ m to 75 μ m size powders; (a) RSR, (b) REP.



Figure 4. SEM views of rapidly solidified powders; (a) and (b) are coarse ($>150\mu\text{m}$) and fine ($\sim 30\mu\text{m}$) powders of RSR, respectively, (c) and (d) are coarse ($>150\mu\text{m}$) and fine ($\sim 20\mu\text{m}$) powders of REP, respectively.

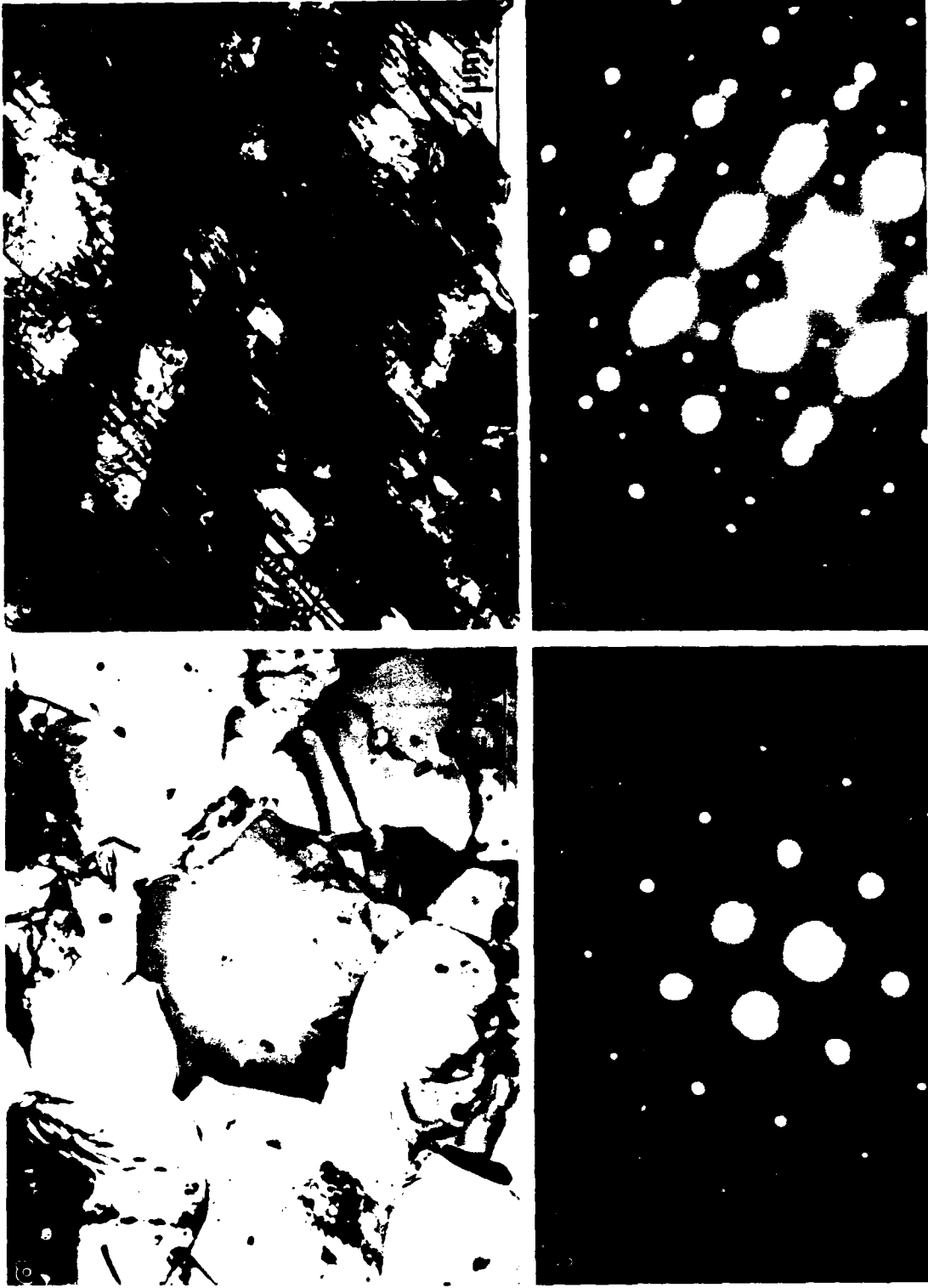


Figure 5. TEM micrographs of vacuum hot forged billet prior to high temperature X-ray; (a) fine grained γ , (b) $[101]_{\gamma}$ zone axis, (c) area containing γ twins and α_2 laths, (d) zone axis showing a single $[1210]_{\alpha}$ zone and two twin related $[110]_{\gamma}$ zones.

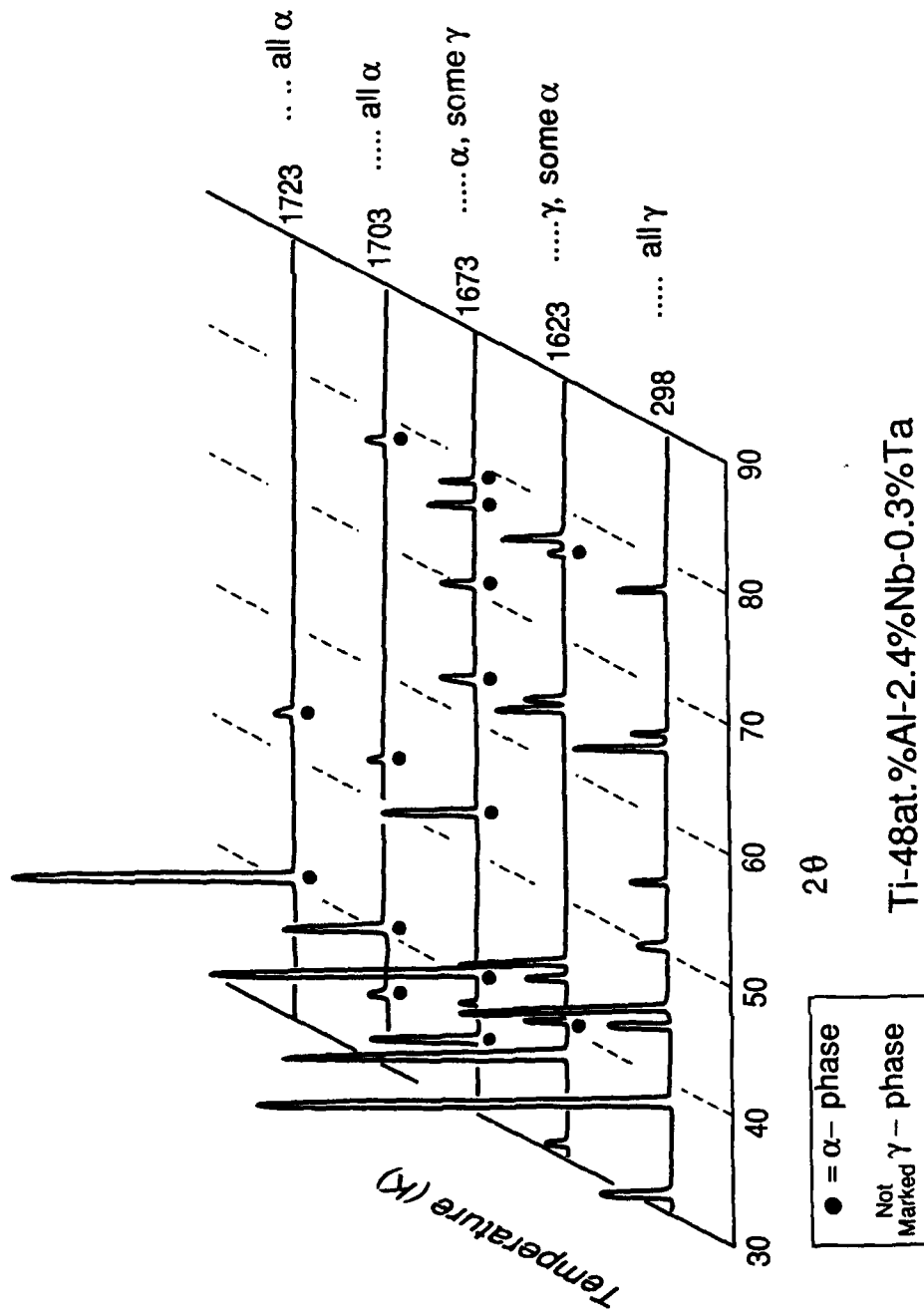


Figure 6. X-ray diffraction spectra of Ti-48%Al-2.4%Nb-0.3%Ta alloy taken at selected temperatures. Note the progressive change from γ to α with increasing temperature.

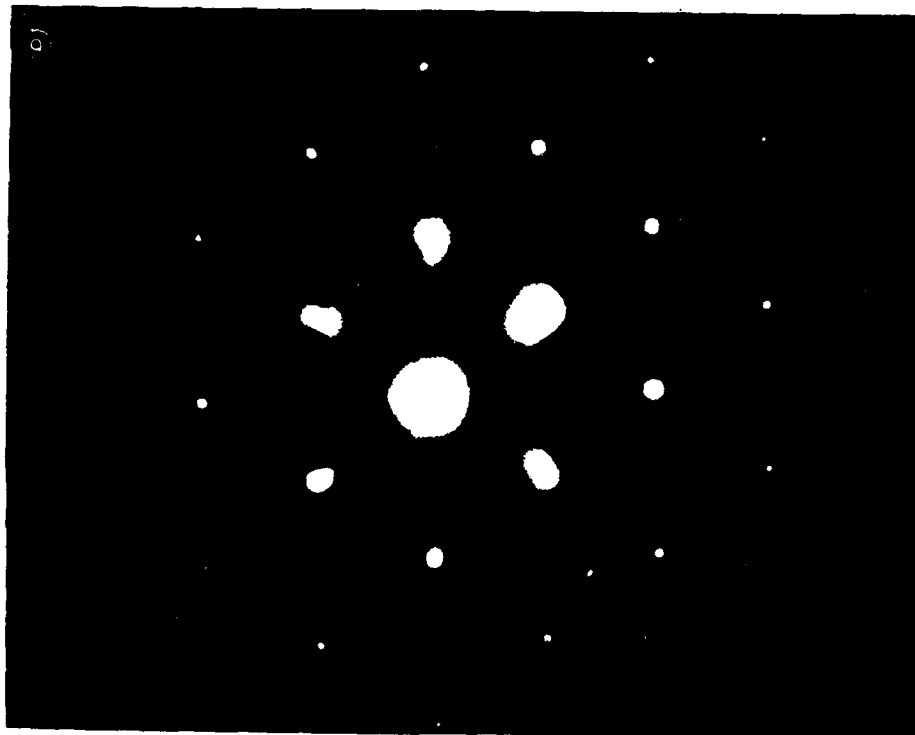


Figure 7. Consolidated microstructure of Ti-50.3%Al-1.8%Nb alloy made from REP powder; (a) fine grained γ , (b) $[101]_{\gamma}$ diffraction pattern from a single γ grain.

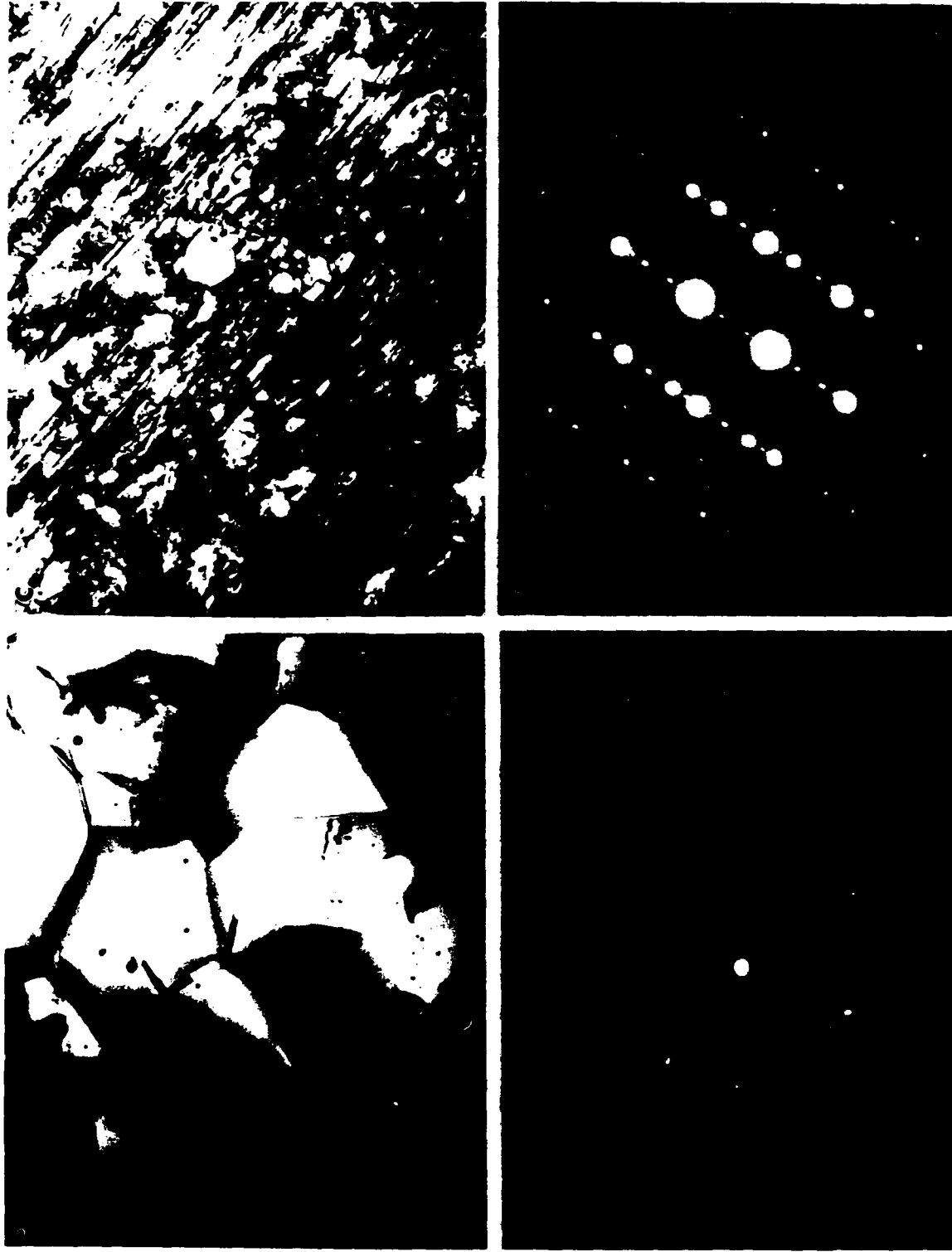


Figure 8. Consolidated microstructures of Ti-48%Al-2.4%Nb-0.3%Ta alloy made from RSR powder; (a) fine grained γ region and (b) diffraction pattern, $[101]_{\gamma}$ zone axis, (c) region of γ twins and α_2 lath, (d) diffraction pattern showing a $[1210]_{\alpha_2}$ zone and two twin related $[110]_{\gamma}$ zones.

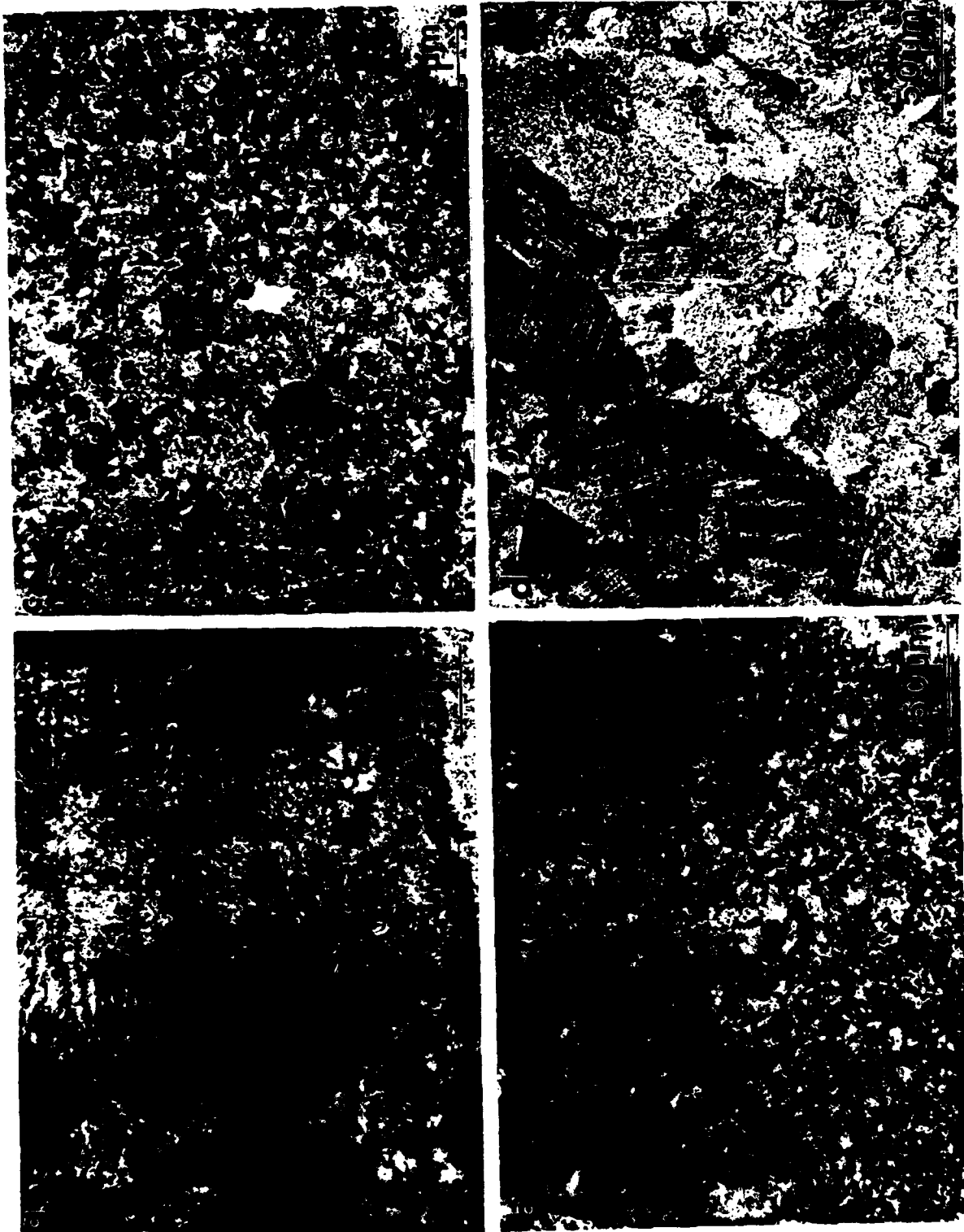


Figure 9. Effect of increased HIPing temperatures at 182MPa and 4 hours on the grain size of REP material; (a) 1073K, (b) 1173K, (c) 1223K, and (d) 1339K.



Figure 10. Duplex grain structure in REP powder consolidated at 1339K and 182MPa for 1 hour.

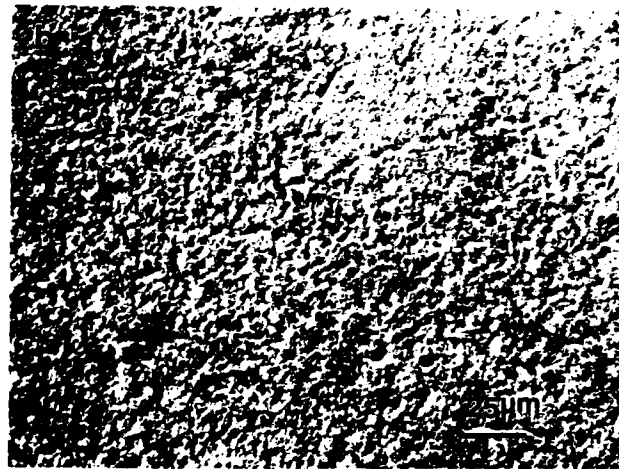


Figure 11. Material consolidated at 1339K for 4 hours; (a) REP Ti-50.3%Al-1.8%Nb exhibiting cracks, and (b) RSR Ti-48%Al-2.4%Nb-0.3%Ta which is free from cracks.

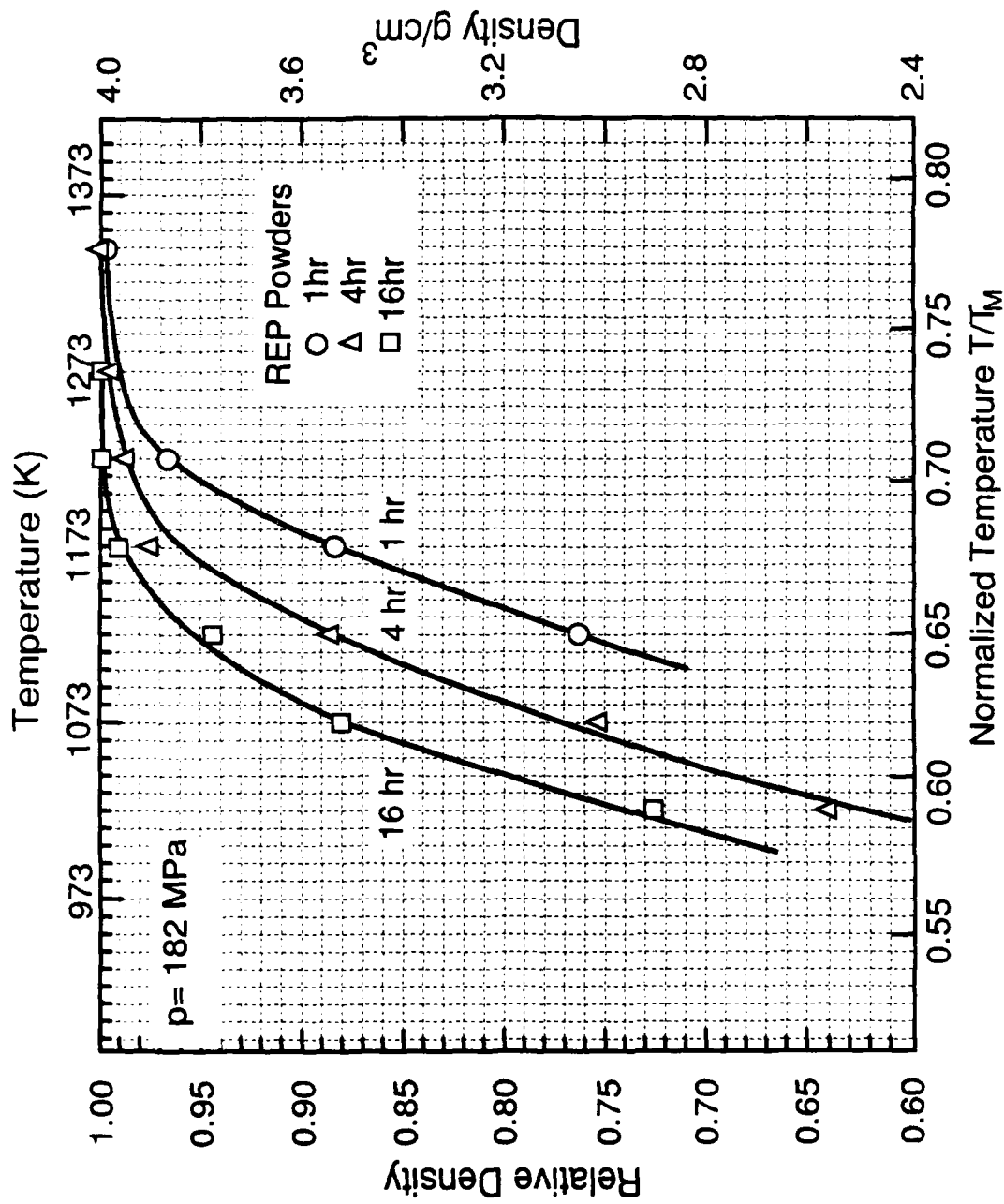


Figure 12. Experimental consolidation curves, constant time contours, for REP powder showing the influence of temperature and time on densification at 182MPa.

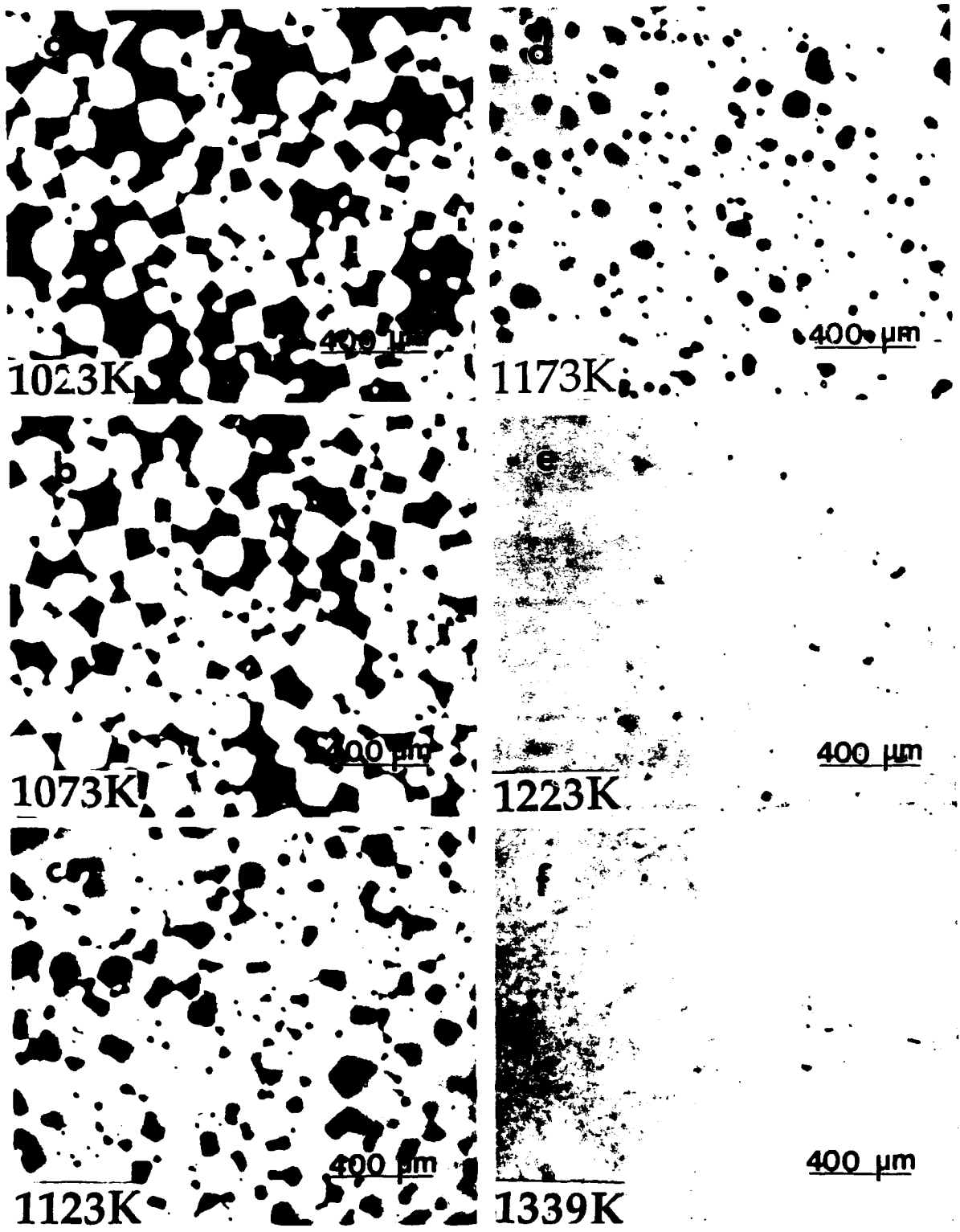


Figure 13. Microstructures of REP powders consolidated at 182MPa for 4 hours; (a) 1023K, (b) 1073K, (c) 1123K, (d) 1173K, (e) 1223K, and (f) 1339K.



Figure 14. Microstructures of REP powders consolidated at 182MPa and 1173K for 1 hour; (a) and (b) are SEM views of a fractured specimen showing particle contact areas and creep deformation, (c) is a cross-sectional view of the polished specimen.

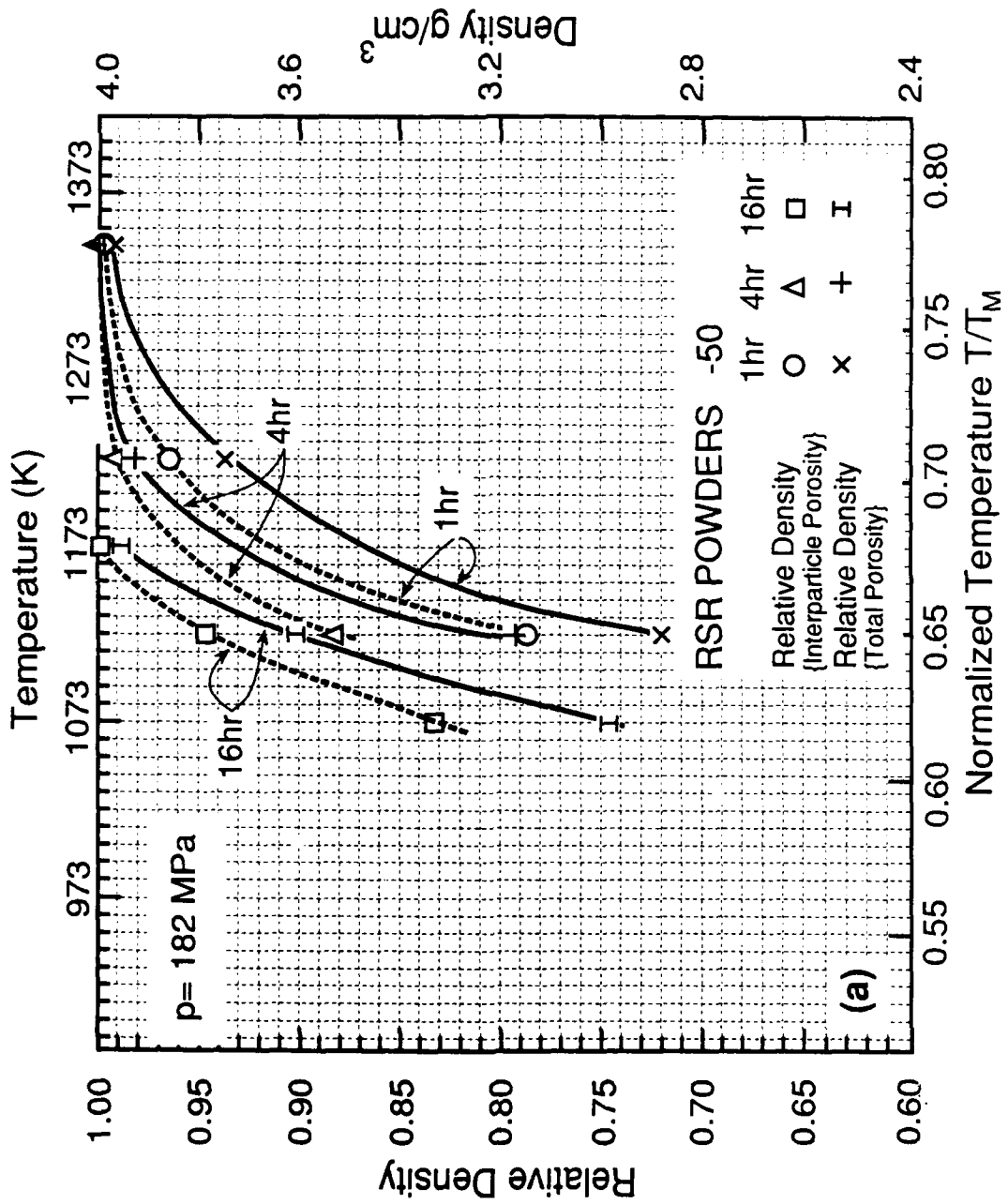


Figure 15

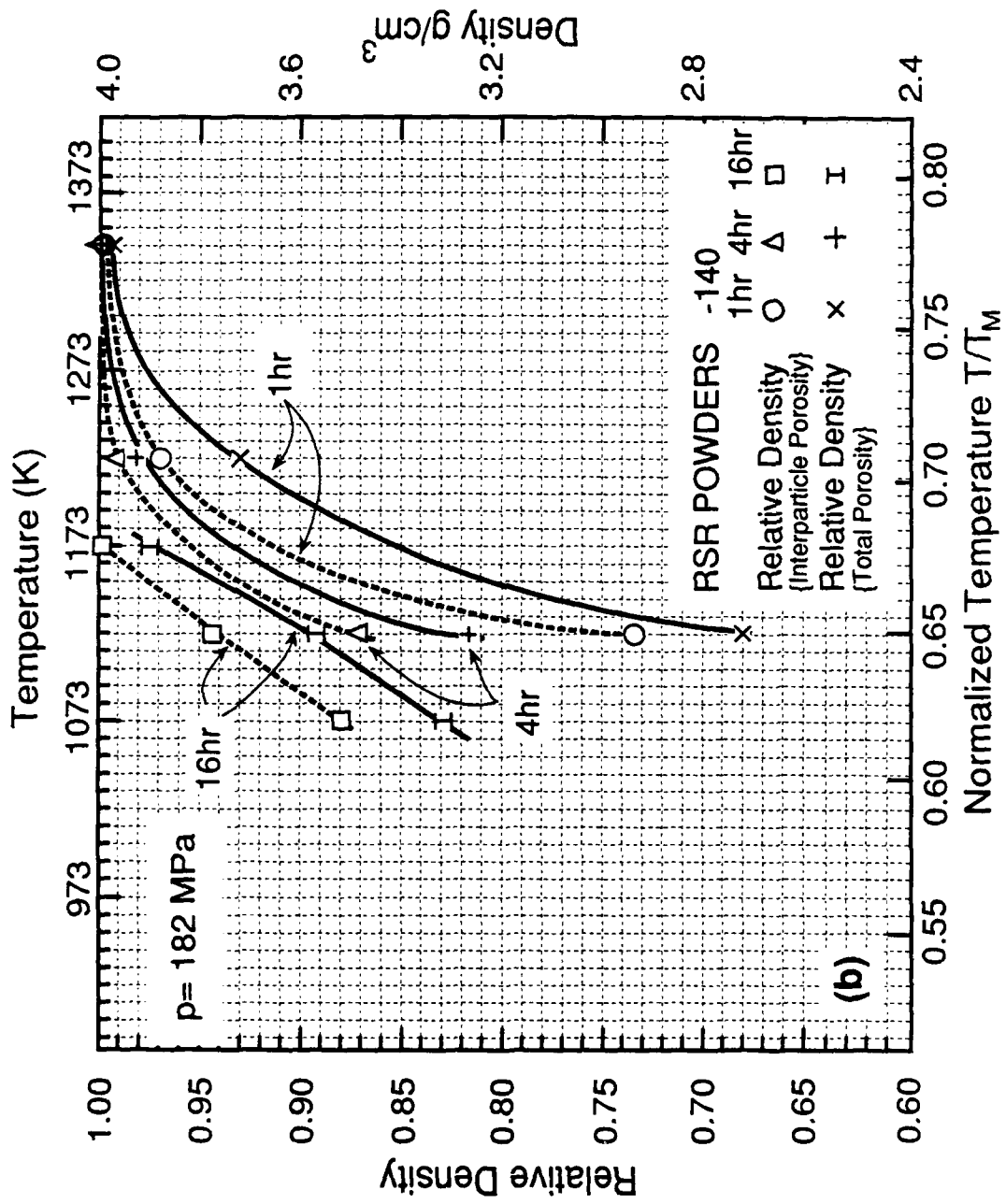


Figure 15.

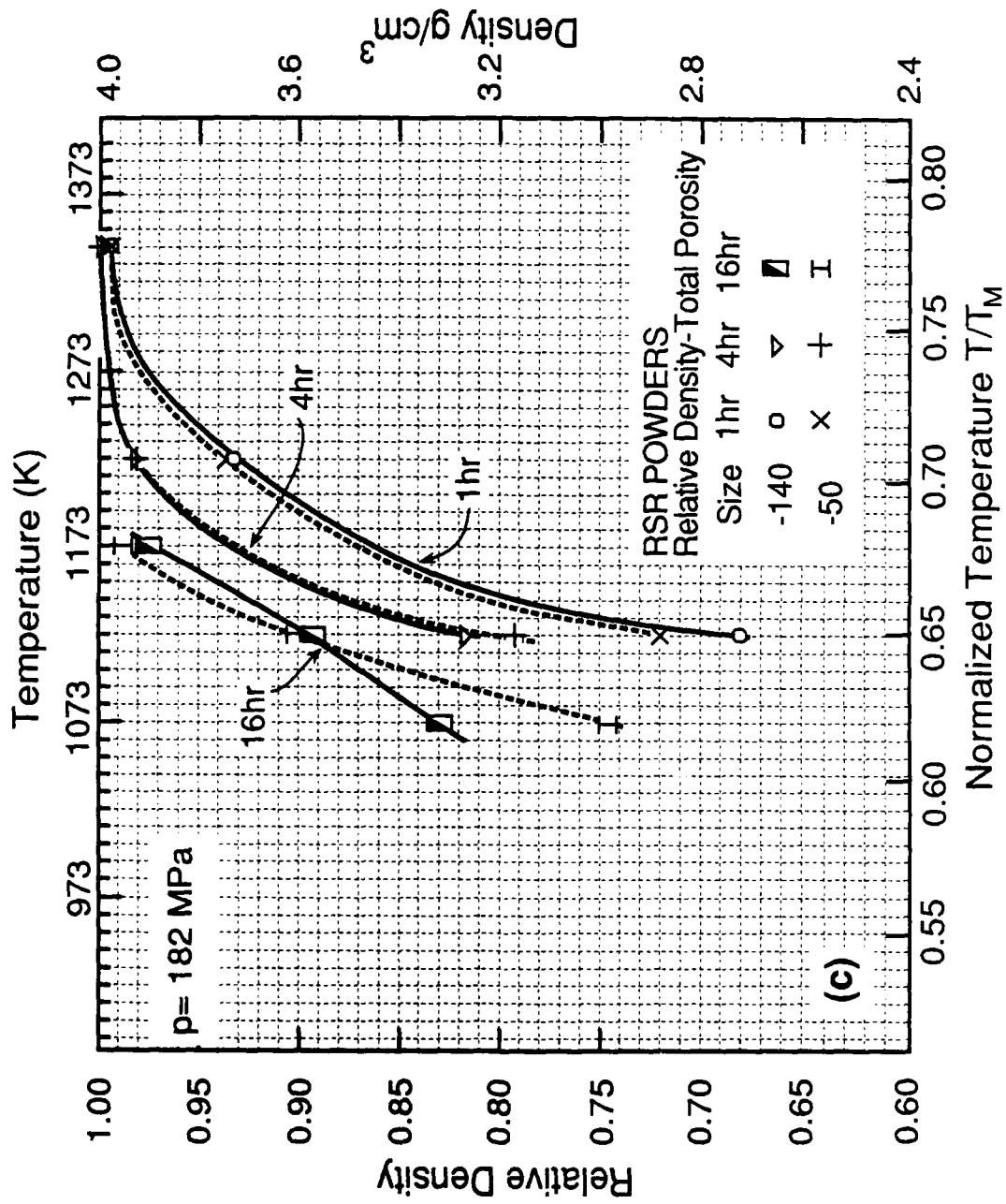


Figure 15. Consolidation curves, constant time contours, at 182MPa for the RSR powders of different size distribution; (a) -50 mesh (<math><106\mu\text{m}</math>), (b) -140 mesh (<math><300\mu\text{m}</math>) and (c) both size distributions.

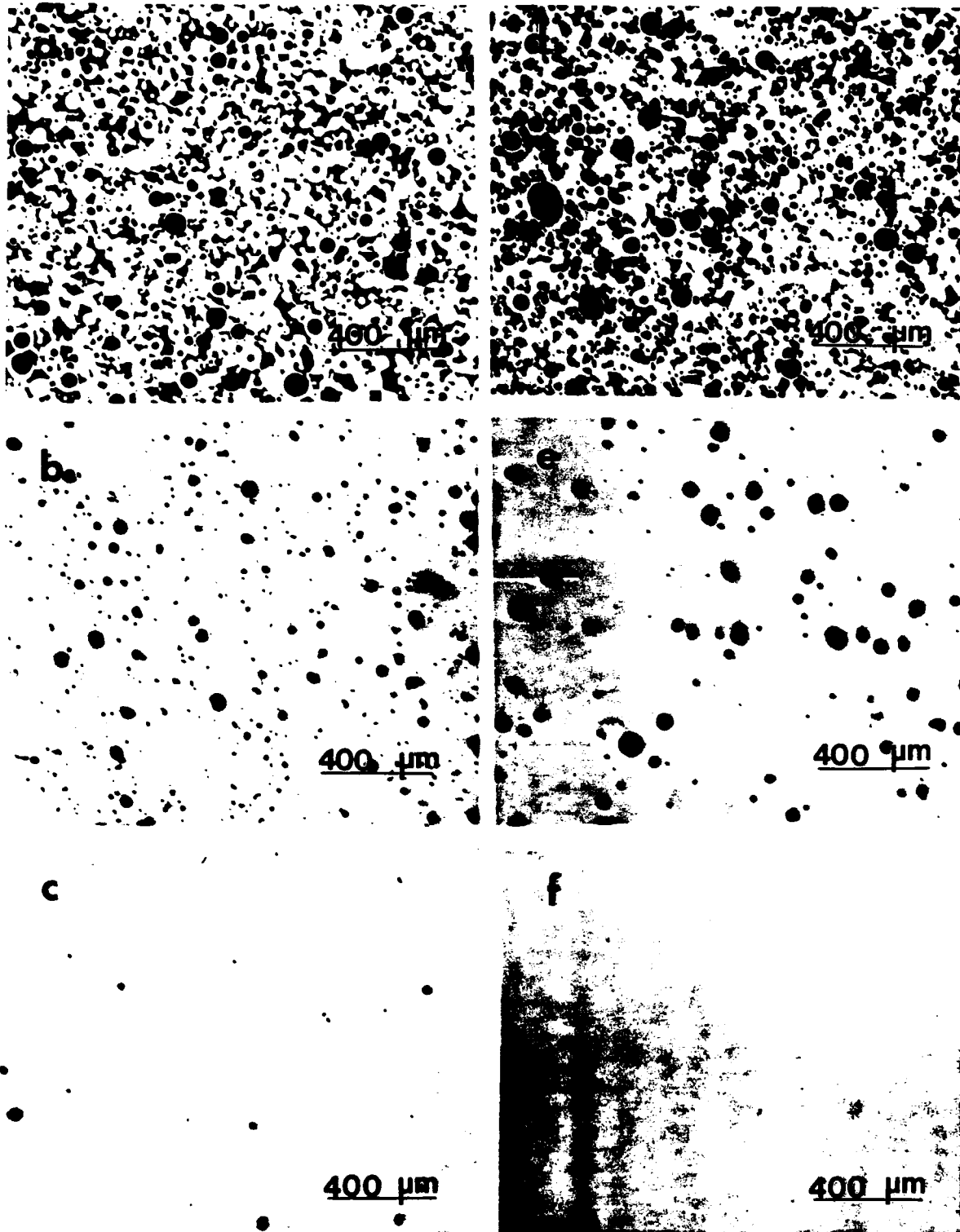


Figure 16. Microstructures of RSR powders, -140 mesh ($<106\mu\text{m}$) consolidated at 182MPa; (a), (b) and (c) for 1 hour at 1123K, 1223K, and 1339K, respectively; (d), (e), and (f) for 4 hours at 1123K, 1223K, and 1339K, respectively.

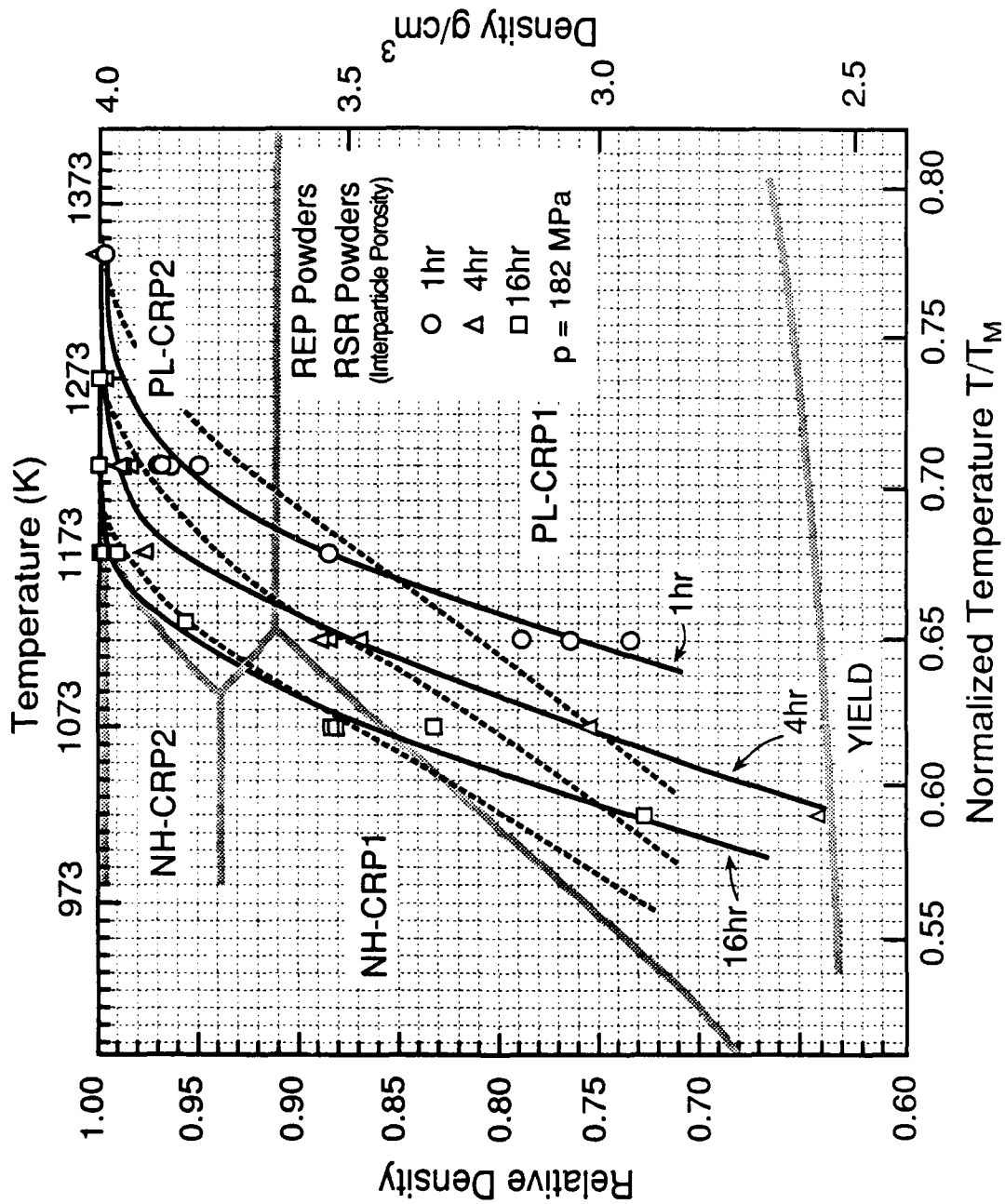


Figure 17. Experimental consolidation curves, constant time contours (solid lines) at 182MPa combining the data for the REP and RSR powders (interparticle porosity only). Calculated HIP map (dotted lines) is superimposed.

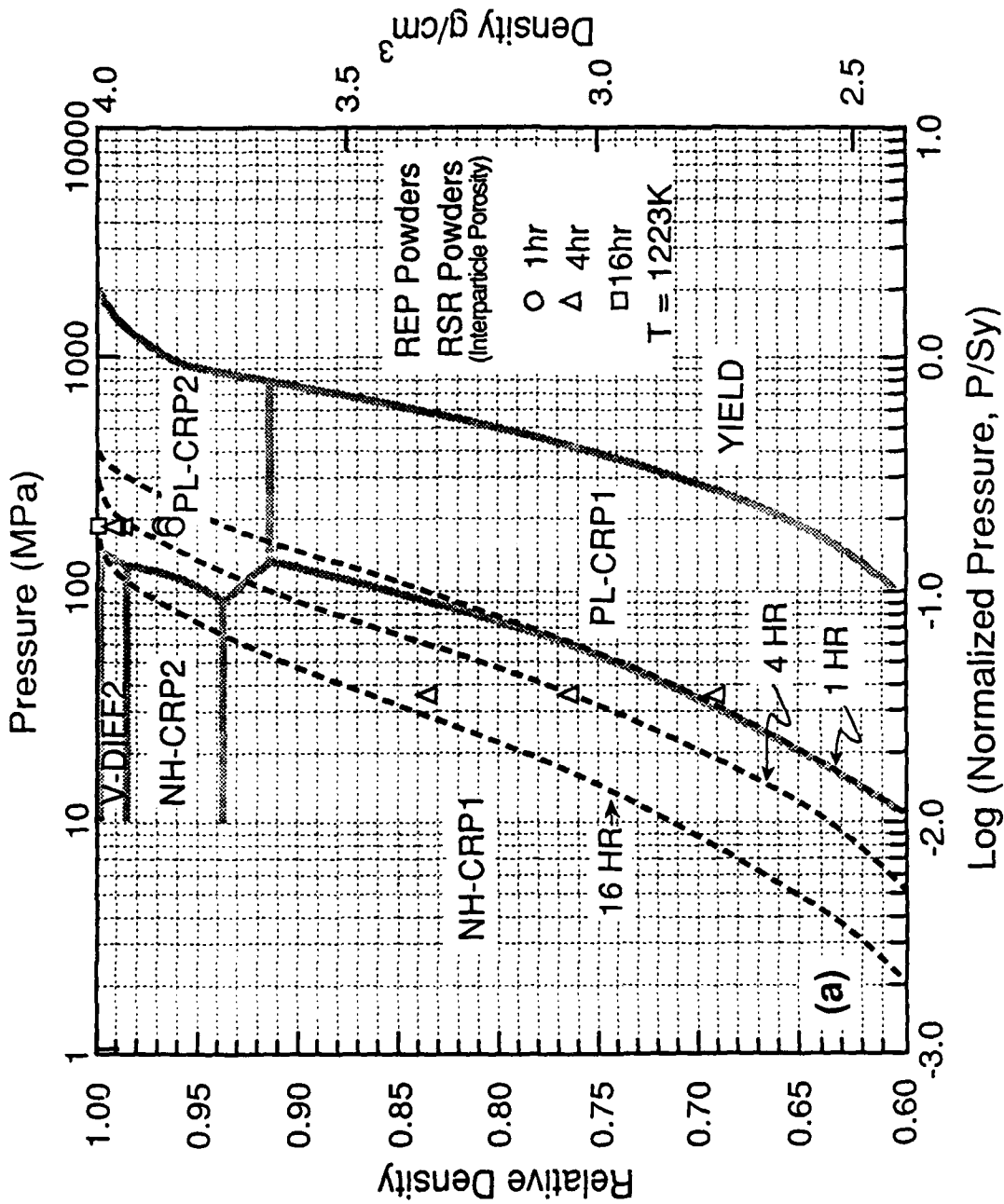


Figure 18.

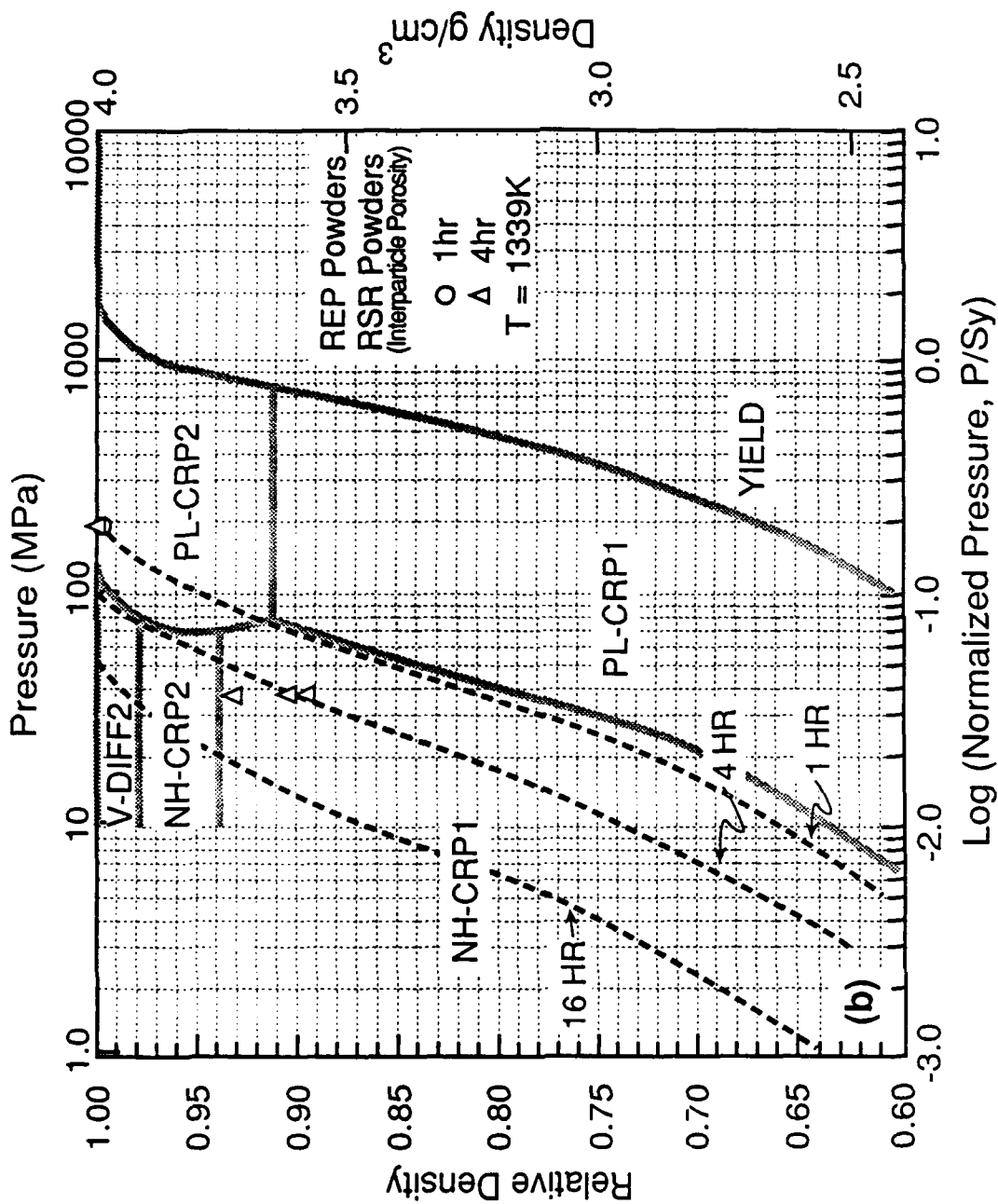


Figure 18. Calculated HIP maps (dotted lines) at constant temperature for REP and RSR powders superimposed on the experimental data; (a) 1223K, and (b) 1339K

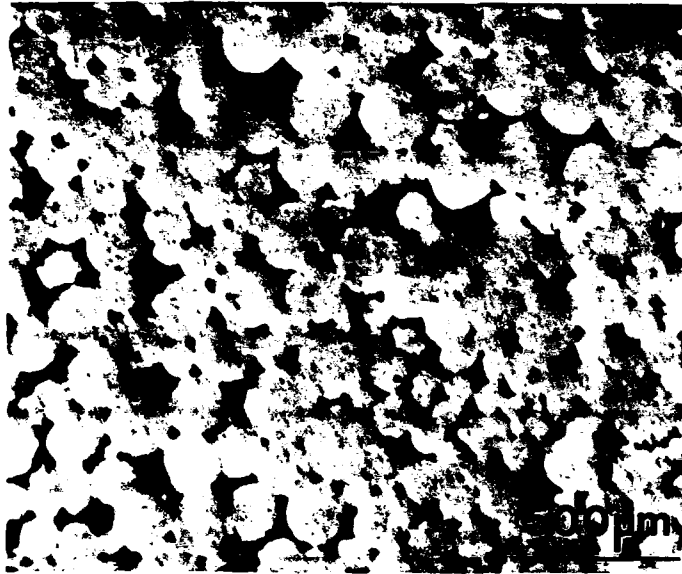


Figure 19. Microstructure of REP powder consolidated at 1339K and 34.5MPa for 4 hours.

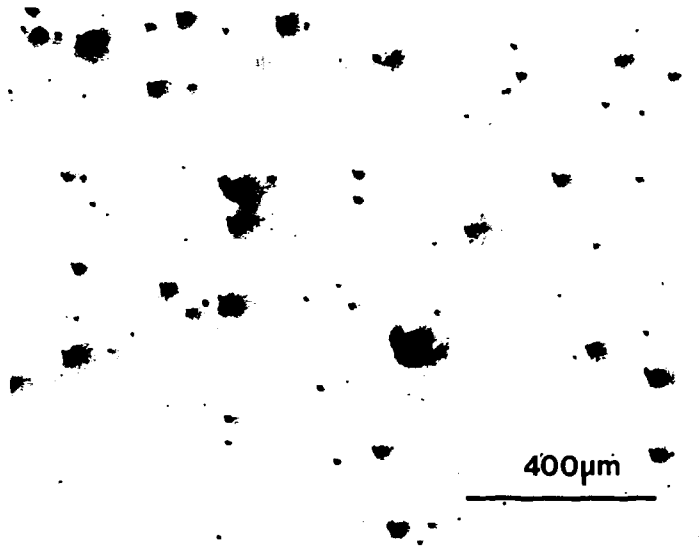


Figure 20. Microstructure (gas porosity) in the -50 mesh RSR powder initially HIPed at 182MPa/1339K/4hours and reheat treated at 0.1 MPa/1339K/1hour.

**Experimental Verification of HIP
Densification Models for γ -Titanium
Aluminide Using In Situ Sensing**

by

B. Paden, B.W. Choi, J. Marschall, Y.G. Deng,
C. McCullough and R. Mehrabian

Materials Department
Mechanical and Environmental Engineering Department
College of Engineering
University of California
Santa Barbara, California 93106

ABSTRACT

Hot Isostatic Pressing (HIP) is an effective process for consolidating powders to produce near-net shapes, while potentially retaining the microstructural advantages of rapid solidification and compositing, required to achieve toughness in intermetallics. The desired microstructures/interface interactions can be preserved provided that the HIP cycle is of sufficiently short duration and/or is performed at a relatively low temperature. Hence, knowledge of the time to full densification is important in optimum HIP cycle design. This time can be estimated by using the Helle-Easterling-Ashby models or by directly sensing the dimensions of the sample *in situ*. In this paper we compare the Helle-Easterling-Ashby models to experimental densification data obtained with an *in situ* sensor on γ -titanium aluminide powders produced by REP. Further, we suggest a hybrid approach for estimating the density on-line which uses the mathematical models to filter the sensor data.

1. INTRODUCTION

Hot Isostatic Pressing is an ideal process for the consolidation of rapidly solidified metallic and intermetallic powders into near-net shapes, thereby retaining the microstructural advantages (e.g. fine dispersoid size) of rapid solidification. Furthermore, it may be a necessary approach for alloys prone to severe segregation and cracking when processed by conventional casting techniques. In the special case of γ -titanium aluminides, compositing of the powders with other more ductile phases (powders) may be necessary to attain acceptable room temperature toughness. Control of interface interactions between the ductilizing phases and the γ -matrices is a critical factor for the toughening process [1]. Requirements for minimizing the diffusional processes leading to microstructure coarsening or interface interactions are that the HIP cycle duration be relatively short and/or the process be carried out at a low temperature relative to the melting point of the powder. Nonetheless, it is common for HIP cycle times to be excessively long to ensure that the powder is fully densified. This results in unnecessary production costs in addition to undesirable diffusional processes noted above.

The possibilities for cost reduction and property enhancement in HIPed materials has motivated the mathematical modelling of densification mechanisms by Helle, Easterling, and Ashby [2], and the development of the HIPing maps [3]. These models describe the effects of powder properties and HIP conditions on the densification of the powder compact. These models have been very useful for interpolating, extrapolating, and understanding experimental data, as well as predicting HIP cycles. However, it is not yet clear if sufficient precision will be achieved to predict optimum complex

pressure/temperature/time cycles, especially when microstructural changes (e.g. dynamic recrystallization occur during consolidation and/or material input parameters are not available [4]).

The need for experimental verification of the Helle-Easterling-Ashby (HEA) models and the associated software for HIP maps, has led to the development of clever sensing schemes capable of measuring dimensional changes of samples in the hostile HIP environment. The first such sensor was an eddy-current dilatometer developed at the National Institute of Science and Technology (NIST) [5]. Other, more direct measurement approaches have also been developed [5].

In this paper we use a sensor similar to that developed at NIST to experimentally verify the densification models for a γ -titanium aluminide alloy. We focus on a γ -alloy because of the low density and high stiffness which may make this family of alloys, appropriately toughened, suitable for aerospace applications. Further, the likely fabrication route will involve powder metallurgy and the use of HIP for consolidation. In our previous work [4] we showed that the HIP maps generated using the Helle-Easterling-Ashby (HEA) model agreed well with the experimental data for two γ -titanium aluminide alloys, produced by the Rotating Electrode Process (REP) and the Rapid Solidification Rate (RSR) process, except for deviations observed in the low temperature power-law creep regime, and in high-temperature/short-duration HIP cycles. In contrast to the continuous measurements reported here the previous verification experiments involved interrupting HIP cycles at various temperatures and pressures. The additional information provided by the sensor is extremely detailed and allows us to verify the HEA model during pressurization and at a large number of points through the HIP cycle.

The outline of this paper is the following. Section 2 outlines our experiments. In Section 3 we describe the eddy-current sensor used in our experiment and include performance tests verifying the sensor function. Section 4 is a comparison between the HEA model and our experimental data for γ -titanium aluminide REP powder. In Section 5 we show how absolute density can be extracted from the sensor data by fitting the models to the data. Our conclusions are made in Section 6.

2. EXPERIMENTS

Powder The composition of the REP powder used in this study was Ti-50.3at%Al-1.8at%Nb with 0.2at% Oxygen as contaminant. The as-received powder was sieved into different size fractions to determine the size distribution which has a mean diameter of 140 μ m; the exact size distribution, as well as X-ray and SEM characterization of the powder, is given in a recent paper [4].

Sample Preparation The REP powder was carefully "canned" in a length of commercial purity titanium tubing (12.7mm OD by 0.70mm wall thickness) as follows. The tubing was crimped and TIG (tungsten inert gas) welded to seal one end. Next, in an argon filled glove box, the powder was poured into the tube and a closed valve with a powder-restraining filter was fitted to the open end. The resulting assembly was removed from the glove box, evacuated, degassed at roughly 600K, and the second end of the tube was crimped twice so that the valve could be removed. This end was also TIG welded to ensure a reliable seal.

HIPing Samples were HIPed in an ASEA QIH-3 hot isostatic press at 182 MPa with the temperature and times listed in Table 1. The HIP cycles used in the experiments were "temperature first" in the sense that the sample was heated and allowed to reach thermal equilibrium at the desired HIP temperature before the pressure was ramped from ~ 0.15 MPa to 182 MPa. Once full pressurization was reached the samples were soaked for the times listed t_h (holding time) and then simultaneously cooled and depressurized. The primary reason that temperature first profiles were chosen is that the eddy-current dilatometer we used must be in thermal equilibrium for measurements to be useful.

Density Measurements Density measurements were made, for the loose powder, with (i) a pycnometer, (ii) *in situ* with the eddy-current dilatometer, and, (iii) at the end of each run with an image analyzer. The pycnometer measurements were straight-forward and were averaged to obtain a loose packing density of 0.607. The *in situ* technique is quite sophisticated and is the subject of the next section. The density measurements made at the end of each run were made with cut and polished samples. The magnified image of a $478\mu\text{m} \times 638\mu\text{m}$ section of the polished sample was captured using the image analyzer. The resulting greyscale image was compared to a threshold level to generate a black and white image with pores being identified with the black regions. The results from seven images were averaged to find the fractional area occupied by pores. The relationship "area fraction equals volume fraction" was used to estimate the porosity.

3. DENSIFICATION SENSING

In our experiments, the relative density of a cylindrical γ -titanium aluminide sample is computed from changes in its cross sectional area during HIPing. The measurement of the area is made *in situ* using an eddy-current sensor similar to the sensor developed at the National Institute for Science and Technology [3]. Our sensor is shown in Figure 1 and consists of two concentric coils encircling a cylindrical conductive sample tube. The details of the sensor construction material are listed in Table II.

The outer primary coil is driven with a sinusoidal input current with frequency ω rad/sec (typically $2\pi \times 500\text{kHz}$), and the induced voltage in the inner secondary coil is taken as the output. The amplitude and phase of the output relative to input is dependent on the cross-sectional area and conductivity of the sample, and is used to sense the dimension of the sample during HIPing.

The key instrument of the sensing system is the Hewlett-Packard 4192A impedance analyzer, see Figure 2 for an electrical schematic for the system. This analyzer synthesizes a sinusoidal reference signal and also measures the gain and relative phase between its *reference* and *test* inputs. The *reference* input is taken to be the primary coil current and the *test* input is the voltage on the secondary. The relationship between the cross section of the sample tube and the gain/phase measurement is as follows.

The axial magnetic induction phasor, H_0 , in the region between the sample and the primary coil is easily determined from Ampere's law and the symmetry of the coil. Using the approximation that the primary coil is infinitely long and that the diameter of the coil is small relative to the wavelength $\lambda = (\text{speed of light})/2\pi\omega$, we have:

$$H_0 e^{j\omega t} = \frac{n_1 I_0 e^{j\omega t}}{l_1} \quad (1)$$

where n_1 is the number of turns on the primary, I_0 is the primary current phasor, and l_1 is the length of the primary. The magnitude of the magnetic induction inside the sample is less than the magnitude of H_0 , since eddy-currents in the conductive sample tube (and powder) act to cancel magnetic fields penetrating the sample tube. In fact, the magnetic field in the sample tends to zero as $\omega \rightarrow \infty$. In the special case that the sample is a uniform conductor, the induced voltage per turn in the secondary coil is given by:

$$e(a, K) = -n_2 \omega \mu \pi H_0 \left[a^2 \left(\frac{2}{ka} \right) \frac{\text{ber}' ka + j \text{bei}' ka}{\text{ber} ka + j \text{bei} ka} + j(b^2 - a^2) \right] \quad (2)$$

where $k = (\omega \mu \sigma + j \omega^2 \mu \epsilon)^{0.5}$ ($\approx (\omega \mu \sigma)^{0.5}$ for typical metals and frequencies), μ is the magnetic permeability of the sample, σ is the conductivity, ϵ is the permittivity, a is the radius of the sample, b is the radius of the secondary coil, and ber and bei are the bessel-real and bessel-imaginary functions respectively [7]. In terms of these variables, we measure a^2/b^2 , the fractional area of the secondary occupied by the sample tube.

Equation 2 can be simplified if we introduce a normalized impedance $Z_n(a, k)$ as follows. Define the impedance $Z(a, k) = -e(a, k) / H_0$ and $Z_n(a, k) = jZ(a, k) / Z(0, k)$. From Equation 2 we have:

$$Z_n(a, k) = \left[\frac{a^2}{b^2} \left(\frac{2}{ka} \right) \left(\frac{\text{ber}'ka + j\text{bei}'ka}{\text{ber}ka + j\text{bei}ka} \right) + j \left(\frac{b^2 - a^2}{b^2} \right) \right] \quad (3)$$

A plot of $Z_n(a, k)$ for $a^2 = 0.65b^2$, and ka ranging from 0 to ∞ is shown in Figure 3. There are three features to observe in this plot (1) $\lim_{k \rightarrow \infty} Z_n(a, k) = j(1 - a^2/b^2)$; hence the cross sectional area of sample relative to that of the secondary can be read directly from the impedance plot. (2) The curve approaches the j -axis at an angle of 45 degrees; that is $\lim_{k \rightarrow \infty} \arg(Z_n(a, k) - a^2/b^2) = \pi/4$. (3) $\lim_{k \rightarrow 0} Z_n(a, k) = j$; in words, the sample is invisible to the sensor at low frequencies. These properties can be verified analytically using asymptotic expressions for the ber and bei functions [8]. The first property alone would be sufficient to obtain the cross sectional area of the uniform cylindrical sample if we could operate the sensor at very high frequencies. However, there is parasitic capacitance in the sensor leading to resonances which invalidate the relationship of Equation 2 at high frequencies. (In our sensor the first resonance occurs at 2.4MHz). Hence, we use properties (1) and (2) together to estimate the diameter of the sample tube. The sensor is used at a frequency considerably below its first resonance but high enough that we are operating near the 45 degree asymptote of the impedance curve in Figure 3. The normalized impedance at this frequency is simply projected along the 45 degree line to the j -axis and the intercept is approximately $j(1 - a^2/b^2)$. From this intercept the cross-sectional area of the sample can be computed directly.

The performance of our sensor was verified at room temperature with a solid commercial purity titanium rod. One measurement was made to check the theoretical normalized impedance curve, and a series of measurements with the rod successively turned down on a lathe was used to verify the linearity of the sensor output in the cross-sectional area of the

sample. Figure 4 shows the plot of the normalized impedance of the sensor with a 12.7mm titanium rod. The match with the theory is good although the impedance curve does deviate from the 45 degree line at frequencies above 500 kHz due to the aforementioned electrical resonances in the primary coil. Figure 5 shows a comparison of the dimension of the solid titanium rod when measured with the sensor versus calipers¹. The linearity is excellent over a large range.

To this point we have only considered uniform cylinders. Before using the sensor on samples consisting of REP powder packed in titanium tubes we must establish that the sensor output is equivalent at high frequencies in these two cases. Recall that electromagnetic radiation decays exponentially as it penetrates a conductor. The distance at which the fields decay to $1/e$ of its value at the surface of the conductor is called the "skin depth" and is equal to $(2/\sigma\omega\mu)^{0.5}$. Hence, a tube with a wall thickness greater than the skin depth is virtually indistinguishable electrically from a solid rod, i.e. only the change in position of the outer surface is monitored. In our samples a titanium tube is used which has a wall thickness of 0.7mm and has a conductivity² of roughly 8.0×10^5 mho/m at 1339K. Thus, the skin depth at 500kHz is 0.77mm which is comparable to the wall thickness. Hence we can use our sensor to measure the dimensions of our sample. Ideally, the wall thickness would be much greater than the skin depth, but this would require increasing the frequency of operation of the sensor or increasing the thickness of the tubing, both of which are undesirable. Increasing the frequency brings us too close to the

¹ The initial sensor reading with the 12.7mm rod was used as a calibration point to determine the cross-sectional area of the secondary coil (3.62cm^2). Thus, the point $(\pi 1.27^2 / (4 \times 3.62), \pi 1.27^2 / (4 \times 3.62)) = (3.50, 3.50)$ is necessarily on the curve in Figure 5.

² This conductivity is measured with the eddy-current sensor.

sensor resonance and increasing the wall thickness would mean that the load bearing effect of the sample tube could not be ignored.

4. COMPARISON WITH THE DENSIFICATION MODELS

The eddy-current sensor provides a method for monitoring dimensional changes in a sample during HIPing. In this section we describe the generation of experimental densification versus time plots and compare them to theoretical plots obtained from the HEA models.

A typical plot of sensor output versus time is shown in Figure 6 together with the HIP pressure and temperature trajectories. The sensor output shows thermal transients during temperature ramping which are due to thermal expansion of the sample and coils, and, to some degree, changes in the conductivity in the sample tube. In addition, observe the large reduction in the cross section of the sample as the pressure is applied and the smaller dimensional changes after full pressure is attained. There are additional transients in the sensor output during cooling.

The sensor output cannot be calibrated for the entire HIP cycle since the dynamic thermal behavior of the sensor is far too complex to model. However, static compensation following the thermal transients can be made. The compensation is relatively straight-forward and can be computed using Equation 2 and the coefficients of thermal expansion for the sensor components (a detailed analysis is given in Reference [5]). The errors are gain errors and offsets in the sensor output. The gain of the sensor is affected by the lengthening of the primary coil which causes a proportional reduction of

the magnetic field in the secondary coil. This is compensated using knowledge of the coefficient of expansion of the Mullite coil form. The offset in the sensor output is caused by an increase in the diameter of the secondary, and to field penetration through the wall of the titanium tubing. These offsets are compensated in the density calculation by knowing the precise density at some point in the HIP cycle. In our case we cut the HIP sample and measure the final density directly with the image analysis system. The expansion in the sample need not be compensated in constant temperature runs since the fractional dimensional change is all that is required in our density calculations.

With the assumption that densification is uniform throughout the powder during HIPing, the relative density, Δ , of the powder compact is given by the relation:

$$\Delta = \Delta_f \frac{V_f}{V} \quad (4)$$

where Δ_f is the final relative density, V is the volume of the compact, and V_f is the final volume of the compact. The assumption of uniform densification is justified since the pure titanium sample tubes used are much softer than the REP powder. Using the eddy-current sensor we have direct measurement of the cross-sectional area of the sample - then we can use the relationship:

$$\Delta = \Delta_f \left(\frac{A_f}{A} \right)^{\frac{3}{2}} \quad (5)$$

where A is the cross-sectional area of the powder in the sample tube and A_f is its final value. (The fractional contribution of the titanium tubing to the cross sectional area of the sample is subtracted from the sensor output.)

The relationship of Equation 5 was used with sensor data corresponding to segments V and VI in Figure 6 to generate experimental densification curves. Figures 7 and 8 show these curves for the $t_h = 3.5$ hours at 1223K and the $t_h = 2$ hours at 1339K HIP cycles (samples #5 and #7 in Table I). The final relative densities from the other HIP cycles, measured with the image analyzer, are superimposed on the plots together with the pycnometer data for the initial packing density. Figure 9 shows microstructures of REP powders consolidated during the pressure ramp-up, samples #1 and #6 in Table I. Our comments on the data are the following. (1) The small scale fluctuations in the density measured with the sensor are attributed to electrical noise. (2) The sensor densification curves are calibrated with the final relative density measured with the image analyzer. Hence, the experimental curves necessarily pass through the final image analyzer data point. (3) There is some disparity between the sensor curve for 1223K and the measured relative density data points from the shorter time HIP cycles. (4) The initial packing density predicted by the calibrated sensor readings match the independent pycnometer measurement very well. (5) Again we see significant densification early in the cycle while pressurization is underway.

Theoretical curves for HIP runs in Figures 7 and 8 were generated from the HEA models for comparison with the experimental data. The HEA models are differential equations relating densification rate to pressure, temperature, and powder properties. Individual densification rate equations have been derived for individual mechanisms including; plastic yielding, volume diffusion, boundary diffusion, power-law creep, and Nabarro-

Herring creep. With an abuse of notation we denote the contributions by these mechanisms to the overall densification rate by $\dot{\Delta}_{yield}$, $\dot{\Delta}_{vol-diff}$, $\dot{\Delta}_{bnd-diff}$, $\dot{\Delta}_{pl-crp}$, and $\dot{\Delta}_{NH-crp}$ respectively. Simplified expressions for these contributions are given by [3]

$$\dot{\Delta}_{yield} = \frac{d}{dt} \left[\frac{(1-\Delta_o)}{1.3S_y(t)} P + \Delta_o^3 \right]^{1/3} S_1 + \frac{d}{dt} \left[1 - \exp \left(-\frac{3P(t)}{2S_y(t)} \right) \right] S_2 \quad (6)$$

$$\dot{\Delta}_{vol-diff} = 43C (1-\Delta_o) \frac{D_v}{r^2} \frac{P\Omega}{kT} S_1 + 270 (1-\Delta)^{1/2} \left[\frac{1-\Delta}{6} \right]^{1/3} \frac{D_v}{r^2} \frac{P\Omega}{kT} S_2 \quad (7)$$

$$\dot{\Delta}_{bnd-diff} = 43C^2 \frac{\delta D_b}{r^3} \frac{P\Omega}{kT} S_1 + 270 (1-\Delta)^{1/2} \frac{\delta D_b}{r^3} \frac{P\Omega}{kT} S_2 \quad (8)$$

$$\dot{\Delta}_{pl-crp} = \frac{3.1}{C^{1/2}} D_{crp} \Delta \left(\frac{CP}{3S_{ref} \Delta^2} \right)^n S_1 + 1.5 D_{crp} \Delta (1-\Delta) \left[\frac{1.5}{n} \frac{P}{S_{ref}} \frac{1}{(1-(1-\Delta)^{1/n})} \right]^n S_2 \quad (9)$$

$$\dot{\Delta}_{NH-crp} = 14.4 \left[\frac{D_v}{G_2} + \frac{\pi\delta D_b}{G^3} \right] \frac{C^{1/2}}{\Delta} \frac{P\Omega}{kT} S_1 + 32 \left[\frac{D_v}{G^2} + \frac{\pi\delta D_b}{G^3} \right] (1-\Delta) \frac{P\Omega}{kT} S_2 \quad (10)$$

(See Appendix for notation.)

These five mechanisms are combined into a single differential equation for the densification rate:

$$\dot{\Delta} = \dot{\Delta}_{yields} + \dot{\Delta}_{vol-diff} + \dot{\Delta}_{bnd-diff} + \dot{\Delta}_{pl-crp} + \dot{\Delta}_{NH-crp} \quad (11)$$

with the initial condition that $\Delta(0)$ is the initial packing density. To validate this model we set $\Delta(0) = 0.607$ (the measured loose packing density) and integrated Equation 11 numerically. The material parameters we used were the realistic-but-tuned parameters we obtained in our previous work [4]. These are listed in Table III. The temperature and pressure trajectories were the actual trajectories we programmed in the HIP and include the pressure-ramp shown in Figure 6. The resulting theoretical density trajectories are superimposed on our experimental data in Figures 10 and 11. The overall match is reasonable considering the uncertainties in the input parameters and the assumptions of the models, e.g. mono-size powder. There is, however, significant deviation, from a predictive perspective, in the 1223K run after full pressurization.

5. ON-LINE DENSITY ESTIMATION

In the previous section we used the final density of a sample to calibrate offsets in the sensed densification curve. This is acceptable for experimental verification of the HEA models, but is not useful in most applications where final density is not known and on-line monitoring of densification is desired. In this section we exploit the mathematical HIPing models to estimate the initial packing density and thus calibrate the density curve on-line. The idea is to use the theoretical shape of the densification curves to extrapolate the sensor data and estimate the asymptotic value of the sensor data corresponding to full densification. The distance between the asymptotic value and the present value determines the density.

The theoretical prediction for the densification trajectory $\Delta_\theta(t)$ (θ for theoretical) is obtained by numerically integrating the HEA models. Equation 5 gives a sensor based estimate, $\Delta_s(t)$. In both cases the density trajectory depends on knowledge of the true density on some point of the trajectory (e.g. initial packing density). We use the condition that the two estimated density trajectories should be as close as possible to obtain a good estimate of the initial packing density. The measure we choose for quantifying "close as possible" is the integral-squared-error between the two estimates of the density. Formally, we estimate the initial density by

$$\bar{\Delta}_0 = \operatorname{argmin}_{\Delta_0 \in [0,1]} \int_0^T (\Delta_s(\Delta_0, t) - \Delta_\theta(\Delta_0, t))^2 dt \quad (12)$$

where the dependence of $\Delta_\theta(t)$ and $\Delta_s(t)$ on the initial packing density is made explicit. The minimization in Equation 12 is carried out numerically and the best estimate of the density at time T is taken to be $\Delta_s(\bar{\Delta}_0, T)$.

This procedure was applied to the interval [120 and 214 minutes] in HIP cycle #4 in Table I, $t_h = 1.5$ hours and 1223K, with the enhancement that the optimization allowed several of the material input parameters to vary within reasonable limits. This helps improve the fit to the data and the quality of the density estimate. The resulting curves $\Delta_\theta (\bar{\Delta}_O, t)$ and $\Delta_s (\bar{\Delta}_O, t)$ are plotted in Figure 12 as the calculated (theoretical) and the experimental (sensor) trajectories, respectively. The density estimate at 214 minutes is the final point on the experimental curve. The sample was cut and polished and analyzed to give the true relative density, 0.964. This data point is noted on the plot and shows a small deviation of about 1.2% from the estimate.

6. CONCLUDING REMARKS

The key observation we make in this work is that the sensor provides a wealth of information about HIP densification of γ -titanium aluminide during HIPing. First, the densification curves in Figures 7 and 8 show that a significant amount of densification occurs during pressurization. Even in the lower temperature experiments (1223K) we measure 0.92 relative density with the sensor after the 26 minute pressurization ramp. Due to the fact that temperature and pressure ramps are not modeled in the HIP 487 software [3], maps are generated that may not be as accurate as possible. The densification during pressurization is a possible explanation for the disagreement we observed between the predicted maps and our previous high-temperature/short-cycle-time experiments [4]. The sensor also reveals asymptotic errors in the theory, as revealed in Figures 10 and 11. As previously noted, no account has been taken of observed dynamic recrystallization during densification or allowance made for a different low

temperature power-law creep regime [4]. The computer program used herein coupled to the sensor data are currently being used to address these issues and refine the input parameters. Finally, the discrepancy between density measurements and sensor data at 1223K at short times needs to be addressed. Earlier microstructural and high temperature X-ray data [4, 9] showed that the as-solidified REP powder consists of primary hexagonal α -dendrites which subsequently transform to a $\alpha_2 + \gamma$ lath structure, with γ segregate in the interdendritic spaces. This microstructure reverts to all γ during high temperature heat treatment. The transformation is not accounted for in the model and may also cause some stiffening, in the absence of dynamic recrystallization, during short cycle times at 1223K. The latter may explain the discrepancy between the sensor and image analyzer data noted in Figure 7.

ACKNOWLEDGEMENTS

This work was sponsored by the Defense Advanced Research Projects Agency under a University Research Initiative Grant N00014-86-K-0753, supervised by Dr. Ben Wilcox and monitored by Steven Fishman of the Office of Naval Research. The authors are grateful to Dr. Martin Blackburn of Pratt and Whitney for providing the REP powders. Discussions with Professor Mike F. Ashby are gratefully acknowledged.

7. APPENDIX

Nomenclature

Δ, Δ_0	Relative Density, Initial Relative Density
$\dot{\Delta}$	Densification rate
δD_b	Boundary diffusion coefficient times boundary thickness (m^3/s)
D_v	Volume diffusion coefficient (m^2/s)
D_{ov}, D_{ob}	Pre-exponentials for volume and boundary diffusion (m^2/s)
G	Grain size in powder (m)
k	Boltzmann's constant ($1.38 \times 10^{-23} J/K$)
n	Creep exponent
P	HIP pressure (MPa)
Q_b	Activation energy for boundary diffusion (KJ/mol)
Q_{crp}	Activation energy for creep (KJ/mol)
Q_v	Activation energy for volume diffusion (KJ/mol)
r	Powder radius
R	Gas constant ($8.314J/mol - degree Kelvin$)
S_1, S_2	Smoothing factors
T, T_m	Absolute temperature, Absolute melting temperature (K)
t	Time (s)
S	Stress (MPa)
S_y, S_0	Yield stress, Yield stress at $293^\circ K$ (MPa)
S_{ref}	Reference stress for creep (MPa)
Ω	Atomic or molecular volume (m^3)
α	T-dependence of yield stress

$$D_v = D_{ov} e^{-\frac{Q_v}{RT}} \quad (13)$$

$$\delta D_b = \delta D_{ob} e^{-\frac{Q_b}{RT}} \quad (14)$$

$$D_{crp} = 10^{-6} e^{-\frac{Q_{crp}}{RT_m}} [T_m / T - 2] \quad (15)$$

$$C = \frac{1 - \Delta_o}{\Delta - \Delta_o} \quad (16)$$

$$S_y = S_o + \alpha(T - 293) \quad (17)$$

REFERENCES

- [1] H.E. Deve, A.G. Evans, G.R. Odette, R. Mehrabian, M.L. Emiliani and R.J. Hecht, submitted to *Acta Metall.*
- [2] A.S. Helle, K.E. Easterling, and M.F. Ashby, "Hot Isostatic Pressing Diagrams: New Developments" *Acta Metall.*, 33, 1985, pp. 2163-2174.
- [3] M.F. Ashby, "Operating Manual for HIP487 - A Program for Constructing Maps for Hot Isostatic Pressing," Cambridge University Engineering Department, September, 1987.
- [4] B.W. Choi, Y.G. Deng, C. McCullough, B. Paden, and R. Mehrabian, "Densification of Rapidly Solidified Titanium Aluminide Powders During Hot Isostatic Pressing," Submitted to *Acta Metall.*, 1989.
- [5] A.H. Kahn, M.L. Mester, and H.N.G. Wadley "Eddy-current techniques for HIP sample dimension measurements", Second International Conference on Hot Isostatic Pressing - Theory and Applications, Gaithersburg, MD, June 7-9, 1989.
- [6] H. P. Buchkremer, R. Hecker, D. Stöver, H. Raes "Development and Use of a HIP Dilatometer," Second International Conference on Hot Isostatic Pressing - Theory and Applications, Gaithersburg, MD, June 7-9, 1989.
- [7] M. Abramowitz and I. Stegun, (eds.) *Handbook of Mathematical Functions*, Dover, New York, 1972, pp. 379-382.
- [8] H. L. Libby, *Introduction to Electromagnetic Nondestructive Test Methods*, Wiley, 1971, pp. 323-327.
- [9] C. McCullough, J.J. Valencia, C.G. Levi and R. Mehrabian, *Acta Metall.*, 37, 1989, pp. 1321-1336.

TABLE I

Measured Relative Density Versus Consolidation
Conditions for Ti-50.3at%Al-1.8at%Nb REP Powder

Sample #	Temperature	Holding Time, t_h , at Full Pressure (hr)	Final Relative Density
1	1223	0	0.895
2	"	0.5	0.924
3	"	1.0	0.950
4	"	1.5	0.964
5	"	3.5	0.980
6	1339	0.0	0.978
7	"	2.0	0.998

TABLE II**Materials Used in Sensor Construction**

Coils	Alumel
Coil Forms	Mullite (Machinable Ceramic)
Temp. Coefficient of Coil Forms	$5.3 \times 10^{-6}/K$
Primary Coil Diameter	31mm
Secondary Coil Diameter	19mm
Primary Winding	Bifilar-40 Double turns at 1.4mm/turn
Secondary Winding	36 turns at 1 mm/turn
1st Resonance in Primary	2.4MHz

TABLE III**Input Parameters for HIP Maps**

<u>Input Parameter</u>	<u>Value</u>
1. Melting point (K)	1730
2. Surface energy (J/m ²)	1.76
3. Young's modulus (GPa)	168
4. T-dependence of modulus	0.313
5. Yield stress (MPa)	981
6. T-dependence of yield stress	0.775
7. Atomic volume (m ³)	1.63 × 10 ⁻²⁹
8. Pre-exp. vol. diffusion (m ² /s)	8.30 × 10 ⁻⁷
9. Activ. energy, vol diff. (kJ/mol)	200
10. Pre-exp. bdry. diff. (m ³ /s)	7.60 × 10 ⁻¹³
11. Activ. energy. bdry. diff. (kJ/mol)	180
12. Pre-exp. surface diff. (m ³ /s)	7.60 × 10 ⁻⁹
13. Activ. energy surf. diff. (kJ/mol)	150
14. Power law creep exponent	3.00
15. Reference stress, P-L creep (MPa)	2350
16. Activ. energy for P-L creep (kJ/mol)	320
17. Solid density (kg/m ³)	4.00 × 10 ³
18. Particle radius (m)	7.03 × 10 ⁻⁵
19. Initial relative density	0.607
20. Initial pore pressure (MPa)	0.1
21. Grain diameter in particle (m)	3.00 × 10 ⁻⁵

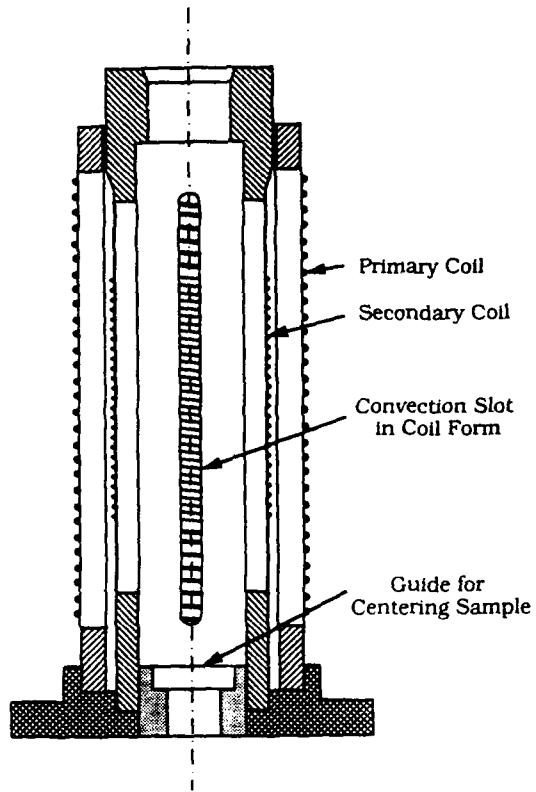


Figure 1: Schematic cut-away view of the eddy-current sensor.

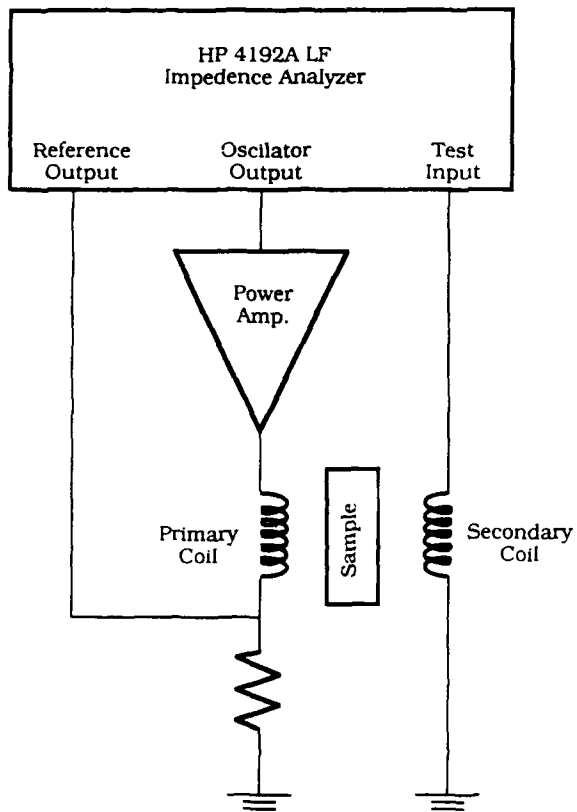


Figure 2: Schematic diagram of the sensor system

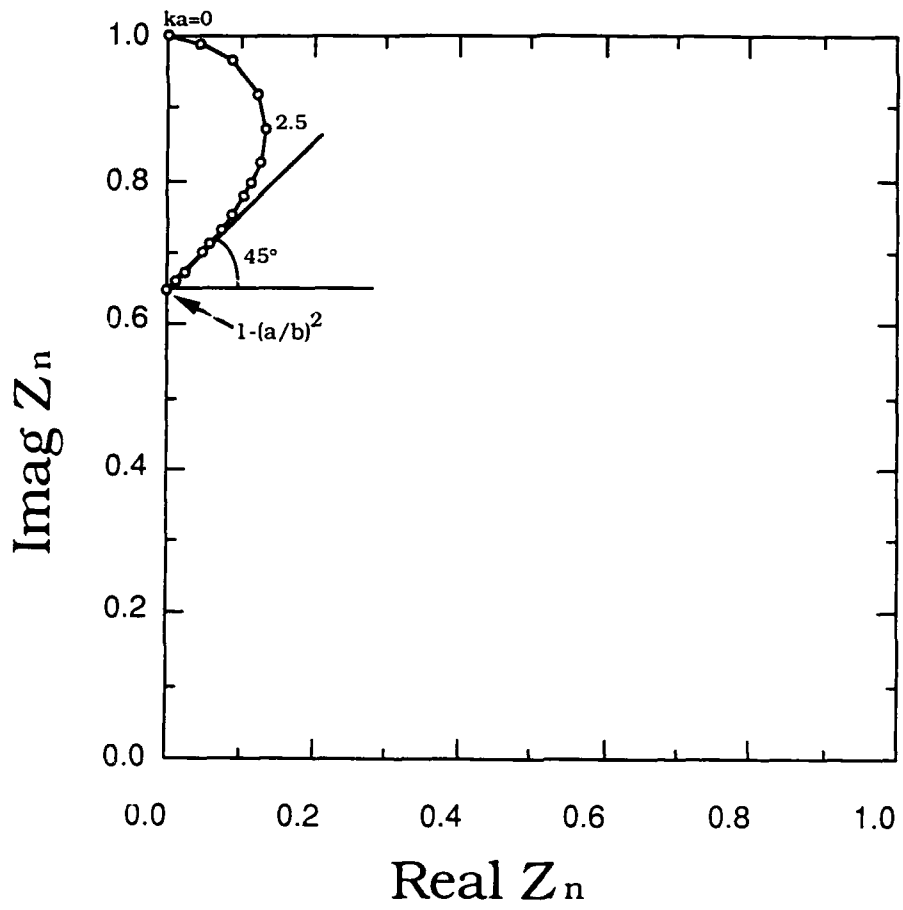


Figure 3: Theoretical normalized impedance curve

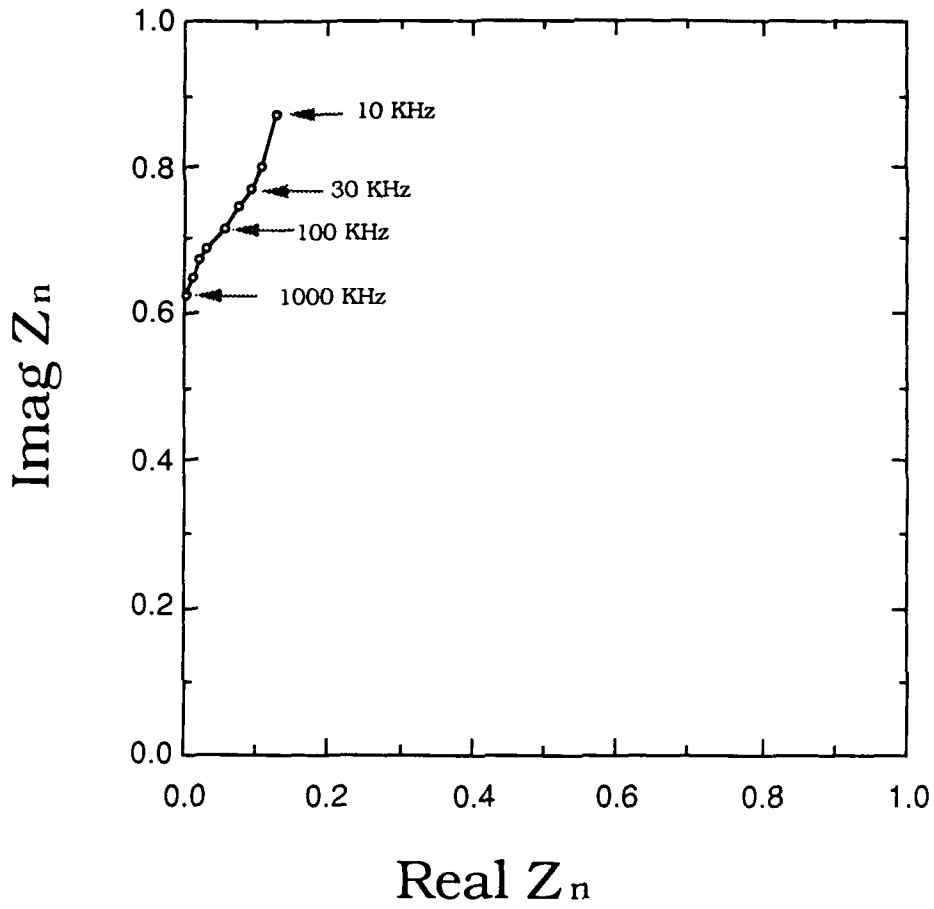


Figure 4: Experimental normalized impedance curve for a pure titanium rod.

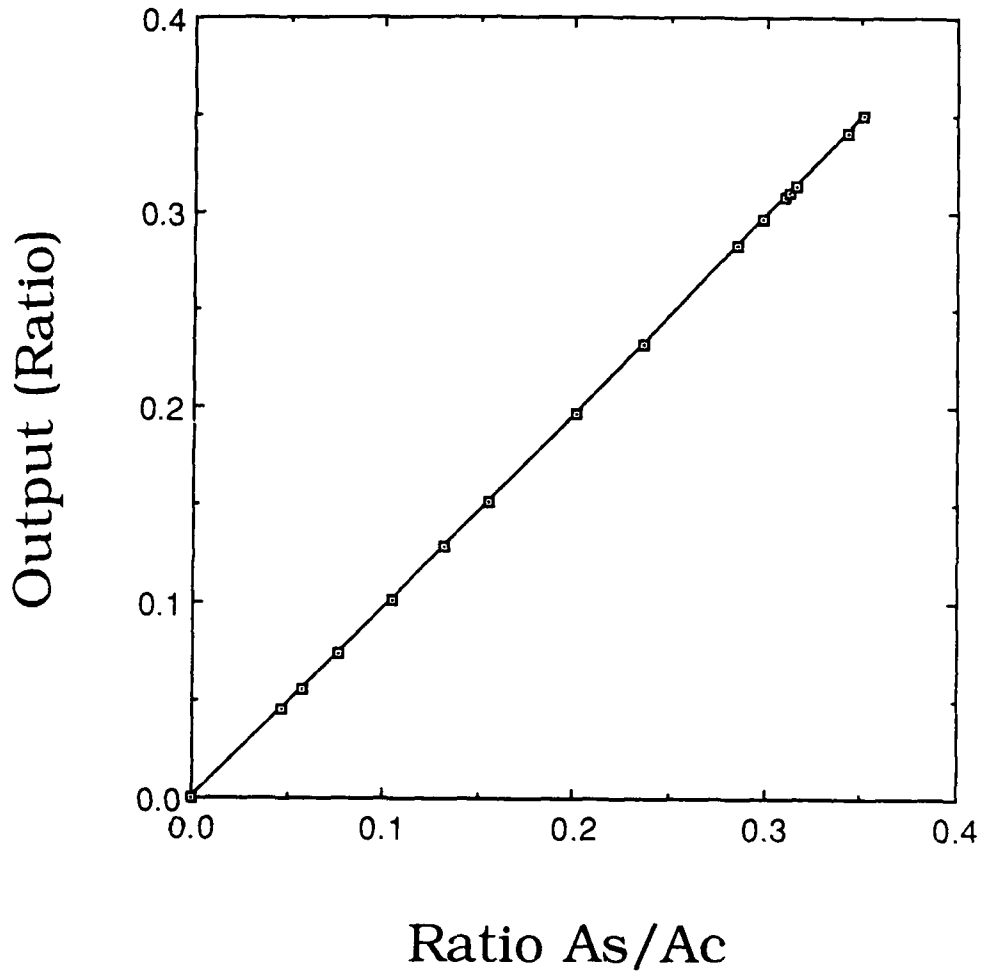


Figure 5: Plot of sensor output vs. the ratio (area of sample/area of secondary coil) for a solid titanium rod.

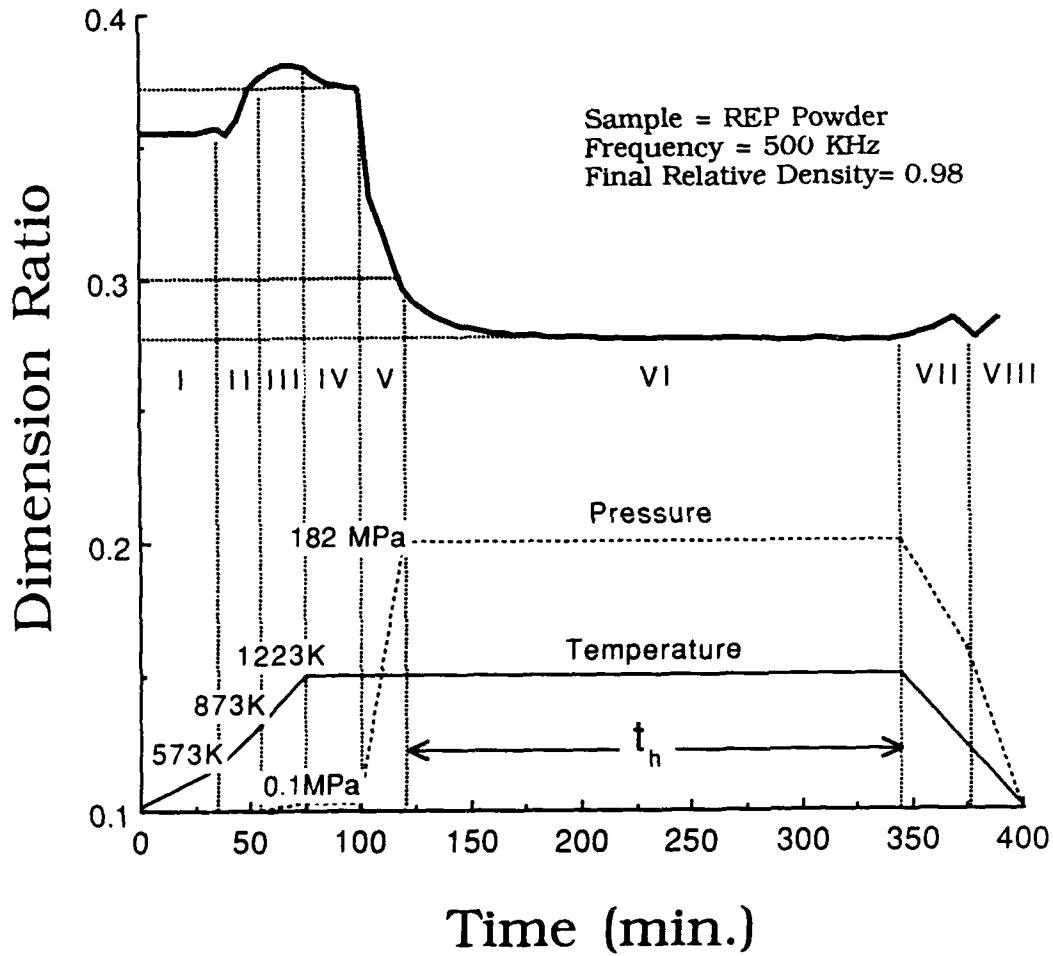


Figure 6: Sensor output vs. time during a complete HIP cycle.

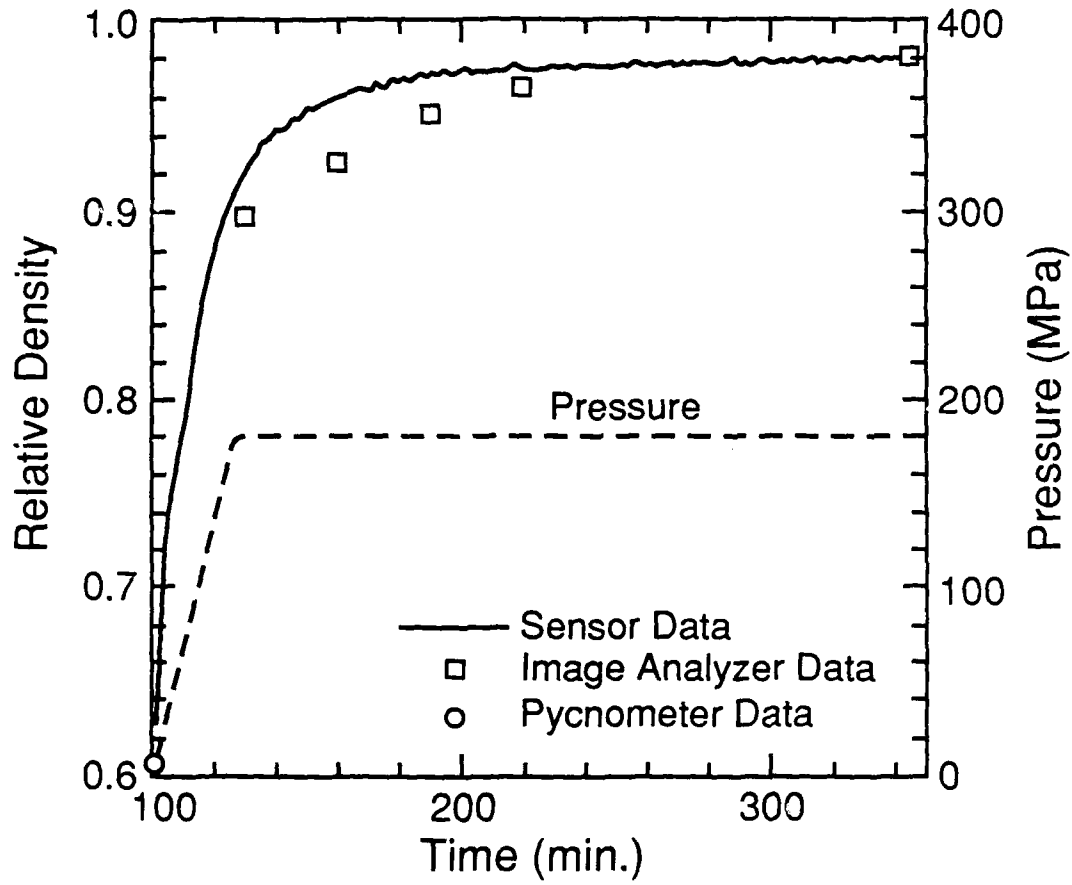


Figure 7. Experimental sensor curve and measured relative densities at 1223 K as a function of pressure and time.

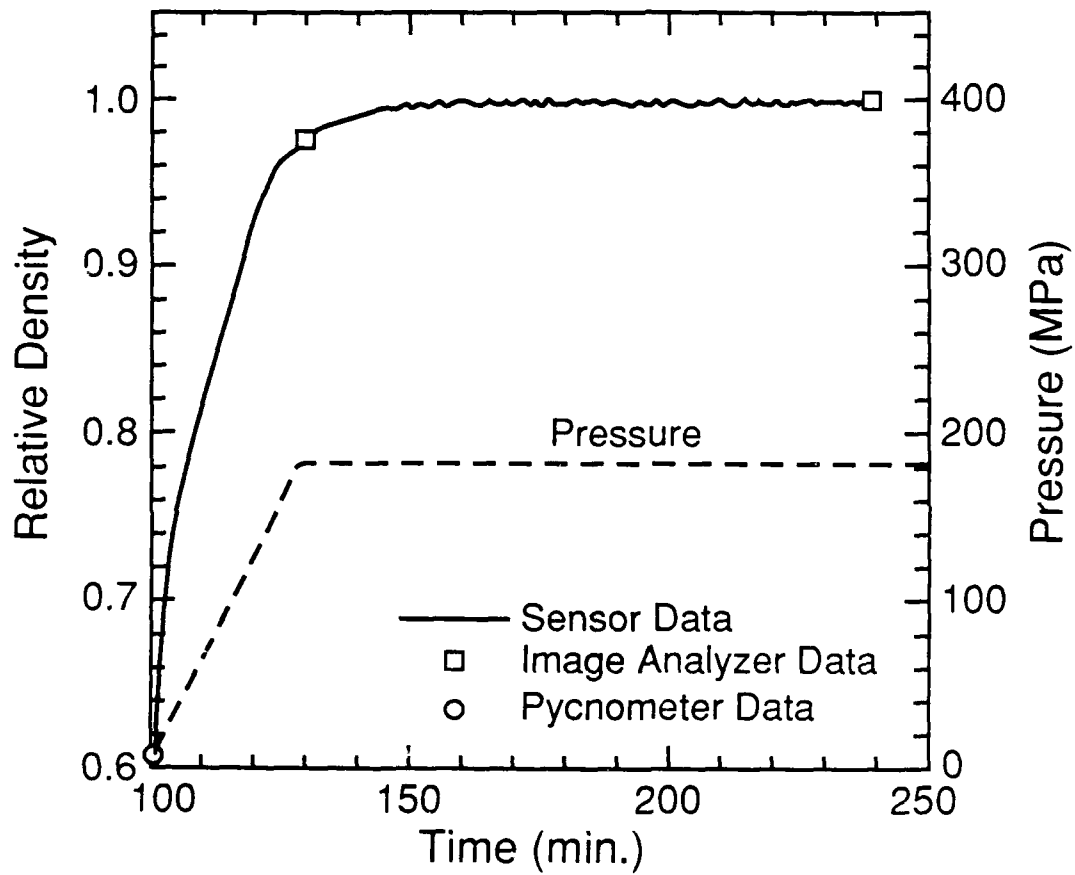


Figure 8. Experimental sensor curve and measured relative densities at 1339 K as a function of pressure and time.



Figure 9. Microstructures of REP powders consolidated at 1223 K (top) and 1339K (bottom). The HIP cycle was interrupted immediately, $t_h=0$, after reaching full pressure of 182MPa.

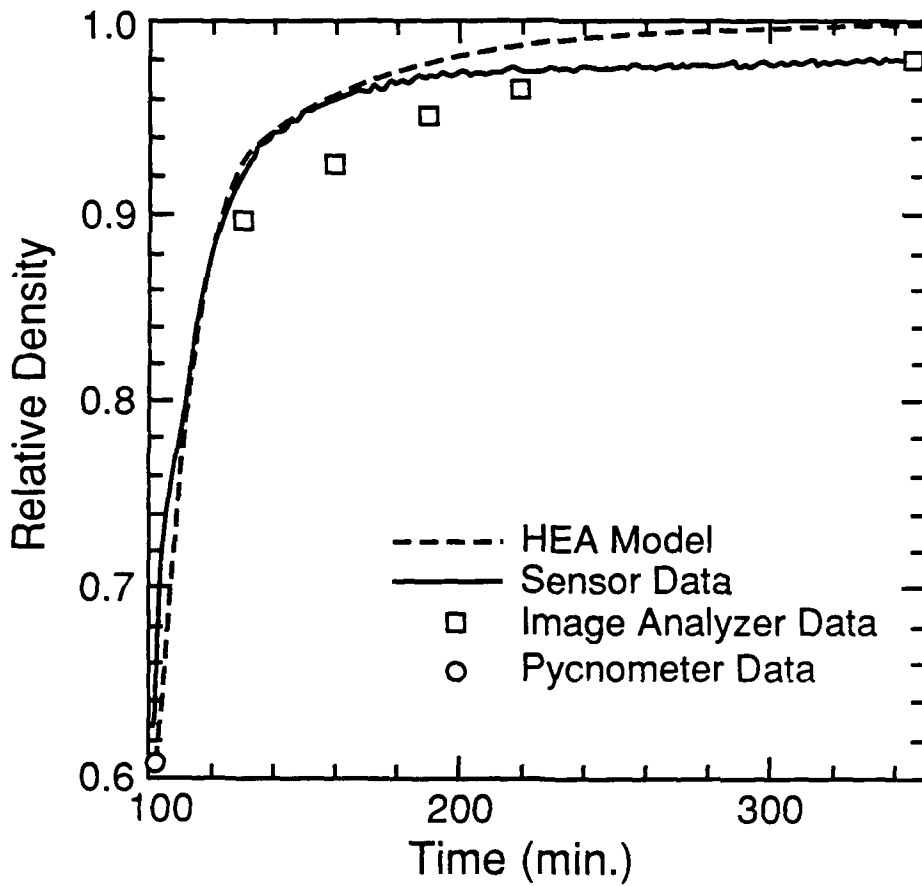


Figure 10. Theoretical densification calculated from HEA model superimposed on the experimental curve at 1223 K.

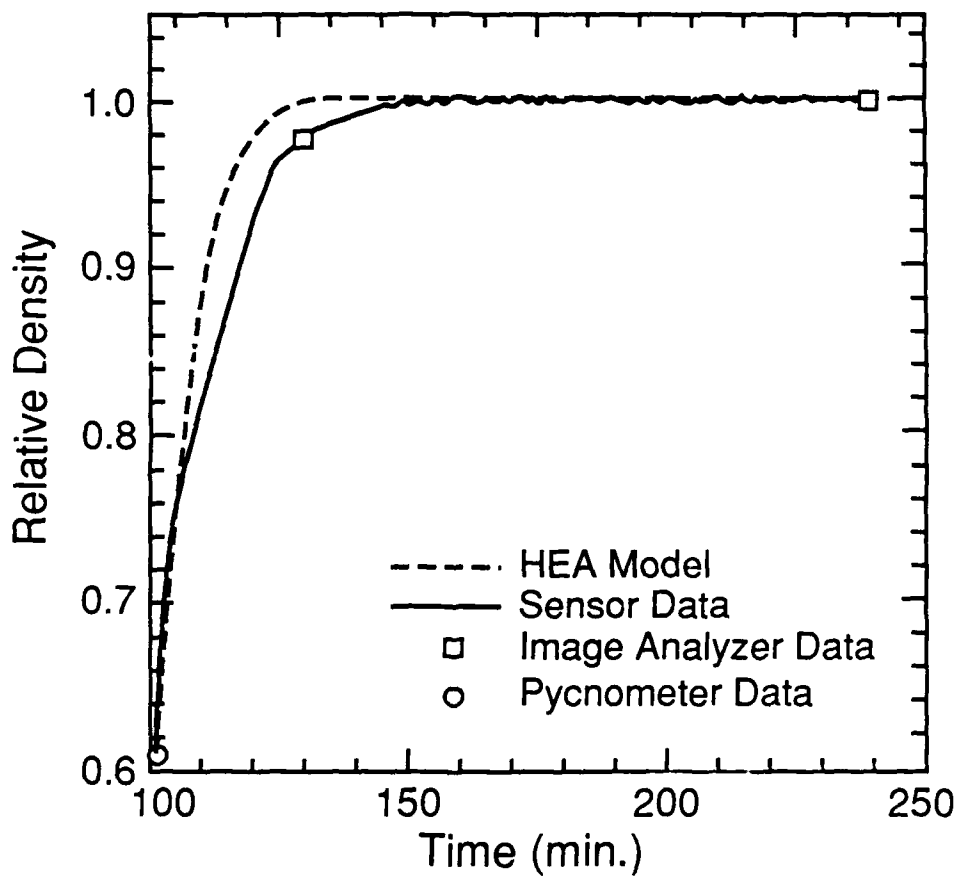


Figure 11. Theoretical densification calculated from HEA model superimposed on the experimental curve at 1339 K.

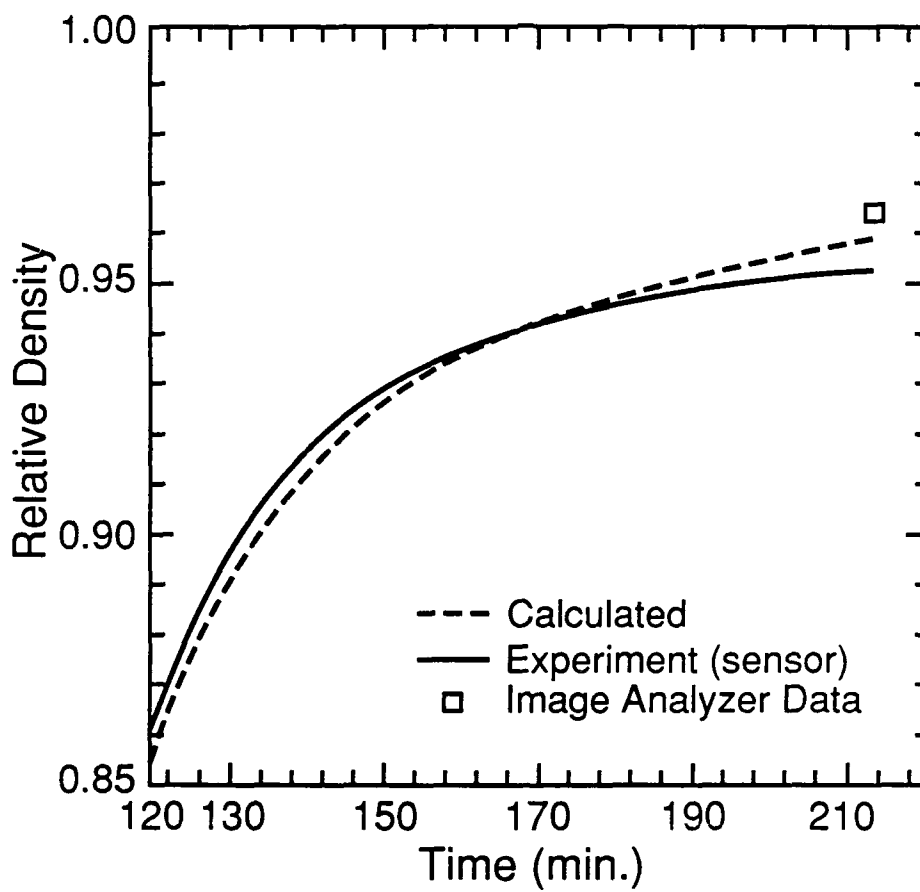
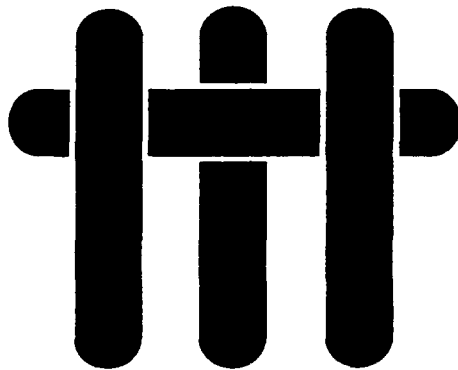


Figure 12. Least-squares fit of theory and experimental data ($T=1223\text{K}$, $t_h=1.5$ hours, $p=182\text{MPa}$).

M A T E R I A L S



**EVOLUTION OF BORIDE MORPHOLOGIES
IN TiAl-B ALLOYS**

M. E. Hyman, C. McCullough, C. G. Levi and R. Mehrabian

**Materials Department
College of Engineering
University of California, Santa Barbara
Santa Barbara, California 93106**

EVOLUTION OF BORIDE MORPHOLOGIES IN TiAl-B ALLOYS

by

M.E. Hyman, C. McCullough, C.G. Levi and R. Mehrabian¹

ABSTRACT

The solidification of γ -TiAl alloys with relatively low (<2at%) additions of boron is discussed. Binary Ti-Al alloys of near equiatomic composition (49 to 52 at%Al) form primary α -(Ti) dendrites from the melt which are subsequently surrounded by γ segregate as the system goes through the peritectic reaction $L + \alpha \rightarrow \gamma$. Boron additions to the binary alloy do not change the basic solidification sequence of the matrix, but introduce the refractory compound TiB_2 in a variety of morphologies. The boride develops as highly convoluted flakes in the leaner alloys (<1at%), but needles, plates and equiaxed particles gradually appear as the B content increases to ~ 1.5 at%. Increasing the solidification rate initially promotes the formation of flakes over plates/needles and ultimately gives way to very fine equiaxed TiB_2 particles in the interdendritic spaces of the metallic matrix. Furthermore, the primary phase selection changes from hexagonal α -(Ti) to cubic β -(Ti) at supercoolings of the order of 200 K. The different boride morphologies are fully characterized and their evolution is rationalized in terms of differences in their nucleation and growth behavior, and their relationship to the solidification of the intermetallic matrix.

¹ M.E. Hyman is Graduate Research Assistant, C. McCullough is Assistant Research Engineer, C.G. Levi is Associate Professor of Materials and Mechanical Engineering and R. Mehrabian is Dean of Engineering and Professor of Materials, University of California, Santa Barbara, CA 93106.

1. INTRODUCTION

Development of engineering alloys based upon γ -TiAl requires increasing toughness and creep strength while maintaining the attractive modulus and oxidation resistance of the intermetallic compound. Promising toughness values have been produced by dispersions of Ti-Nb alloy ductile phases in γ -TiAl [88E11], but this benefit seems to be accompanied by a reduction in high temperature creep strength [89Ros]. Most current efforts to enhance the creep properties of γ alloys involve refractory second phases that would constrain the plastic flow of the matrix during high temperature service. Micromechanics considerations indicate that these reinforcements must have morphologies with high aspect ratios (i.e. rods, plates) and a long dimension appreciably larger than the dislocation cell size (i.e. a few micrometers) [89McM].

Reinforcing phases may be incorporated in the aluminide matrix by compositing techniques, or may be grown in-situ by suitable design of the alloy chemistry and processing route. In one novel approach, TiB_2 and other refractory compounds are grown by reaction of the constituent elements in a molten Al bath yielding a "master" composite which is subsequently alloyed with the proper amounts of Ti, Al, etc., to reach the desired intermetallic matrix composition [88CPC]. A peculiar feature of this approach is that the strengthening phase remains largely undissolved during the final alloying stage. This allows for lower processing temperatures but may limit the composite stability if the compound that grows in the original reaction bath (Al) is not a phase that can achieve equilibrium with the final matrix. Alternatively, reinforcements may be grown as primary phases from a melt with the proper chemistry. For example, Ti_2AlC plates with aspect ratios of ~ 20 and volume fractions up

to ~ 0.12 have been produced in γ alloys with $\sim 3\% \text{C}^1$ [89Val]. Preliminary results indicate that both routes result in materials with improved creep resistance [88CPC,89Mar,89Val], but the strengthening contribution of the reinforcements is obscured by concomitant changes in the matrix grain size and solute content.

A fundamental understanding of the mechanisms that control the size and shape of reinforcements grown from the melt is clearly desirable. Previous work by the authors revealed that TiB_2 exhibits various morphologies when growing from Ti-Al melts of approximately equiatomic composition with additions of 0.9 and 5.4%B [89Hym]. The leaner alloys form only secondary borides which may evolve as plates, needles and/or flakes. The alloys higher in boron form in addition primary TiB_2 which grows as blocky faceted particles 10-20 μm across. Crystallographic considerations indicate that TiB_2 , which has the hexagonal C32 structure, is likely to grow as equiaxed crystals, in agreement with the observations for primary borides. The non-equiaxed morphologies were tentatively ascribed to the constraint imposed by the matrix as it grows concurrently with the secondary borides [89Hym].

The present investigation was undertaken to elucidate the origin of the multiple TiB_2 morphologies in $\gamma\text{-TiAl} + \text{B}$ alloys, and to study their dependence on important solidification parameters like bulk supercooling and cooling rate. Of particular interest were the potential for controlling the boride phase morphology, distribution and size scale by solidification processing, and the concomitant effects on the evolution of the matrix microstructure. The research focused on alloys containing 49-52 %Al and ~ 1 %B (Table I), largely because higher boron contents were found to exhibit little or no potential for supercooling.

¹ All compositions in atomic percent unless specified otherwise.

2. EXPERIMENTAL

The selected experimental approach involved electromagnetic levitation and melting followed by gas cooling and/or splat quenching with a double-anvil device. These techniques permit the monitoring of part or all of the thermal history and the establishment of more quantitative relationships with microstructural observations. They have been applied quite successfully to studies of various binary and ternary γ -TiAl alloys [89VML].

The alloys were prepared by arc-melting in a gettered-argon atmosphere (<0.1 ppb O_2) using high purity Ti buttons (<200 ppm O), Al pellets (99.99%Al) and nitrogen-free B powder (99.7%B, 60 mesh)¹. Extensive precautions were taken to avoid N contamination, which was previously found to produce spurious ternary nitrides that complicate the interpretation of the microstructures [89Hym]. The materials were melted following the procedure established in a previous publication [89Hym], wherein B is first dissolved in Ti to form a homogeneous Ti-B master alloy, and Al is subsequently added to achieve the desired matrix composition. Al losses can be minimized in this manner because the Ti-B master alloy melts at temperatures lower than those necessary to dissolve elemental B in molten TiAl. Some buttons were cut into pieces ~ 400 mg in weight which were then remelted into spheres, ~ 5 mm in diameter, suitable for the levitation experiments.

The two configurations of the experimental apparatus used in this investigation are schematically depicted in Figure 1. In general, the sample was suspended in a flow of Ar gas within a Pyrex tubular chamber by means of a levitation coil driven by a 20 kW, 450 kHz RF power supply. The chamber was

¹ Ti buttons were supplied by Timet, Al pellets and B powder by Alfa Morton-Thiokol.

built with an expanded middle section to prevent contact between the walls and the sample as the latter undergoes vibrational, rotational and oscillatory motions due to dynamic interactions with the RF field during melting [88Kri]. Once liquid, the sample was superheated and held for about 30-90 s to permit dissolution of the refractory phases and homogenization of the melt. Temperature control in this period is critical to avoid evaporation of Al and is effected by manipulating the power level and gas flow. The liquid droplet could then be quenched by switching to a rapid flow of He gas, Figure 1(a) or dropped between two electromagnetically-driven Cu-Be anvils, Figure 1(b). The anvils were polished to 50 nm Al₂O₃ finish and triggered by a photodetector which is activated by the sample radiation. The splats produced in this setup ranged from 50 to 150 μ m thick.

The thermal history of the samples (through solidification or until the moment of splatting) was recorded by a fast response (40 Hz) Ircon-Maxline two-color pyrometer and recorded to disk on a microcomputer. The pyrometer was calibrated for the temperature range of interest using the emissivity correction factor of 1.07, determined from the melting point of a pure Ti standard¹. Given a minimum target area of 2 mm, and an instrument repeatability of 0.1% of full scale (2086 K), the accuracy of the temperature measurements should be within ± 2 K.

Figure 2 depicts a schematic thermal history for a sample that was completely solidified by He gas cooling. The thermal arrest upon heating represents the melting process, which is followed by rapid superheating and a holding period at a constant temperature above the liquidus. The liquid is then rapidly cooled until nucleation of the primary phase occurs leading to reca-

¹ It is assumed that the emissivity of the alloys is similar to that of the clean, smooth, unoxidized pure metal and does not depend on alloy composition.

lescence. The supercoolings reported here were determined from the extent of the recalescence excursion and thus are slightly underestimated [89VML]. Thermal arrests after recalescence are associated with the nucleation of secondary phases during solidification. Samples with no distinguishable recalescence are assumed to nucleate without appreciable supercooling and their microstructures should reflect primarily the effects of the cooling rate, which can be determined from the slope of the thermal history curve.

The solidified specimens were sectioned and polished for characterization by optical and scanning electron microscopy (SEM). Additional studies of the boride morphologies were made on samples electrolytically deep-etched using a solution of 7vol% HCl in methanol and a voltage of 20 VDC for 30-45 seconds. Transmission electron microscopy (TEM) was performed on specimens electropolished in a perchloric acid/butanol/methanol solution following the procedure described in earlier publications [89McC,89MVL]. Since the thicker boride particles were not thinned by electropolishing, their TEM analysis required dimpling and ion-milling at 5 kV, 1 mA with Ar ions. Finally, two-stage extraction replicas from the deep-etched samples were used to facilitate the examination of the thinner borides and the correlation of crystallographic information to the external features of the different morphologies.

3. RESULTS AND DISCUSSION

A large fraction of the borides grow concurrently with the metallic matrix and hence are significantly influenced by the presence of the latter. We shall focus first on the broader aspects of the microstructure, which pertain to the evolution of the matrix microconstituents under conventional and rapid solidification conditions, noting where appropriate the morphological charac-

teristics of the boride phases. Subsequently, we will discuss the crystallographic aspects of the different boride morphologies and attempt to shed some light on their evolution.

3.1 Conventional Solidification

The conventional solidification path for γ alloys containing 49 to 52 %Al and $\sim 1\%$ B closely parallels that of binary Ti-Al alloys of similar composition. The recently revised Ti-Al phase diagram in Figure 3(a) [89McC,89Mis] suggests that the matrix in these alloys should solidify as α -(Ti) dendrites surrounded by γ -TiAl segregate in the interdendritic spaces. This is confirmed by optical examination of the as-cast ternary buttons in Figures 4(a) and (b), where the hexagonal symmetry of the α -(Ti) dendrites is clearly evident. Also note in this figure that the proportion of segregate increases quite rapidly with Al content. Alloys below 49%Al (e.g. 47-1 in Table I) do not exhibit hexagonal dendrites and show evidence of having formed cubic β -(Ti) at the start of solidification, as expected from the binary phase diagram.

The γ segregate is stable and can be retained through the post-solidification cooling. However, the primary α dendrites undergo a series of solid state transformations which eventually yield the characteristic "lath" microconstituent seen in Figure 4. The latter has been shown to consist of alternating lamellae of α_2 and two twin-related variants of γ with the close packed planes and directions in the two phases parallel to each other [89McC].

The large majority of the boride phases in these alloys appear in three basic morphologies: needles, plates¹ and convoluted flakes, all of them with

¹ The plate morphology is not easily distinguishable from the needles in polished sections, but it will be evident in the micrographs of deeply etched specimens presented later.

thicknesses of $\sim 1 \mu\text{m}$ or smaller--see Figures 4(c) and (d). The composition leanest in B (0.72%B) was shown to contain only flakes, whereas all others exhibit the three morphologies. In contrast, alloys above 1%B consistently show a small fraction of boride particles in a somewhat larger scale, e.g. Figure 4(b), which are believed to be primary TiB_2 .

The microstructural observations suggest that the TiB_2 liquidus boundary runs along and slightly below the 1%B isoconcentrate in the region of interest, as schematically depicted in Figure 3(b). The TiB_2 liquidus intersects the β , α and γ fields emerging from the Ti-Al binary and forms a descending monovariant line of the type $L \rightarrow M + \text{TiB}_2$, where the metallic phases M evolve in the same sequence as in the double peritectic cascade of the binary diagram: $M = \beta \rightarrow \alpha \rightarrow \gamma$. Since all compositions in this study fall reasonably close to the suggested monovariant line, most of the solidification is expected to involve concurrent growth of the boride with a matrix which evolves in the same manner as in a binary alloy of equivalent composition.

3.2 Effect of Supercooling

Boron additions were found to rapidly curtail the undercoolability of molten γ -base alloys. Prior levitation-melting studies revealed that nucleation could be readily suppressed in the binary alloys, with the achievable supercooling increasing from 262 K for Ti-45%Al to 384 K for Ti-55%Al [89VML]. However, no appreciable supercooling could be produced in any of the alloys above 1%B (e.g. 49-5 or 52-3), presumably because primary TiB_2 is readily formed and triggers the nucleation of the metallic phase. Lower B alloys did supercool quite significantly; for example, the 0.72%B alloy (49-1) achieved a maximum ΔT of 278 K, which is comparable to the 286 K produced in the binary

Ti-50ZAl alloy, while three other alloys ranging from 0.82 to 1.0ZB (49-3, 50-1 and 52-1) achieved supercoolings of the order of 200 K.

The effects of supercooling on the solidification microstructure are similar for all the alloys noted above and are illustrated for the leaner B composition (49-1) in Figure 5. At $\Delta T \sim 100$ K the microstructure is not much different from the arc-button material, except for a slight reduction in the amount of segregate. The primary phase selected from the melt is still α -(Ti), as evidenced by the hexagonal dendrites in Figure 5(a), and the borides exhibit predominantly the flake morphology, Figure 5(c). As the supercooling increases above ~ 150 K both the matrix and the boride phase experience substantial refinement, as shown in Figures 5(b) and (d). Dendrites are no longer evident in the microstructure and the borides appear as very fine (< 500 nm) equiaxed crystals which vaguely seem to delineate dendrite or cell boundaries; compare with Figure 7(e) below.

TEM analysis of the Ti-49.1ZAl-0.72ZB (49-1) sample supercooled 278 K reveals well developed packets of the ($\alpha_2 + \gamma$) lath microconstituent, as shown in Figure 6(a). The prior α grain (or lath packet) size ranges from 5 to 20 μm in this sample, compared with the 100 to 200 μm grain size associated with the dendritic microstructures. Upon closer examination, Figure 6(b), the laths were seen to contain very fine plate-like precipitates with the external crystallographic features of TiB_2 and dimensions of 20-50 nm wide by 10 nm in thickness. These are significantly finer than the small equiaxed boride particles depicted in Figure 5(d) and are believed to be a product of solid state precipitation rather than solidification. The population of these ultrafine boride precipitates is only significant at $\Delta T > 200$ K and increases with the initial supercooling, suggesting a progressive extension of B solubility produced by the concomitantly higher interface velocities.

Selected area diffraction of neighboring lath packets revealed that their habit planes frequently form 120° angles with each other. For example, the $\{111\}_\gamma$ habit planes of the three lath packets in Figure 6(c) are all viewed end-on down the $[1\bar{1}0]_\gamma$ zone axis, as shown by the SAD pattern of one of the packets in Figure 6(d). The $\{111\}_\gamma$ planes of the γ variants in the lath are parallel to the basal plane of the α_2 [70B1a], and hence to the basal planes of the parent α . Thus, the three packets depicted in this figure originated from three neighboring α grains which had their (0001) planes mutually oriented at 120° angles. This is precisely what would be expected if the α grains evolved from a solid state transformation of a single grain of parent β phase following the Burgers orientation relationship [76Wil]:

$$(0001)_\alpha \parallel \{110\}_\beta \quad ; \quad \langle 1\bar{2}10 \rangle_\alpha \parallel \langle 111 \rangle_\beta \quad (1)$$

The γ laths would then be related back to this parent β phase in the following manner¹:

$$\{110\}_\beta \rightarrow \{111\}_\gamma \quad ; \quad \langle 111 \rangle_\beta \rightarrow \langle 1\bar{1}0 \rangle_\gamma \quad (2)$$

Thus, the evidence suggests that the fine microstructure of the highly supercooled samples results from the solid state transformation of a metastable primary β phase selected from the liquid. This is consistent with recent work on the phase selection hierarchies in the binary Ti-Al system, where β was found to be the kinetically preferred phase at high supercoolings even in the composition range where α and/or γ have a larger thermodynamic driving force

¹ Note that this is not an actual orientation relationship but describes the effective crystallographic relation between two phases that never existed together.

for solidification [89VML].

One could also argue that the apparent increase in B supersaturation observed above $\Delta T \sim 200$ K may be associated with the change in the primary phase selection from α to β . Boron is normally considered an interstitial solute, but its relatively large atomic size drastically limits the solubility in both structures, and more so in the β phase, which has smaller interstices. There is evidence, however, that large supersaturations of B may be produced in β -(Ti) by rapid solidification [86Wha], presumably because a sizable fraction of the B is trapped as a substitutional element. The excess B would readily precipitate in the post-recalcescence period as the cooling rates characteristic of the gas quenching process are relatively modest.

3.3 Effect of Cooling Rate

While the different boride morphologies (plates/needles/flakes) were present throughout the microstructures of all but one of the buttons, it was clearly evident that the flakes tended to be more numerous near the chill surfaces, suggesting an influence of the cooling rate on the growth pattern of the boride phases. Hence, a series of experiments were undertaken to assess the effects of varying quenching conditions on the microstructure. To isolate these effects from those arising from bulk supercooling, the analysis was limited to samples showing negligible recalcescence excursions in the thermal history curve¹. The cooling rates produced by gas quenching were controlled by varying the gas flow and the relative quantities of He and Ar in the mixture flowing through the tubular chamber. These cooling rates could be directly

¹ This can only be ascertained in the gas cooling experiments but not in the splat quenching, where the thermal history cannot be followed after the sample is dropped between the anvils.

quantified from the thermal history recorded by the pyrometer and were typically of the order of 10^2 K/s prior to nucleation, and of the order of 10 K/s during solidification. Splat quenching produced cooling rates which are presumably $>10^5$ K/s [68Ruh]. It should be noted, however, that the latter are not constant; high speed video photography has shown that the anvils recoil after the initial impact and detach from the splat, although they rapidly close again and reestablish contact with the chill surfaces.

Most of the work in this area was done on alloys which are not prone to supercooling, i.e. 1%B or higher. The effects are similar in all cases, and are illustrated in Figure 7 for the microstructures of the Ti-51.5%Al-1.15%B alloy (52-3). The most striking effect is on the shape of the borides, which are predominantly plates and needles at the slower cooling, ~ 5 K/s, but change almost completely to the convoluted flake morphology with a relatively modest increase in quenching rate to ~ 15 K/s--compare Figures 7(a) and (b). This is consistent with the observations that the flakes are more abundant near the chill surfaces in arc-buttons.

The higher solidification rates characteristic of splat cooling bring about much more significant changes in the microstructure. Figure 7(c) shows a cross sectional view of a ~ 80 μm thick Ti-51.5%Al-1.15%B splat. The small featureless zone on the chill side (left) is associated with a nucleation event on the surface, from which the primary phase grows in a very fine microcellular pattern with segregate spacings smaller than ~ 0.5 μm , see Figure 7(d). As the cellular front moves away from the chill the solidification rate decreases, partly because of the inherent resistance to heat transfer imposed by the solid already formed, and possibly because the splat detaches from the chill surface due to shrinkage and/or anvil recoil after the initial impact. The cellular microstructure coarsens significantly and starts to develop den-

dritic branching, as seen in the middle section of Figure 7(c), with segregate spacings of 1 to 2 μm , as noted in Figure 7(e). Finally, the central region in the splat consists of equiaxed dendrites but with finer spacings than those observed in the previous region, see Figure 7(f). This equiaxed zone could be ascribed to dendrite tip breakage due to the high flow velocities which are developed in the center plane of the droplet as it is squeezed into a splat¹. One might also speculate that the finer microstructural scale in the center is associated with an enhanced cooling rate, presumably due to the anvils reestablishing contact with the splat after the recoil event. However, the intractability of monitoring the thermal history in this process makes it difficult, if not impossible, to confirm this hypothesis.

The boride morphology and distribution also change dramatically in the splat quenched material. The borides appear now as very fine (~ 50 nm) discrete equiaxed particles similar to those observed in the highly supercooled samples ($\Delta T > 200$ K). In this case, however, the borides are clearly decorating the intercellular or interdendritic spaces with only a few particles detected inside the primary phase regions--e.g. Figure 7(e). This suggests that the boride phases nucleate after the metallic phase and under a fairly high supersaturation, and are pushed by the advancing cells/dendrites into the last pockets of liquid.

It should be noted that the equiaxed dendrites, and even some of the columnar ones, often show a clearly hexagonal symmetry, as in Figure 7(f). This indicates that the primary phase in the splats is α -(Ti) and hence that only moderate supercoolings were achieved in the liquid prior to nucleation. However, the TEM micrograph in Figure 8(a) shows the matrix in the center of

¹ This pattern of fluid flow out of the droplet center has been observed by high-speed video photography during the splat quenching experiments.

the splat to be fine polycrystalline γ with grain sizes of the order of 500 nm and random orientations. In addition, the borides appear normally inside the γ grains, rather than at the grain boundaries, Figure 8(b). These features can only be reconciled with the cast structure observed in the SEM if the primary α phase transforms in the solid state to γ , possibly by growth from the γ present in the segregate regions at the end of solidification. This epitaxial growth from the γ segregate has been previously observed in binary Ti-Al alloys during cooling, but is normally superseded by the $\alpha \rightarrow \alpha_2$ ordering in the bulk of the dendrite. The latter gives way to the ($\alpha_2 + \gamma$) lath structure by precipitation of γ plates at the stacking faults in the α_2 phase [70Bla, 88McC]. When the dendrite arms are relatively large ($\gg 1 \mu\text{m}$), the growth of γ from the segregate regions would only consume part of the dendrite before reaching the temperature where the ordering transformation becomes feasible. Note, however, that the segregate spacings in the splat are much smaller--of the order of the typical lath spacings in Figure 6(c)--suggesting that the density of sites for the growth of γ is sufficiently large to allow complete transformation of the primary α phase before the ordering temperature is reached. On the other hand, it is somewhat surprising that no α (or α_2) was retained in the splat microstructure suggesting that the cooling rates after solidification may not be as high as previously anticipated.

We have so far focused on the evolution of the matrix microstructure and the broader characteristics of the boride phases, i.e. their shape and size, as well as their dependence on important solidification parameters like supercooling and cooling rate. It is clear at this point that some borides tend to exhibit plate and needle morphologies at the lowest solidification rates. Increasing the transformation rate, hence the supersaturation, by either bulk supercooling or faster heat extraction, gradually changes the morphology to

convoluted flakes, and finally to very fine equiaxed particles. We will now proceed to examine the borides in more detail and try to elucidate the differences in crystallography and growth mechanism of the different morphologies.

3.4 Crystallography of the Boride Phases

Notwithstanding the wide variety of morphologies and sizes, all the boride particles were positively identified as TiB_2 (C32) by transmission electron microscopy¹. The structure of TiB_2 consists of close packed Ti planes (A) stacked with graphite-like boron planes (H) in an AH AH sequence along the c-axis of the crystal, as shown in Figure 9 [89Hym]. Growth of this phase is expected to take place by a ledge mechanism, whereupon the morphology should be determined by the slowest growing facets in the crystal, although the interfacial energy may also play a significant role. In the case where secondary borides grow from a melt dilute in boron, as in the present investigation, diffusional effects and physical constraints imposed by the matrix are also relevant, as discussed below.

Crystals of TiB_2 growing unconstrained from various melts consistently show facets of the basal (0001) and prism $\{10\bar{1}0\}$ types [70HiA,74NHI,85AHH], suggesting that the growth rates normal to these planes are the slowest. This may be rationalized from the stacking sequence, which in both cases involves alternate planes containing all-Ti and all-B atoms [89Hym], see Figure 9. Calculations of the attachment energy for various low-index facets of the TiB_2 crystal suggest the following hierarchy of growth rates [85AHH]:

¹ The occasional ternary flakes reported in an earlier study [89Hym] were not found in these samples and thus were dismissed as possible contamination products.

$$(0001) < \{10\bar{1}0\} < \{10\bar{1}1\} < \{1\bar{2}10\} < \{1\bar{2}11\}$$

The ranking essentially reflects the density of strong bonds (B-B > Ti-B > Ti-Ti) or "Periodic Bond Chains" [73Har] in the various crystal planes.

Figure 10 shows TiB_2 plates found in the shrinkage cavity of a slowly cooled Ti-51.5%Al-1.15%B levitated sample. The borides are clearly embedded in a dendrite arm, Figure 10(a), suggesting that they solidified concurrently with the matrix down the α/TiB_2 two-fold saturation line. The facets of the TiB_2 platelike crystals are still indicative of the hexagonal C32 geometry, as noted in Figure 10(b). Indeed, SAD analysis of an extracted plate-boride particle in Figure 11 shows the habit plane of the plate to be $\{10\bar{1}0\}$, from where the facets of the plate can be inferred to be of the basal and prismatic type. Thus, the growth mechanism is similar to that of the primary borides, but two of the prism directions are evidently constrained by the matrix, as shown in Figure 10(b), resulting in the elongated plate morphology.

Closer examination of the plates in deeply-etched specimens revealed that they are often connected to needles in various stages of development, e.g. Figures 12(a) and (b). The needles exhibit facets parallel to those of the plate, implying that they correspond to equivalent crystal planes, but have a more equiaxed cross section. They seem to thicken by growth of prismatic ledges along the axis of the needle, as illustrated in Figure 12(c), and occasionally exhibit branching at angles which suggest a twin relationship between the original stem and the branch, as shown in Figure 12(d). TEM analysis of an extracted needle in Figure 13 confirmed that the needle axis is indeed $[0001]$ and the facets are of the $\{10\bar{1}0\}$ type. Furthermore, small pyramidal facets of the $\{10\bar{1}1\}$ family were also detected at the tip of the needle crystal, Figure 13(b). These facets are expected to grow faster than the (0001) and $\{10\bar{1}0\}$

planes, as noted above, and could be responsible for the rapid propagation of the needle tip along the c-axis. The latter could not be justified based on growth normal to the basal plane, which is the slowest in TiB_2 [85AHH].

Figure 14 presents close views of the flake borides, which tend to be thinner and much longer than the plates and to exhibit extensive meandering and branching, as previously seen in Figures 4(c), 5(c) and 7(b). TEM analysis of flakes extracted from deeply etched samples, e.g. Figure 14(c), confirmed that they are also TiB_2 but with a habit plane of the $\{1\bar{2}10\}$ type, as shown by the diffraction pattern in Figure 14(d). These higher index prismatic planes contain Ti and B atoms in the correct stoichiometric proportions and thus have growth rates higher than those of the $\{10\bar{1}0\}$ prism facets characteristic of the plates and needles--see ranking above. Ledge growth on the plane of the flake is clearly evident in Figures 14(b) and (c), where the ledges are parallel or perpendicular to the c-axis. In addition, these borides exhibit numerous defects like holes and incomplete layers, suggesting that ledge propagation may be frequently interrupted by matrix encroachment and/or site poisoning by impurities or solute atoms [58Cab].

Finally, the small equiaxed borides produced at the higher supercoolings exhibit facets of the basal and $\{10\bar{1}0\}$ prism type like the plates and needles, as shown by the TEM image and diffraction pattern in Figure 15. The fine boride particles in the interdendritic spaces of the splat quenched material seen in Figure 8(b) are smaller and not as well defined, but the facets are believed to be of the same type.

3.5 Evolution of the Boride Phases

The microstructural and crystallographic evidence suggest that there are two basic morphologies of "secondary" TiB_2 , i.e. borides that grow concurrently with the intermetallic matrix. These two basic morphologies are the flakes and the plates, which exhibit fundamental differences in their growth mechanism manifested by their different habit planes, their shape and their size scale. The needles are believed at this point to be variants of the plates which originate from morphological instability of the boride-liquid interface due to the diffusional limitations to solute redistribution¹. Since TiB_2 contains 66%B and is growing from a melt with ~1%B, there is significant rejection of Ti and especially Al as the boride particles grow. Furthermore, Ti segregates preferentially to the metallic phase forming concurrently with TiB_2 (either α or γ), resulting in an effective enrichment of Al in the liquid phase. The needle morphology is more efficient than the plate in optimizing the diffusional processes required for solute redistribution and should be favored as the liquid supersaturation increases. Thus, even though the growth mechanism involves essentially the same ledges in both plates and needles, the morphology changes in response to a diffusional constraint. Plate-to-rod transitions are quite common in faceted/non-faceted systems with a low volume fraction of second phase, although their origin is still a subject of debate [83E11].

The rationale for two distinct secondary boride morphologies is more elusive. Plates and flakes appear mixed with both dendrites and segregate, suggesting that they evolve simultaneously and not sequentially. However, the

¹ One could visualize without much difficulty the similarity between Figure 12(a) and the classical cellular breakdown of a planar interface under constitutional supercooling.

highly elongated and convoluted flakes are more representative of the irregular eutectic-like growth behavior that would be expected for solidification along the $L \rightarrow \alpha + \text{TiB}_2$ monovariant line. Note, for example, the extensive branching which is typical of two-phase growth in faceted/non-faceted systems [79KuF]. The flakes are thus believed to be the "true" morphology for secondary TiB_2 in this system. This hypothesis is further supported by the following observations.

Firstly, the alloy leanest in B (49-1) contains only flakes, whereas all others also exhibit plates/needles and occasionally primary TiB_2 . Secondly, the plates/needles exhibit facets which are identical to those of primary TiB_2 and are thus believed to have nucleated in the melt divorced from the matrix. On the other hand, the flakes have a habit plane and external facets different from all other morphologies, perhaps because they nucleated in contact with the matrix. The lack of an orientation relationship between the flakes and the matrix is not necessarily inconsistent with the proposed nucleation scheme, since the coupled growth would be irregular due to the faceted nature of TiB_2 . Thirdly, the flakes are significantly thinner than the plates, even though their lateral $\{1\bar{2}10\}$ facets should enable them to thicken faster than the $\{10\bar{1}0\}$ facets characteristic of the plates. Thus, the flakes are more likely to have grown coupled with the matrix, whereas the plates/needles probably spent some time growing freely in the melt before they were trapped and constrained by the matrix, as depicted in Figure 10.

Assuming that the flakes are the normal form of the secondary borides, one could then infer that the plates/needles nucleate originally as primary TiB_2 slightly above the monovariant line. This implies that, with the exception of sample 49-1, all other alloys actually fall on the TiB_2 region of the liquidus surface--see Figure 3(b). However, since most alloys are dilute in B

and also very close to the monovariant line, the primary TiB_2 seeds do not grow or coarsen significantly before the matrix phase nucleates. Once the latter appears, the existing TiB_2 seeds will be randomly trapped and evolve as plates/needles with the advancing liquid/solid interface, but new TiB_2 will also nucleate and grow as flakes coupled with the matrix.

As the supercooling (or cooling rate) increases in these alloys, formation of primary TiB_2 is progressively suppressed and fewer "seeds" will be present when the matrix phase appears, increasing the relative population of flakes. The latter are also favored because they can grow faster under higher supersaturations due to coupling with the matrix. One could readily establish an analogy between this behavior and that of a binary hypereutectic alloy that moves into the coupled zone as the solidification rate increases [82Boe, 88TrK]. However, since this system involves a faceted/non-faceted combination, the coupled zone would be skewed toward the phase with the highest kinetic hindrance [79KuF], i.e. TiB_2 . Thus, as the solidification rate increases the interfacial temperature eventually falls below the coupled zone where nucleation and growth of primary α (or β at higher supercoolings) is favored. The metallic phase hence evolves as cells or dendrites with TiB_2 forming as fine equiaxed particles divorced from the matrix in the supersaturated liquid behind the cellular/dendritic front.

CONCLUSIONS

The solidification path for γ -TiAl alloys with dilute additions of B has been elucidated. The microstructural evidence suggests that the β , α and γ liquidus emerging from the binary Ti-Al diagram meet the TiB_2 liquidus descending from the Ti-B binary along a monovariant line of the type $L \rightarrow M + TiB_2$.

This line runs along and slightly below the 1%B isoconcentrate in the Ti-Al-B ternary system, with the metallic phases M showing the same sequencing as in the binary, $M = \beta \rightarrow \alpha \rightarrow \gamma$. Therefore, except for the presence of the boride, solidification of the matrix in these alloys follows the same path as binary Ti-Al alloys of equivalent composition (49-52%Al), forming initially α -(Ti) dendrites from the melt which are subsequently surrounded by γ segregate.

Alloys near the monovariant line exhibit three morphologies of the TiB_2 phase under conventional solidification conditions: flakes, plates and needles. The flakes grow coupled with the matrix in the manner expected for an irregular eutectic consisting of a faceted second phase in a non-faceted matrix. The plates are believed to start as primary particles and should be present in alloys with B contents slightly above the monovariant line. These primary particles nucleate in the liquid and thus exhibit different crystallographic features from the flakes. However, they are subsequently trapped by the matrix which constrains their growth and forces them to develop anisotropic shapes. The needles are produced by breakdown of the plates due to morphological instability resulting from the diffusional boundary layer at the boride-melt interface.

Increasing the solidification rate produces transitions which are reminiscent of those of a hypereutectic alloy in a binary system with a faceted second phase. The initial effect is to suppress the formation of primary TiB_2 and to favor coupled growth, thus resulting in a predominance of the flake borides. Higher solidification rates promote the formation of primary α or β , with TiB_2 forming as fine, divorced equiaxed particles in the interdendritic spaces. The selection of β at the higher supercoolings is consistent with the behavior of binary Ti-Al alloys of similar composition.

ACKNOWLEDGEMENTS

This investigation was sponsored by the Defense Advanced Research Projects Agency under a University Research Initiative Grant No. N00014-86-K-0753, supervised by Dr. B. Wilcox and monitored by Dr. S. Fishman of the Office of Naval Research. The authors are grateful to Dr. Ursula Kattner of the National Institute of Standards and Technology, for discussions concerning the ternary diagram, and to Dr. J.J. Valencia for his technical assistance in the early stages of this work.

REFERENCES

- [58Cab] N. Cabrera and D.A. Vermilyea: **Growth and Perfection of Crystals**, J. Wiley, New York, NY, 1958.
- [68Ruh] R.C. Ruhl: Mater. Sci. Eng. 1(1967), 313-320.
- [70Bla] M.J. Blackburn: in **The Science, Technology and Application of Titanium**, eds. R.I. Jafee and N.E. Promisel, Pergamon Press, London, UK, 1970, p. 633.
- [70HiA] I. Higashi and T. Atoda: J. Crystal Growth, 7(1970), 251-253.
- [73Har] P. Hartman: in **Crystal Growth: An Introduction**, ed. P. Hartman, W. Bardsley, D.T.J. Hurle, and J.B. Mullin, North-Holland Publishing Co., Amsterdam, The Netherlands, 1973, pp. 367-402.
- [74NHI] K. Nakano, H. Hayashi, and T. Imura: J. Crystal Growth, 24/25(1974), 679-682.
- [76Wil] J.C. Williams: in **Precipitation Processes in Solids**, ed. K.C. Russell and H.I. Aaronson, The Metallurgical Society, Warrendale, PA, 1976, pp. 191-221.
- [79KuF] W. Kurz and D.J. Fisher: Int. Metal Reviews, (5/6)(1979), 177-204.
- [82Boe] W.J. Boettinger: in **Rapidly Solidified Amorphous and Crystalline Alloys**, eds. B.H. Kear, B.C. Giessen and M. Cohen, North Holland Publishing Co., Amsterdam, The Netherlands, 1982, p. 15.
- [83E11] R. Elliott: **Eutectic Solidification Processing**, Butterworths, London, 1983, p. 135-139.
- [85AHH] A.A. Abdel-Hamid, S. Hamar-Thibault, and R. Hamar: J. Crystal Growth, 71(1985), 744-750.
- [86Wha] S. Whang: J. Mater. Sci. 21(1986), 2224-2238.

- [88CPC] L. Christodoulou, P.A. Parrish, and C.R. Crowe: in **High Temperature/ High Performance Composites**, ed. F.D. Lemkey, S.G. Fishman, A.G. Evans and J.R. Strife, MRS Symp. Proc. vol. 120, Materials Research Society, Pittsburgh, PA, 1988, pp. 29-34.
- [88E11] C.K. Elliott, G.R. Odette, G.E. Lucas, and J.W. Sheckherd, in **High Temperature/ High Performance Composites**, ed. F.D. Lemkey, S.G. Fishman, A.G. Evans and J.R. Strife, MRS Symp. Proc. vol. 120, Materials Research Society, Pittsburgh, PA, 1988, pp. 95-101.
- [88Kri] S. Krishnan, G.P. Hansen, R.H. Hauge, and J.L. Margrave: Metall. Trans. A, **19A**(1988), 1939-1943.
- [88TrK] R. Trivedi and W. Kurz: in **Solidification Processing of Eutectic Alloys**, eds. D.M. Stefanescu, G.J. Abbaschian and R.J. Bayuzick, The Metallurgical Society, Warrendale PA, 1988, pp. 3-34.
- [89Hym] M.E. Hyman, C. McCullough, J.J. Valencia, C.G. Levi and R. Mehrabian: Metall. Trans. A, **20A**(1989), 1847-1859.
- [89Mar] P. Martin, Los Alamos National Laboratory, unpublished research.
- [89Mis] J.C. Mishurda, J.C. Lin, Y.A. Chang, and J.H. Perepezko, MRS Symp. Proc. vol. 133, Materials Research Society, Pittsburgh, PA, 1989, pp. 57-62.
- [89McC] C. McCullough, J.J. Valencia, C.G. Levi and R. Mehrabian: Acta Metall. **37**(1989), 1321-1336.
- [89McM] R.M. McMeeking, University of California at Santa Barbara, unpublished research.
- [89Ros] J. Rösler, T.C. Lu, and R. Mehrabian, University of California at Santa Barbara, unpublished research.
- [89VML] J.J. Valencia, C. McCullough, C.G. Levi, and R. Mehrabian: Acta Metall. **37**(1989), 2517-2530.

- [89Val] J.J. Valencia, C. McCullough, J. Rösler, C.G. Levi and R. Mehrabian:
in **Solidification of Metal Matrix Composites**, ed. P. Rohatgi, The
Minerals, Metals and Materials Society, Warrendale, PA, 1989 (in
press).

Table I. Alloy Compositions Investigated¹

Alloy	%Al	%B
47-1	46.9	1.15
49-1	49.1	0.72
49-2	49.3	1.00
49-3	49.4	1.00
49-4	48.6	1.24
49-5	49.2	1.54
50-1	50.3	0.85
50-2	50.4	1.60
52-1	51.7	0.82
52-2	51.9	0.95
52-3	51.5	1.15
52-4	52.3	1.15

¹ All compositions in atomic percent. Al by AAS method, B by DCPES method.
Al compositions verified by EDS.

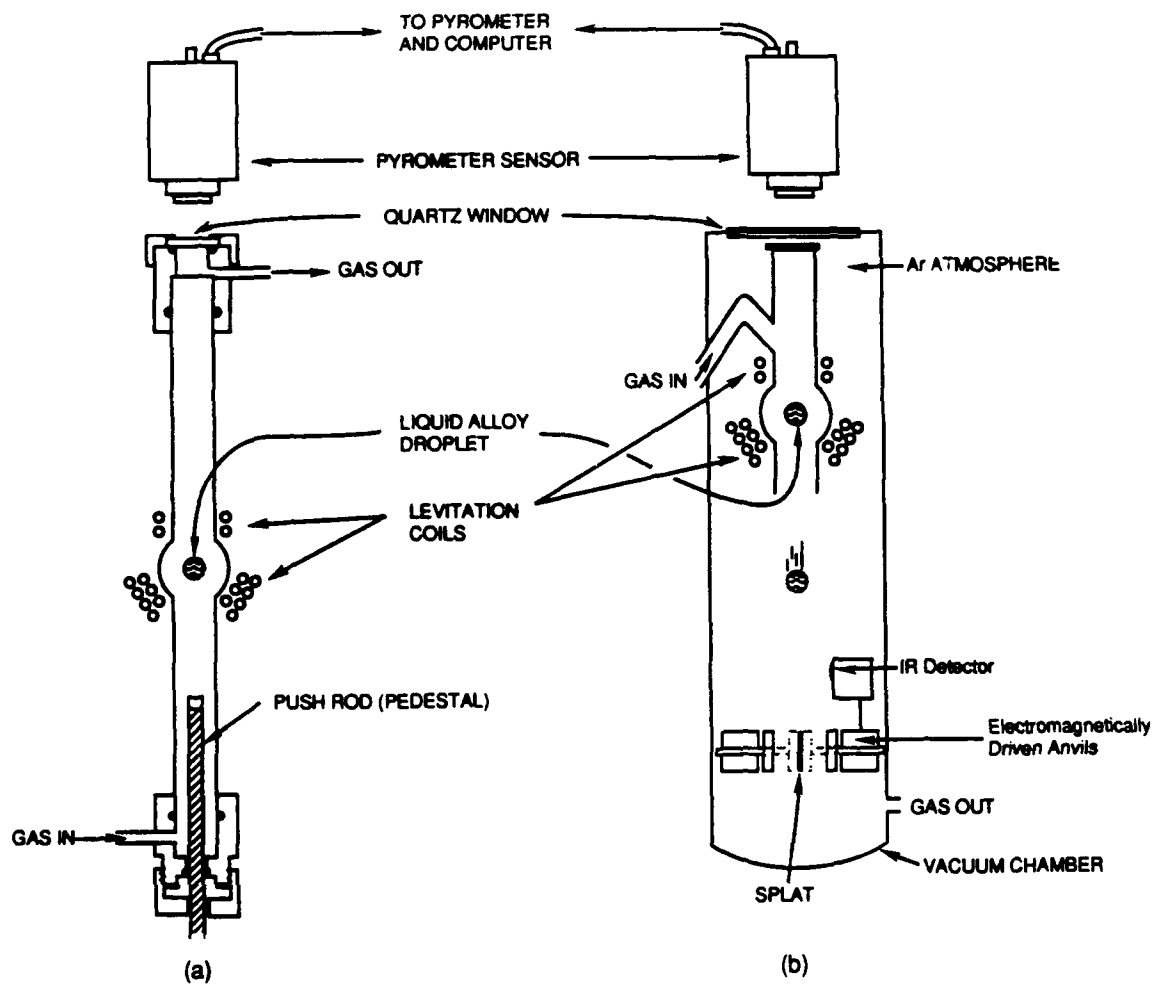


Figure 1. Schematic diagram of electromagnetic levitation/melting apparatus. (a) used for supercooling and gas-cooling experiments, (b) used for splat quenching experiments.

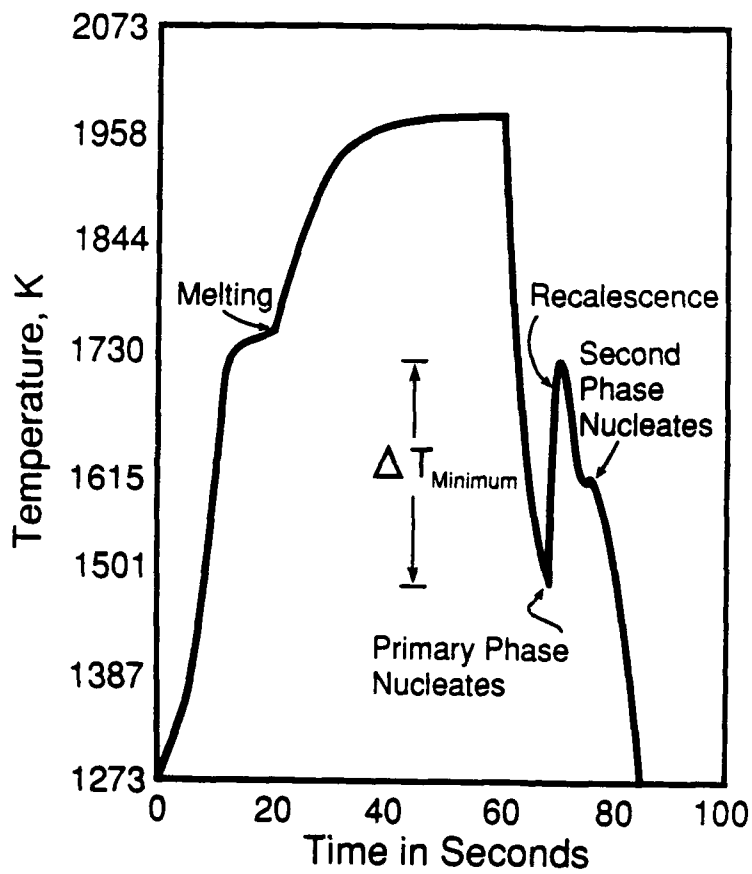


Figure 2. Typical thermal history curve of a supercooled droplet showing two nucleation events. The extent of supercooling is determined from the initial recalescence excursion.

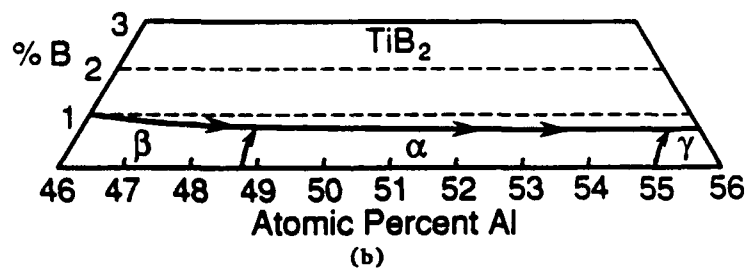
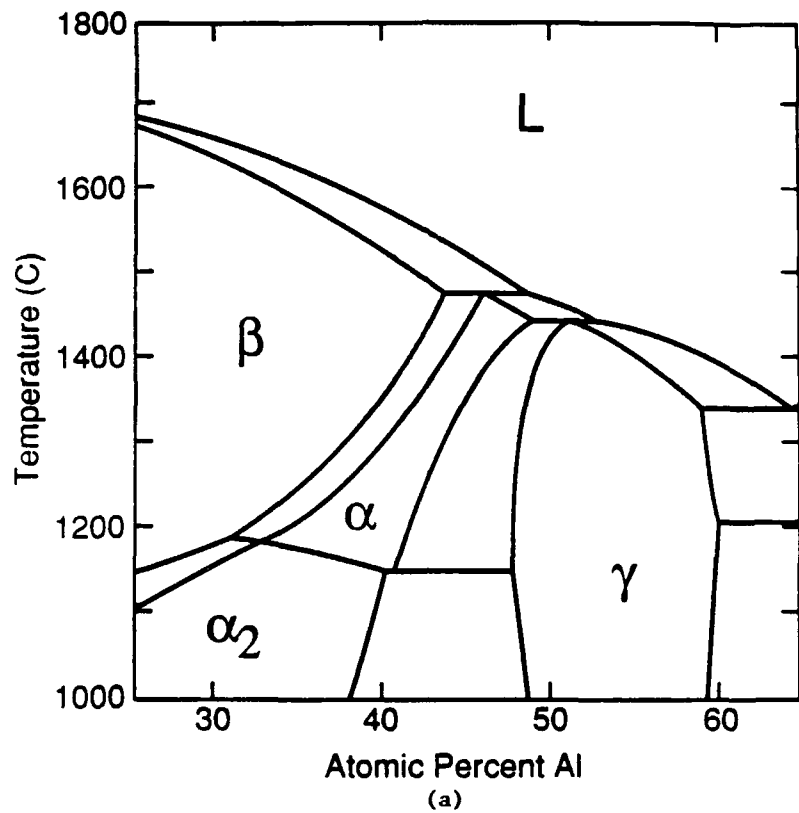


Figure 3. Phase equilibria relevant to this investigation: (a) Binary Ti-Al phase diagram near the γ field [89McC, 89Mis]; (b) Suggested liquidus projection for the ternary Ti-Al-B system in the vicinity of the equiatomic TiAl composition.

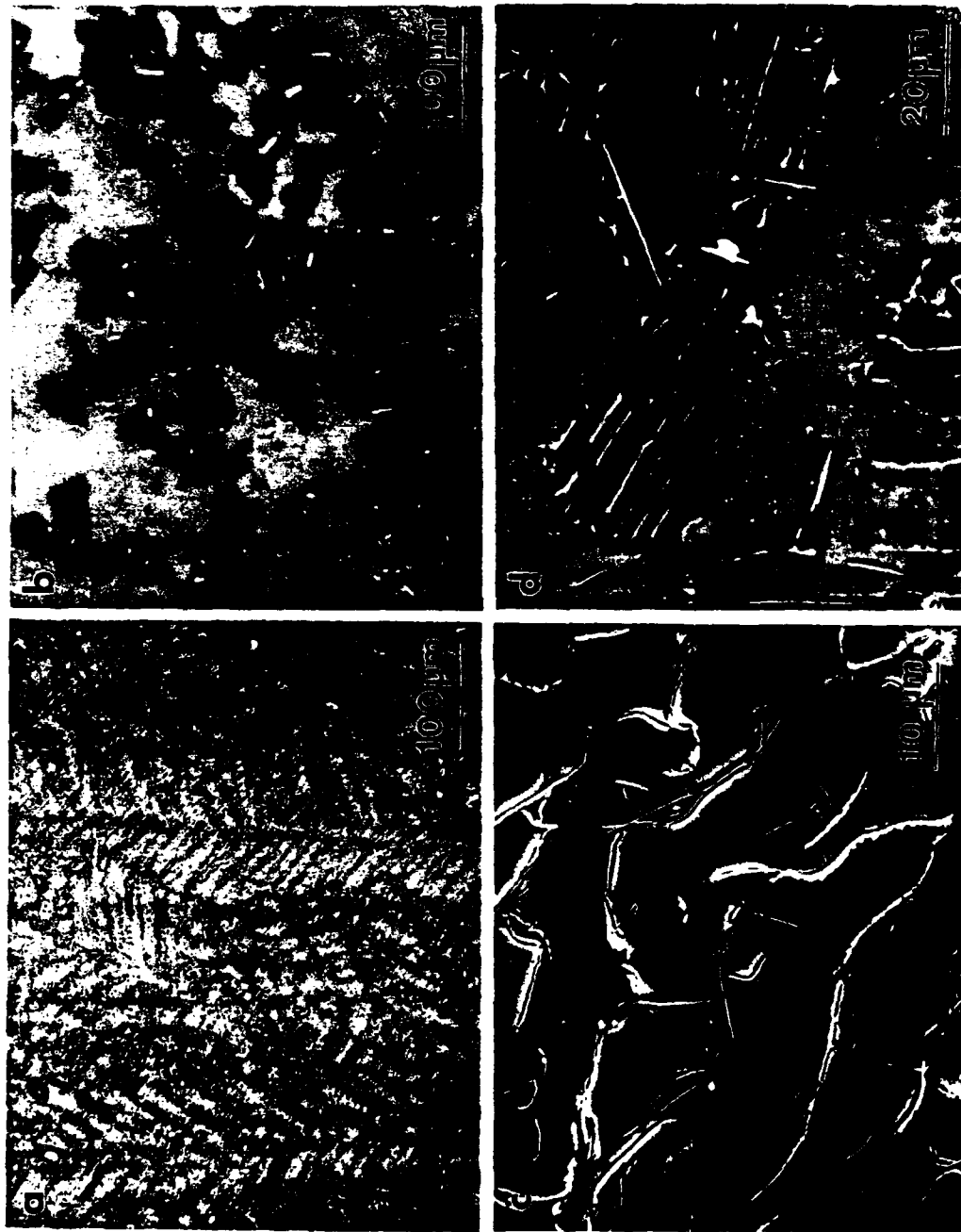


Figure 4. Solidification microstructures of the arc-melted buttons. (a) Alloy 52-3 (51.5Al-1.15B) showing dendrites near chill face; (b) Alloy 49-3 (49.4Al-1B) showing α -Ti dendrites, and some primary TiB_2 particles; (c) Alloy 49-1 (49.2Al-0.72B) showing TiB_2 plates and needles; and (d) Alloy 52-3 (51.5Al-1.15B) showing dendrites near chill face and some primary TiB_2 particles.

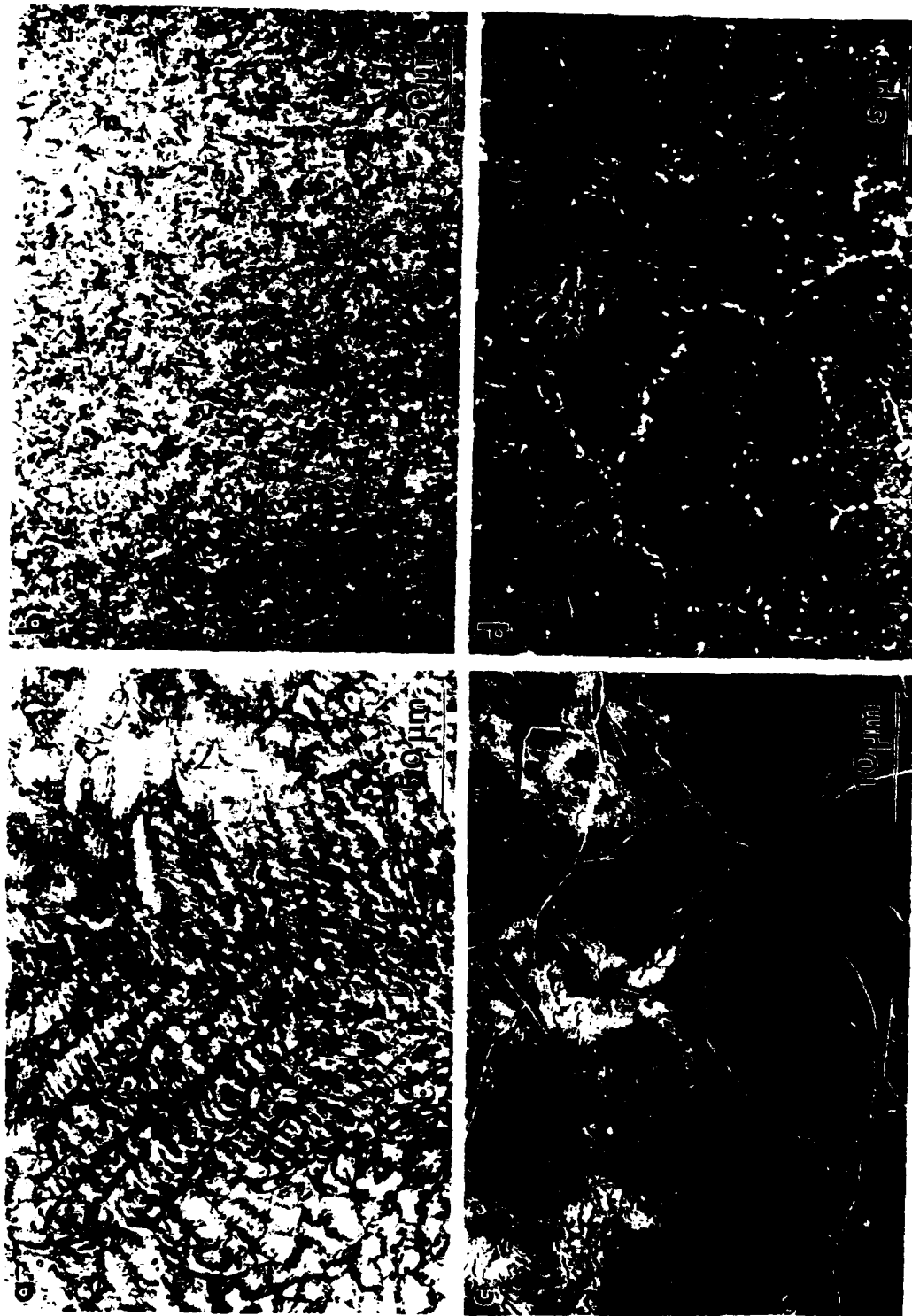


Figure 5. Microstructures of supercooled Ti-49.2Al-0.72B (alloy 49-1). (a) and (c) show primary α -Ti and flake TiB_2 after $\Delta T = 100$ K; (b) and (d) show fine-grained microstructure with small equiaxed borides after $\Delta T = 218$ K.

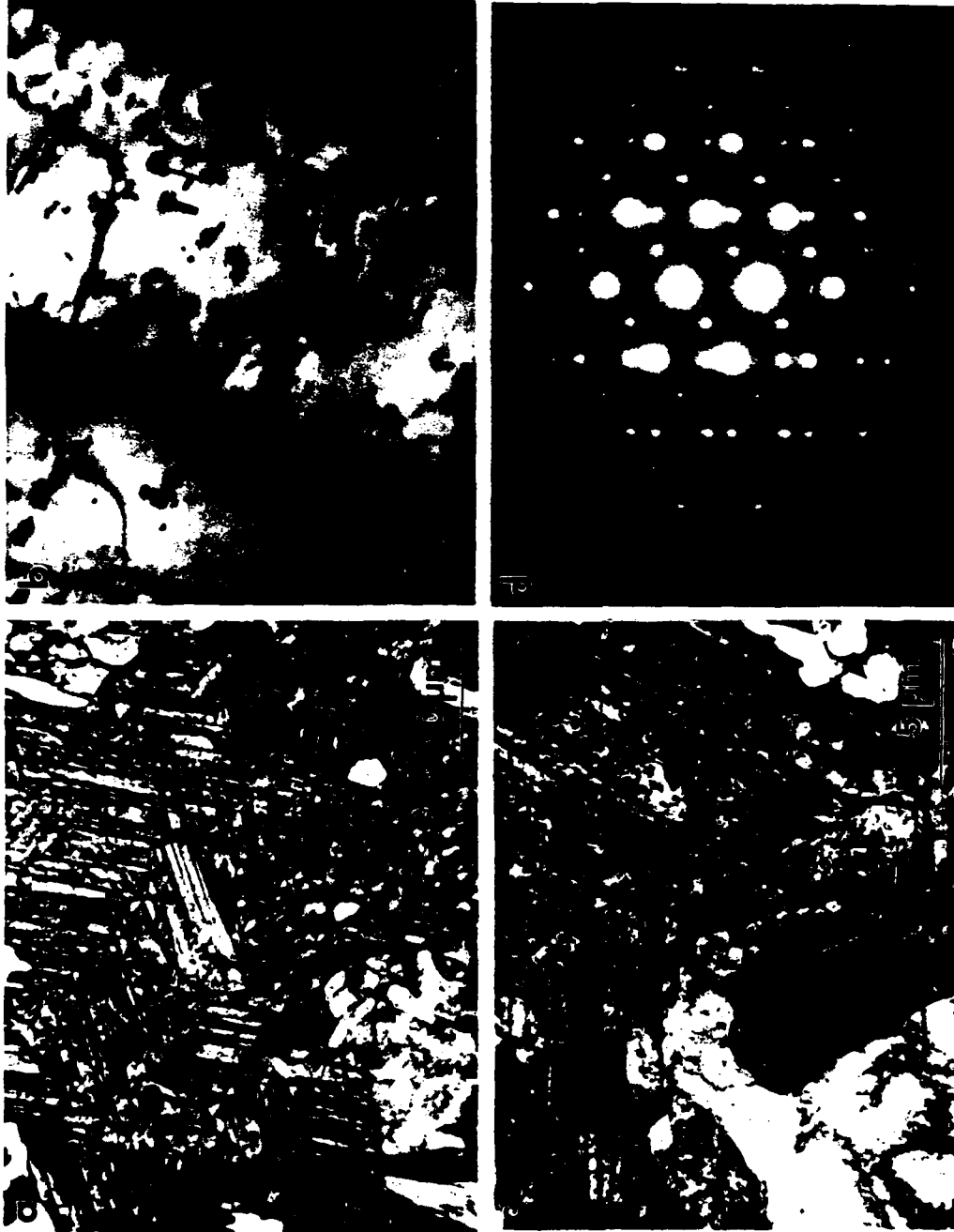


Figure 6. TEM micrographs of a Ti-49.2Al-0.72B supercooled 278 K, revealing (a) packets of $\alpha_2 + \gamma$ lath with small amounts of γ segregate, (b) ultrafine boride precipitates inside γ laths, (c) three lath variants with their habit planes oriented 120° from each other, and (d) SAD pattern from a single lath packet showing two twin related $[110]_\gamma$ zones and a single $[1210]_{\alpha_2}$ zone.

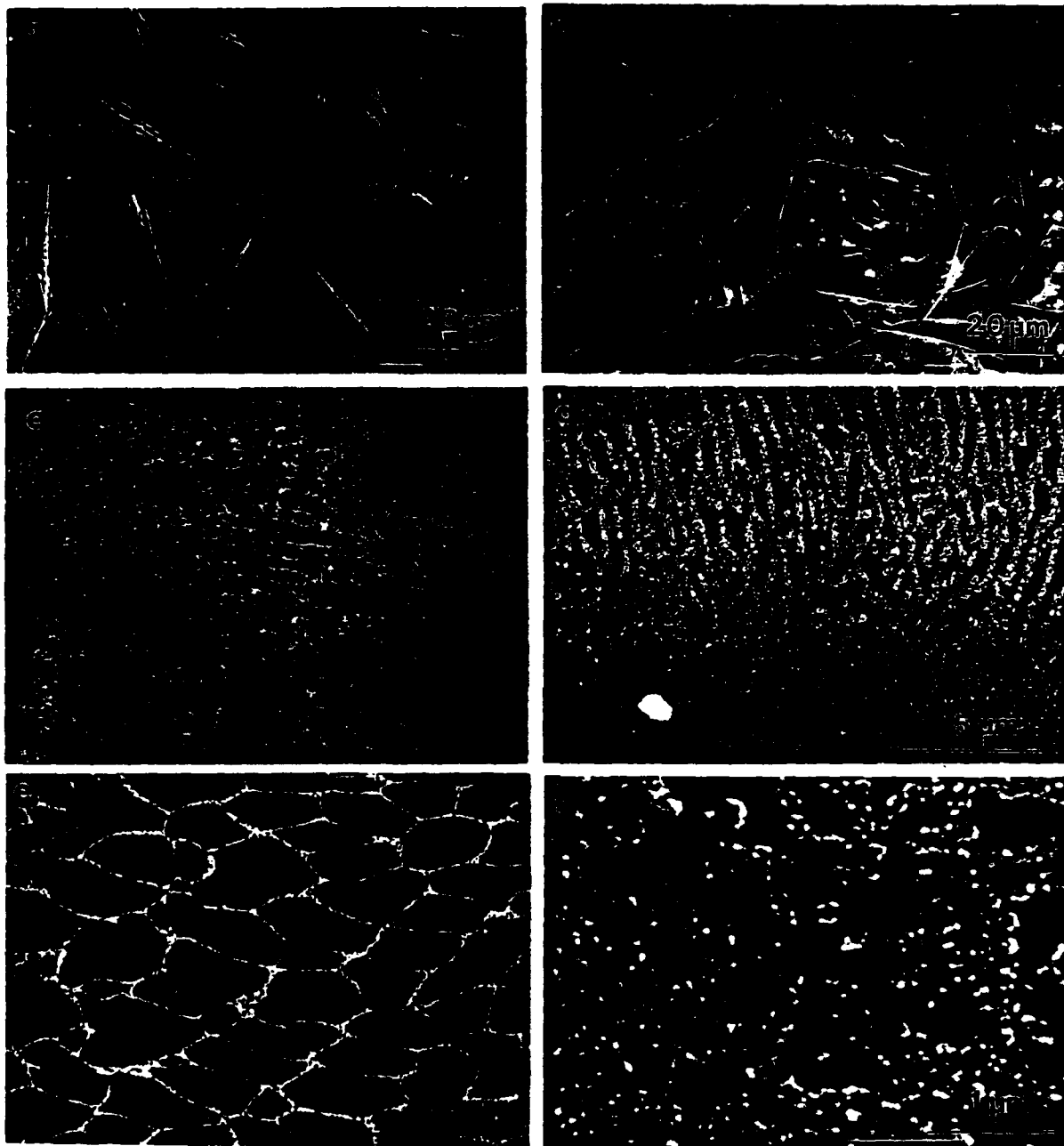


Figure 7. SEM micrographs showing the effect of cooling rate on Ti-51.5Al-1.15B (alloy 52-3). Microstructure contains plates and needles after cooling at 5 K/s (a), but only flakes after cooling at 15 K/s (b); (c) cross sectional view of a splat with the chill zone on the left side of the micrograph and the center of the splat on the right; (d) microcellular pattern near chill zone, (e) cellular/dendritic growth in the bulk of the splat, and (f) equiaxed α -Ti dendrite in the core of the splat.

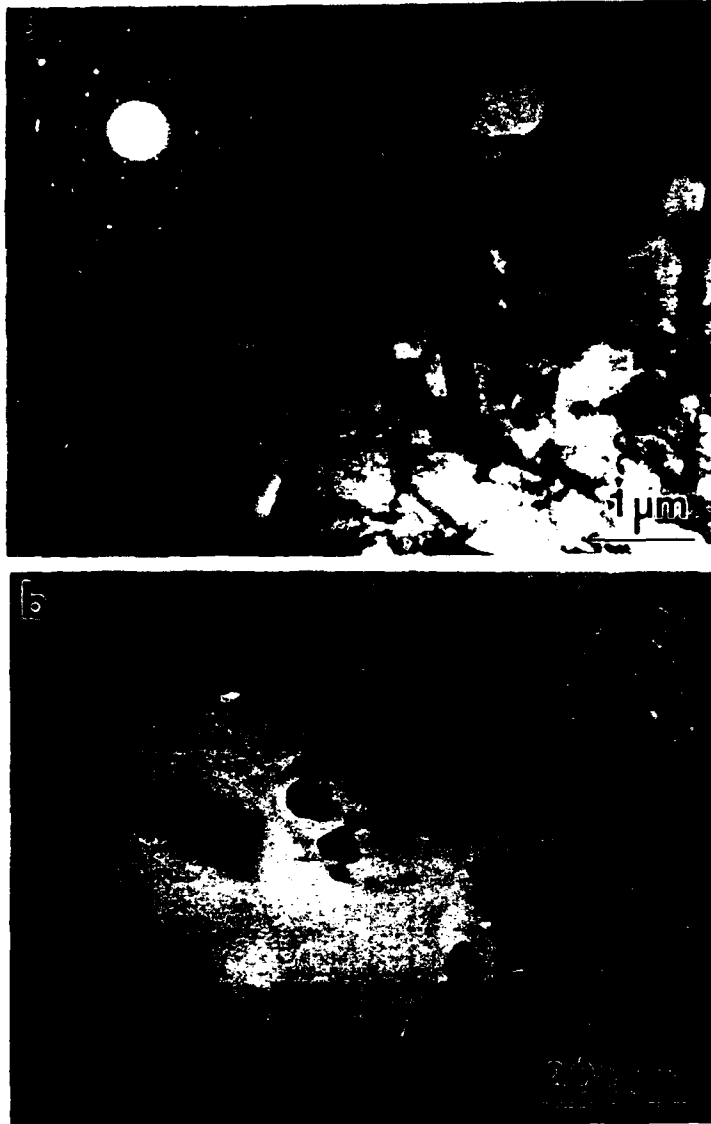
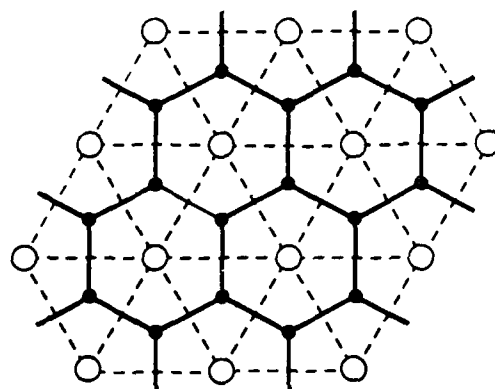
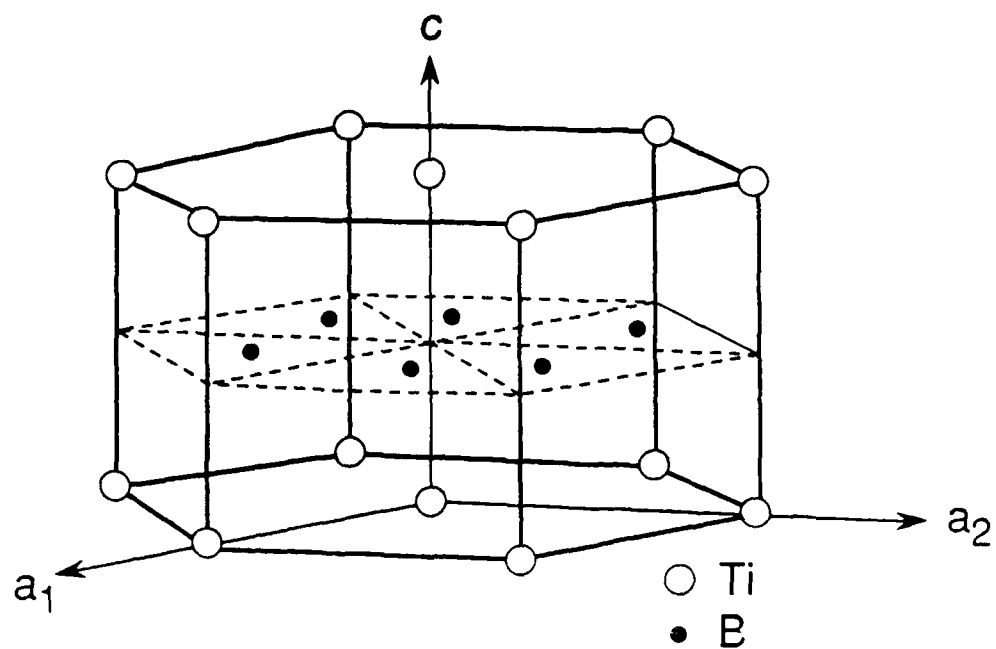


Figure 8. TEM microstructure of a Ti-51.5Al-1.15B splat showing (a) fine polycrystalline γ matrix and (b) very fine equiaxed borides within the γ grains.



Ti \circ 0, 1

B \bullet 1/2

Figure 9. Crystal structure of TiB_2 showing the AH AH stacking of Ti and B layers along the c -axis. Note the difference in stacking of the $\{10\bar{1}0\}$ and $\{1\bar{2}10\}$ prismatic planes.



Figure 10. TiB_2 plates in the shrinkage cavity of a Ti-51.5Al-1.15B alloy clearly showing (a) matrix constraint during growth, and (b) basal and prismatic facets bounding the plate.

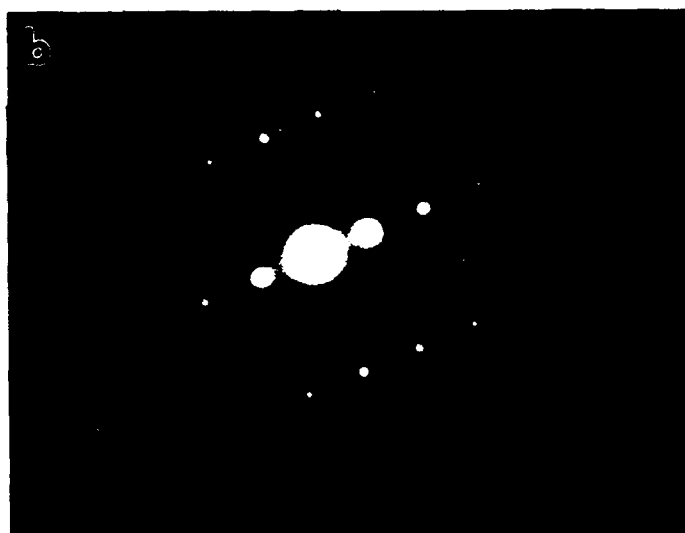
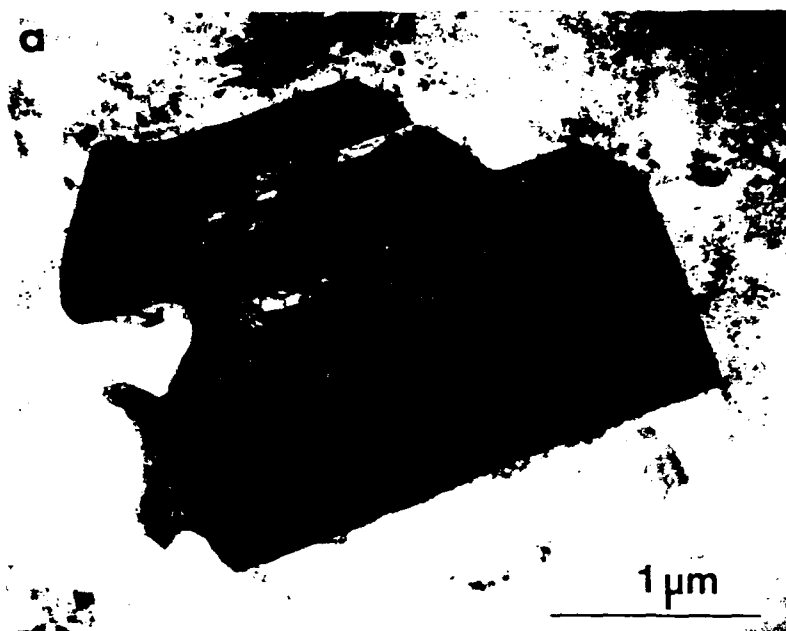


Figure 11. TEM micrograph of a TiB_2 plate extracted from a deep-etched specimen (a) and diffraction pattern normal to the plane of the image (b) showing a $[10\bar{1}0]$ TiB_2 zone axis.

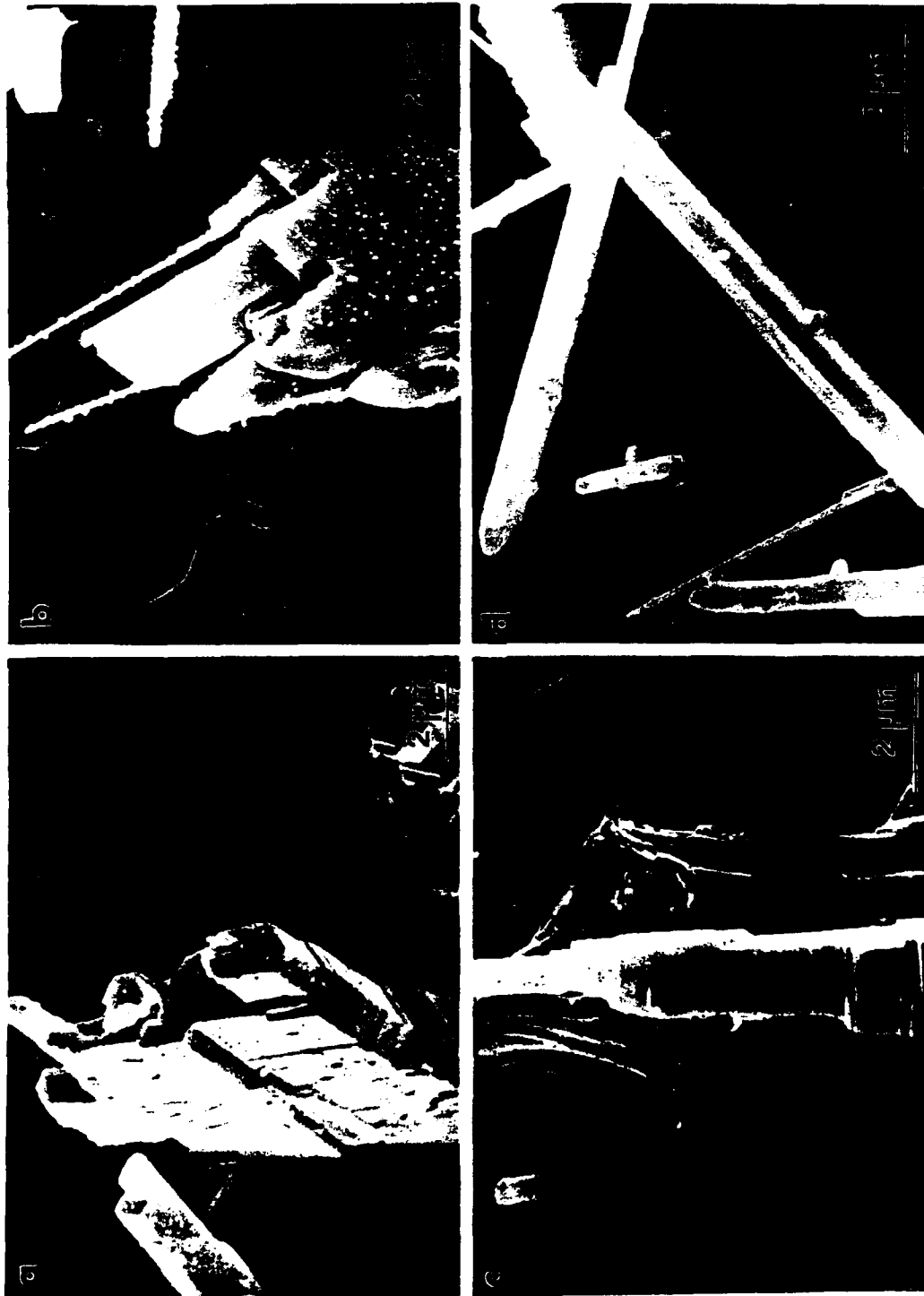


Figure 12. Deeply etched Ti-51.5Al-1.15B arc-button sections showing plates breaking into needles (a) and (b), thickening of needles by prismatic ledges (c), and branching of needles (d). Also note that the angular tips of the needles suggesting that they are bound by pyramidal planes.

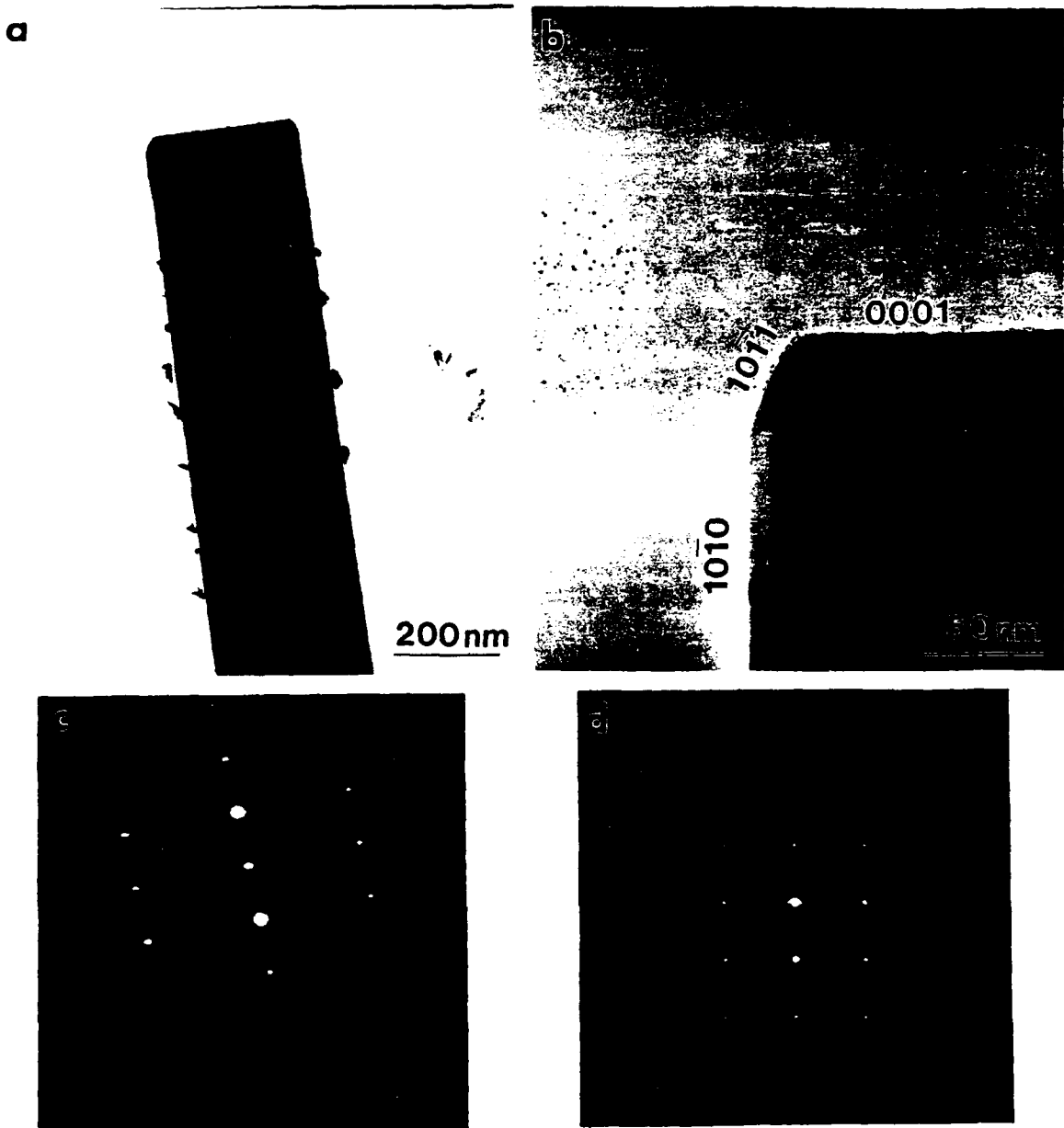


Figure 13. TEM micrograph of an extracted TiB_2 needle showing the growth axis to be the $[0001]$ direction of the TiB_2 structure and a tip bounded by basal, prism and pyramidal facets. The diffraction patterns in (c) and (d) correspond to the $[01\bar{1}0]$ and $[1\bar{2}10]$ zone axes of TiB_2 , respectively.

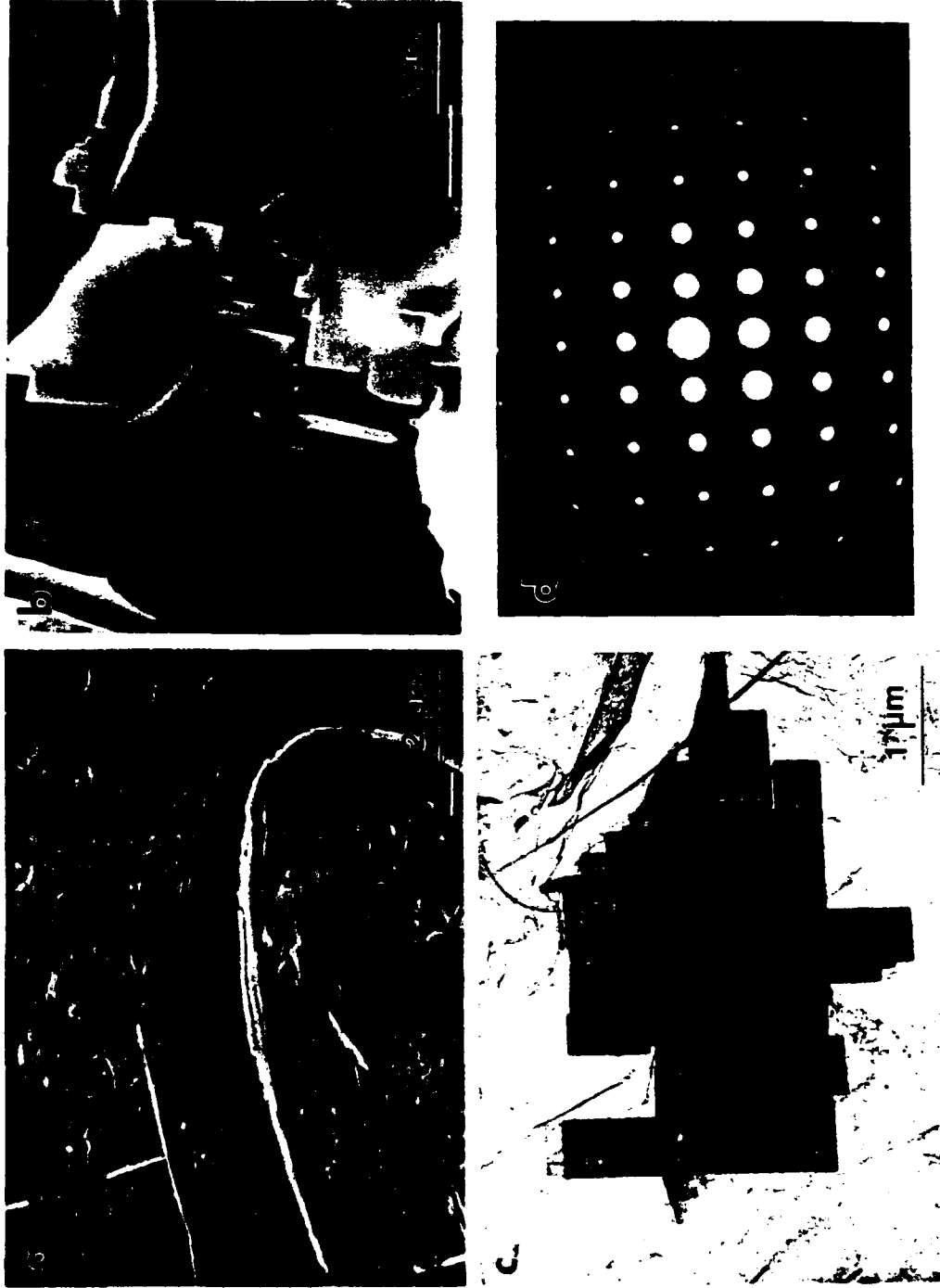


Figure 14. SEM and TEM views of the TiB_2 flake morphology showing (a) a curved growth pattern with apparent layers within the flake; (b) thin flakes on the surface of a deep-etched specimen; (c) an extruded flake with the habit plane parallel to the plane of the image, and (d) the corresponding diffraction pattern with a $[1\bar{2}10]$ zone axis.

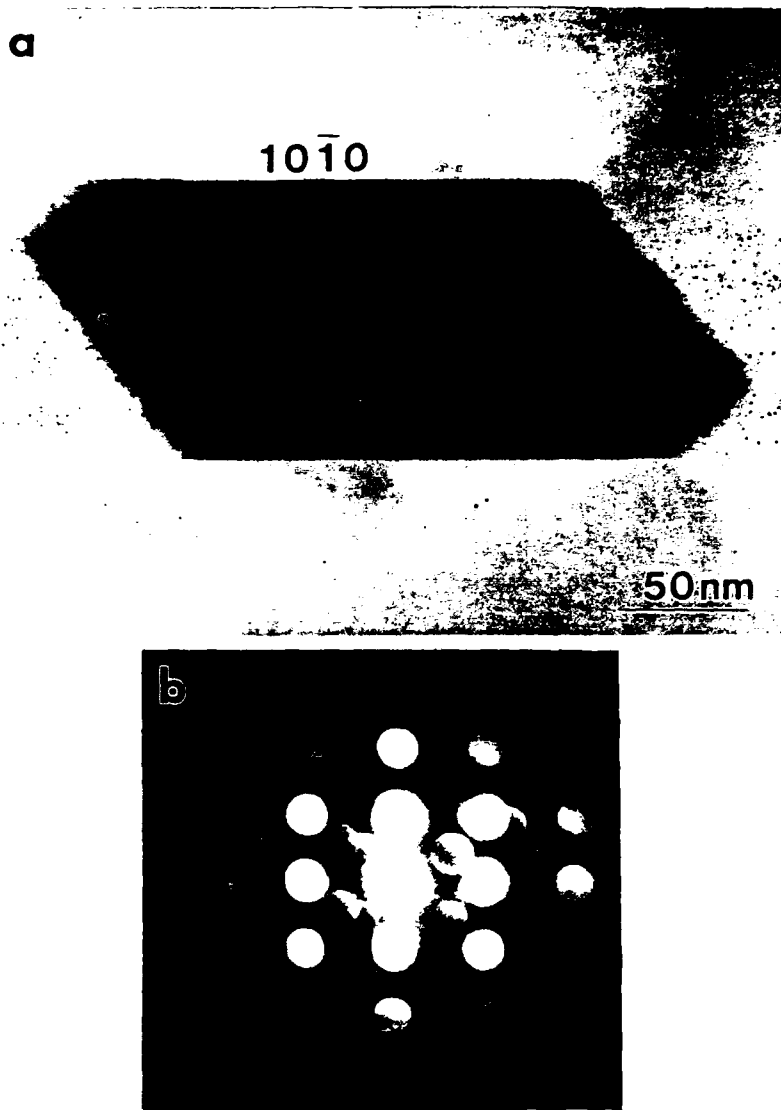
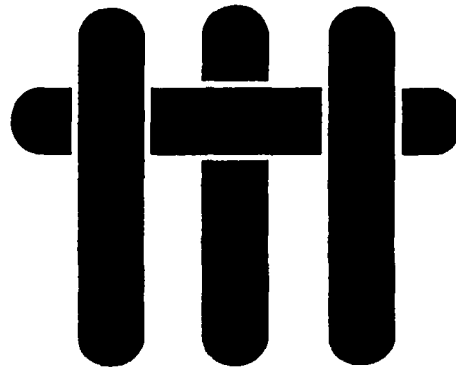


Figure 15. TEM image and diffraction pattern of the fine equiaxed TiB_2 found in the highly supercooled specimens. The facets shown are of the $\{10\bar{1}0\}$ prismatic type. The zone axis of the diffraction pattern is $[1\bar{2}16]$.

M A T E R I A L S



**DEVELOPMENT OF TiAl
INTERMETALLIC MATRIX COMPOSITES
BY SOLIDIFICATION PROCESSING**

J. J. Valencia, C. McCullough, J. Rösler, C. G. Levi and R. Mehrabian

Materials Department
College of Engineering
University of California, Santa Barbara
Santa Barbara, California 93106

DEVELOPMENT OF TIAL INTERMETALLIC MATRIX COMPOSITES
BY SOLIDIFICATION PROCESSING

J.J. Valencia, C. McCullough, J. Rösler, C.G. Levi and R. Mehrabian

Materials Department
College of Engineering
University of California
Santa Barbara, CA 93106

Abstract

This investigation focused on solidification processing as a route to produce in-situ refractory reinforcements in γ titanium aluminides. The desirable reinforcements must be thermodynamically stable phases at the temperatures of interest, have dimensions appreciably larger than the dislocation cell size and anisotropic morphologies with fairly high aspect ratios. Carbon additions to γ -TiAl produce primary Ti_2AlC , which grows from the melt as plates with aspect ratios of ~ 20 . Nitrogen behaves in a similar manner, but the plates are somewhat shorter and hence less desirable for strengthening purposes. Boron additions to the binary γ -TiAl produce equiaxed TiB_2 , but when Ta or Nb are added the primary phase changes to a ternary monoboride, isomorphous with TiB , which grows as highly elongated rods $\sim 5 \mu m$ thick and with aspect ratios of ~ 20 or larger. Selection of the reinforcement volume fraction, shape and size can be effected by suitable control of the alloy chemistry and solidification parameters. Preliminary testing at 1255 K indicates that these in-situ composites have much higher creep strengths than an unalloyed single phase γ -alloy, although some of the strengthening may arise from solute hardening of the matrix. The boride phases appear to be superior both from processing and mechanical behavior viewpoints.

Introduction

It is well known that alloys based on the γ -TiAl intermetallic are potential candidate materials for high temperature structural applications. The γ -phase has the L1₀ crystal structure and remains ordered up to near its melting point, resulting in high modulus retention with temperature. The strong bonding and the ordered lattice reduce the atomic activity leading to potentially attractive creep properties [1]. However, there is sufficient dislocation mobility above 900 K [2] to limit the high temperature strength below the levels desirable for the more demanding applications. Furthermore, current efforts to improve the toughness of γ -TiAl are mainly based on crack bridging by incorporating ductile-phase Ti-alloy particles via powder metallurgy techniques [3]. Some promising results have been achieved by this approach but with a concomitant reduction in creep strength relative to the matrix [4].

Creep strengthening of γ -TiAl can be addressed by incorporating hard refractory reinforcements to constrain the plastic flow of the matrix at high temperatures. Theoretical analyses based on continuum mechanics suggest that the creep rate of the composite is related to that of the intermetallic by an expression of the following form [5]

$$\dot{\epsilon}_{\text{composite}} = A(f,s,n) \dot{\epsilon}_{\text{matrix}}$$

where the strengthening factor A is a function of the volume fraction (f) and the shape (s) of the reinforcement, and the creep exponent of the matrix (n). Calculations for spherical reinforcements based on an analysis by Duva [6] and the creep exponent of γ -TiAl (n = 4.5) predict the trend shown in Figure 1. More recent work by McMeeking [7] and He et al. [8] suggests that anisotropic reinforcements (i.e. rods and plates) with high aspect ratios should further reduce the creep rate below the level predicted for spheres, as schematically depicted in Figure 1. In general, all these reinforcements must be of a scale larger than the dislocation cell size in the matrix, i.e. a few micrometers.

The present investigation was predicated on the foregoing discussion. Its goal was to explore solidification processing routes to develop refractory reinforcements with desirable morphologies and aspect ratios in γ -TiAl alloys. The refractory phases of interest are borides, carbides and nitrides which may be formed by the addition of B, C and N to binary Ti-Al and ternary Ti-Al-(Ta,Nb) alloys. The morphology and scale of the reinforcing phases depend on important material and process parameters such as the crystallography of the

compound, the stage of the solidification process in which they evolve, whether they grow in a coupled or divorced fashion, and the solidification rate. It is important to indicate at this point that the reinforcements studied in this investigation evolve mainly as primary phases during the solidification of γ -TiAl based alloys. This is different from the XDTM(1) process of current interest, where the reinforcements are first produced by reaction of the constituent elements in an Al bath, yielding a master composite alloy which is subsequently mixed with suitable amounts of Ti, Al and any other desirable elements to form the final composite [9].

Experimental

All alloys used in this investigation were produced by arc-melting in a slightly pressurized atmosphere of gettered argon containing less than 0.1 ppb oxygen. The starting materials were Ti buttons, (<200 ppm O₂), 99.99%Al pellets, 99.7% 60-mesh B powder, 99.9%C graphite rods and 99.5% 325-mesh TiN powder.(2) The melting procedure is particularly crucial to the control of the Al composition, which tends to evaporate heavily if the compound-forming additions are added directly to TiAl. The ternary Ti-Al-X alloys (X = C, N, B) were prepared by first dissolving X in molten Ti to make a Ti-X alloy to which Al was later added to achieve the desired matrix composition [10]. The quaternary Ti-Al-R-B alloys (R = Ta, Nb) were made in a similar manner, preparing ternary Ti-R-B and Ti-R-Al alloys of the proper stoichiometry and then crushing and remelting them together to achieve the final alloy chemistry. The arc-buttons were flipped over and melted-down six times to ensure complete homogenization, and then remelted into ingots approximately 8 cm long and 1 cm² in cross section. The alloys in Table 1 were produced in this manner. Small pieces were cut from some of the ingots and subsequently arc-melted into spheres of approximately 500 mg for use in the levitation experiments.

Electromagnetic levitation/melting coupled with controlled gas cooling was used to study the effect of solidification rate on the morphology of the reinforcing phases. This technique allows continuous monitoring of the thermal history during solidification and the development of more quantitative relationships between the microstructural features and important parameters like supercooling and cooling rate.

(1) XDTM is a trademark of Martin Marietta Corporation.

(2) Ti buttons were supplied by TIMET, Al pellets and B powder by Alfa/Morton-Thiokol, graphite rods by UNION 76 and TiN powder by CERAC.

The levitation apparatus and technique have been described in detail elsewhere [11]. Briefly, a small spherical sample was placed inside a tubular glass chamber within an induction coil which was designed to both levitate and melt the material. Throughout the heating process the temperature of the specimen was controlled by a small flow of gettered Ar (<0.1 ppb O_2) mixed with high purity He (<5 ppm O_2). Once the sample was molten, the liquid was superheated by approximately 150 K and kept for 60-90 s at this temperature to ensure the complete dissolution of the refractory phases in the liquid. While still levitated, the liquid droplets were cooled at rates ranging from ~ 0.2 to ~ 40 K/s. The slower rates were achieved by increasing the levitation force (i.e. the RF power output) which lifted the sample into a region of the coil with lower field density allowing it to cool at a very slow rate without changing the gas flow. Higher solidification rates were achieved by increasing the gas flow and the proportion of He in the gas mixture. Once solidification was completed the droplet was cooled with a high flow of He gas; the power was then cut off to allow the sample to fall to the bottom of the tube, from where it is retrieved. The thermal history of the sample was continuously monitored by an Ircon-Maxline two-color pyrometer with a response time of 25 ms and recorded to disk in a microcomputer.

Ingots of the unreinforced γ alloy and some of the composite alloys were packed in pure Ti chips and wrapped in Ta foil for heat treatment. The latter was carried out at 1473 K for 100 hours in an environmental furnace filled with gettered Ar at a partial pressure of ~ 75 kPa. Cylinders 6 mm in diameter and 12 mm long were electro-discharge machined for conducting compression creep testing. The creep testing was performed in air at 1255 K using a MTS 810 servo-hydraulic testing machine at a constant crosshead speed. SiC rams were used to load the specimens inside the furnace. The temperature was controlled during the test to an accuracy of ± 1 K by an S type thermocouple placed near the specimen. The specimen strain was monitored outside the furnace by an LVDT.

Samples of the specimens above were taken for chemical analysis and microstructural characterization by optical, scanning (SEM) and transmission (TEM) electron microscopy. Microchemistry was determined by energy dispersive X-ray spectroscopy (EDS) in the SEM and TEM. Most alloy compositions were verified by wet chemistry at an external laboratory. The volume fraction and aspect ratio of the reinforcements were determined by quantitative metallography in an automated image analysis system. Additional samples of the ingot materials were deep etched in hot sulfuric acid to dissolve the matrix and subsequently study the three-dimensional morphology of the reinforcing phases.

Rod Reinforcements

This section addresses the microstructures containing rodlike reinforcements, which correspond to the TiAl alloys with B and Ta or Nb additions. Platelike second phases, which evolve primarily in the ternary alloys containing C and N, are discussed later in the article.

Most of the research efforts in composite materials based on titanium aluminides with boron additions have been focused on the mechanical behavior of these alloys, with limited emphasis (at least in the open literature) on the processing aspects. It is evident, however, that the ability to modify the boride phase morphology depends on a clear understanding of the solidification behavior as a function of alloy chemistry and process conditions [10, 12]. We shall first discuss the opportunities for morphological selection offered by the crystallographic characteristics of the available boride structures. We will then present some microstructural observations reflecting the crystallographic influence on the growth of the actual boride phases.

Crystallographic considerations

The crystal structures of the relevant refractory borides are all based on the trigonal prismatic array of six metal atoms with a B atom at the center [13]--see Figure 2. Different boride structures can then be built by arranging these trigonal prisms in various patterns, as illustrated in this figure. Stacking the prisms in a close packed array, sharing all their triangular and rectangular faces as shown in Figure 2(a), leads to the hexagonal C32 structure characteristic of TiB_2 (AlB₂-type). This structure can also be visualized by stacking close packed Ti planes (A) with graphite-like boron planes (H) in an AH AH sequence along the c-axis of the crystal. On the other hand, the orthorhombic B27 structure of TiB (FeB-type) consists of trigonal prisms stacked in columnar arrays sharing only two of their three rectangular faces with neighboring prisms, as depicted in Figure 2(b). The B atoms in this case form a zigzagging chain of bonds along the [010] direction. To account for stoichiometry, the columns of prisms are connected only at their edges forming boron-free "pipes" of metal atoms with a trapezoidal cross section, as shown by the (010) projection in Figure 2(b). Alternatively, the prisms could be stacked to form sheets by sharing both their triangular faces and two of the rectangular faces, as depicted in Figure 2(c). By stacking these sheets parallel to each other in a PM PM sequence, where the M layers are displaced 1/2

[100] relative to the P layers, one obtains the orthorhombic structure characteristic of TaB and NbB (CrB-type).

Since crystals growing from the melt are usually bound by the slowest-growing facets, one would anticipate that the various stacking patterns shown in Figure 2 should lead to significantly different crystal morphologies. Typically, growth normal to planes containing both metal and B atoms in the same stoichiometry as the crystal would be faster than growth along directions involving alternating planes of metal and B atoms. Moreover, planes with a higher density of strong bonds ($B-B > B-M > M-M$) or "Periodic Bond Chains" [14] also tend to grow at a faster rate. Based on the arguments above one could show that the slowest growing planes in TiB_2 are of the basal (0001) and prism $\{10\bar{1}0\}$ families, suggesting that TiB_2 should grow with a fairly equiaxed morphology⁽³⁾ [10]. On the other hand, TiB should exhibit much faster growth along the [010] direction than normal to the (101) and (100) planes, developing a needle or rod-like morphology. For similar reasons, TaB/NbB might grow faster in the [100] and [001] directions (i.e. on the plane of the "sheets") than normal to the (010) planes, leading to a plate-like morphology.

Microstructural evidence

Analysis of the solidification microstructures of ternary Ti-50Al-5B⁽⁴⁾ and quaternary Ti-50Al-11Nb-3.5B and Ti-48Al-9Ta-4.3B alloys reveals a variety of boride morphologies which are essentially consistent with the crystallographic arguments presented above.

The primary boride formed in the Ti-50Al-5B alloy is TiB_2 and grows in fairly equiaxed crystals, 10-20 μm across, which sometimes appear associated in clusters, as shown in Figures 3(a) and (b). The facets of the crystals exhibit a distinct hexagonal symmetry and have been identified as basal (0001) and prismatic $\{10\bar{1}0\}$ planes by TEM work reported elsewhere [10]. Secondary borides in this system are also TiB_2 but they typically develop flake, plate and needle-like morphologies, depending on the alloy composition and solidification parameters [10, 12]. However, while these secondary borides have more desirable geometries for strengthening purposes than the primary phase

(3) In some dilute melts TiB_2 grows as plates with an (0001) habit plane since the growth rate of the prism planes is somewhat higher than that normal to the basal plane [15].

(4) All compositions in atomic percent unless specified otherwise.

particles, their relative proportion in the microstructure is quite low (~1 vol%) and cannot be readily increased due to constraints imposed by the phase diagram [12].

Addition of ~10% Ta or Nb substituting for Ti in the basic γ -TiAl-B composition changes dramatically the morphology of the primary boride to rods, ~5 μm in diameter and aspect ratios of 20 or higher, as shown in Figures 3(c) to (f). TEM work identified these rod-like borides as having the crystal structure of TiB with the axis of the crystal (i.e. the fastest growth direction) along the [010] axis of the B27 structure [16], as expected from the crystallographic considerations discussed above. Similar morphologies have been reported for primary TiB in binary hypereutectic Ti-B alloys [10]. However, EDS analyses indicated that the rod borides in these quaternary alloys contain large amounts of Ta or Nb in solid solution within the TiB structure. Thus, the Ta/Nb additions essentially change the boride morphology by shifting the alloy composition from the C32 to the B27 liquidus region in the quaternary system.

Alloys investigated up to this time have not shown plate-like primary borides, although secondary phases with this shape have been identified in the above quaternary compositions--see for example Figure 4. Preliminary TEM work suggests that these phases have the CrB-type crystal structure corresponding to TaB/NbB [16], with the habit plane of the plates normal to the [010] direction (i.e. the one of slowest growth). While these observations are essentially consistent with the crystallographic arguments presented above, one cannot dismiss in this case the possible influence of the matrix constraint or the solidification rate, which have been shown to play significant roles in the development of secondary TiB₂ phases in the Ti-Al-B alloys [12]. Additional research is underway to elucidate the evolution of these phases in the quaternary alloys.

Plate Reinforcements

Ongoing modelling work on plasticity and creep of composites [7] suggests that plate reinforcements are also desirable for strengthening in three dimensional arrays, although their relative effectiveness compared to the rods is still a subject of debate. Previous work by the authors on the solidification of γ -TiAl alloys containing small amounts of C revealed that highly elongated plate-like primary phases appeared above ~0.5%C [17]. An investigation was then undertaken to assess the feasibility of producing significant volume fractions of these plate-like phases and assess their potential as reinforcements for TiAl.

Crystallographic considerations

A cursory review of the available ternary diagram for the Ti-Al-C system [18] reveals that the stable carbide phase in equilibrium with γ -TiAl is Ti_2AlC , which has the hexagonal crystal structure illustrated in Figure 5. The atomic arrangement can be first visualized as a stacking of close-packed Ti and Al planes along the c-axis in an AB AB' A'B' sequence resembling that of a conventional HCP crystal, where A and B' are Ti planes and B and A' are Al planes. The C atoms in this structure would then occupy the octahedral interstices between two consecutive Ti layers (AB' or B'A), producing the final stacking sequence ABAC B'A'B'C. Similarly, the equilibrium nitride is Ti_2AlN which has the same crystal structure with the N substituting for C.

Examination of Figure 5 clearly suggests that the complicated stacking sequence along the c-axis should significantly slow down the crystal growth in this direction. On the other hand, growth along the a-axes could be quite rapid since it involves the stacking of $\{1\bar{2}10\}$ planes which contain all three atoms in the correct stoichiometric proportions, as depicted in Figure 5(c). Thus, it is anticipated that the Ti_2AlC and Ti_2AlN phases will exhibit highly anisotropic growth that should result in plate-like crystals with a habit plane parallel to the basal plane of the structure.

Microstructural evidence

Metallographic views of the as-cast buttons in Figures 6(a) to (d) clearly show the presence of platelets in γ alloys containing approximately 48 and 52%Al, and 3%C or N (Table 1). The plate morphology is more clearly appreciated in the deep-etched specimens, Figures 6(e) and (f), although the crystal facets are not as defined as in the case of the borides since the compound phases are partially attacked by the etchant. The volume fraction of reinforcements determined by quantitative metallography is between 10 and 12% for all these alloys, which is close to the amount expected if all the C/N were combined in compounds of stoichiometry Ti_2AlX .⁽⁵⁾ The average aspect ratio of the platelets is ~20 for the carbides and somewhat smaller for the nitrides.

⁽⁵⁾ This assumes a theoretical density of 4.06 Mg/m³ for Ti_2AlC , 4.30 Mg/m³ for Ti_2AlN and 3.75 Mg/m³ for γ -TiAl.

Figure 6 also shows substantial matrix segregation during solidification, especially in the N-bearing alloys and the lower Al contents. Assuming a compound stoichiometry of Ti_2AlX , the matrix should always be richer in Al than the nominal composition, ranging from ~51 to ~55%Al for the alloys investigated. Binary alloys in this range exhibit a solidification microstructure consisting of a characteristic $(\alpha_2 + \gamma)$ lath microconstituent resulting from the solid state decomposition of the primary α -(Ti) phase, and γ segregate [19]. The Ti-48Al-3N alloy in Figure 6(b) clearly shows the same microconstituents, but the relative amount of lath decreases with the addition of Al or C, and practically disappears in the Ti-51.4Al-2.9C alloy, Figure 6(c). Homogenization of these alloys consistently produces a single phase γ matrix, following the behavior of binary alloys of similar Al content.

TEM analysis of the platelets presented in Figure 7 identified the compounds as Ti_2AlC and Ti_2AlN by a combination of electron diffraction and energy-dispersive X-ray spectroscopy. The habit plane of the platelets is (0001) in both cases, in agreement with the growth anisotropy predicted from the crystallographic arguments above. The matrix was confirmed to be single phase polycrystalline γ in the higher Al alloys with small amounts of $(\alpha_2 + \gamma)$ lath in the leaner compositions.

Closer examination of the as-cast microstructure by TEM revealed the presence of (presumably C) clustering within the γ matrix of the Ti-51.4Al-2.9C alloy, Figure 8(a). Note the additional spots in the diffraction pattern of this alloy, Figure 8(c), suggestive of ordering in the γ matrix. Similar diffraction effects have been reported in the literature for binary alloys about the equiatomic composition [20, 21] and were initially ascribed to the formation of ordered fcc-based superstructures. More recent work, however, suggested that these effects are due to fine precipitation of Ti_2AlN (from N contamination) within the γ matrix [22].

An alloy slightly richer in C but lower in Al, Ti-48Al-3.5C shows a more developed pattern of very fine precipitation along the (001) planes of the γ phase, Figures 8(b) and (d). It is somewhat surprising that the fine precipitation is only incipient in spite of the relatively modest cooling rates obtained in arc-melting and the potentially rapid diffusion of interstitial carbon. One should note, however, that the precipitation may also involve the transport of substitutional Ti and Al atoms, which requires vacancy diffusion. The precipitate-free zone commonly observed along the grain boundaries, e.g. Figure 8(b), is consistent with the latter hypothesis.

While the information available at this time is not sufficient to clearly identify the precipitate or its mechanism of evolution, the precipitation eventually leads to the formation of Ti_2AlC , as shown below. More importantly, the microstructures in Figure 8 provide clear evidence of significant solubility of C in the γ phase at higher temperatures. This is particularly relevant to the mechanical behavior of these materials due to the potential superposition of solute hardening on the strengthening effect of the reinforcements. Indeed, significant solute hardening effects have been reported for small N levels in TiAl [22, 23].

Effect of alloy composition

Reducing the C content of the alloys has a dramatic effect on the aspect ratio of the reinforcing phases, as noted in Figure 9. The Ti-48Al-1C alloy exhibits carbides with a measured average aspect ratio of ~400, or 20 times larger than those observed in the 2.9%C alloys of Figure 6(a). The effect is less pronounced in the Ti-51.7Al-1.2C alloy of Figure 9(b), wherein the carbide platelets have aspect ratios of ~40. Unfortunately, these promising increments in aspect ratio with decreasing %C are obviously accompanied by a reduction in the volume fraction of reinforcement, limiting the potential for optimizing strength.

The diminishing aspect ratio with increasing C for a given Al content may be rationalized as a consequence of enhanced nucleation due to the increased supersaturation of C in the parent melt. The role of Al is less clear, but could be associated with the apparent formation of the primary metallic (α) phase on the carbide platelets noted in Figure 9. When both phases are present, the carbide plate may continue growing into the melt ahead of the α phase, increasing its length and aspect ratio. Alternatively, the α phase may grow faster than the carbide, enveloping the latter and terminating its growth. As the Al content increases, the latter mechanism may be favored leading to shorter carbide plates. On the other hand, at the higher C contents most of the growth occurs prior to the solidification of the metallic phase, and the scale of the carbide should not be affected significantly by the Al content. Further investigation of these issues is necessary in order to assess the potential for producing the desirable aspect ratios and volume fraction of these platelets in a given microstructure.

Effect of solidification rate

The effect of the solidification rate on the Ti_2AlC reinforcement phase is illustrated in Figure 10. In general, these samples do not experience any significant supercooling prior to solidification. Thus, the solidification rate is primarily controlled by the rate of heat loss to the cooling environment. Figure 10 illustrates the structural refinement produced in Ti-51.4Al-2.9C by increasing the cooling rate during solidification from 0.2 to 36 K/s. This is accompanied by a modest increase in the average aspect ratio from ~10 to ~15; note that the platelets are generally thicker in Figure 10(a) but the average length is comparable to that in Figure 10(b). This suggests that coarsening plays a significant role in the scale and aspect ratio of the final reinforcement, and opens the possibility for further improvements in the microstructure by suitable control of the solidification rate.

The cooling rates investigated in this project were quite modest and are essentially limited by the need for maintaining the droplet levitated in a stable position so that its thermal history could be properly monitored. Since the carbide aspect ratio in the arc-buttons is somewhat higher than in either of the two droplets in Figure 10, one may infer that the average cooling rate in the former is higher than 36 K/s. Much higher cooling rates, albeit unquantifiable in most practical cases, are certainly achievable in atomization and melt spinning processes, but their effects were not assessed in this project.

Stability of the carbide plates

Specimens of the Ti-(48-52)Al-3C alloys were heat treated at 1473 K for 100 hours in an inert gas atmosphere to assess their high temperature stability. The resulting microstructures are compared with those of the as-cast materials in Figure 11. The plates appear to be morphologically stable after the long high temperature exposure, although they are slightly coarsened in both cases. Some coarsening was expected from the C solubility in the γ phase discussed above, but the limited degree in which it occurs is indicative of relatively low diffusion rates. The morphological stability suggests that the basal facets have the lowest interfacial energy with the matrix. Indeed, the basal plane in Ti_2AlC exhibits less than ~7% disregistry with the {111} close packed plane of the γ phase, but seldom are the plates found in such an orientation relationship with the matrix [17].

Heat treatment also produces homogenization of the matrix and dissolution of residual α_2 present in the lath constituent. The final matrix is polycrystalline single phase

γ in both compositions, albeit slightly leaner in Al (by ~0.6%) than the cast structure due to evaporation of this element during the heat treatment (Table 1). Fine carbide precipitation is also noted at the grain boundaries after heat treatment, Figure 12(a). TEM work identified these precipitates as Ti_2AlC and revealed the absence of any residual C clustering within the matrix--compare Figure 12(b) with Figure 8(a). This suggests that the C retained in the matrix at the moderate cooling rates associated with the casting process had sufficient time to precipitate at the grain boundaries under the slower (furnace) cooling after heat treatment.

Creep Properties

High temperature creep testing was carried out on homogenized samples of Ti-47.6Al-3C, Ti-50.8Al-2.8C, Ti-48Al-9Ta-4.3B and an unreinforced single phase γ alloy of composition Ti-52.3Al. The measured creep strength at 1255 K and various levels of strain rate is plotted in Figure 13. The stress exponent of $n \sim 4.5$ for the matrix material is basically unchanged in the reinforced alloys, suggesting that the controlling mechanism is power-law (dislocation) creep in all cases. The strength increments are quite encouraging, especially in the boride material. The range of strengthening factors observed is compared with the theoretical predictions for spheres in Figure 1. As expected, the apparent strengthening produced by these high aspect ratio reinforcements is significantly higher than that predicted for equiaxed particles. One should note, however, that the matrices in the composite alloys are not exactly equivalent to the binary γ alloy tested. They may contain varying levels of Al, as noted in Table 1, plus other elements in solid solution, notably C in the carbide-reinforced alloys and Ta in the boride-reinforced material. Further investigation is necessary to separate the true reinforcement contribution from other strengthening mechanisms like solute hardening.

Concluding Remarks

This study has demonstrated the feasibility of developing in-situ reinforcements for titanium aluminide matrices by solidification processing. Refractory compounds of B, C and N can be grown as primary phases from the melt in various morphologies and aspect ratios by careful selection of the alloy chemistry and solidification parameters.

Alloys with plate (carbide) and rod (boride) reinforcements showed significantly higher creep strengths than the unalloyed γ matrix when tested at 1255 K at strain rates

ranging from 10^{-6} to 10^{-3} s^{-1} . However, it is anticipated that some of the strengthening may be arising from solute hardening of the matrix.

Boride reinforcements seem to offer better potential for creep strengthening and more flexibility for microstructural control through processing. Further work on the quaternary Ti-Al-(Ta,Nb)-B alloys will be reported in a forthcoming publication.

Acknowledgements

This work was sponsored by the Defense Advanced Research Projects Agency under a University Research Initiative Grant N00014-86-K-0753, supervised by Dr. B. Wilcox and monitored by Dr. S. Fishman of the Office of Naval Research. The authors are grateful to Ms. Suzanne Garber for her assistance in typing the manuscript.

REFERENCES

1. H.A. Lipsitt, "Titanium Aluminides - An Overview," in High-Temperature Ordered Intermetallic Alloys, Mat. Res. Soc. Symp. Proc., vol. 39, ed. C.C. Koch, C.T. Liu, and N.S. Stoloff (Pittsburgh, PA: MRS, 1985), 351-364.
2. H.A. Lipsitt, D. Shechtman, and R. E. Shafrik, "The Deformation and Fracture of TiAl at Elevated Temperatures," Metall. Trans. A, 6A(1975), 1991-1996.
3. C.K. Elliott, G.R. Odette, G.E. Lucas, and J.W. Sheckherd, "Toughening Mechanisms in Intermetallic γ -TiAl Alloys Containing Ductile Phases," in High Temperature/High Performance Composites, Mat. Res. Soc. Symp. Proc., vol. 120, ed. F.D. Lemkey, S.G. Fishman, A.G. Evans, and J.R. Strife (Pittsburgh, PA: MRS, 1988), 95-101.
4. J. Rösler, T.C. Lu., and R. Mehrabian. To be published.
5. A.G. Evans, in Summary Report of the Summer Conference DARPA - Materials Research Council, (Ann Arbor, MI: The University of Michigan, July, 1988).
6. J.M. Duva, "A Self-Consistent Analysis of the Stiffening of Rigid Inclusions on a Power Law Material," J. Eng. Mat. Tech., 106(1984), 317-321.

7. R.M. McMeeking, private communication with authors, University of California at Santa Barbara, 1989.
8. M.Y. He, R.M. McMeeking, and A.G. Evans, Mat. Res. Soc. Symp. Proc., MRS, 1990 Spring Meeting. To be published.
9. L. Christodoulou, P.A. Parish, and C.R. Crowe, "XD™ Titanium Aluminide Composites," in High Temperature/High Performance Composites, Mat. Res. Soc. Symp. Proc., vol. 120, ed. F.D. Lemkey, S.G. Fishman, A.G. Evans and J.R. Strife (Pittsburgh, PA: MRS, 1988), 29-34.
10. M. E. Hyman, C. McCullough, J.J. Valencia, C.G. Levi, and R. Mehrabian, "Microstructure Evolution in Ti-Al Alloys with B Additions: Conventional Solidification," Metall. Trans. A, 20A(1989), 1847-1859.
11. J.J. Valencia, C. McCullough, C.G. Levi, and R. Mehrabian, "Solidification Microstructure of Supercooled Ti-Al Alloys Containing Intermetallic Phases," Acta Metall., 37(1989), 2517-2530.
12. M. E. Hyman, C. McCullough, C.G. Levi, and R. Mehrabian, "Evolution of Boride Morphologies in TiAl-B Alloys," submitted for publication to Metallurgical Transactions, 1989.
13. T. Lündstrom, "Transition Metal Borides," in Boron and Refractory Borides, ed. V. I. Matkovich, (New York, NY: Springer-Verlag, 1977), 351-376.
14. P. Hartman, "Structure and Morphology," in Crystal Growth: An Introduction, ed. P. Hartman, W. Bardsley, D.T.J. Hurle, and J.B. Mullin (Amsterdam: North-Holland Publ. Co., 1973), 367-402.
15. A.A. Abdel-Hamid, S. Hamar-Thibault, and R. Hamar, "Crystal Morphology of the Compound TiB₂," J. Cryst. Growth, 71(1985), 744-750.
16. J.J. Valencia, C. McCullough, C.G. Levi, and R. Mehrabian. To be published.

17. C. McCullough, J.J. Valencia, C.G. Levi, and R. Mehrabian, "Microstructural Analysis of Rapidly Solidified Ti-Al-X Powders." To be published in Mat. Sci. and Eng., 1989.
18. J.C. Schuster, H. Nowotny, and C. Vaccaro, "The Ternary Systems: Cr-Al-C, V-Al-C and the Behavior of H-Phases (M_2AlC)." J. Sol. State Chem., 32(1980), 213-219.
19. C. McCullough, J.J. Valencia, C.G. Levi, and R. Mehrabian, "Phase Equilibria and Solidification in Ti-Al Alloys," Acta Metall., 37(1989), 1321-1336.
20. A. Loiseau and A. Lasalmonie, "Nouvelles Surstructures Ordonnées dans le Composé TiAl Non Stoechiométrique," Acta Cryst., B39(1983), 580-587.
21. A. Loiseau, R. Portier, G. Van Tendeleo, and F. Ducastelle, "High Resolution Study of Long Period Structures in $Ti_{1+x}Al_{3-x}$ Alloys: A Devil's Staircase," Inst. Phys. Conf. Ser. No. 78, Proc. Conf. EMAG '85, ch. 9, (Newcastle, England, Sept. 1985), 351-354.
22. M.J. Kaufman, D.G. Konitzer, R.D. Schull, and H.L. Fraser, "An Analytical Electron Microscopy Study of the Recently Reported Ti_2Al Phase in γ -TiAl Alloys," Scripta Metall., 20(1986), 103-108.
23. A. Loiseau and A. Lasalmonie, "Influence of Thermal Stability of TiAl on its Creep Behavior at High Temperatures," Mat. Sci. and Eng., 67(1984), 163-168.

Table 1. Chemical Compositions of the Alloys Investigated (Atomic Percent)

Alloy	Condition	Al	Nb	Ta	B	C	N
M	as cast	53.5					
	heat treated	52.3					
C523	as cast	51.4				2.9	
	heat treated	50.8				2.8	
C483	as cast	48.2				2.9	
	heat treated	47.6				3.0	
C521	as cast	51.7				1.2	
C481	as cast	48.0				1.0	
N523*	as cast	52.0					3.0
N483*	as cast	48.0					3.0
B50*	as cast	50.0			5.0		
B50Nb*	as cast	50.0	11.0		3.5		
B48Ta*	as cast	48.0		9.0	4.3		

* Nominal compositions of N and B. Al, Nb and Ta determined by EDS with standards.

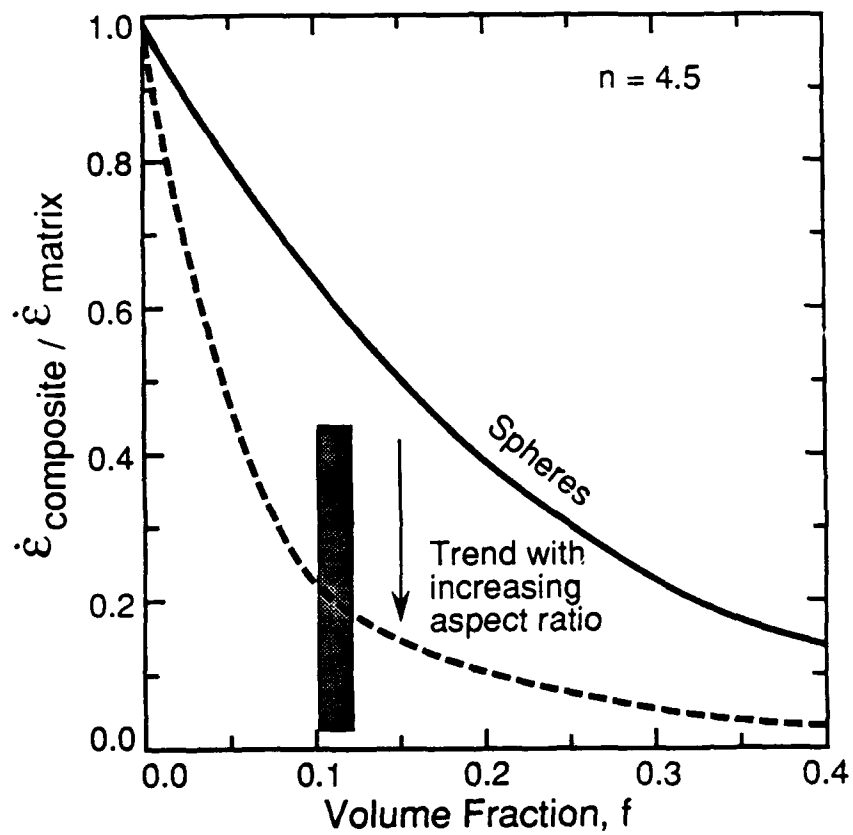


Figure 1.- Reduction in the creep rate of γ -TiAl ($n=4.5$) due to the incorporation of rigid reinforcements. Shaded area represents the range of strengthening observed in this study. The calculated curve for spherical particles is based on reference [6].

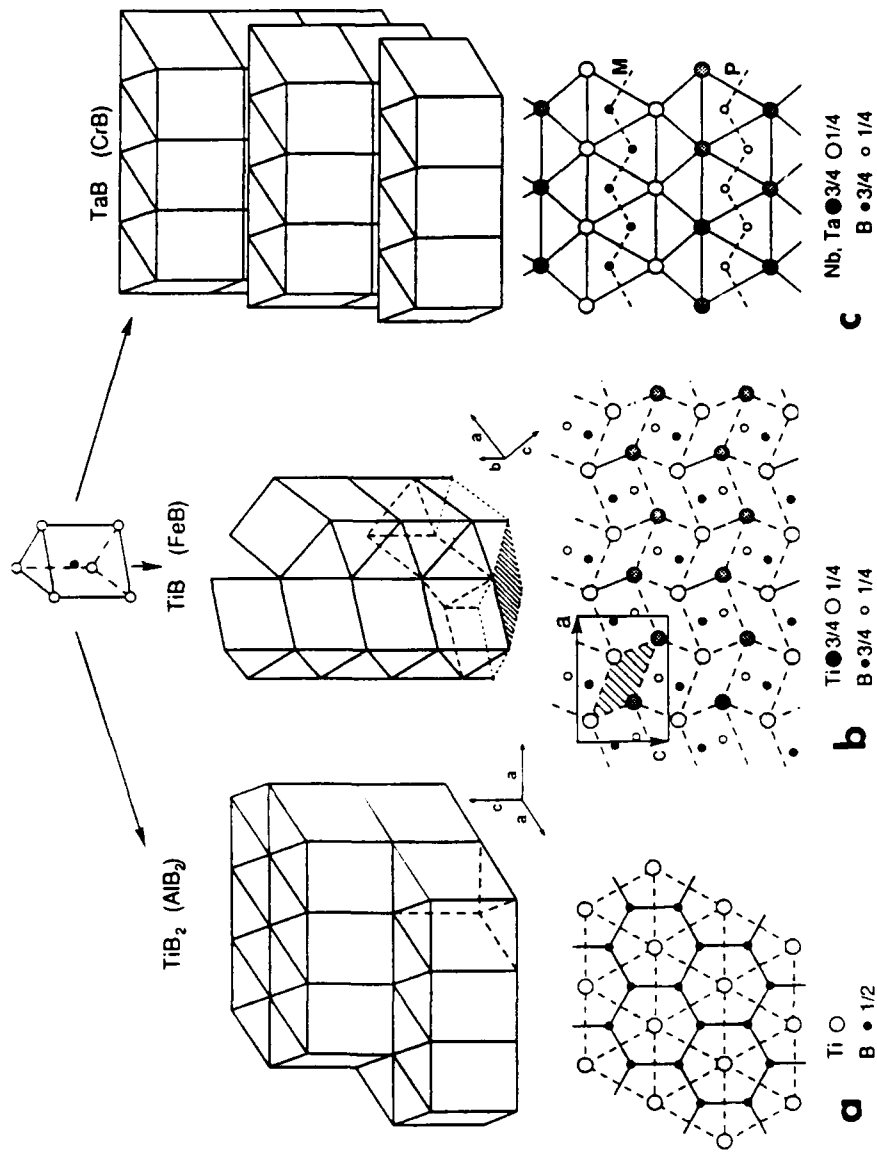


Figure 2. Boride structures relevant to this study and their relationship to the basic trigonal prism containing one B atom surrounded by 6 metal atoms. From left to right: (a) Hexagonal structure of TiB_2 (C32), (b) orthorhombic structure of TiB (B27) and (c) orthorhombic structure of TaB and NbB .

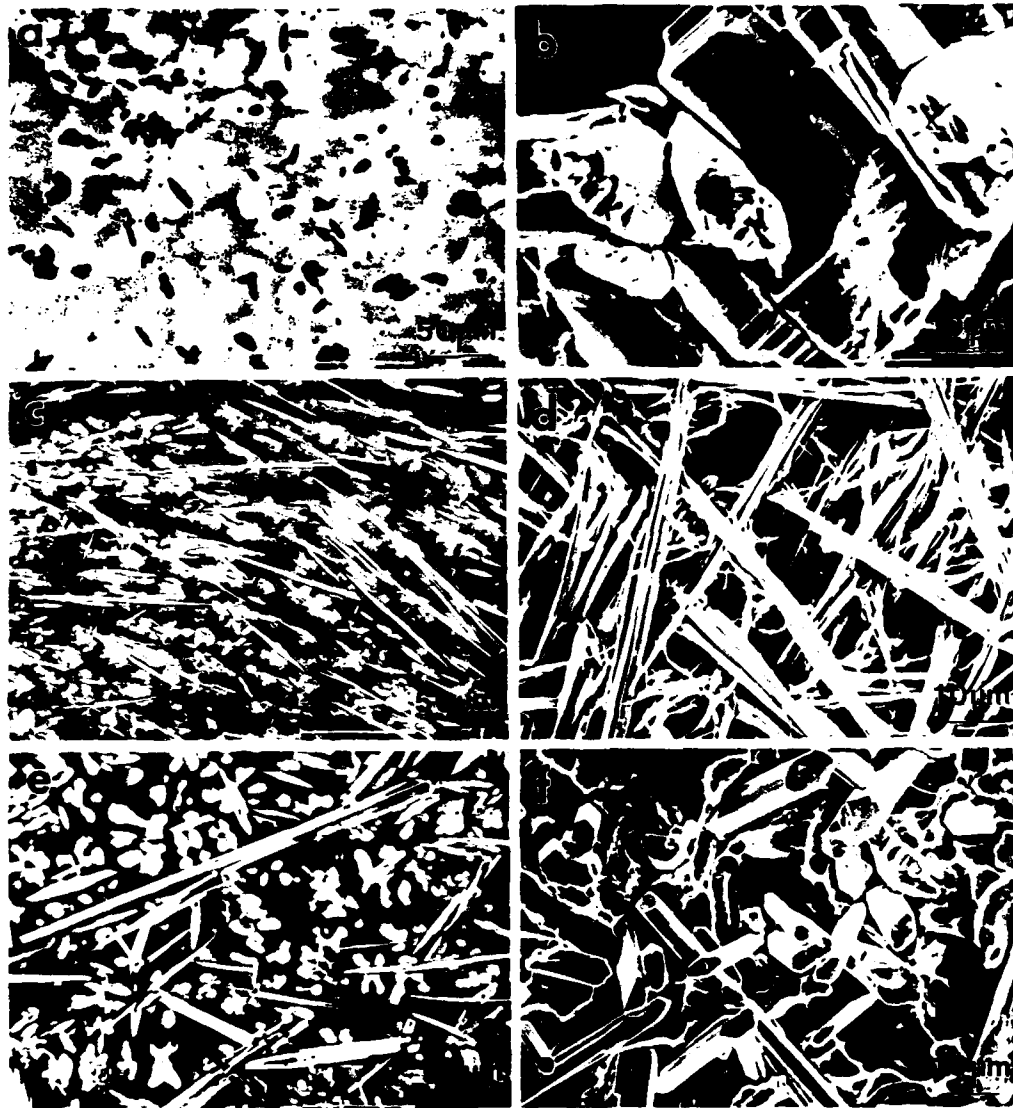


Figure 3.- Boride morphologies in polished and deep etched sections of as-cast buttons: (a)-(b) Equiaxed TiB_2 in Ti-50Al-5B, (c)-(d) Rodlike (Ti,Nb) B in Ti-50Al-11Nb-3.5B, (e)-(f) Rodlike (Ti,Ta) B in Ti-48Al-9Ta-4.3B.



Figure 4.- Secondary boride plates with the CrB type structure in as cast microstructures of (a) Ti-50Al-11Nb-3.5B and (b) Ti-48Al-9Ta-4.3B

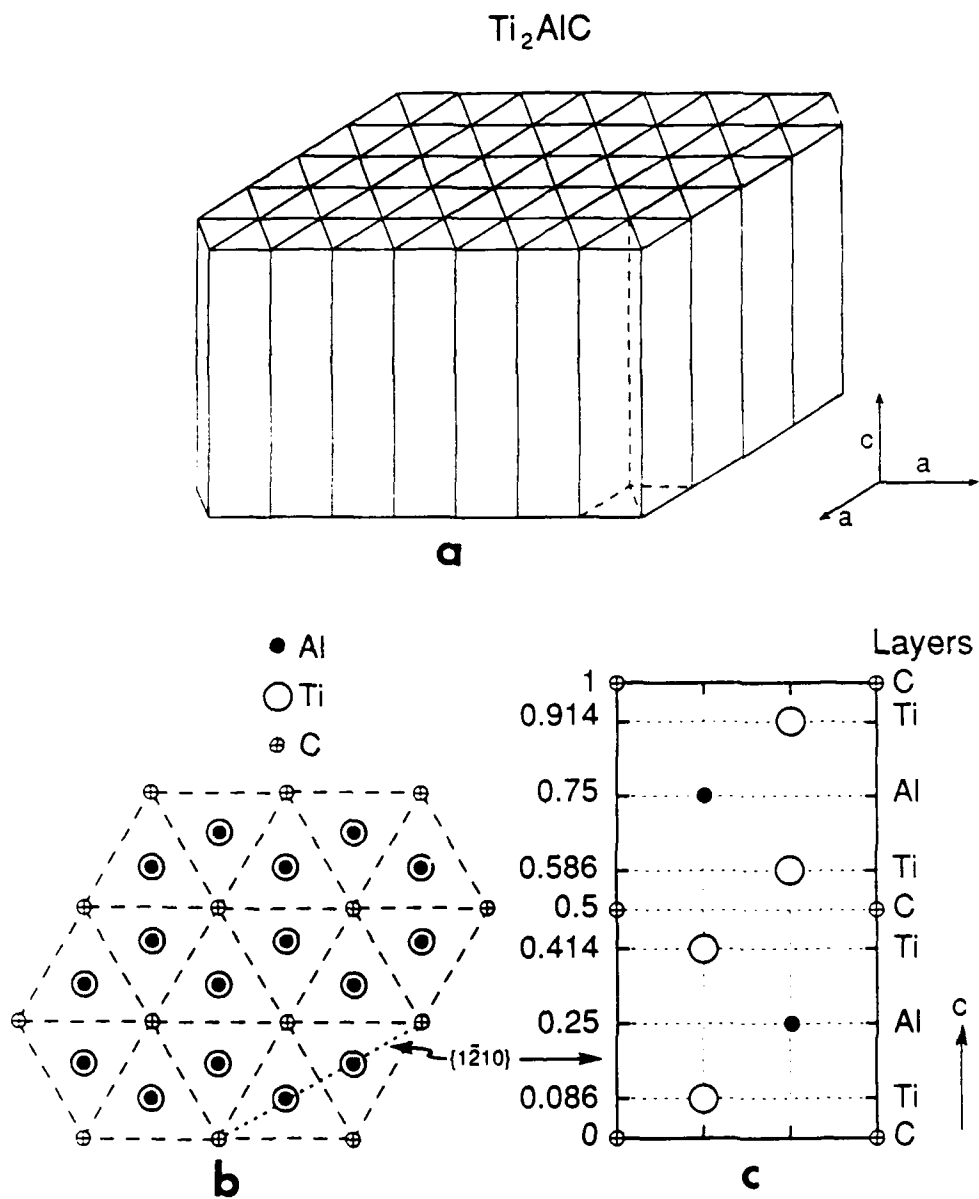


Figure 5.- Structure of the Ti_2AlC and Ti_2AlN crystals. (a) shows unit cell orientation in the plate morphology. (b) atomic projection on the basal plane, and (c) atomic arrangement in the $\{1\bar{2}10\}$ type planes.

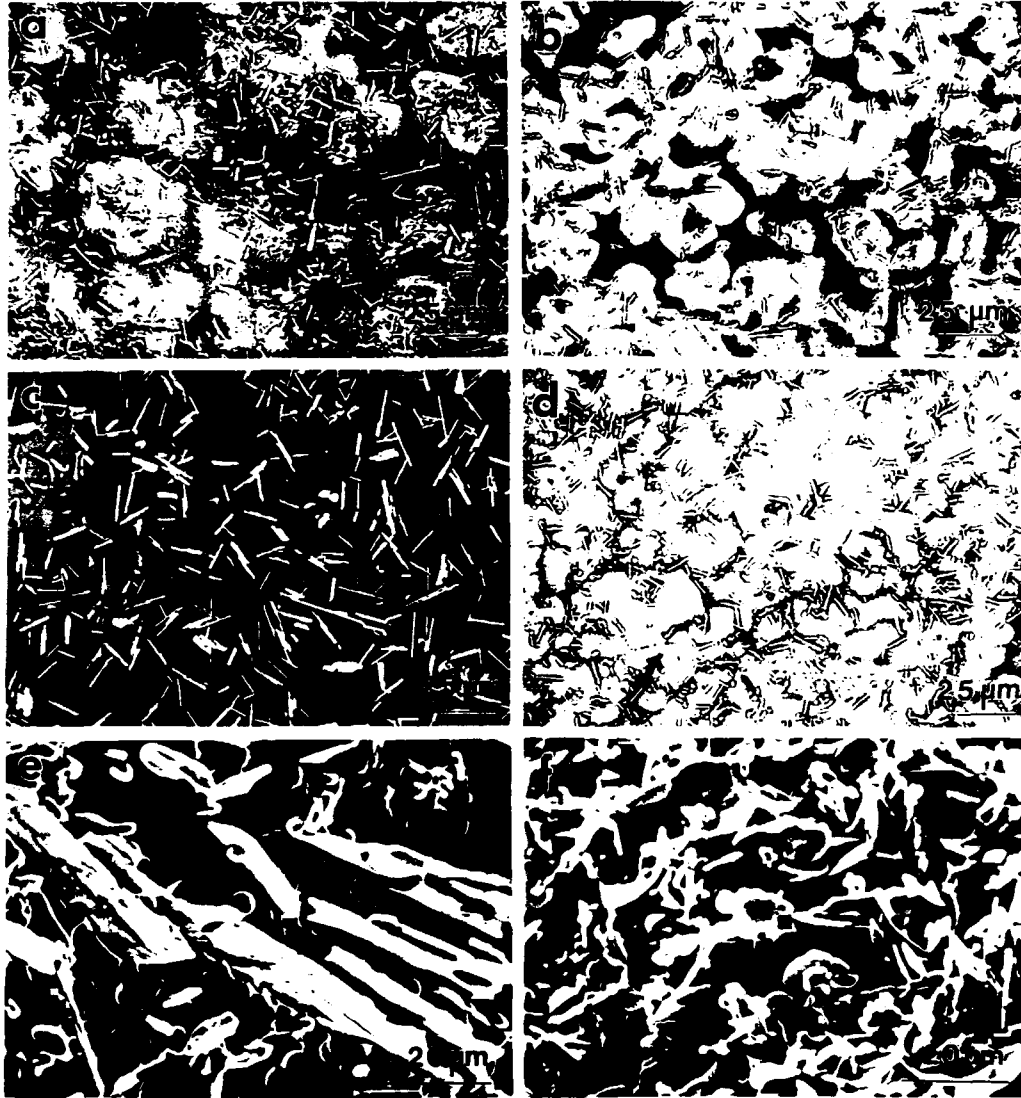


Figure 6.- Primary phase platelets in as-cast (a) Ti-48.2Al-2.9C, (b) Ti-48Al-3N, (c) Ti-51.4Al-2.9C, (d) Ti-52Al-3N, (e) and (f) are secondary electron images of deep etched specimens of (c) and (d) revealing the 2-D morphology of the platelets.

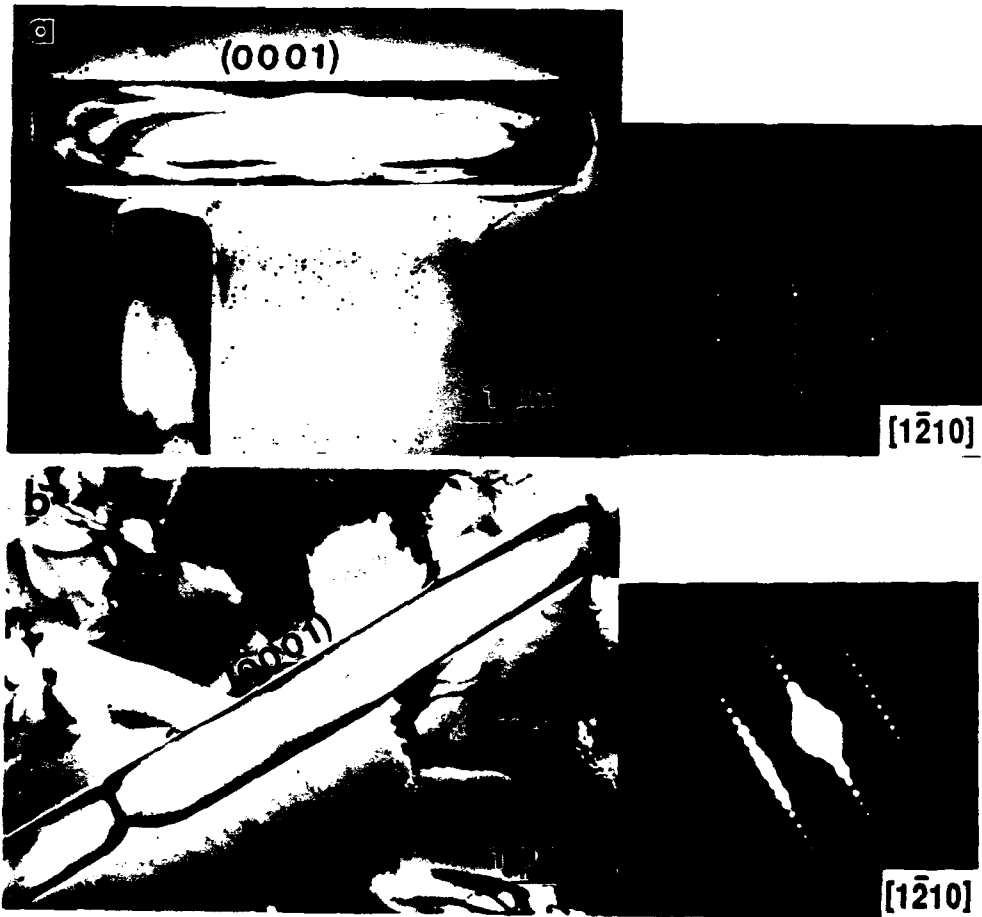


Figure 7.- TEM images and SAD patterns of (a) Ti_2AlC in Ti-51.4Al-2.9C and (b) Ti_2AlN in Ti-52Al-3N. The habit plane of platelets is (0001) in both cases.

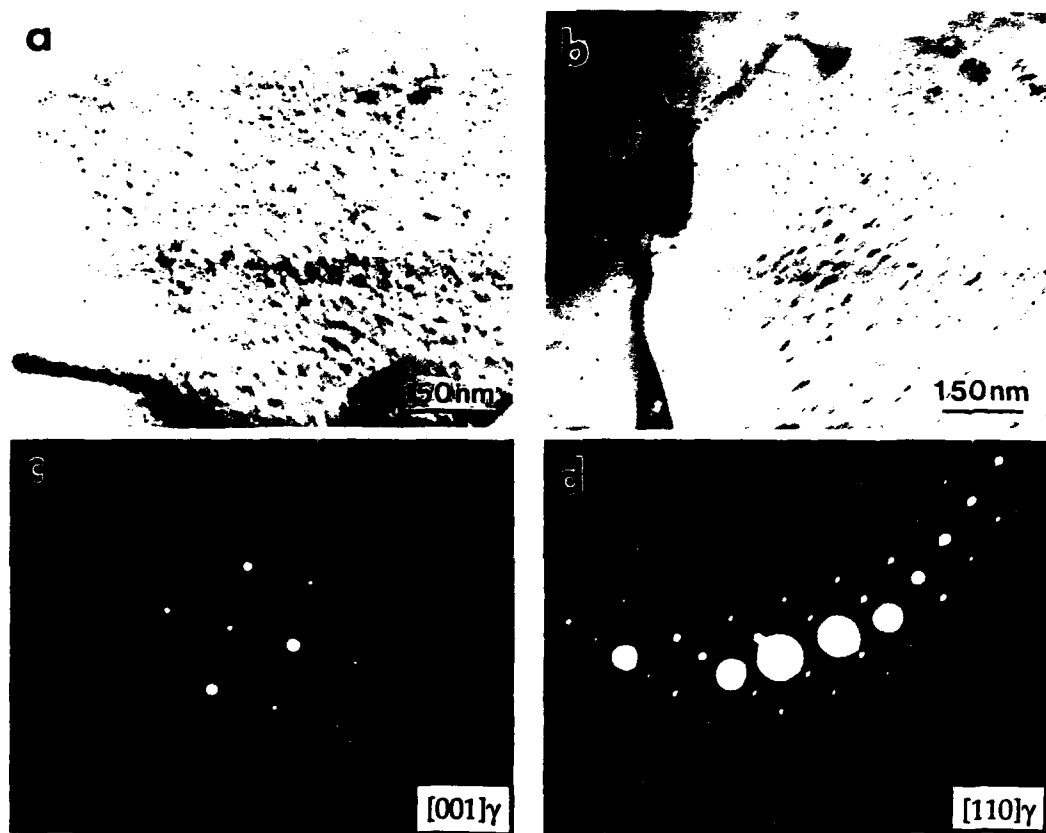


Figure 8.- TEM views of the matrices in (a) Ti-51.4Al-2.9C and (b) Ti-48Al-3.5C. Note the extra reflections arising from clustering or precipitation in the diffraction patterns (c) and (d).



Figure 9.- Backscattered electron images of (a) Ti-48Al-1C and (b) Ti-51.7Al-1.2C showing plates with large aspect ratios; compare with Figures 6(a) and (c).

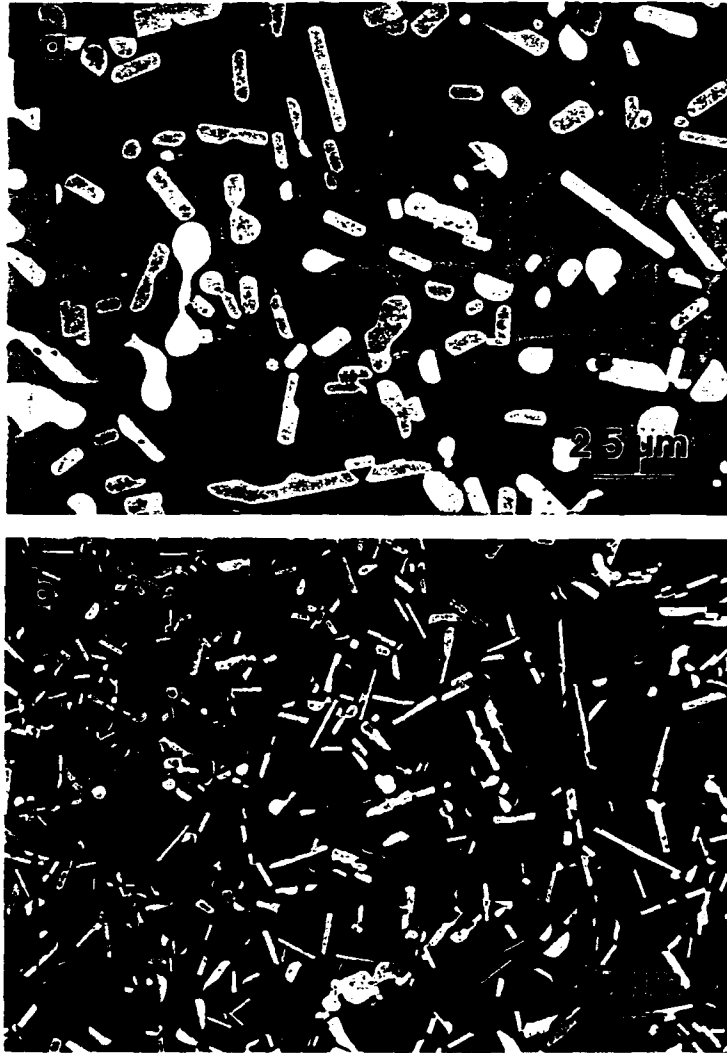


Figure 10.- BEI of Ti-51.4Al-2.9C alloy solidified at; (a) 0.2 K/s and (b) 36 K/s.

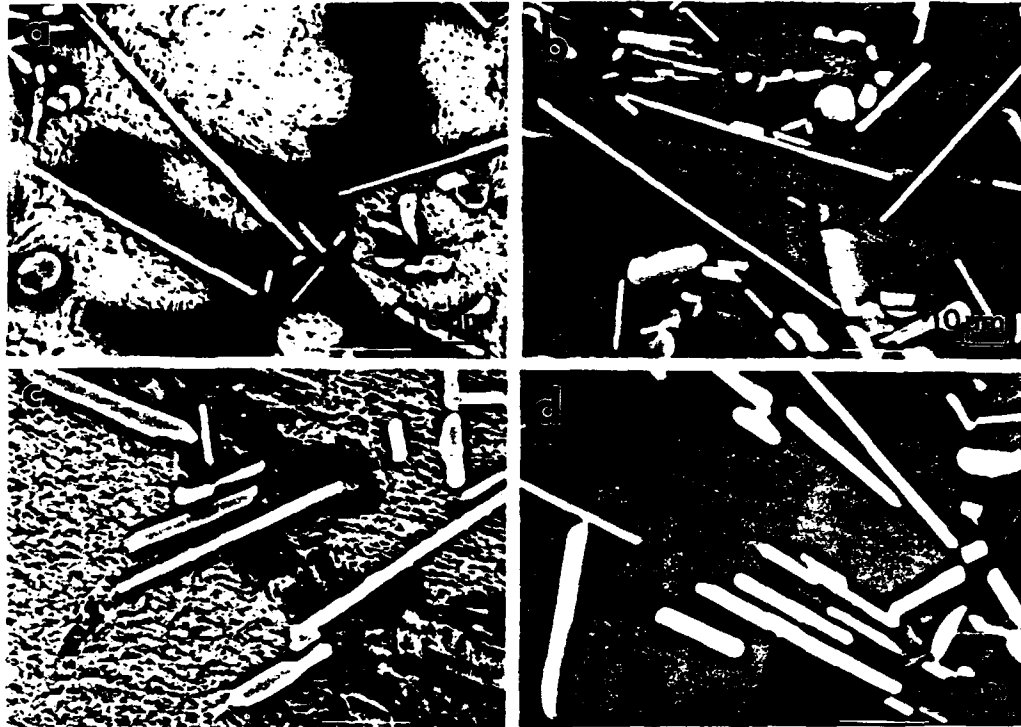


Figure 11.- Microstructures of Ti-48.2Al-2.9C (a,c) and Ti-51.4Al-2.9C (b,d) in as-cast condition (a,b) and after heat treating at 1473 K for 100 hrs. (c,d).

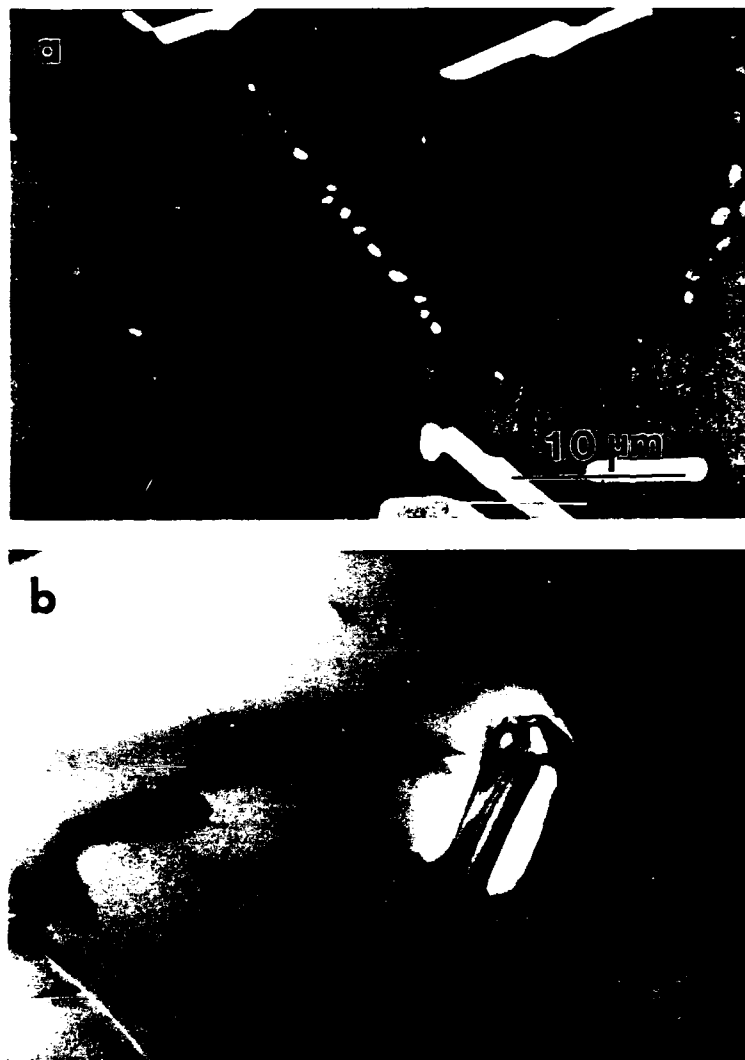


Figure 12.- Precipitation of equiaxed Ti_2AlC in Ti-50.8Al-2.8C after heat treatment (1473 K/100 hrs.) (a) BEI of precipitates at grain boundary. (b) TEM view of carbide particle and matrix devoid of fine clustering (compare with Figure 8a).

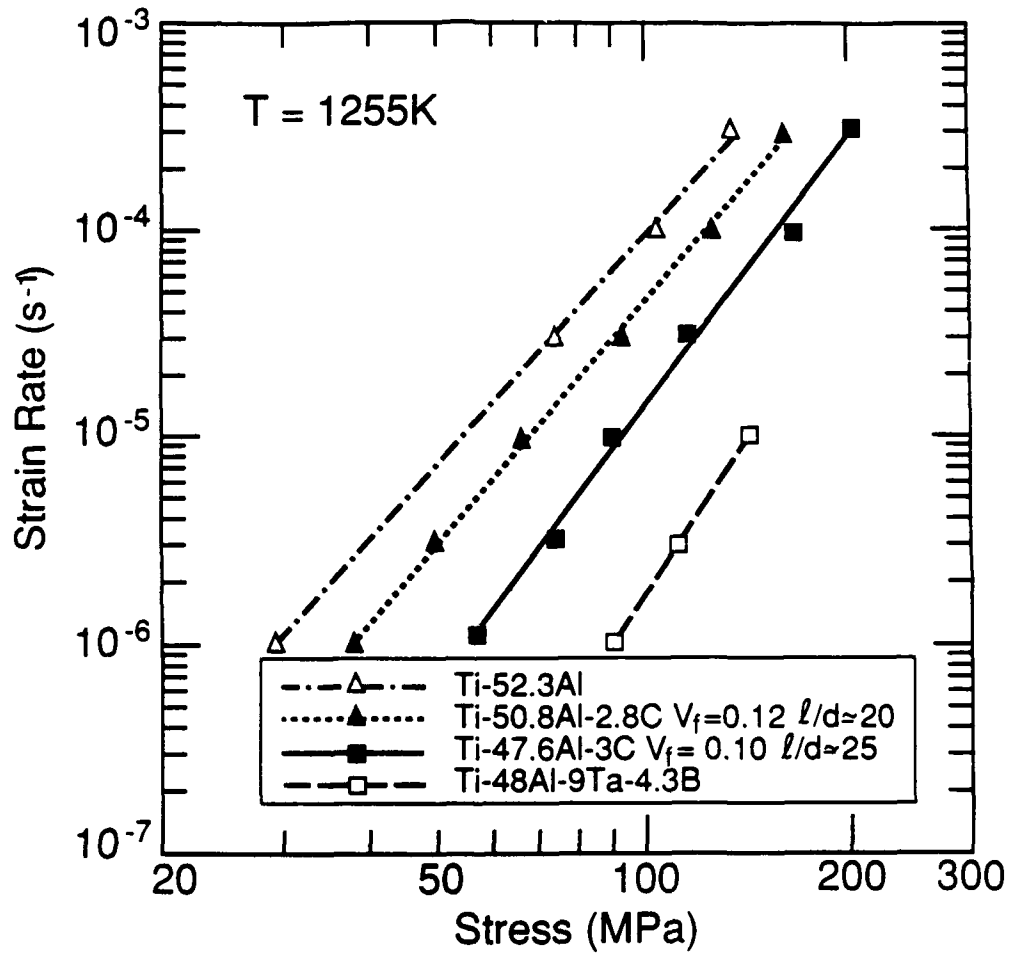


Figure 13.- Creep rate at 1255 K as a function of compressive stress for homogenized Ti-52.3Al, Ti-50.8Al-2.8C, Ti-47.6Al-3C and Ti-48Al-9Ta-4.3B.

NUMERICAL MODELLING OF THE PLANAR FLOW MELT-SPINNING PROCESS,
AND EXPERIMENTAL INVESTIGATION OF THE SOLIDIFICATION PUDDLE DYNAMICS.

Z. Gong, P. Wilde, and E.F. Matthys

Department of Mechanical Engineering
University of California
Santa Barbara, CA 93106, USA

Abstract

We have developed a numerical model for the Planar Flow Melt-Spinning process that is based on two-dimensional boundary layer equations. The coupled continuity, momentum, energy, and phase change equations are solved simultaneously. The velocity and temperature distributions in the puddle and ribbon, the cooling rate at any location, and the shape and location of the solid / liquid interface and of the downstream meniscus can then all be evaluated numerically. Parametric studies have been conducted, and some examples of isotherm and streamline maps are shown for various values of the main process parameters. We have also conducted an experimental investigation of the dynamics of the solidification puddle by high-speed video recordings, and some results such as photographs of high-frequency surface waves and of the establishment of a typical solidification puddle are shown. The experimental results were used to obtain estimates of the thermal contact resistance at the substrate by matching the measured detachment point and meniscus shape with numerical modelling results.

(Submitted to *International Journal of Rapid Solidification* in September 1989)

1. Introduction

Rapid solidification processes are of great interest to Materials Scientists and Engineers. Indeed, it is well-known that the microstructure of solidified alloys is critically dependent on the thermal history during solidification [1,2]. Rapidly-solidified alloys, in particular, often exhibit refined microstructure with reduced grain size and metastable phases. These characteristics may then result in improved mechanical properties that could be very beneficial, in particular for high-temperature applications. Among other rapid solidification techniques, Melt-Spinning ("MS") has been actively studied over the last few years in part because it appears that it could be relatively easily implemented as a large-scale industrial process. Two main variations of the melt-spinning technique are the Free Jet Melt-Spinning ("FJMS") and the Planar Flow Melt-Spinning ("PFMS"). In both cases, a jet of molten metal is ejected under pressure from a crucible through a nozzle and onto a cold rotating cylindrical roller where it is rapidly cooled and solidified as it is dragged along by the moving substrate, finally constituting a thin metal ribbon.

In the FJMS case, the crucible is located relatively far from the cooling wheel so that the ejected molten metal forms a free jet before impinging on the wheel. In the PFMS case, on the other hand, a flat-bottomed crucible is positioned very close to the wheel, and the extended solidification puddle is therefore confined between the crucible land and the wheel surface. PFMS is believed to result in better-quality ribbons than FJMS, apparently because of the increased stability of the solidification puddle due to its physical confinement [3]. In addition, this confinement makes it possible to use long rectangular ejection nozzles for the PFMS process, and therefore also to produce much wider ribbons than with the FJMS process (which usually uses small circular nozzles). On the other hand, the PFMS process is more difficult to model and to control than the FJMS process, and appears to have been much less studied than the latter. In the present study we are investigating primarily the PFMS process.

The modelling of this process is -predictably enough- a difficult task because of the coupled heat, momentum, and mass transports that are taking place in a solidification puddle which is bounded in part by free surfaces and is undergoing in addition a solid / liquid phase change. Modelling approaches ranging from analytical solutions to finite-differences and finite-elements computer codes have been used in the past with varying degrees of sophistication and success. These studies have usually assumed rather simple and idealized configurations, and have usually not taken into account significant phenomena such as undercooling, nucleation thermodynamics, and growth kinetics. Indeed, the numerical treatment of these phenomena is complex and its inclusion would greatly complicate the numerical solution schemes. The scarcity of detailed experimental data has also impaired the development of sophisticated models. A brief summary of some of the most recent modelling work in this area is mentioned here for the reader's convenience.

Yu [4] developed a low-Reynolds number PFMS model which is based on assumed one-dimensional fully-developed flow in the nozzle and one-dimensional Couette flow in the crucible / wheel gap. A closed-form solution based on lubrication theory was then obtained which can be used to study the effect of wheel speed and nozzle passage resistance on ribbon thickness. This particular model did not, however, take explicitly into account the heat transfer phenomena that are coupled with the fluid flow. Gutierrez's model [5] is also based on lubrication theory but addresses heat transfer considerations as well. This model predicts a recirculation zone inside the puddle. One of the major limitations of the lubrication theory, however, is that it is applicable only to low Reynolds number flows, whereas PFMS processes normally operate in a higher Reynolds number regime. Takeshita [6] pointed out that momentum transport may indeed play a major role in the processes, and solved momentum and energy equations simultaneously for amorphous solidification, using an explicit finite differences method. More recently [7], he used the SOLA-VOF computer code to model the flow field for PFMS, but heat transfer, however, was not explicitly addressed in this work.

Berger [8] models the fluid flow during the PFMS process by dividing the flow field into four

zones (reservoir, nozzle, liquid pool, and solid region) and using one-dimensional steady state flow assumptions, a control volume formulation and algebraic rather than differential equations. Sun [9] studies how the displacement boundary layer thickness in the liquid melt varies with wheel speed and heat transfer coefficient. Poopisut [10] developed empirical relations which predict ribbon thickness in terms of flow rate, wheel speed and pouring velocity. His model is based on momentum transport and incorporates some surface tension effects.

Katgerman [11] used transient momentum equations combined with a moving solidification front and solved them numerically using an explicit finite differences scheme. His model is an one-dimensional one, neglecting motion in the direction normal to the wheel surface. It can determine the ribbon thickness, and the momentum boundary layer is found to be substantially decreased as a result of the moving solid-liquid interface. Recent numerical work was also carried out using the FIDAP finite element code for fluid mechanics and heat transfer modelling of a simplified puddle consisting of two regions [12].

In view of this past work, it appears -to the best of our knowledge- that a full two-dimensional model including both the fluid flow and the heat transfer during PFMS of crystalline materials is still unavailable. To address this problem, we have recently initiated the development of such a model. The model is presently limited to boundary layer equations, but will soon be extended to the full Navier-Stokes equations. The numerical scheme chosen is a semi-implicit finite differences marching technique. This numerical work is conducted jointly with experimental investigations of the solidification puddle in order to generate information on the boundary conditions that must be used in the model. We will limit ourselves in this article to some examples of modelling and experimental results that we obtained recently, and to a brief discussion of the type of information that can be obtained from the comparison of these two approaches.

2. Problem formulation and numerical approach

PFMS is a complicated process to model because of the coupled momentum and heat transports and the presence of a phase change inside the puddle. Some assumptions and simplifications were therefore necessary in order to reduce the problem to a level manageable in the first phase of this study :

An examination of typical PFMS solidification puddles reveals that their dimensions in the main flow direction (x) are larger than their dimensions in the direction normal to the wheel surface (y). Typical numbers are, for example, 10 mm vs 0.5 mm. In addition, except below the nozzle, the bulk of the fluid flow takes place in a narrow region roughly parallel to the wheel surface. These conditions suggest that the use of boundary layer equations rather than the full Navier-Stokes equations might be a reasonable approach over most of the flow field. On the other hand, the Reynolds numbers based on the large surface velocity normally used for PFMS would often be of the order of 1,000. This relatively high Reynolds number implies that the inertial terms in the boundary layer equations may not be negligible, and that the lubrication theory which neglects the inertial contributions might be of limited generality for the modelling of this process. Full boundary layer equations are therefore preferable, and considering in addition that the width of the ribbon is usually close to that of the nozzle, we have chosen to use a two-dimensional steady laminar boundary layer representation for our initial model. Naturally, both the continuity, momentum, and the energy equations must be used. (Mass transport was not examined in the first phase of this work.) The wheel surface is modelled as a fiat surface, and radial acceleration is neglected. No-slip conditions are assumed at all interfaces. The upstream meniscus is assumed to drop vertically from the upstream side of the nozzle all the way to the wheel. The heat transfer flux at the wheel / puddle interface is modelled by a heat transfer coefficient times the temperature difference between the near-wheel puddle and the wheel surface. It should be noted

that this expression is representative of the localized thermal contact resistance between the puddle and wheel rather than of the overall heat transfer between the bulk of the fluid and the substrate (as in the classical convective heat transfer sense).

The wheel surface is assumed to remain at a uniform temperature under the puddle. The radiative energy loss through the downstream meniscus is neglected. No undercooling and mushy zone at the solid / liquid interface are considered in the present study which is limited to crystalline materials assumed to have a discrete melting temperature. The physical properties are assumed to be phase-dependent but independent of temperature. The liquid metal is also assumed to detach from the bottom of the crucible upon an onset of separation determined by the usual zero-shear stress criterion. It is considered that there is no pressure drop across the downstream meniscus. Body forces and viscous dissipation are assumed to be negligible as well.

Using these simplifications, the full Navier-Stokes equations reduce to the classical boundary layer equations. It is important to note that the momentum and energy equations will be coupled because of the presence of the solid / liquid interface. A number of boundary conditions must be used as well, in particular the conservation of energy at this interface. This relationship relates the heat fluxes by conduction in the liquid and solid metal to the interface velocity (because of the latent heat release at that location). A no-shear stress condition is assumed at the liquid / gas interface, and the crucible land is supposed to be at the superheated melt temperature. The mathematical expressions for all the equations and boundary conditions are described in detail in [13]. In order to simplify discretization of the governing equations, various changes of variable are also introduced in order to render these equations dimensionless.

A semi-implicit finite differences marching scheme [14] is then used to solve the dimensionless momentum and energy equations. Upstream-differencing is used in regions of large crossflow to ensure numerical stability. The solid / liquid interface location is determined by interface velocity considerations or by the enthalpy method, as most appropriate, and uses dummy nodes for greater accuracy. The downstream meniscus shape and location are computed iteratively based on global flow conservation through the use of additional moving nodes. Additional considerations on stability will also impose constraints on grid size. Convergence of the results was tested with a number of combinations of grid spacing in both directions. The resulting discretized equations are not presented here in the interest of conciseness, but can also be found in [13]. The computational strategy to solve the momentum and energy equations is then straightforward :

With the velocity and temperature profile at location x known from boundary condition or an upstream solution, the temperature profile at $x+dx$ can be calculated using the discretized energy equation and expression for the heat transfer at the substrate. If solidification occurs, the location of the solid / liquid interface can be determined. For the region where the flow has not yet detached from the crucible, the velocity profile at $x+dx$ can then be calculated using the discretized momentum equation. For the region where the flow has detached from the crucible, however, both the location of the meniscus and the velocity profile are unknown, and an iterative process is carried out to determine these quantities by ensuring that both the global mass conservation and the momentum equations are satisfied. The previous steps are repeated during the march downstream until all the metal is solidified, after which the problem becomes limited to solid-body motion and heat conduction.

The computer program is operational and can be used to calculate the length and shape of the puddle and downstream meniscus, the solid / liquid interface location, the temperature and velocity distributions anywhere inside the flow field as well as the cooling rates at any location. Streamlines and isotherms can also be readily computed. Various cases have been modelled, and we are presenting here some typical results for illustration.

3. Numerical results

Some numerical results are shown to demonstrate the potential of the numerical model for design or analysis applications. The calculations were performed using parameters and properties corresponding to PFMS experiments conducted in our laboratory with Al-4%Cu alloys. The physical properties that were used in the computations for this material are listed in Table I. The node spacing used in this case is $5 \cdot 10^{-5}$ m (or about 200 nodes) in the tangential (x) direction and 60 nodes (or from about $5 \cdot 10^{-6}$ m to $8 \cdot 10^{-6}$ m) in the normal (y) direction.

3.1. Typical calculation results

As mentioned above, the model computes the shape and location of both the downstream meniscus and the solid / liquid interface. It also calculates the velocity and temperature fields within the puddle, thereby providing us with both quantitative and qualitative information that may help us develop a better understanding of the fluid dynamics and heat transfer phenomena taking place during the PFMS process.

A schematic of the solidification puddle is shown in Figure 1 for easier interpretation of the following numerical results. As an illustration of typical numerical results, we are showing in Figure 2 a map of selected isotherms and streamlines for PFMS of Al-4%Cu. In this plot the x-axis is the wheel surface and the y-axis is aligned with the upstream edge of the nozzle. The calculated solid / liquid interface and the liquid / gas downstream meniscus are shown in the plot as well. The solidification is completed where these two surfaces intersect, and the distance from the upstream meniscus to this point is taken as the solidification length.

It should be noted that this graph is not plotted to scale, and is greatly magnified in the y-direction. In reality, the solidification puddle is much longer than it is high, and both the solid / liquid interface and downstream meniscus would appear much more parallel to the wheel surface than in the figure (as it should be for a flow field modelled by boundary layer equations). To aid in the visualization of the flow field, the stream function has been normalized by the total flow rate, so that the values listed indicate the fraction of the total flow rate below the corresponding streamline. The numerical results were validated by showing their good agreement with results of approximate analytical methods based on integral solutions of the one-dimensional solidification problem. Global energy conservation estimates of the solidification distance also matched well our results.

Upon inspection of the streamlines and of their stream function values, this figure reveals that the majority of the flow takes place close to the wheel and that the portion of the puddle near the crucible consists mostly of slow-moving fluid. (For instance, it can be seen that the 50% streamline is not located at about mid-puddle as one might expect, but is in fact much closer to the wheel than this, indicating that much more than 50% of the liquid flows below mid-puddle.) The temperature gradients in the liquid are small in the region under the crucible for our small superheat system, but are large in the solidified region. Because of the considerable source of energy due to the release of latent heat, the isotherms in the solid can also be seen to run about parallel to the solid-liquid interface until solidification is complete. Beyond this point, the variation in temperature across the ribbon (normally to the wheel) becomes small because of the high thermal conductivity of aluminum. Of particular interest to the materials scientist are the cooling rates experienced by the metal. These can also be computed by the program at any desired location. It can be seen by looking at the streamlines and isotherms that the cooling rate is much higher for the metal located close to the wheel than for the metal that will end up in the upper part of the ribbon. If the temperature histories are computed for, say, the 0.1 and the 0.9 streamlines, one would observe that just before solidification the corresponding cooling rates would be respectively about 10^6 and 10^4 K/s. In some cases, there may well be 3 orders of magnitude of difference between the cooling rates on the top and bottom of the ribbon. This large

discrepancy is probably related to the clear variations in microstructure that are observed between the top and bottom of melt-spun ribbons.

Another noticeable feature of the computed flow field is that there is no recirculation zone seen in the puddle. Such a region was predicted by a model using the simpler lubrication theory analysis [5]. It is not clear at this point what causes this difference. On the one hand, the boundary layer equations -unlike the lubrication theory equations- do include inertial terms, which, because of the high Reynolds numbers involved could be predominant. Such terms would tend to stabilize the flow or delay the apparition of a recirculation zone in a model. On the other hand, our assumption of detachment from the crucible land based upon zero-stress onset or the marching technique we used could perhaps mask the existence of a recirculation region near the meniscus. Some work conducted with Navier-Stokes equations did show a recirculation zone for PFMS under certain conditions [7], but this model did not include heat transfer and solidification in the puddle and cannot therefore be directly compared to ours. We are in fact presently improving the model by developing a fully-implicit solution scheme and by expanding the system of equations to the full Navier-Stokes level while still solving the energy equation for the temperature field. When fully operational, this new model should indicate much more conclusively whether the lack of recirculation region is indeed a feature of this flow field.

In fact, it should always be kept in mind during this discussion that this model involves a large number of assumptions and simplifications and that most of the boundary conditions used can not even be directly evaluated experimentally at this point. Conclusions even at the qualitative level should therefore be regarded with caution and their implied limitations should be recognized. This is, of course, the case with all numerical work that cannot be directly or totally validated by experiments. On the positive side, naturally, the advantage of a model is that it allows us to obtain information on parameters or flow regions that are not directly accessible to the experimentalist. In other words, the experiments are needed to validate the model, but the model can give us information that might not be readily obtainable from experiments. It is precisely for this reason that closely-linked experimental and modelling investigations may prove particularly fruitful for the study of this process, a particularly difficult one to study experimentally. These reservations kept in mind, a reasonable model, even though perhaps imprecise in absolute terms, will generally be useful for comparisons on a relative basis, and in particular for parametric studies. To illustrate the potential of this approach, we are presenting hereafter some results showing the effect of main process parameter variations on the temperature and flow fields.

3.2. Effect of process parameter variation on the PFMS solidification puddle

3.2.1. Effect of wheel speed

Figure 3 shows the effect of wheel speed variation on the computed puddle shape and flow characteristics for Al-4%Cu solidification. In this figure, the nozzle mass flow rate and gap remain constant while wheel speed is increased from 10 to 25 m/s. Naturally, with our assumptions the final ribbon thickness varies in inverse proportion to the wheel speed because of mass conservation. At higher speed, the detachment distance is also predicted to decrease as the wheel speed increases. If other parameters remain unchanged, calculations show that the solidification length decreases only slightly as the wheel speed increases. This relative insensitivity may result from the fact that, even though the solid ribbons are thinner at higher speed (which should accelerate the cooling), the residence time in puddle is also shorter (which should increase the solidification distance for a given cooling rate). It should be noted that we are considering here variations in wheel speed alone for this parametric study, but in reality a change in wheel speed would also induce a change in heat transfer coefficient (contact resistance) as well as a change of flow rate for a given crucible pressure.

3.2.2. Effect of crucible / wheel gap

The effect of crucible / wheel spacing variations is illustrated in Figure 4. As shown in this figure, increasing the crucible / wheel gap spacing decreases the detachment distance, all other parameters remaining unchanged. If one would increase the gap even further, the detachment point would at some point reach the downstream edge of the crucible slit. This situation would then correspond to the case of Free Jet Melt-Spinning, and no longer to Planar Flow Melt-Spinning. The solidification distance, on the other hand, is not affected as significantly as the detachment distance is, and remains practically constant as the gap increases. The slight increase in overall solidification distance that is sometimes observed for smaller gaps might be due to the fact that the temperature gradients in the liquid region are greater for a smaller gap, therefore inducing a greater heat transfer from the crucible region to the interface region.

3.2.3. Effect of flow rate

Figure 5 shows the calculated effect of flow rate on the puddle shape for Al-4%Cu. The calculation shows that the puddle length increases greatly with the increase of melt flow rate while other parameters remain unchanged. The ribbon thickness increases proportionally to the increase of the flow rate, therefore requiring a much longer solidification distance because of the decrease in temperature gradients and heat transfer in the puddle and ribbon. In this figure, the flow rates have been chosen to illustrate the changes in puddle morphology corresponding to variations from quasi-FJMS conditions all the way to more typical PFMS situations. Naturally, the detachment distance increases also greatly with the flow rate.

4. Experimental investigations

It is widely believed that the solidification puddle is the most significant region in the PFMS process. Both its overall dynamics and the characteristics of its temperature and flow fields are indeed very likely the determining factors in the quality (both micro- and macroscopic) of the ribbon. Whereas some photographic [15] and cinematographic [16] investigations have been conducted to study the FJMS puddle, it appears that much less similar information is available on the PFMS process. Most relevant to the present study, perhaps, are a photograph of the PFMS puddle [17], and some infrared camera measurements [18]. As the dynamics of the puddle, in particular, is suspected to be of great importance for the formation of the ribbon it appears that real-time cinematography of this region might be a very valuable tool for the study of the PFMS process as well. As in the case of the FJMS [19], for example, ribbon geometry variations could well be caused by various melt puddle instabilities. Naturally, a better understanding of these instabilities would be necessary if we are to endeavour to reduce or cancel them by an adequate choice of the parameters or geometry of the process.

In view of these considerations we have initiated a program of experimental investigation of the PFMS solidification puddle shape and dynamics using high-speed video recordings. Direct information on the process that could be generated by this type of investigation would be very useful. In addition, a better knowledge of the PFMS puddle dynamics and shape could also lead to an improved quantitative understanding of the process through the validation and improvement of numerical models such as that described above. We are presenting here for illustration some results obtained in our experimental investigations.

4.1. Experimental installation and procedure

Figure 6 is a schematic diagram of our PFMS apparatus. A 28-cm diameter Cu-Be alloy wheel serves as the substrate for the casting of various metallic ribbons. The substrate surface velocity can be set between 5 and 50 m/s within 0.01 m/s. A high-vacuum stainless steel chamber provides a casting atmosphere of pure argon, typically at 500 mm Hg. The pressurized argon which is used to eject the liquid metal from the crucible is applied by opening a solenoid valve to an external accumulator tank. The ejection pressure (defined as the difference between the pressure in the external tank and in the casting chamber) can be measured by pressure gauges.

The graphite crucible assembly was designed so that the crucible could be reloaded with material without removing the crucible from the clamp, therefore achieving better position reproducibility. The crucible support system possesses several degrees of freedom to allow us to investigate such factors as the effect of inclination or offset of the crucible with respect to the wheel surface or center. The graphite crucibles and replaceable nozzles used for the aluminum alloys experiments are manufactured using CNC machines. Control of the crucible / substrate spacing was achieved from outside the casting chamber with a rotary feed-through and a vertical micrometric table. The crucible / wheel gap before and during casting was measured optically using the cameras.

An Ektapro 1000 high-speed video system was used for the high-speed video recording of the casting runs. This system is capable of up to 6000 images per second. The camera is mounted on a micrometric table fixed to the outside chamber, allowing a focusing distance accuracy of 0.125 mm, a necessary feature considering the extremely short depth-of-fields characteristic of our optical system. Indeed, because of the rather small dimensions of the solidification puddle, an optical system capable of high magnification had to be designed. We are using for this purpose a 75 mm lens fitted with a 105 mm extension tube, located outside the chamber at approximately 100 mm of the crucible, and aimed through a quartz window. The system gives us an image magnification of about 80X on a 19-inch monitor. Using this setup, the distance between each pixel in the digitized video image corresponds then to about 20 microns. Accordingly, the gap measurement error was believed to be about 20 microns as well. In this respect, it should be mentioned that some variations of the gap under rotation are caused by a slight eccentricity of the wheel axle. These oscillations of the substrate surface position were observed to change the crucible / wheel gap by about 50 microns over the course of one revolution of the wheel. This variation did not prove to be a major difficulty for our measurements, however, because of the large circumference of the wheel and the high frame rate of the camera which enable us to obtain many measurements over the course of one wheel revolution.

For the low-temperature aluminum alloy experiments reported here, the temperature of the melt inside the crucible was measured directly with a K-type thermocouple embedded in a grounded stainless steel sheath. (For titanium alloys and other high-temperature or reactive materials, a crucible cap with a quartz window allows us to use a computerized two-color pyrometer to measure the temperature of the melt inside the crucible.) The molten metal mass flow rate was obtained after each run by measuring the length and weight of a ribbon section. Unbroken ribbons of excellent quality and very uniform geometry can be obtained in this installation.

4.2. Experimental results

4.2.1. Surface waves

Figure 7 shows a schematic diagram of the PFMS solidification puddle and two photographs from a high-speed recording of the PFMS solidification puddle. The puddle is dark on these photographs because we are using back-lighting in order to minimize reflections and to improve the definition of the outline of the puddle. In addition, the melt (Al-4%Cu) is ejected from the crucible slit at a relatively low 1000 K or so, which prevented us from taking advantage of the natural glow of higher-temperature melts. It is worth mentioning that to achieve adequate lighting

conditions was among the most difficult problems to solve during the development of these experiments, primarily because of the combination of reflections, high-magnification optics, and high frame rate of the video camera.

These photographs, obtained after an overall steady-state had been achieved, show the existence of surface waves on the downstream meniscus (the substrate moves to the right in this case). These waves are rather large when compared to the overall dimensions of the puddle. Similar waves were observed in many other cases. The crucible / substrate spacing shown here is approximately 300 microns. The wavelength of these surface waves was approximately 250 microns. The waves are not as large in the second photograph, even though it was recorded only 1/6000th of a second later. Subsequent frames show them absent altogether and then reappearing again. This implies that the phenomenon is highly-dynamic and that these waves could perhaps be eliminated by an adequate choice of the process parameters. Analysis of other frames from this video recording suggests that these surface waves propagate in the downstream direction, which - if confirmed - could imply that there might not be any recirculation region in these puddles for these operating conditions. It is not known at this point what phenomena are responsible for the apparition of these surface waves. Presumably, these could include crucible pressure variations, hydrodynamic instabilities, surface tension effects, equipment vibration or misalignment etc. Our current experiments are aimed at developing a better understanding of this wave phenomenon and also at investigating the relationship between the surface waves and both micro- and macroscopic ribbon defects.

In the case of the run shown here, for example, the ribbon produced had one ragged edge, a defect which may perhaps be related to the observed waves. Upon reinspection of the crucible positioning system after this run it was noticed that the crucible axis was not perfectly normal to the wheel surface and that the crucible / wheel gap was slightly wider on one side of the wheel edge than on the other in this particular experiment. It is not clear at this point whether this slight asymmetry may have been responsible for the surface waves and for the ragged ribbon edge. Systematic experiments will be conducted in the future to clarify this question.

4.2.2. Establishment of the solidification puddle

Figure 8 shows a silhouette of the establishment of a PFMS puddle for a casting run which produced a ribbon with rather uniform thickness (variations in local thickness of less than five percent according to our micrometer measurements). In this figure, a sequence of four photographs of the puddle is shown, each image separated from the previous one by 1/4000th of a second. The top image shows the liquid alloy jet barely emerging from the crucible slit. The actual dimension of the slit drawn on this image is approximately 1.2 mm. The second image from the top reveals some of the alloy being already dragged downstream with the substrate. Note that the upstream and downstream menisci have not yet moved appreciably away from the slit edges. The third and fourth images show both menisci changing shape and moving away from the slit in a fairly symmetrical fashion. The motion of these menisci are probably related to the static surpressure in the crucible which is in turn counterbalanced by viscous forces generated by the substrate motion, and by surface tension effects.

As indicated by the analysis of subsequent video images in this sequence, both menisci stabilized then at approximately one slit-width away from the edges of the actual slit. It appears thus that the PFMS puddle was able in this particular case to develop to a "steady" configuration in about one millisecond after the apparition of the molten jet from the crucible.

4.2.3. Influence of molten mass flow rate

Figure 9 illustrates the influence of ejected metal mass flow rate on the downstream meniscus shape and location for the case of a relatively large gap. The horizontal axis is the distance from the downstream edge of the crucible slit. The vertical axis is the distance from the wheel surface. The curves shown were obtained by digitization of the high-speed video

recordings. Both menisci exhibit a noticeable bulge that was observed consistently throughout the recording of this run. It is possible that this bulge may be related to the presence of a recirculation zone close to the downstream meniscus. Considering that recordings of runs with larger gap generally do show a bulge, it is possible that a recirculation zone may only be present at large enough gaps. The wheel speed, on the other hand, seemed to be less clearly correlated with the apparition of bulges. These curves do not include the lowest part of the meniscus. When considering their shape, one should keep in mind the large difference in the scale of the axes used in this graph. In fact, the meniscus looks much more "horizontal" in reality (see Figure 7 and 8).

In this particular case, approximately doubling the flow rate led to a similar increase in the downstream detachment distance. It is of course not so surprising that increasing the flow rate would increase the detachment distance, considering that the increase in flow rate is obtained by an increase of pressure in the crucible. If the meniscus is not capable of sustaining a large pressure difference, this additional surpressure must then be counterbalanced by the increase in pressure drop in the gap that is induced by the longer detachment distance.

5. Comparison between numerical and experimental results

The value of the heat transfer coefficient "h" between the puddle and the substrate is one of the major parameter controlling the PFMS process, and therefore also a critical boundary condition for the numerical model. This parameter, which quantifies the level of thermal contact resistance between the wheel and the melt, remains still a largely unknown quantity. It is probably depending on the condition of wheel, the type of materials used for the wheel and the melt, the atmosphere used, the level of gas entrainment, the ambient and local pressure, the temperature, the wheel speed etc. There is apparently no general model available at the present time that could predict accurately the value of this coefficient for various operational conditions. Some attempts have been made, however, to estimate the value of the heat transfer coefficient using experimental results. The main approach used has been to measure the surface temperature of the ribbon with infrared pyrometers or cameras [20,21,22] or color photography [23] and then to compare these temperatures to results predicted by heat transfer analysis. Such an indirect approach is necessary because it would be extremely difficult to measure directly all the quantities required to compute this coefficient. This is after all an interface buried in the midst of a molten metal puddle.

The PFMS process being controlled by coupled momentum and heat transfer, the contact heat transfer coefficient should therefore have a strong effect on the puddle shape, detachment point, and solidification length in addition to the velocity and temperature distributions. Given that we have obtained new data on puddle shape measurements, we have investigated an approach somewhat different from that described above for the indirect evaluation of the contact coefficient. (Systematic thermal measurements of the puddle and ribbon will be conducted shortly for confirmation of these results.) Our approach has been to estimate the value of h by comparing the detachment distance and shape of the downstream meniscus obtained from experimental measurements to the results of parametric studies performed with our numerical model. This technique is illustrated in Figure 10 which shows together an experimental measurement of the downstream meniscus and several menisci computed for different values of the heat transfer coefficient, all other parameters being the same as in the experimental case. It can be seen that the best match occurs for a value of the heat transfer coefficient of approximately $4 \cdot 10^5 \text{ W/m}^2\text{-K}$ for this wheel speed of 14 m/s. Given the nature of the matching technique, this value could be considered to be an average over the length of the puddle.

Using some other experimental results, it was observed that the value of h determined by this matching method varies only within the relatively narrow range of about $3 \cdot 10^5$ to $6.5 \cdot 10^5 \text{ W/m}^2\text{-K}$.

K for our runs corresponding to gaps of 340 to 540 microns, metal flow rate of 20 to 40 g/s, and wheel speed of 14 to 23 m/s. The values found by this matching method are of the same order of magnitude as some other results reported so far: e.g. an h ranging from $5 \cdot 10^5$ to $7.5 \cdot 10^5$ W/m²-K [24]; from $5 \cdot 10^5$ to $2 \cdot 10^6$ W/m²-K [25]; from $6 \cdot 10^4$ to $2 \cdot 10^5$ W/m²-K [23]; from $7 \cdot 10^5$ to $1.3 \cdot 10^6$ W/m²-K in the puddle region and at about $2 \cdot 10^5$ W/m²-K further downstream in the ribbon region [20], $2.5 \cdot 10^5$ W/m²-K and above [21]. The rather wide range covered by these results reflects variations in the melt and wheel materials, wheel speed, surface finish, etc. In addition, the heat transfer coefficient is also likely to vary greatly with location: e.g. perhaps from 10^8 to 10^5 W/m²-K in as little as 1.5 milliseconds [22] after impingement of the melt on the wheel.

As expected, the solidification length decreases with an increase of the heat transfer coefficient, all other things being equal, because the better thermal contact between the puddle and substrate would lead to a greater heat transfer between them. Some other observations were made by comparing experimental results to our parametric study results. For example, it was seen that a larger metal flow rate results in a larger value of the estimated heat transfer coefficient. A larger wheel speed corresponds also to a higher value of this coefficient. These effects might be related to larger gradients of velocity in the melt next to the substrate. Similarly, and perhaps for the same reason, the value of the heat transfer coefficient increases slightly with a decrease of the gap.

Of course, the values of the heat transfer coefficient obtained by this matching technique are only rough estimates. The accuracy of these indirect estimates is indeed entirely dependent on the validity and completeness of the numerical model itself, which as pointed out earlier, contains numerous approximations and assumptions. Furthermore, these estimates are based primarily on detachment distance and meniscus shape which in reality may not be as sensitive to variations in the substrate contact resistance as the temperature distributions themselves. The reasonable agreement between these results and those obtained by other researchers is therefore particularly encouraging, and may be taken as another *a posteriori* validation of the model. This technique for the evaluation of a quantity not directly accessible to the experimentalist via matching to results of a numerical model is a very good illustration of the type of information that can be generated by synergetic experimental and modelling investigations.

Further developments planned for the numerical model include the implementation of full Navier-Stokes equations and the inclusion of undercooling, solidification kinetics, mushy zones, and mass transport phenomena. On the experimental side, investigations on puddle dynamics and in particular on surface instabilities will be pursued, together with direct temperature and heat fluxes measurements. Melt-spinning experiments are also presently conducted with higher temperature materials such as titanium alloys.

6. Conclusions and summary

A two-dimensional numerical model based on boundary layer equations has been developed for Planar Flow Melt-Spinning. This model solves both momentum and energy equations and is able to predict the velocity and temperature distributions in the puddle and ribbon, the cooling rate at any location, and the shape and location of the solid / liquid interface and of the downstream meniscus. It is found that the melt close to the wheel has a high velocity whereas the melt below most of the crucible moves rather slowly. The cooling rates before solidification may be 2 or more orders of magnitude higher near the wheel (10^6 K/s) than near the top of the ribbon (10^4 K/s). The temperature gradients are generally much greater in the solid region than in the liquid region. The recirculation region predicted by some of the simpler lubrication theory models is not observed in the results of this boundary layer equations model. The model can be readily used for studies of the effect of variations in the main process parameters on the puddle and ribbon

characteristics. For example, graphs showing isotherms and streamlines illustrate the large modifications caused by variations in wheel speed, crucible / wheel gap, and flow rate. It is found that the solidification length decreases moderately with increasing wheel speed, remains about constant for increasing crucible / wheel gap, and increases greatly with increasing flow rate.

Our experimental investigations of the dynamics of the solidification puddle by high-speed video recordings allow us to investigate the variations in shape and size of the puddle and menisci as a function of operational parameters. Both large-scale oscillations of the puddle and high-frequency surface waves on the downstream meniscus were observed. Video recordings of the establishment of the puddle showed that it may require on the order of one millisecond for the development of a steady configuration. Digitized video frames give us quantitative information on the variations of meniscus position with flow rate for example, and confirm the existence of steady bulges on the downstream meniscus for certain combination of parameters.

Estimates of the thermal contact resistance at the substrate were obtained by matching the measured detachment point and meniscus shape with numerical modelling predictions. Values of about $5 \cdot 10^9 \text{ W/m}^2\text{-K}$ for the average heat transfer coefficient over the puddle length were obtained in this fashion. This number is in good agreement with other published estimates for this coefficient.

In conclusion, a combination of numerical modelling and experimental work for the investigation of the PFMS process is likely to be particularly fruitful because of the many complementary and interrelated aspects of these two approaches. This type of broad-based investigation should enable us to develop a much better understanding of both the basic phenomena taking place during the process itself and of the related question of most appropriate hardware design. In addition, and perhaps more importantly, we hope to learn how the process can be modified and controlled in order to obtain a rapidly-solidified foil of desired geometry and microstructure.

Acknowledgements

We are gratefully acknowledging the sponsorship of the Defense Advanced Research Projects Agency (contract No. N00014-86-K-0753). The senior author (EFM) would like to thank Prof. C. Levi (UCSB) for his constant support and for many valuable discussions. The numerical modelling work was conducted by Mr. Gong and the experimental work by Mr. Wilde, both graduate students at UCSB. Mr. M. Eskenazi (M.Sc.'88 - UCSB) developed the first version of the computer code. Some of the results discussed here were presented at the Symposium on *Intelligent Processing of Materials* at the TMS Fall meeting, Indianapolis, October 1-5, 1989.

References

1. R. MEHRABIAN, *International Metals Review*, 1982, 27 (4), 185-208.
2. C.G. LEVI and R. MEHRABIAN, in *Rapid Solidification Processing Principles and Technologies IV*, eds: R. Mehrabian and P.A. Parrish, Claytor Pub., 1988, pp. 26-65.
3. L.E. COLLINS, *Canadian Metallurgical Quarterly*, 1986, 25 (1), 59-72.
4. H. YU *Metallurgical Transactions B*, 1987, 18B, 557-563.
5. E.M. GUTIERREZ and J. SZEKELY, *Metallurgical Transactions B*, 1986, 17B, 695-703.

6. K. TAKESHITA and P.H. SHINGU, *Transactions of the Japan Institute of Metals*, 1983, 24 (7), 529-536.
7. K. TAKESHITA and P.H. SHINGU, *Transactions of the Japan Institute of Metals*, 1986, 27 (2), 141-148.
8. S.A. BERGER and D.K. AI, *Metallurgical Transactions B*, 1988, 19B, 571-579.
9. Z. SUN and H.A. DAVIS, *Materials Science and Engineering*, 1988, 98, 71-74.
10. A. POOPISUT, *Fluid Mechanics and Heat Transfer in Chill-Block Melt Spinning and Planar Flow Casting*, Ph.D. thesis, State University of New York at Buffalo, 1988.
11. L. KATGERMAN, in *Proceedings of the Second International Conference on Numerical Methods in Laminar and Turbulent Flow*, Venice, 1981, July 13-16.
12. A.T. MALE, *Technology Development for Thin Strip Metal Casting - Phase II*, Report No. 87-9D4-STRIP-R4, Westinghouse R&D Center, 1988.
13. M.I. ESKENAZI and E.F. MATTHYS, *Modelling of Planar Flow Melt Spinning using the Boundary Layer Equations*, Report No. UCSB-ME-88-4, University of California, Santa Barbara, 1988.
14. R.W. HORNBECK, *Numerical Marching Techniques for Fluid Flows with Heat Transfer*, Report No. SP-297, NASA, 1973.
15. H.HILLMAN and H.R.HILZINGER, in *Rapidly Quenched Metals III*, ed. B. Cantor, The Metals Society, London, 1978, pp. 22-29
16. J.L. WALTER, in *Rapidly Quenched Metals III*, ed. B. Cantor, The Metals Society, London, 1978, pp. 30-33.
17. S.C.HUANG, R.P. LAFORCE, A.M. RITTER, and R.P. GOEHNER, *Metallurgical Transactions A*, 1985, 16A (October), 1773-1779.
18. G. STEPHANI, H. MUHLBACH, H. FIEDLER, and G. RICHTER, *Materials Science and Engineering*, 1988, 98, 29-32.
19. T.R ANTHONY and H.E.CLIN, *Journal of Applied Physics*, 1978, 49 (2), 829-837.
20. K. TAKESHITA and P.H. SHINGU, *Transactions of the Japan Institute of Metals*, 1983, 27 (6), 454-462.
21. E. VOGT, *International Journal of Rapid Solidification*, 1987, 3, 131-146.
22. H. MUHLBACH, G. STEPHANI, R. SELLEGER, and H. FIEDLER, *International Journal of Rapid Solidification*, 1987, 3, 83-94.
23. A.G. GILLEN and B. CANTOR, *Acta Metallurgica*, 1985, 33 (10), 1813-1825.
24. M.G. CHU, A. GIRON, And D.A. GRANGER, in *Proceedings of ASM's 1986 International Conference on Rapidly Solidified Materials* (American Society for Metals, Metals Park, Ohio, 1986, pp. 311-316.
25. S.C. HUANG and H.C. FIEDLER, *Materials Science and Engineering*, 1981, 51, 39-46.

Table I : Parameters used in Al-4%Cu PFMS computations

Nozzle width	1.2 mm
Nozzle length	8.3 mm
Pouring temperature of melt	983 K
Melting temperature	933 K
Wheel temperature	300 K
Melt viscosity	$1.26 \cdot 10^{-3}$ kg/m-s
Density of liquid metal	2700 kg/m ³
Density of solid metal	2340 kg/m ³
Specific heat of liquid metal	1200 J/kg-K
Specific heat of solid metal	1060 J/kg-K
Thermal conductivity (liquid)	100 W/m-K
Thermal conductivity (solid)	200 W/m-K
Latent heat of fusion	$3.9 \cdot 10^5$ J/kg

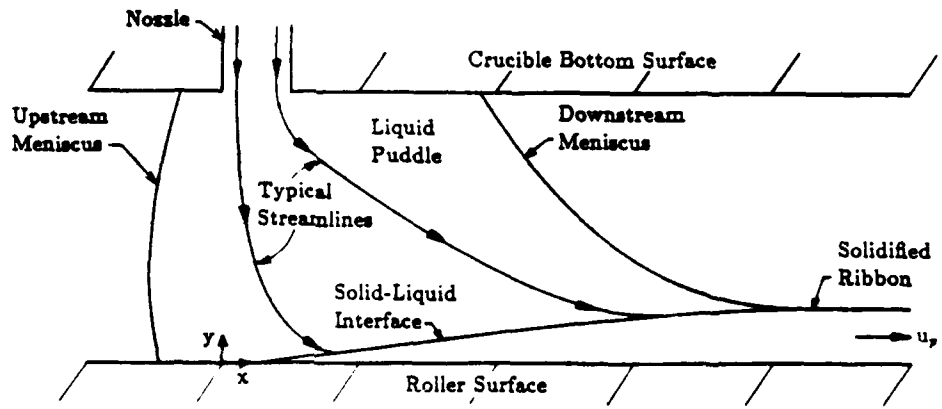


Figure 1 : Schematic of the Planar Flow Melt-Spinning solidification puddle.

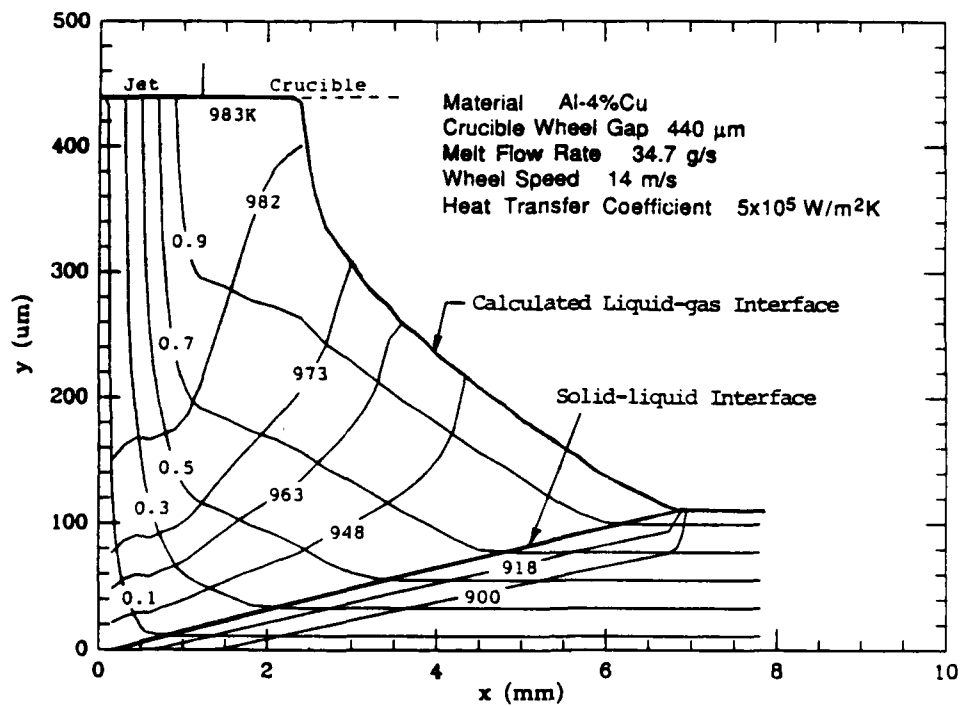


Figure 2 : Modelling of Al-4%Cu PFMS solidification puddle : typical streamlines and isotherms. (Physical properties : see Table I.)

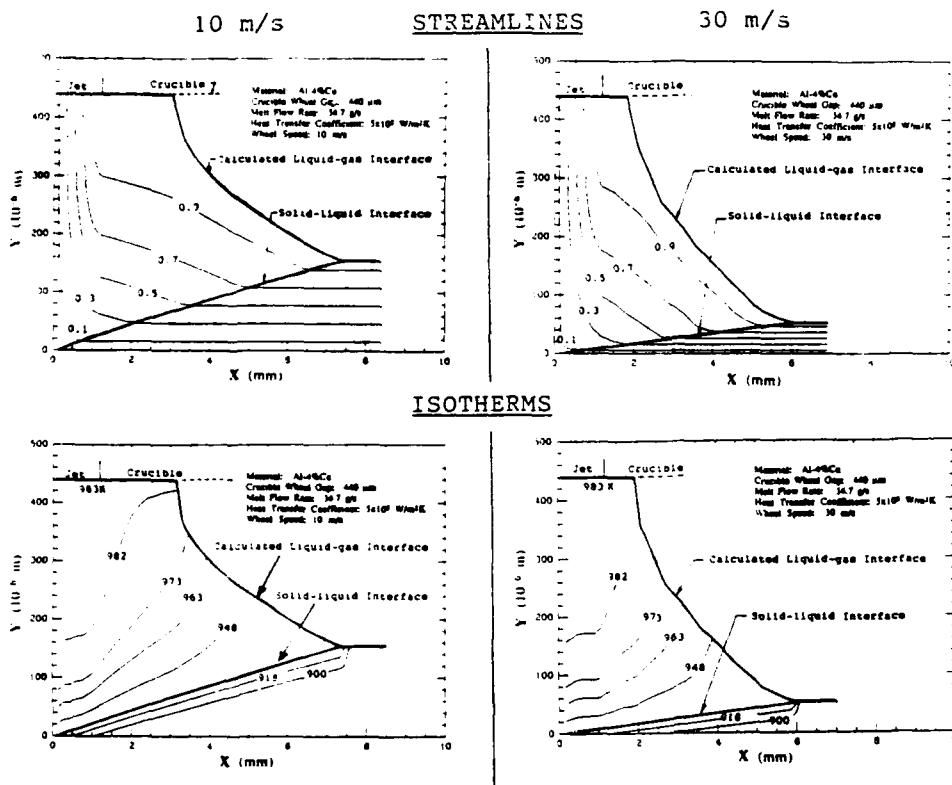
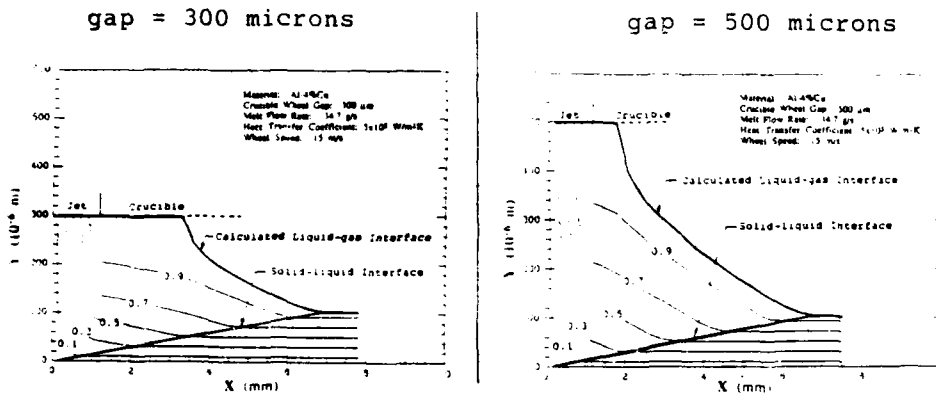


Figure 3 : Effect of wheel speed variation on solidification puddle shape, streamlines and isotherms. The streamlines map is on top, the isotherms map is below. The low wheel speed (10 m/s) is on the left-hand side and the high wheel speed (30 m/s) on the right. [Gap: 440 micrometers; flow rate: 34.7g/s; heat transfer coefficient: $5 \cdot 10^5 \text{ W/m}^2\text{-K}$.]

STREAMLINES



ISOTHERMS

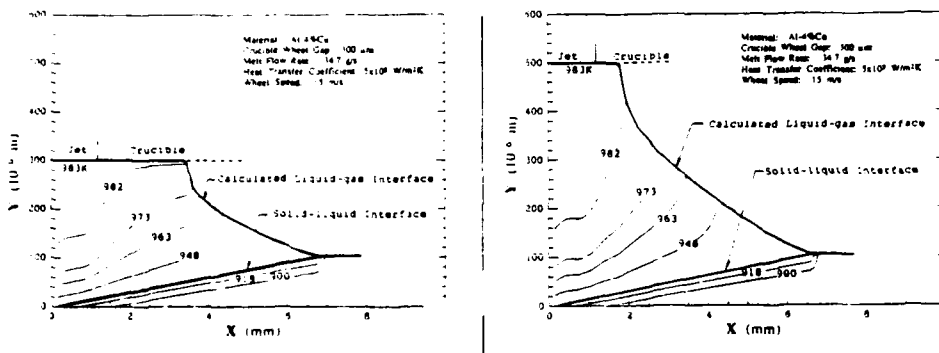
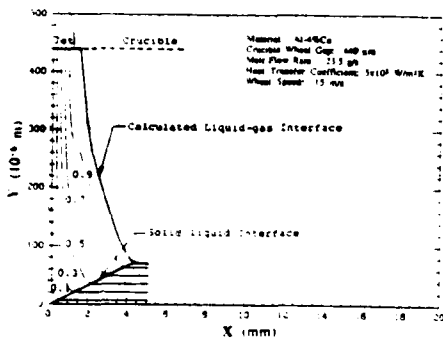


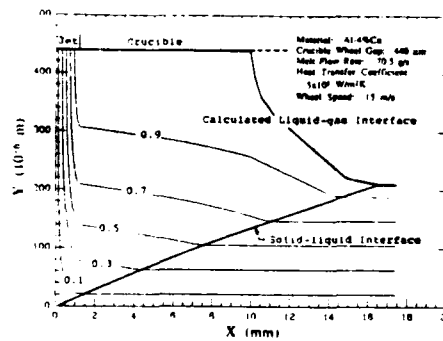
Figure 4: Effect of wheel / crucible gap variation on solidification puddle shape, streamlines and isotherms. The low gap (300 micrometers) is on the left-hand side, and the high gap (500 micrometers) on the right. [Flow rate: 34.7 g/s; wheel speed: 15 m/s; $h: 5 \times 10^5 \text{ W/m}^2\text{-K}$.]

STREAMLINES

flow rate = 23.5 g/s



flow rate = 70.5 g/s



ISOTHERMS

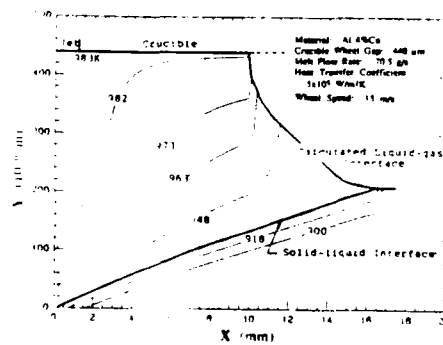
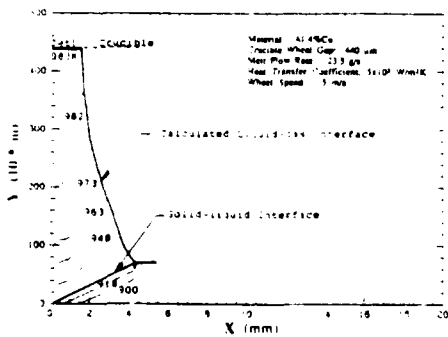


Figure 5 : Effect of flow rate variation on solidification puddle shape, streamlines and isotherms for Al-4%Cu. The low flow rate case (23.5 g/s) is on the left-hand side, and the high flow rate (70.5 g/s) on the right. [gap: 440 microns; wheel speed: 15 m/s; heat transfer coefficient : $5 \cdot 10^5 \text{ W/m}^2\text{-K}$.]

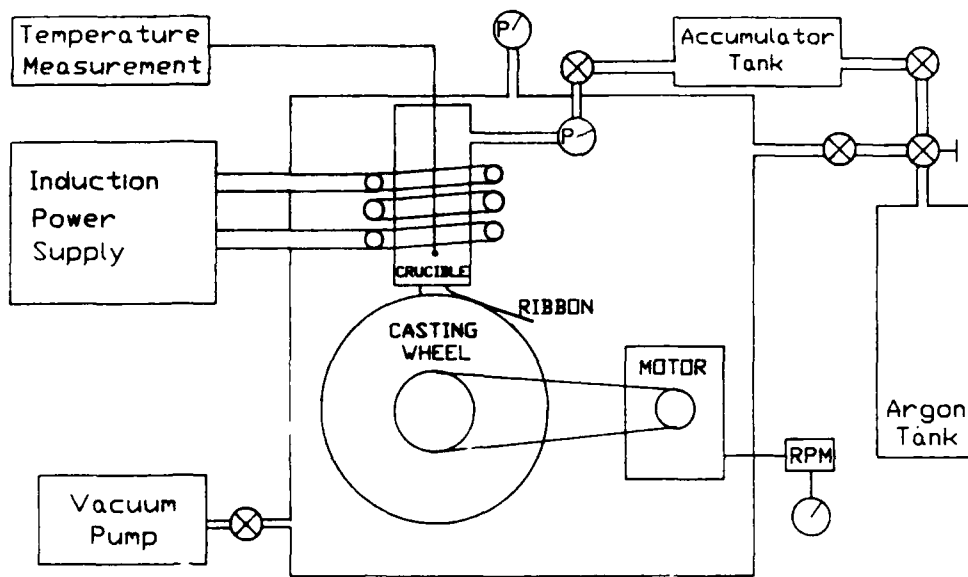


Figure 6 : Schematic of the UCSB Planar Flow Melt-Spinning installation.

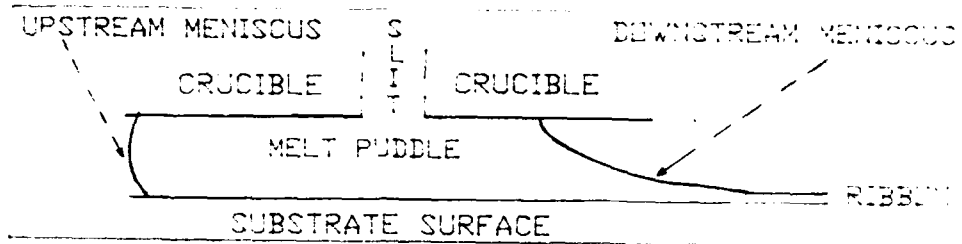


Figure 7 : Backlit photographs of PFMS solidification puddle showing surface waves on the downstream meniscus. Photographs separated by 1/6000th of a second. [Al-4%Cu alloy; wheel speed: 23 m/s; gap: 300 micrometers.]

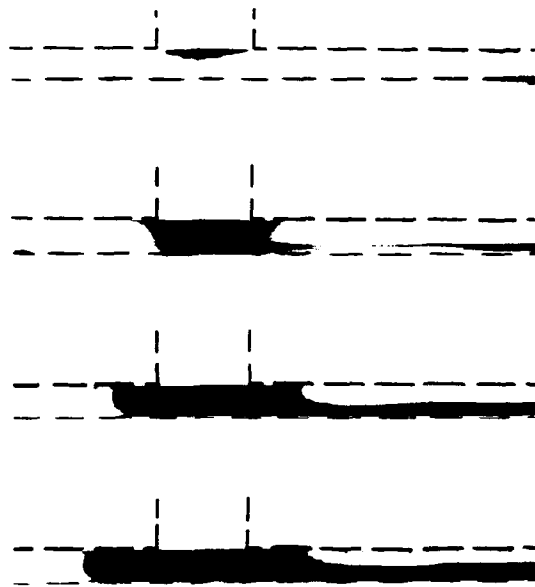


Figure 8 : Establishment of a PFMS solidification puddle. These 4 photographs are separated by $1/4000$ th of a second from one another. The top photograph shows the melt barely emerging from the nozzle slit. The estimated positions of the crucible and of the wheel surface are drawn on the photographs for reference. [Al-4%Cu; wheel speed: 14 m/s; gap: 370 micrometers; flow rate: 21 g/s; ribbon thickness: 75 micrometers.]

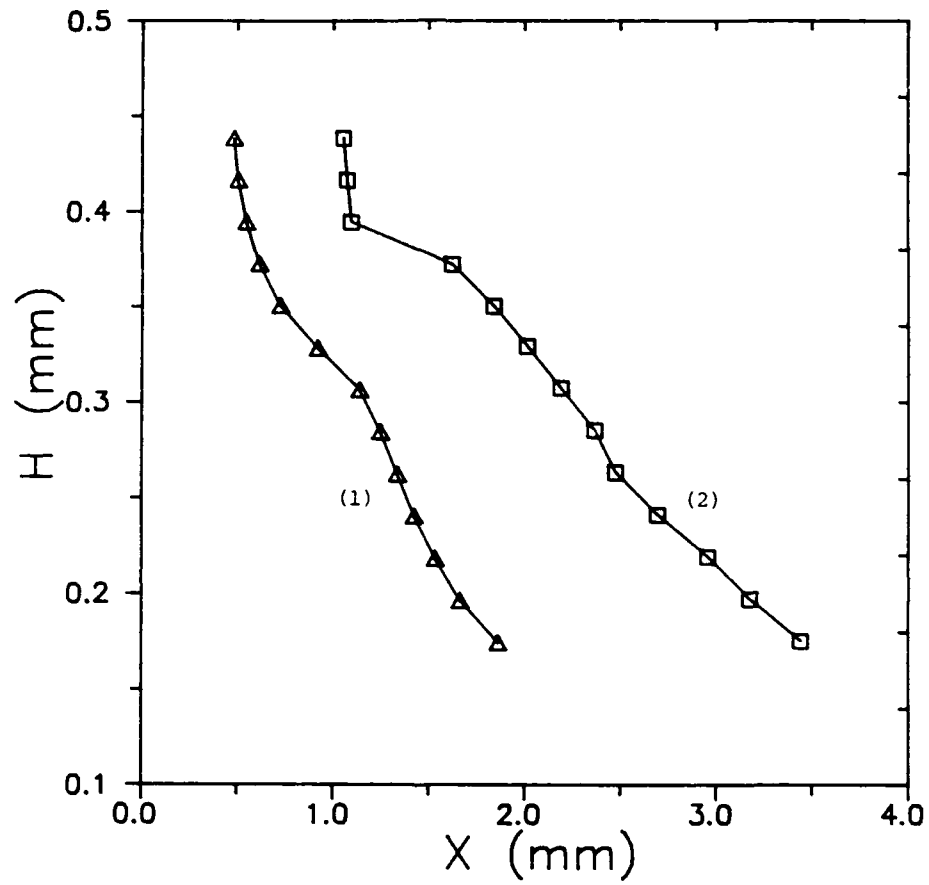


Figure 9 : Shape and location of downstream meniscus as a function of flow rate. Curve (1) : flow rate = 16 g/s and ribbon thickness = 65 microns; Curve (2) : flow rate = 35 g/s and ribbon thickness = 110 microns. [Gap = 440 microns, wheel speed = 14 m/s.]

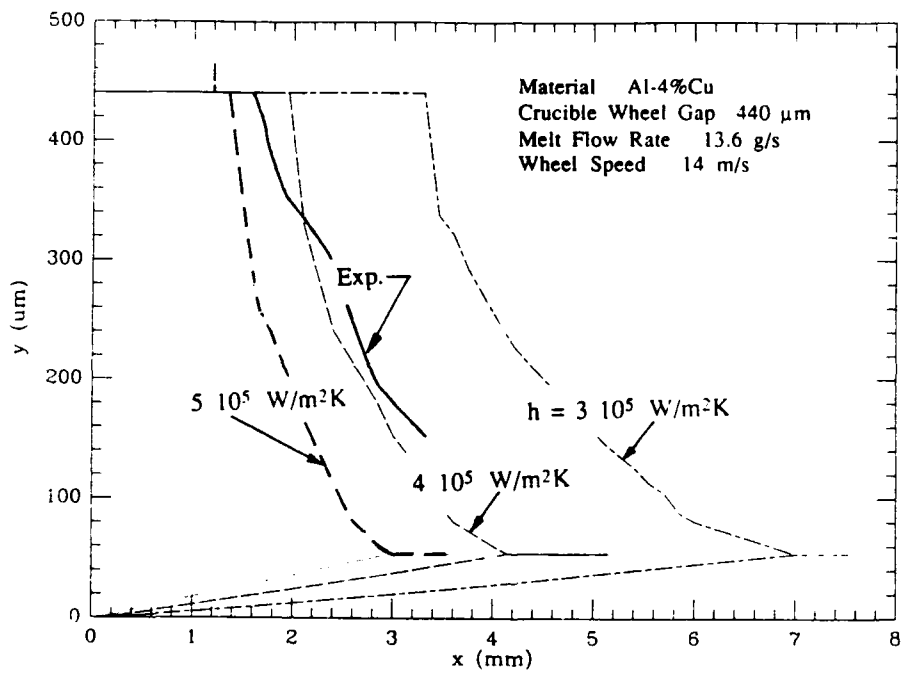
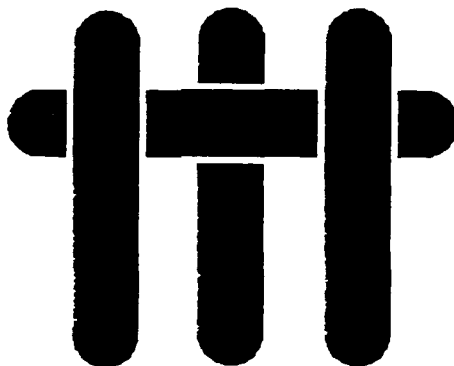


Figure 10 : Comparison of measured detachment point and downstream meniscus shape with predicted values corresponding to different heat transfer coefficients at the wheel. The best match is for $4 \cdot 10^5 \text{ W/m}^2\text{-K}$. [Al-4%Cu; gap: 440 microns; flow rate: 13.6 g/s; wheel speed: 14 m/s.]

M A T E R I A L S



DENSIFICATION BEHAVIOR OF
 Al_2O_3 POWDER CONTAINING ZrO_2 INCLUSIONS

by

O. SUDRE, D.C.C. LAM and F.F. LANGE

Materials Department
College of Engineering
University of California
Santa Barbara, California 93106

Presented at:

Materials Research Society Meeting, Spring 89, San Diego, CA.

DENSIFICATION BEHAVIOR OF Al_2O_3 POWDERS CONTAINING ZrO_2 INCLUSIONS

O. SUDRE, D.C.C. LAM and F.F. LANGE
Materials Department, College of Engineering, University of California
Santa Barbara, CA 93106.

ABSTRACT

Densification experiments using ZrO_2 single crystal particles in an Al_2O_3 powder matrix were performed to examine the microstructural changes produced by constrained densification. Observations showed the formation of large low density regions within a denser material network. Enlargement of pores by de-sintering of necks between grains were observed during grain coarsening within these low density regions. This pore opening behavior was also investigated in a model experiment.

INTRODUCTION

Retardation of densification of a powder matrix by inclusions has been observed for a number of systems, i.e. SiC-ZnO [1], $\text{Al}_2\text{O}_3\text{-TiO}_2$ [2]. Numerous models have been proposed to model this densification behavior [3-6]. These models ascribe to the concept that powder shrinkage generates compressive stresses in the inclusions and tensile stresses in the powder matrix during densification. The tensile stresses generated within the matrix are thought to oppose the compressive 'sintering stresses' and thus retard densification. However, experiments [7] have shown that the creep rate is comparable to the densification rate which implies that the tensile stresses are relaxed quickly. In addition, a model specimen consisting of an alumina powder ring slip cast around a dense alumina plug was performed [8] to simulate the geometry used in the theoretical models. The results showed that the densification of the powder ring is not retarded by the central inclusion.

Evidently, existing models based on retardation stresses are inadequate in explaining the phenomenon of constrained densification. In an alternative approach, Lange [9] suggested that the densification constraint arises from the interaction between inclusions. Lange proposed that the inclusions constitute the nodes of a network. The distance between nodes varies and the amount of powder between inclusions determines the shrinkage between nodal pairs. It was concluded from this geometrical argument that the matrix can fully densify only if extensive network deformation occurs. If matrix creep is insufficient, then local variations of inclusion spacings would generate local tensile constraint giving rise to matrix disruptions such as crack-like voids.

In the present study, the microstructural evolution of an Al_2O_3 powder matrix containing ZrO_2 inclusions was investigated. The observations suggested that variation in density did arise and that neck between grains in low density regions broke contact as grains coarsened after initial sintering. This mechanism of de-sintering of necks was also investigated using a model geometry.

EXPERIMENTAL PROCEDURE

ZrO₂ single crystals, 30-50 μm in size (Ceres Corporation), were mixed into a dispersed colloidal Al₂O₃ (Sumitomo AKP-50) slurry [10]. The volume fraction of crystals was 9 vol.% based on the theoretical composite density. The slurry was then flocced to prevent inclusion segregation. The composite slurry was pressure filtrated at 5 MPa to form cylindrical specimens. Large cracks were observed after both die removal and drying. The densification behavior was examined by dilatometry at constant heating rate (5°C/min) up to 1550°C. The microstructures of polished specimens sintered at different temperatures were examined using a SEM (JEOL 840). Additionally, the evolution of a specific region on a sintered specimen was followed after successive heat treatment periods at 1600 °C.

Another specimen of polycrystalline cubic ZrO₂ containing 8 mole% Y₂O₃ (Tosoh Corporation, TZ-8Y) was used as a model to study the effect of constraint on the microstructural development of polycrystalline bridges between the faces of a crack. Dispersed slurry of cubic ZrO₂ was slip cast into a plaster tube. As shown in Fig. 1, the dried specimen had a dense shell around a lower density core. A discontinuous crack developed in the middle of the specimen after drying. Powder bridges between the crack surfaces developed into polycrystalline ligaments upon sintering. Evolution of these bridges was followed by SEM during subsequent heat treatments.

OBSERVATIONS

The densification behavior of the Al₂O₃-ZrO₂ inclusion composite and that of the pure matrix is shown in Fig. 2. Microstructural observations showed that the slight decrease in matrix density in the composite was due to formation of inclusion related cracks with large opening displacements (Fig. 3) and to density variations within the matrix (Fig. 4). Low density regions were frequently observed along the length of high aspect ratio inclusions whereas dense regions were often associated with the tip of the inclusions. In areas where inclusions were in close proximity, a higher matrix density was noticed but this observation may be biased by the two dimensional character of the cut and polished specimens.

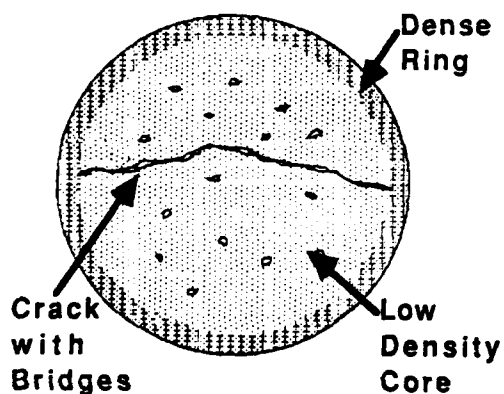


Figure 1: Model specimen to follow polycrystalline bridges across crack

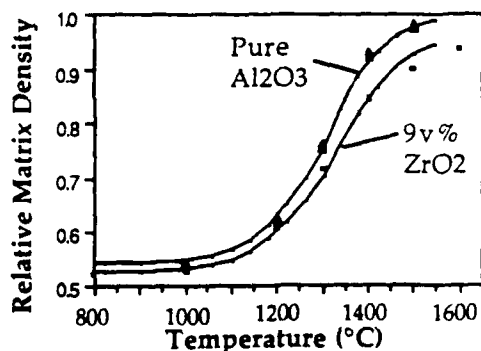


Figure 2: Densification of the composite and a pure matrix



Figure 3: Large macro-cracks associated with inclusions



Figure 4: Low density regions and surrounding denser material



Figure 5: Differential grain growth in denser regions relative to lower density regions



Figure 6: Region followed in Figure 7

As shown in Fig. 5, differences in average grain size between the low density and high density areas became apparent after further heat treatments at 1600°C. The evolution of microstructure for a cut and polished specimen in a low density region near an inclusion cluster (Fig. 6) is shown in Fig. 7. At first some densification occurred leading to some pore closure. Upon further heat treatment, some initially sintered grains separated. This process resulted in the coalescence of the pores located on both sides of the neck. Three of these events are shown but the reader can readily identify others. Grain growth has concurrently occurred during this evolution

As shown in Fig. 5, differences in average grain size between the low density and high density areas became apparent after further heat treatments at 1600°C. The evolution of microstructure for a cut and polished specimen in a low density region near an inclusion cluster (Fig. 6) is shown in Fig. 7. At first some densification occurred leading to some pore closure. Upon further heat treatment, some initially sintered grains separated. This process resulted in the coalescence of the pores located on both sides of the neck. Three of these events are shown but the reader can readily identify others. Grain growth has concurrently occurred during this evolution

Evolution of the bridge in the model experiment is shown in Fig. 8. The grain size increased with annealing time. The bridging material eventually developed into large grain pairs. Further heat treatments caused grain pairs to separate by desintering which led to the coalescence of the adjacent cracks.

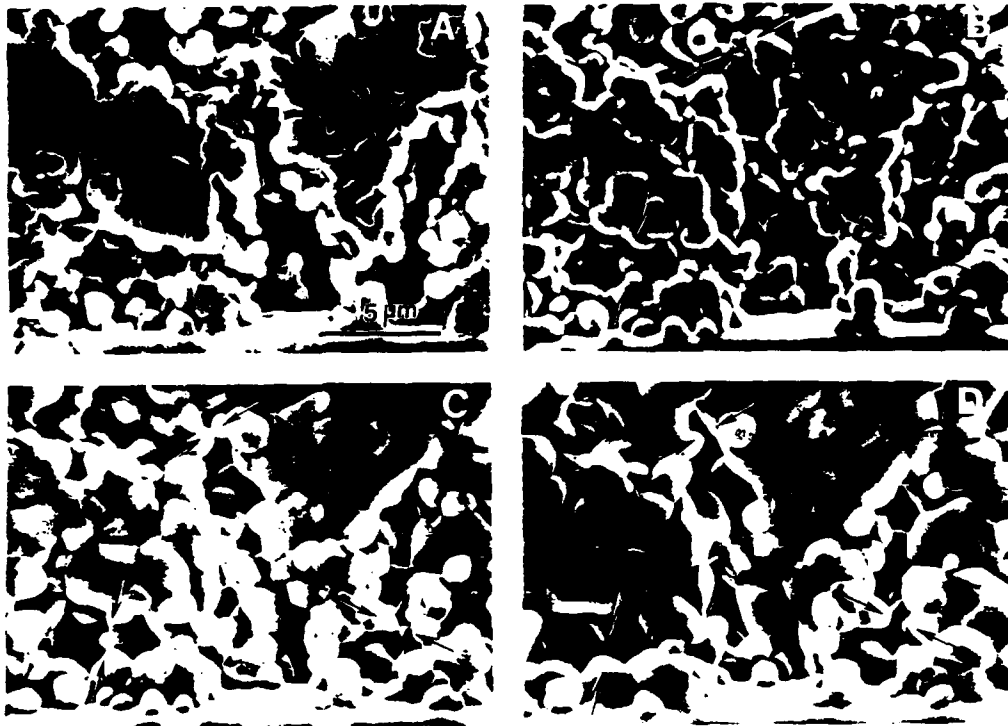


Figure 7: Evolution of the region outlined in Fig. 6 at 1600°C after (A) polishing, (B) 10 mins, (C) 2 hours, (D) 3 hours .

DISCUSSION

Large cracks in the composite matrix are believed to have developed during sintering from hair line defects in the green body. It is thought that these defects are created by the differential strain relaxation in the green compact during pressure release after pressure filtration or during drying. It has been shown that the number of defect can be reduced by using a dispersed suspension that will flow upon strain recovery and prevent the formation of these cracks [11].

The microstructural observations of sintered specimens suggested that the partially dense composite was composed of a 3-D network of denser matrix which surrounded lower density regions. These density and grain size variations will create a differential in the viscoelastic properties of the matrix. These observations led to propose the following retardation mechanism. During sintering, a network of denser material developed between inclusions. This denser network surrounded lower density regions. Densification of the lower density regions would require the deformation of the higher density network. Under constraint, material within the low density regions decreased its free energy via grain growth and de-sintering. De-sintering relieved the local constraint but increased the average pore size. This mechanism created stable pores with higher coordination numbers and thus decreased the driving 'stress' to deform the denser regions. Consequently, densification was retarded.

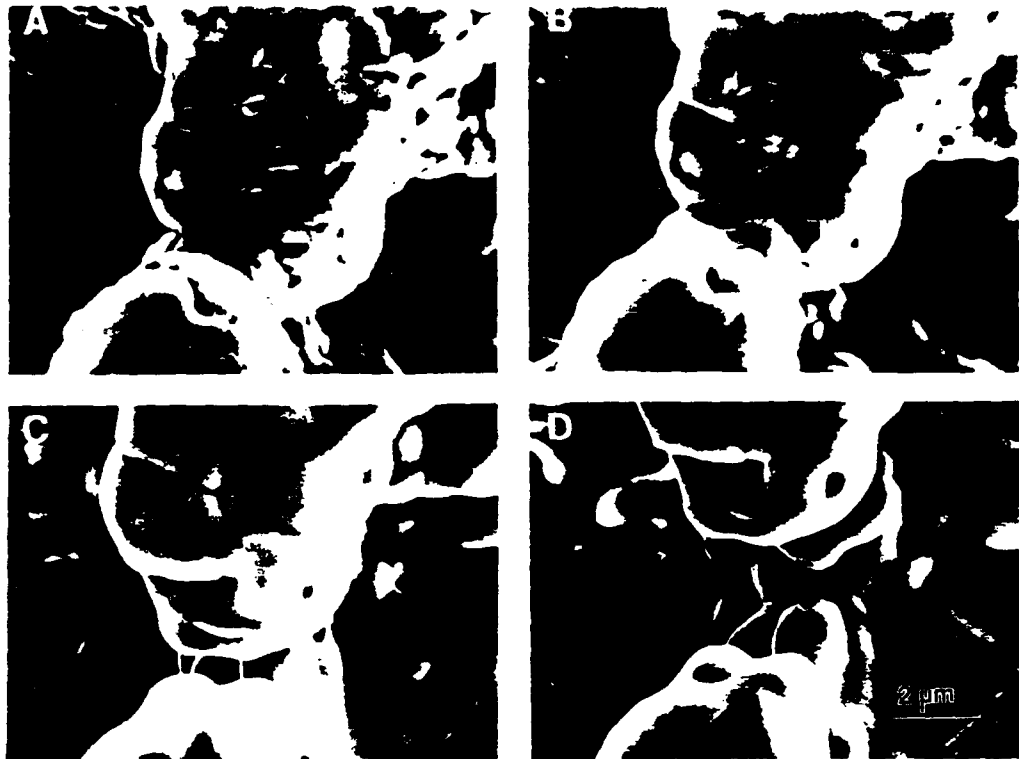


Figure 8: Evolution of a polycrystalline bridge in the model experiment with consecutive heat treatments at (A) 1450°C for 10 mins and then at 1600°C for (B) 10 mins, (C) 2 hours, (D) 3 hours.

The de-sintering mechanism is shown in a more dramatic fashion in the model experiment in which the polycrystalline bridge is constrained from shrinkage. The dense shell densify quickly. An equilibrium is established between the low density core and the polycrystalline bridges preventing any shrinkage. The grains initially coarsened into a line of monocrystals so as to decrease the free energy of the bridge. Constrained from further shrinkage, it eventually led to de-sintering of the bridge to produce one large, continuous crack.

This de-sintering process has been observed and the energetics modelled for the cases of the constrained polycrystalline fibers [12] and thin films [13]. A schematic of the microstructural evolution is shown in Fig. 9. Thermodynamic modelling has shown that the de-sintering of these grains could only occur after the grains have reached a critical aspect ratio (grain diameter to mass-center distance). Therefore, grain coarsening plays an active role in this mechanism by increasing the aspect ratio of the grains.

CONCLUSIONS

The present investigation described the microstructure of a Al_2O_3 composite powder containing ZrO_2 inclusions. Large cracks and large crack opening displacements originated from processing flaws were observed. More important, during densification of the powder matrix, a network of higher density material

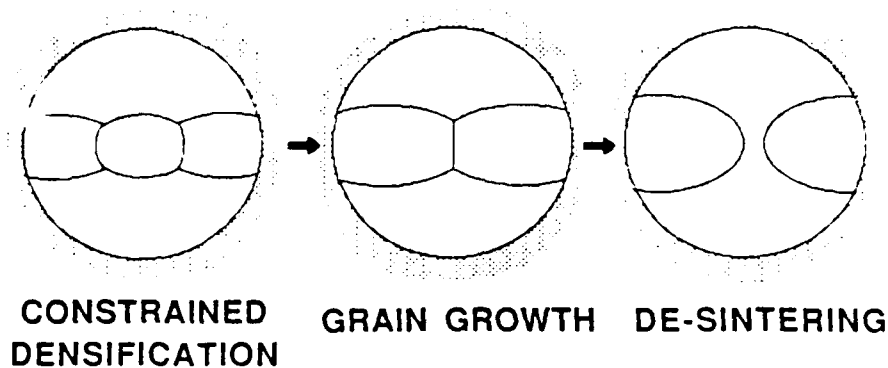


Figure 9: Schematic of de-sintering mechanism produced by coarsening.

was formed which encompassed low density regions. Further densification of these low density regions was constrained by the deformation of the denser material. These regions decreased their free energy by allowing de-sintering and the enlargement of pores which subsequently led to the decrease in the driving 'stress' for further densification. The de-sintering process has also been shown using a model specimen. Previous works on constrained fibers and thin films have already described this thermodynamic instability.

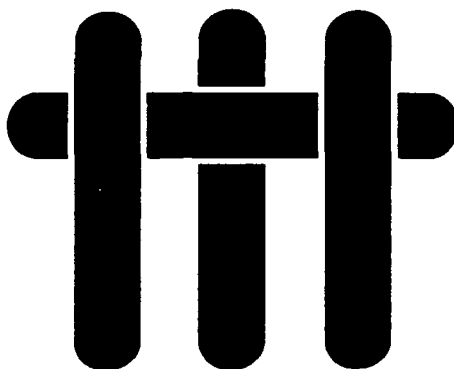
ACKNOWLEDGEMENTS

The authors gratefully acknowledge stimulating and enlightening discussions with P. Mataga, A. G. Evans and K. T. Miller. E. B. Slamovich is acknowledged for supplying the specimen used in the de-sintering model experiment. This work was supported by grants from U.R.I. (contract n° N00014-86-K-0753), N.S.F. (contract n° DMR-87-13919) and the 'Société Européenne de Propulsion'.

REFERENCES

1. L.C. De Jonghe, M.N. Rahaman and C.H. Hsueh, *Acta Metall.* **34**, 1467 (1986).
2. R.K. Bordia and R. Raj, *Adv. Cer. Mat.* **3** [2], 122 (1988).
3. R. Raj and R.K. Bordia, *Acta Metall.* **32**, 1003 (1984).
4. C. H. Hsueh, A.G. Evans and R.M. McMeeking, *J. Am. Cer. Soc.* **69**, C-64 (1986).
5. P. A. Mataga and J. L. Bassani (private communication).
6. R.K. Bordia and G.W. Scherer, *Acta Metall.* **36**, 2393 (1988).
7. M.N. Rahaman and L.C. De Jonghe, *J. Am. Cer. Soc.* **67**, C-205 (1984).
8. F.F. Lange, *Acta Metall.* **37**, 697 (1989).
9. F.F. Lange, *J. Mater. Res.* **2** 59 (1987).
10. F.F. Lange, B.I. Davis and E. Wright, *J. Am. Cer. Soc.* **69**, 66 (1986).
11. B. Velamakani and F.F. Lange, submitted to *J. Am. Cer. Soc.*
12. K.T. Miller and F.F. Lange, *Acta Metall.* in press.
13. K.T. Miller, F.F. Lange, and D.B. Marshall, p.823-830 in Better Ceramics Through Chemistry III, edited by C.J. Brinker, D.E. Clark, and D.R. Ulrich, Materials Research Society (1988).

M A T E R I A L S



**DENSIFICATION BEHAVIOR OF
SINGLE CRYSTAL AND POLYCRYSTALLINE
SPHERICAL PARTICLES OF ZrO_2 MADE
BY ELECTROSTATIC ATOMIZATION**

Elliott B. Slamovich and Frederick F. Lange

Materials Department
College of Engineering
University of California, Santa Barbara
Santa Barbara, California 93106

Densification Behavior of Single Crystal and Polycrystalline Spherical Particles of ZrO_2 Made by Electrostatic Atomization

Elliott B. Slamovich* and Frederick F. Lange*

Materials Department
College of Engineering
University of California, Santa Barbara
Santa Barbara, CA 93106

ABSTRACT

Micron-size polydispersed spheres of zirconia were produced via electrostatic atomization and pyrolysis of zirconium acetate-yttrium acetate precursors. Varying precursor composition in the ZrO_2 rich portion of the ZrO_2 - Y_2O_3 binary system resulted in the production of either single crystal (0 and 10 mole % Y_2O_3) or polycrystalline (3 mole % Y_2O_3) zirconia spheres of similar size distribution for densification studies. Powders of the either single crystal or polycrystalline particles exhibited contrasting densification behavior, powder compacts composed of polycrystalline particles attaining significantly higher endpoint densities than their single crystal counterparts. The role of grain growth within the polycrystalline particles is discussed in the context of the above results. [Key words: sintering, densification, zirconia, powder fabrication, grain growth]

* Member, American Ceramic Society

INTRODUCTION

Interest in the densification behavior of ceramic powders composed of dense polycrystalline particles arose from recent results suggesting that isolated pores within a polycrystalline body could be thermodynamically stable.¹ It was hypothesized that polycrystalline particles were more likely to produce such pores because the initial void spaces within the powder compact would be coordinated by a larger number of grains relative to single crystal particles. A research program was initiated to produce both polycrystalline and single crystal particles and study their relative sintering behavior. Because initial densification studies showed that polycrystalline particles achieved much higher end-point densities relative to single crystal particles, our research was refocused on the initial densification phenomena rather than the stability/instability conditions of isolated pores.

Routes to powder fabrication may result in the formation of particles that are polycrystalline at some intermediate stage^{2,3}. The effects of particle substructure on densification of TiO_2 have been examined in some detail². However, the large driving force for grain growth associated with the fine intraparticle grains ($<0.1\mu\text{m}$) caused the particle substructure to be transient. In the current work it was recognized that in order for the particles to remain polycrystalline during densification only minimal grain growth could be tolerated. Work in the ZrO_2 -rich portion of the ZrO_2 - Y_2O_3 binary system has shown that grain growth within the apparent tetragonal and cubic two phase field is severely limited, the average grain size increasing from $0.3\mu\text{m}$ to $0.7\mu\text{m}$ after heat treatment for 200 h at 1400°C ⁴. Grain growth for compositions within apparent single phase regions (either tetragonal or cubic) was rapid, producing relatively large-grained material ($>1\mu\text{m}$) for heat treatment periods of only 1 h at 1400°C . In order to exploit this phenomenon a method had to be devised to produce particles with compositions

that either inhibited or allowed grain growth. Electrostatic atomization of liquid³ precursors proved to be a suitable method to produce spherical particles with well defined compositions⁵. Aqueous solutions containing zirconium acetate and yttrium acetate were used to produce solid precursor spheres that pyrolyze to ZrO_2 at temperatures between $400^\circ C$ and $700^\circ C$ ⁶. These spherical particles were used for the densification studies detailed below.

PARTICLE FABRICATION

Atomization of Precursor

Figure 1 schematically illustrates the electrostatic atomization apparatus used to form spherical droplets from liquid precursors. A stainless steel electrode is inserted into a glass capillary tube filled with an aqueous solution of zirconium acetate^{*} to which yttrium acetate^{**} could be added. A high potential (10-15 kV) applied to the solution causes the meniscus at the capillary opening to buldge out forming a cone⁷. At a critical voltage the surface of the cone becomes unstable due to the accumulation of electric charge and ejects fine jets which decompose into droplets by Rayleigh instability. The charged droplets dry to solid spheres of zirconium acetate before they deposit on a grounded substrate (approximately 50 mm from capillary opening). The conditions that produce Rayleigh instability thereby determining the droplet size depend on the precursor rheology. The precursor viscosity was therefore characterized with a capillary viscometer, and surface tension was measured by the capillary rise method. In addition, Poly(ethyleneoxide) (PEO), a water soluble long-chain polymer^{***}, was used to modify the precursor rheology. Precursors containing the equivalent of 0, 3, and 10 mole % Y_2O_3 (based on ZrO_2 content) were used to make three powders. Powders

^{*} 22 wt. % ZrO_2 , Magnesium Elektron Inc.

^{**} Sharpe Chemical Co.

^{***} Poly(ethyleneoxide), MW=200,000, Polysciences

produced at different times were periodically observed with a scanning electron microscope (SEM) to ensure that all powders had a similar size distribution.⁴

Droplets produced with the as received zirconium acetate solution were approximately 0.1 μm in diameter. Since particle sizes $> 1\mu\text{m}$ were required to form polycrystalline particles, methods were sought to increase the precursor droplet size and thus particle size. Although varying the applied potential and distance to the grounded substrate influenced droplet size, manipulating the precursor rheology had a greater affect. Long-chain polymers are known to modify the Rayleigh instability phenomenon producing larger droplets from the same diameter jet.⁸ This effect was achieved by the addition of water soluble PEO to the precursor mixture. As shown in Figs. 2 and 3, additions of 0.06 wt. % PEO increased the droplet size to approximately 2 μm despite only a slight increase in the solution viscosity. At approximately 0.4 wt. % PEO, the solutions exhibited a sharp increase in viscosity and initiated fiber formation (fibers at an intermediate stage of the capillary break-up as shown in Fig. 3d) during electrostatic atomization. At PEO concentrations of 1 wt. % continuous fibers about 0.5 μm in diameter were produced (fig. 4.). A more detailed discussion of the affects of viscosity on droplet formation is presented in the Appendix.

PEO had relatively little affect on surface tension. Surface tension measurements yielded values ranging from 57.1 dyne/cm for the precursor solution without PEO to 54.3 dyne/cm with the addition of 2 wt. % PEO.

A typical solid precursor particle size distribution used for the densification experiments is shown in Fig. 3c. The rate of powder production from a single atomization device was slow, approximately 100 mg per day, but enough powder was fabricated to conduct a series of densification experiments.

Particle Pyrolysis and Characterization

By considering density changes due to pyrolysis, and determining weight loss by thermogravimetric analysis, calculations showed that when zirconium acetate spheres pyrolyzed and densified to solid ZrO_2 spheres they reduced their volume by 80% resulting in a 40% reduction in diameter. Despite this extensive shrinkage, powder compacts formed from the precursor material maintained their mechanical integrity throughout pyrolysis. At 1100°C, regardless of chemical composition, the spherical particles were composed of fine grains (Fig. 5a). Heating to higher temperatures induced grain growth within the particles, and at 1400°C most 1 to 2 μm particles became single crystal spheres for compositions containing 0 or 10 mole % Y_2O_3 , whereas particles containing 3 mole % Y_2O_3 remained polycrystalline (Figs. 5b, 5c). ZrO_2 polycrystalline aggregates of similar morphology and composition have been characterized by van de Graaf³, who showed that they reach 95% of theoretical density at 1050°C. The polycrystalline particles used in this study are fully dense at 1400°C.

Powders fabricated from solutions containing the equivalent of 0, 3, and 10 mole % yttria were characterized by x-ray diffraction (at room temperature) after heating to 1400°C for 1 h. Particles containing 0 mole % Y_2O_3 were primarily monoclinic ZrO_2 . Those containing 3 and 10 mole % Y_2O_3 were tetragonal and cubic ZrO_2 respectively.

SINTERING AND DENSIFICATION EXPERIMENTS

A. Sintering of Particle Pairs

The sintering of pairs of particles was studied by suspending acetate particles in sec-butyl alcohol, a non-solvent liquid, and allowing them to settle on a polished sapphire substrate. After pyrolysis and carbon coating, pairs of touching particles (particle size $1.7 \pm 0.3 \mu m$) of nearly identical size ($\pm 0.1 \mu m$) were located in a SEM.

They were then heated at either 1300°C or 1400°C. Their neck diameter and end to end distances were measured intermittently using enlarged SEM micrographs.

B. Particle Clusters

Many acetate spheres of identical composition were deposited in a thick layer on a polished sapphire substrate. Upon heating, the continuous layer broke into clusters of particles 50 to 100 μ m in diameter. After pyrolysis, the specimens were carbon coated and observed with the SEM. Sequential heat treatments were carried out at 1300°C for a total of 18 h and subsequently at 1400°C for an additional 88 h. Groups of particles were chosen for observation to follow changes in microstructure and to determine cluster shrinkage by measuring distances between particle centers on the cluster surface after each heat treatment. The three powder compositions, each on a different substrate, were simultaneously subjected to the above heat treatments.

C. Powder Compacts

Precursor powders were lightly dry pressed (1.5 to 3.0 MPa) in a stainless steel die to form cylindrical powder compacts (5 mm dia. x 2 mm high). SEM observations showed that the acetate spheres did not fracture during dry pressing. To achieve mechanical integrity the compacts were heated at 1°C/min to 750°C and held for 4 h to allow for complete pyrolysis, then heated at 5°C/min to 1100°C followed by cooling to room temperature at 10°C/min. The resulting compacts were typically 3 mm dia x 1 mm high with a mass of 15 to 20 mg and a relative density of 0.42 ± 0.02 .

Compacts initially heated to 1100°C were reheated at 5°C/min to increasing temperatures between 1100°C and 1400°C in increments of 25°C. After each temperature increment, the specimens were measured with a micrometer to a precision of 1 μ m. Incremental heating was continued for longer time periods at 1400°C. After 64 h at 1400°C, densities were determined by the Archimedes principle

in order to calculate the density at each previous temperature/time period using the⁷ sequentially measured compact strain. The theoretical densities of the respective compositions ($\rho_{\text{monoclinic}} = 5.85 \text{ g/cm}^3$, $\rho_{\text{tetragonal}} = 6.05 \text{ g/cm}^3$, $\rho_{\text{cubic}} = 5.92 \text{ g/cm}^3$)⁹ were used to reduce the data to relative densities.

RESULTS AND MICROSTRUCTURAL OBSERVATIONS

A. Sintering of Particle Pairs

Neck diameter (x), normalized by the initial particle diameter (a) was measured as a function of time at 1300°C and 1400°C for both polycrystalline and single crystal particle pairs (Fig. 6). Each data point is an average of 8 particle pairs. Microstructural changes of the same particle pairs were also followed as a function of time at 1300°C and 1400°C (Fig. 7). The particle pairs sintered to the substrate as well as to one another therefore their center to center approach was constrained. The extent of constraint varied for different particle pairs, but in no case was the linear shrinkage strain greater than 0.10. For comparison, calculations by Exner suggest that in the unconstrained case $x/a = 0.80$ corresponds to a linear shrinkage strain of 0.19.¹⁰

The rate of neck growth for the single crystal particles decreased more rapidly relative to the polycrystalline particles at both 1300°C and 1400°C (Fig. 6). At 1400°C, both Fig. 6 and Fig. 7 show that neck growth virtually stopped after 4 h for single crystal particle pairs, whereas neck growth between polycrystalline particles continued resulting in a nearly spherical mass of grains (Fig. 7 b,c). It can also be seen that grain growth occurred within the sintering polycrystalline particles.

Models used to characterize neck growth kinetics result in an exponential time dependence, $x/a = t^n$, where the value of the exponent, n , depends on the diffusion path¹⁰. At 1300°C, n was determined to be 0.10 and 0.15 for the single

crystal and polycrystalline particle pairs, respectively. At 1400°C, the same exponents⁸ were found for neck growth during the first 4 h. For greater time periods, the curve in the log-log plot significantly deviated from linearity. The time exponent for grain boundary diffusion ($n = 0.17$)¹⁰, a mechanism involving particle center approach, fits the neck growth data, however, only mass transport through surface diffusion ($n = 0.14$)¹⁰ appears consistent with both the experimentally determined exponents and the constraint of particle center approach.

B. Particle Clusters

Although data from distance measurements between particle (or grain) centers exhibited significant scatter, they showed that compacts composed of polycrystalline particles shrank more than compacts composed of single crystal particles.

Figures 8, 9, and 10 illustrate the sequential microstructural development of the polycrystalline (3 mole % Y_2O_3) particle clusters, and the two different single crystal (0 and 10 mole % Y_2O_3) particle clusters, respectively. Each figure shows representative microstructures after 1300 °C/10 h, 1400 °C/12 h, and 1400 °C/40 h of the same area observed on the surface of a cluster of particles deposited on a sapphire substrate. As shown in Fig. 8, continuous neck growth between touching polycrystalline particles caused the particles to lose their identity forming a continuous crystallite network much different from the original network of discrete particles. In addition, grain growth, although inhibited relative to the single crystal particles, proceeded within the particles and connective dense regions. In contrast, for both compositions that developed single crystal particles (Figs. 9 and 10), neck growth between initially touching particles slowed to a virtual stop after 18 h at 1300°C. Single crystal particle networks appear to have changed little when comparing their microstructures between heat treatments at 1300°C, 10 h and 1400°C, 12 h. In both cases the single crystal particles retained their identity and the

configuration of the original particle network changed very little. Although⁹ network shrinkage resulted in the formation of new particle-particle contacts and subsequent neck growth via sintering, changes produced by grain growth had a greater influence on microstructural development. Heating beyond 12 h at 1400 °C produced grain growth via coarsening, involving the shrinkage of smaller particles and the growth of larger particles until conditions were established such that the grain boundary swept through the smaller particle. In many cases, the disappearance of smaller grains during coarsening lead to the formation of irregularly shaped grains which subsequently spheroidized. In addition to grain growth via coarsening, grain growth via boundary motion occurred within dense regions, an occurrence more frequent in the 10 mole % Y_2O_3 composition relative to the pure ZrO_2 . Heating at 1400°C up to 88 h produced further grain growth via coarsening and boundary motion resulting in a denser appearing surface relative to that shown after 40 h at 1400°C. Individual particles and their associated particle networks became impossible to distinguish.

C. Powder Compacts

Measurements of sequential compact shrinkage produced the most reliable data.* Figure 11a shows the relative density vs. time at 1400°C for the three compositions studied. Figure 11b shows the same data for the initial constant heating rate schedule. Each point represents the average of 6 compacts for the 3 and 10 mole % Y_2O_3 compositions and the average of 3 to 5 compacts for the 0 mole %

* Continuous dilatometry experiments were conducted to determine densification behavior, however post-densification dimensional measurements showed greater axial shrinkage than radial shrinkage. This behavior was believed to be caused by the forces exerted by the spring loaded measuring rod on the small specimen diameter and the superplastic behavior of the materials examined.¹¹ Interpretation of densification behavior was thus predicated on the ambiguity of different axial and radial shrinkages, which varied from specimen to specimen. Despite this ambiguity, the data again clearly showed that the compacts formed from polycrystalline particles achieved higher densities than those formed from particles that quickly developed into single crystals.

10
Y₂O₃. For the 3 and 10 mole % Y₂O₃ compositions, the same group of compacts were followed through the entire heating, cooling, and measurement sequence. Because the 0 mole % Y₂O₃ compositions would not retain their mechanical integrity during multiple cycling through the transformation temperature, groups of compacts were fired to different temperatures and then measured after cooling. The error bars in figure 11 represent the total scatter among all compacts associated with the average value. Note that the scatter between polycrystalline and single crystal particle compacts do not overlap and that both the compositions (0 and 10 mole % Y₂O₃) that produced single crystal particles followed the same densification trajectory regardless of chemical composition. These data conclusively show that the compacts composed of particles that retained their polycrystallinity densified more than those composed of particles that developed into single crystal particles. The greatest difference in sintering rate of the single crystal and polycrystalline particles occurred during the first 4 h at 1400°C.

Powder compacts subjected to the systematic heating, cooling and measurement sequence were sectioned and polished after 64 h at 1400 °C (Fig. 12). The material produced from the polycrystalline particles was fine grained (<1µm) and consisted of dense areas containing some large residual pores (Fig. 12a). Similar to the surface observations (Fig. 8), no remnants of the original particle network were observed. In contrast, compacts formed from the single crystal particles with a composition of 10 mole % Y₂O₃ appeared to have a continuously connected network of pore channels consistent with their lower endpoint density (Fig. 12b).

DISCUSSION

The most important observation of this work is that compacts composed of polycrystalline particles achieve higher densities than those composed of single crystal particles. Since both types of powders were of similar size distribution and pack to approximately the same initial bulk density, their contrasting densification

behavior can not be directly related to differences in particle size or initial compact morphology. 11

Each powder used for this study had a different solid-solution composition given by the general formula $Zr_{(1-x)}Y_xO_{(2-x/2)}\dot{O}_{x/2}$, where 1 mole % anion vacancies (\dot{O}) are formed for every 2 mole % Y_2O_3 substituted for ZrO_2 . Since diffusional phenomena associated with sintering can depend on vacancy concentration, it might be argued that the powders exhibited different densification behavior due to their varying vacancy concentrations.¹² This does not appear to be the case since the two precursor compositions used to produce powders composed of single crystal particles (0 and 10 mole % Y_2O_3) exhibited nearly identical densification behavior. Defect chemistry thus appears to play a minor role in the ability of the polycrystalline particles to enhance densification.

The major difference in the microstructural development between single crystal and polycrystalline particles (both constrained particle pairs and unconstrained powders) is that neck growth between polycrystalline particles continues beyond the stable neck size established between single crystal particles (Figs. 8 & 9). By modelling the free energy of simple particle configurations, Kellett and Lange¹³ have shown that regardless of mass transport mechanism sintering between touching particle pairs terminates when the net free energy, combining a decrease in particle surface area with an increase in grain boundary area, is minimized. Lange and Kellett¹⁴ further showed, for mechanisms involving particle center approach, that the metastable equilibrium configuration produced after the termination of initial sintering is progressively altered by coarsening, involving the growth of larger grains and the shrinkage and disappearance of smaller grains via interparticle mass transport. As coarsening alters the metastable equilibrium configuration, the free energy balance between decreasing surface area and increasing grain boundary area is shifted such that sintering is reinitiated. They

12

concluded that coarsening is the rate controlling mass transport phenomenon associated with further densification after sintering has terminated between the initially touching particles. Microstructural observations and densification data concerning single crystal particles presented above are consistent with these concepts. That is, the termination of neck growth corresponds to a sharp decrease in the densification rate as coarsening appears to dictate microstructural change and further densification.

As shown in the microstructural observations, the initial sintering between touching polycrystalline particles never terminates. During sintering, interparticle neck growth increases the amount of grain boundary area. However, the mass transport associated with sintering does not nucleate new grains, therefore, sintering also reduces the amount of boundary area by the elimination of intraparticle grain boundaries. Like single crystal particles, the free energy of polycrystalline particles decreases as their surface area decreases during sintering. However, unlike the single crystal particles, the grain boundary area per unit volume does not necessarily increase. Whereas neck growth between single crystal particles is characterized by a free energy minimum balancing the decrease in surface area and the increase in grain boundary area, the free energy associated with neck growth between polycrystalline particles decreases monotonically due to a decrease in both surface area and net grain boundary area. For this reason, a metastable equilibrium configuration does not exist for sintered polycrystalline particles, as found for single crystal particles, and neck growth via sintering should continue beyond that of single crystal particles.

The above discussion describes the global free energy change of single and polycrystalline particles during sintering. One may also describe mass transport to the neck in terms of a local driving force. For the case of the sintering single crystal particles, a net negative surface curvature is believed to exist at the position where

the grain boundary meets the particle surface.¹⁰ Mass is thereby driven to the neck¹³ until the curvature on the particle surface becomes independent of location (e.g., spherical) and the angle formed between tangents to the spherical surface at the grain boundary junction is equal to the equilibrium dihedral angle. This defines the metastable equilibrium configuration where sintering (i.e., neck growth) between single crystal particles terminates.

For sintering polycrystalline particles, the curvature at the neck is determined by the curvatures of both the particle and the individual grains of which the particle is composed. One might expect that initial contacts between individual protruding grains of the polycrystalline particles would sinter developing a metastable equilibrium configuration on a finer scale than the single crystal particles. The extent of interparticle neck growth would therefore be determined by the localized curvature of the grains rather than the bulk curvature of the particle. However, microstructural observations showed that because the polycrystalline particles exhibit intraparticle grain growth, grains within the neck region of sintering polycrystalline particles are not able to maintain an equilibrium configuration (see Fig. 7). As intraparticle grain growth proceeds the local curvatures are perturbed, re-establishing a driving force for neck growth. In the same manner as coarsening disrupts metastable equilibrium configurations for single crystal particles, intraparticle grain growth will disrupt any possible metastable configurations developed by the sintering of individual grains between polycrystalline particles. However, in contrast to the single crystal powder in which coarsening must take place by surface diffusion or vapor transport between particles, grain growth within the polycrystalline particles occurs by the movement of material across intraparticle grain boundaries involving much shorter diffusion distances.

SUMMARY

Single crystal and polycrystalline particles of similar size distribution have been fabricated by the electrostatic atomization and pyrolysis of a metal organic precursor. Powder compacts composed of polycrystalline particles attain higher end point densities than those composed of single crystal particles. It is proposed that the decrease in grain boundary area per unit volume, e.g., by intraparticle grain growth, continues to drive neck growth in the polycrystalline particles after the single crystal particles have formed a metastable network.

ACKNOWLEDGEMENTS

This work was performed as part of the DARPA funded University Research Initiative Program at UCSB, Contract # N00014-86-K-0753. The authors acknowledge useful discussions with P.E.D Morgan of the Rockwell International Science Center and Professor Paul Smith at UCSB.

REFERENCES

1. F.F. Lange, "Influence of Particle Arrangement on Sintering: A Thermodynamic Viewpoint", *Journal de Physique Colloque C1 47* [2] 205-217 (1986).
2. L.H. Edelson, A.M. Glaeser, "Role of Particle Substructure in the Sintering of Monosized Titania", *J. Am. Ceram. Soc.* 71 [4] 225-35 (1988).
3. M.A.C.G. van de Graaf, A.J. Burggraaf, "Wet-Chemical Preparation of Zirconia Powders: Their Microstructure and Behavior", in *Advances in Ceramics vol. 12, Science and Technology of Zirconia II* 744-65 (1984).
4. F.F. Lange, "Transformation Toughened ZrO₂: Correlations Between Grain Size Control and Composition in the System ZrO₂-Y₂O₃", *J. Am. Ceram. Soc.* 69 [3] 240-242 (1986).
5. Private Communication, Darryl Reneker, Polymers Division, NIST.

6. M. Khavari, I. Nettleship, F.F. Lange, UCSB, unpublished work.
7. G.I. Taylor, "Disintegration of Water Drops in an Electric Field", Proc. Roy. Soc. London 280A 383-397 (1964).
8. M. Goldin, J. Yerushalmi, R. Pfeffer, R. Shinnar, "Breakup of a Laminar Capillary Jet of a Viscoelastic Fluid", J. Fluid Mech. 38 [4] 689-711 (1969).
9. M. Yoshimura, "Phase stability of Zirconia", Am. Ceram. Soc. Bull., 67 [12] 1950-1955 (1988)
10. H.E. Exner, "Principles of Single Phase Sintering", Rev. Powd. Met. Phys. Ceram. 1 [1-4] 1-251 (1979).
11. B. J. Kellett, F. F. Lange, "Hot Forging Characteristics of Fine-Grained ZrO_2 and Al_2O_3/ZrO_2 Ceramics", J. Am. Ceram. Soc. 69 [8] C172-3 (1986).
12. S.X. Wu, R.J. Brook, "Kinetics of Densification in Stabilized Zirconia", Solid State Ionics 14 123-130 (1984).
13. B. J. Kellett and F. F. Lange, "Thermodynamics of Densification: I, Sintering of Simple Particle Arrays, Equilibrium Configurations, Pore Stability, and Shrinkage," J. Am Ceram. Soc. 72 [5] 725-34 (1989).
14. F. F. Lange and B. J. Kellett, "Thermodynamics of Densification: II, Grain Growth in Porous Compacts and Relation to Densification," J. Am Ceram. Soc. 72 [5] 735-41 (1989).
15. E.F. Goedde, M.C. Yuen, "Experiments on Liquid Jet Instability", J. Fluid Mech. 40 [3] 495-511 (1970).
16. C.J.S. Petrie, Elongational Flows: Aspects of the Behaviour of Model Elasticoviscous Fluids, Pitman, London (1979).
17. W.W. Graessley, "The Entanglement Concept in Polymer Rheology", Adv. Polymer Sci. 16 (1974).
18. G.K. Batchelor, "The Stress Generated in a Non-Dilute Suspension on Elongated Particles by Pure Strain Motion", J. Fluid Mech. 46 [4] 813-829 (1971).

19. J. Mewis, A.B. Metzner, "The Rheological Properties of Suspensions of Fibers in ¹⁶Newtonian Fluids Subjected to Extensional Deformation", J. Fluid Mech. 62 [3] 593-600 (1974).

20. P. Schümmer, K.H. Tebel, "Design and Operation of the Free Jet Elongational Rheometer", Rheol. Acta 21 514-516 (1982).

APPENDIX: Influence of PEO on Particle Fabrication

Small additions (< 0.06 wt. %) of PEO were found to dramatically alter the droplet size (and thus particle size), but these same additions did not significantly affect either the viscosity or surface tension. A significant change in viscosity was only observed with PEO additions (> 0.4 wt. %) sufficient to form fibers along with the droplets. At first these observations appear inconsistent with the classical understanding of Rayleigh instability which implies that an increase in viscosity is required to increase the droplet size¹⁵. Measurements indicating little or no increase in viscosity with small PEO additions were made with a capillary viscometer, a device that measures the viscosity of a liquid in a shearing flow. It is recognized however, that dilute solutions of long chain polymers (i.e. PEO) exhibit large elongational viscosities, that is, in elongational flow (e.g. as found in fiber spinning), a solution's viscosity will increase sharply as a function of the strain rate¹⁶. The liquid jet produced at the cone tip is charged and will therefore experience an acceleration due to the potential gradient between the cone tip and the grounded substrate. The acceleration will create a velocity gradient parallel to the flow of the jet thereby generating an elongational flow.

In their static configuration, linear polymer chains form random coils in solution.¹⁷ When a liquid is sheared, a velocity gradient transverse to the direction of flow is established; therefore, shear flow (e.g. as in a capillary viscometer) has a rotational component which causes the molecules to tumble through solution

without substantial chain uncoiling or alignment¹⁶. In pure elongational flow (no rotational component) polymer chains uncoil and align themselves with the velocity gradient, thereby increasing the fluid's resistance to deformation or apparent viscosity* much like rigid fibers increase the modulus of a compliant solid in a composite material.^{18,19} Therefore viscosity measurements of a dilute polymer solution in a capillary viscometer cannot provide information about the fluid's apparent viscosity in elongational flow, and thus the affect of elongational flow on Rayleigh instability. Pure elongational flows that allow the measurement of steady state rheological properties of dilute polymer solutions are difficult to generate and is a topic of current research in the field of rheology.²⁰ Such measurements are beyond the scope of our research interests.

The observed increase in viscosity at approximately 0.4 wt. % PEO corresponds to the critical concentration, c^* , at which the polymer forms an interconnected network of chains in solution.¹⁷ In addition to the effects of chain orientation, there are additional effects associated with chain interaction as they try to uncoil and orient with the elongational flow. The observation of fibers along with particles and finally stable fibers with increasing PEO concentration implies that the elongational viscosity is sufficiently large to kinetically stabilize the jet against break-up due to Rayleigh instability.

Figure Captions

Figure 1: Schematic of electrostatic atomization device. Exit diameter of capillary tube is 1.5 mm.

Figure 2: Precursor particle size and viscosity as a function of wt. % PEO (relative to solution weight).

* nomenclature used in the fluid mechanics literature

Figure 3: Influence of PEO on precursor particle size: a) 0 wt. %, b) 0.02 wt. %, c) 0.06 wt. %, d) 0.40 wt. %.

Figure 4: Fibers of precursor material produced with 1 wt. % PEO.

Figure 5: Intraparticle morphological development of ZrO_2 particles: a) 1100°C, independent of chemical composition, b) 1400°C, $ZrO_2-0Y_2O_3$ and $ZrO_2-10Y_2O_3$, c) 1400°C, $ZrO_2-3Y_2O_3$.

Figure 6: Neck growth with time, normalized by initial particle size, for particle pairs at: a) 1300°C, b) 1400°C.

Figure 7: Pairs of particles sintered on a sapphire substrate at 1400°C for: a) 0.3 h, b) 4 h, c) 12 h. Necks between single crystal particles reach a steady state size while neck growth between polycrystalline particles continues, resulting in a spheroidizing mass of crystallites.

Figure 8: Microstructural development of polycrystalline particles ($ZrO_2-3Y_2O_3$): after heating at 1400°C for 12 h the particles lose their individuality, becoming a mass of fine crystallites.

Figure 9: Microstructural development of single crystal particles ($ZrO_2-0Y_2O_3$): after initial neck formation, microstructural changes occur slowly, coincident with coarsening of the particle network.

Figure 10: Microstructural development of single crystal particles ($ZrO_2-10Y_2O_3$): microstructural changes occur by similar processes as the $ZrO_2-0Y_2O_3$ particles but at an accelerated rate due to extensive grain coarsening.

Figure 11: a) Densification of ZrO_2 powder compacts, the first hour on the time axis represents the constant heating rate portion of the experiment. b) relative density v. temperature for constant heating rate densification at 5°C/min. to 1400°C.

Figure 12: Microstructure of ZrO_2 powder compacts (1400°C, 64 h): a) polycrystalline zirconia ($ZrO_2-3Y_2O_3$) compact consisting of a fine grain matrix with some residual

porosity. b) single crystal ZrO_2 powder compact ($ZrO_2-10Y_2O_3$) with interconnecting
pore channels.

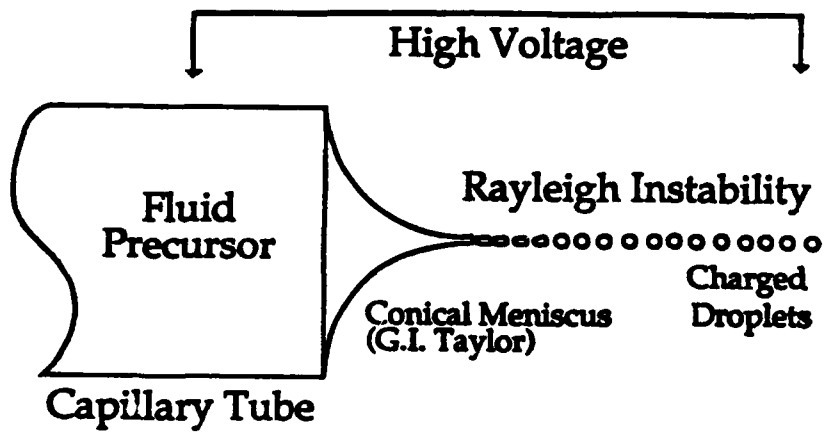


Fig. 1

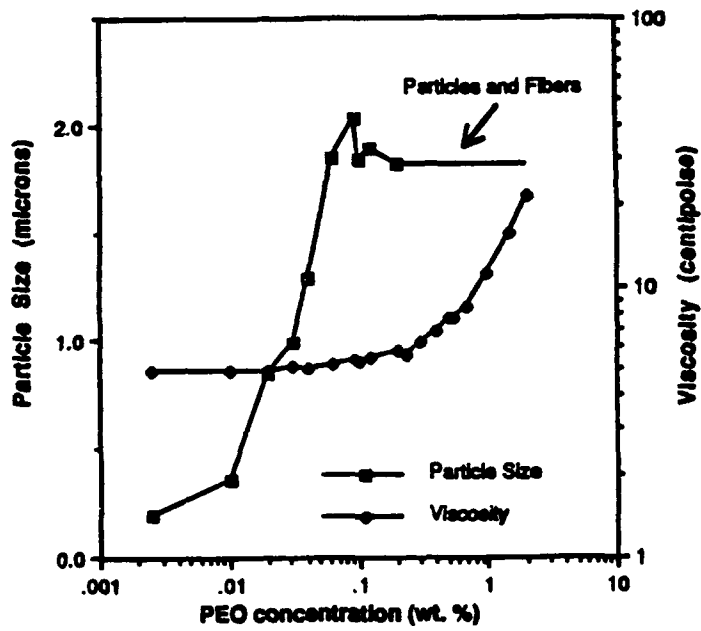
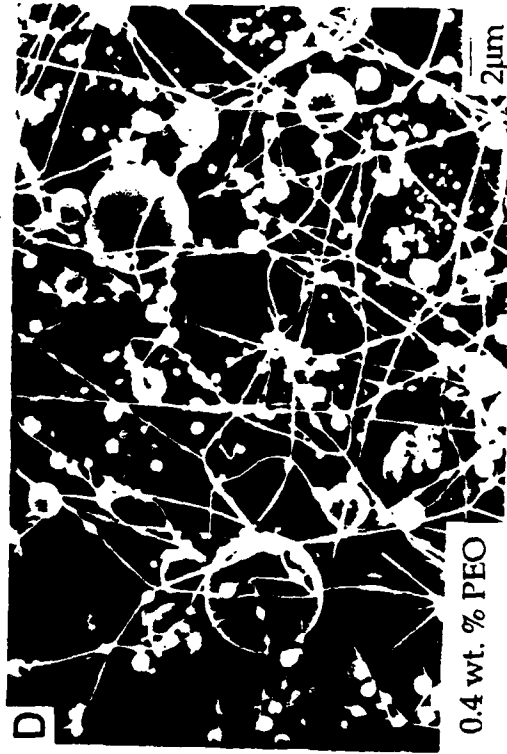
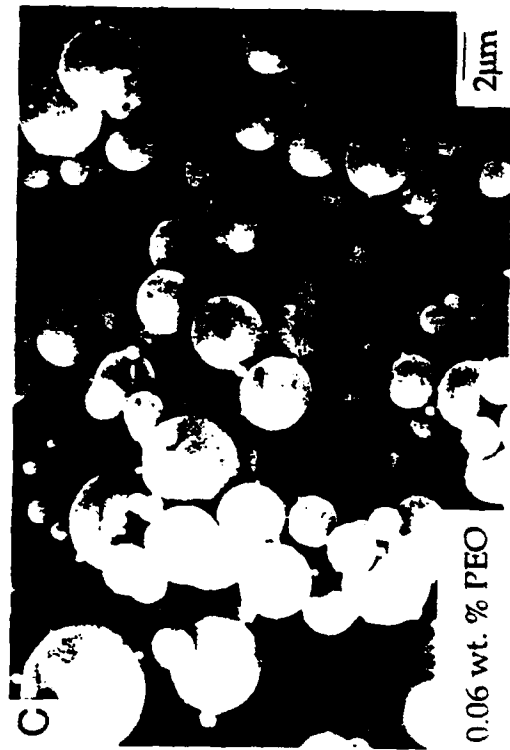
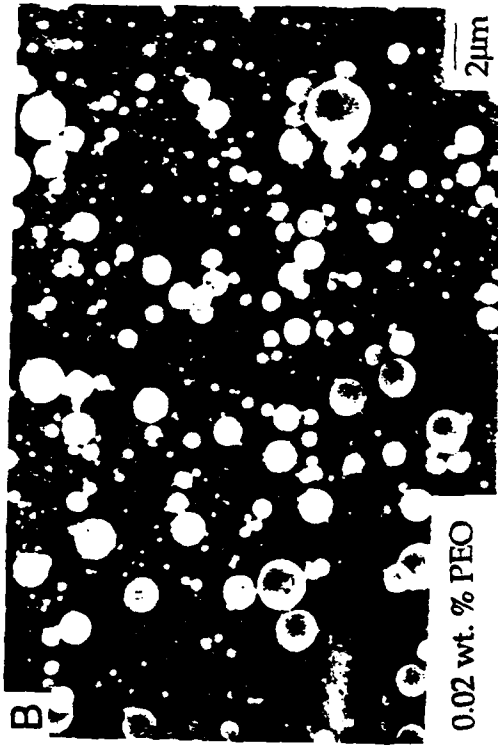
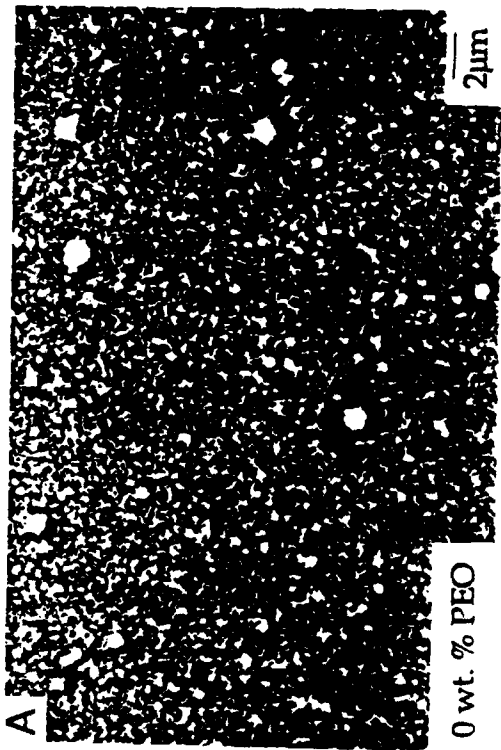
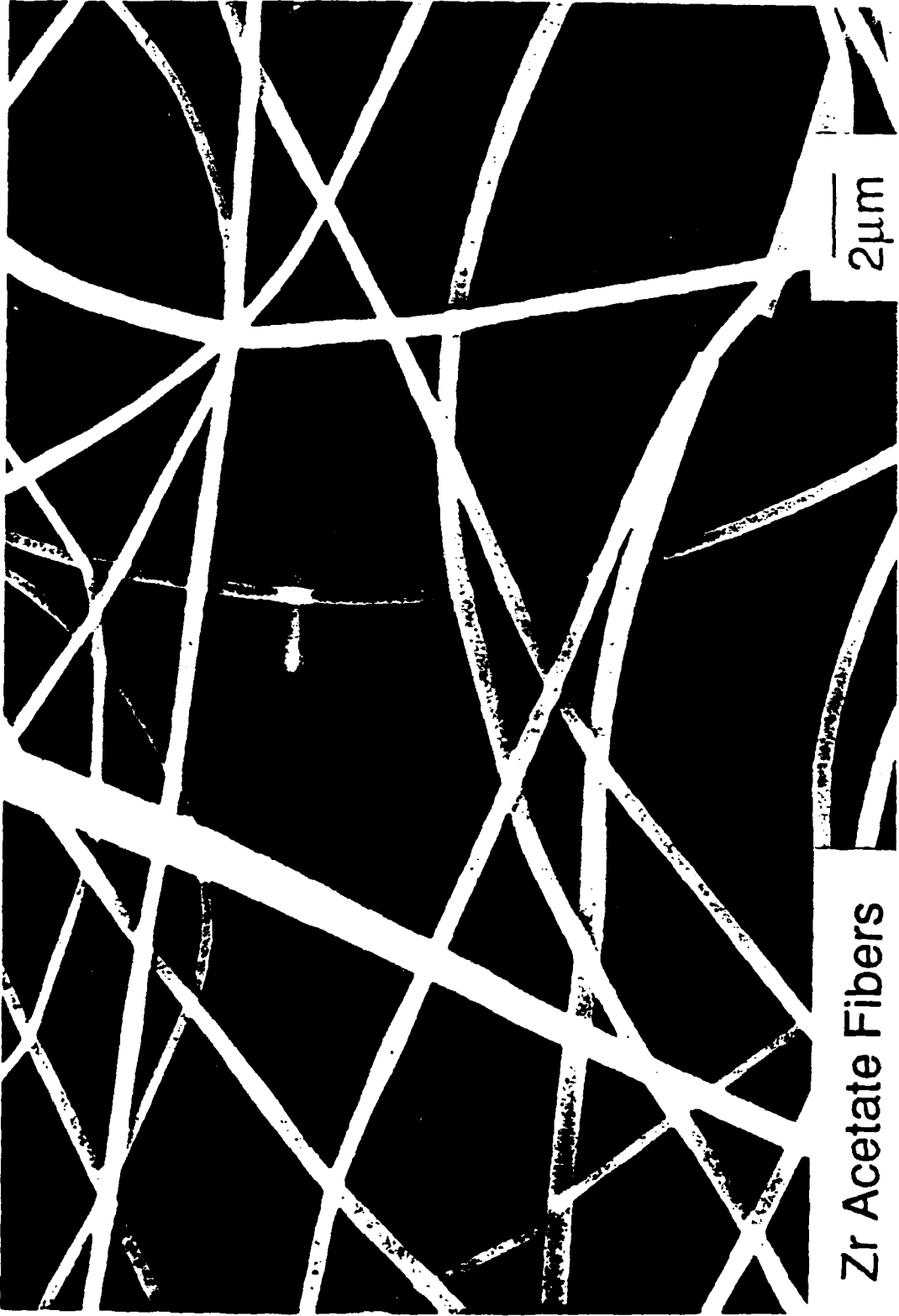


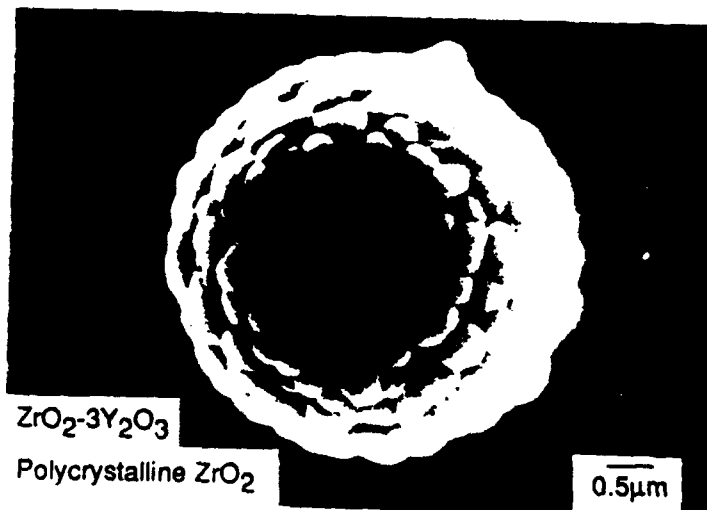
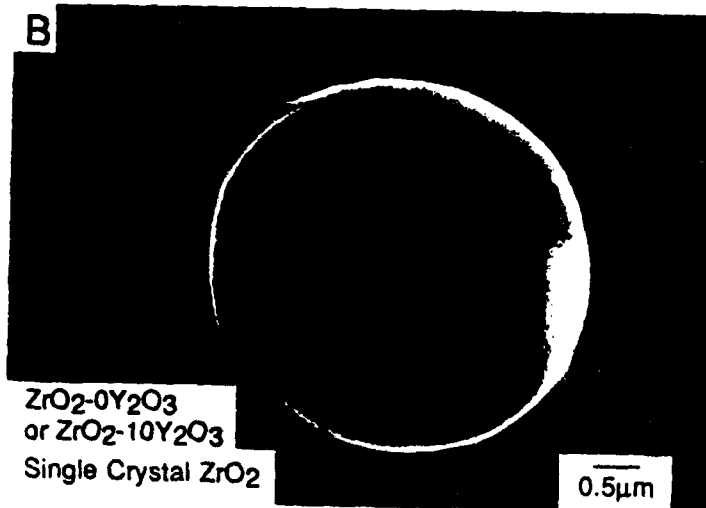
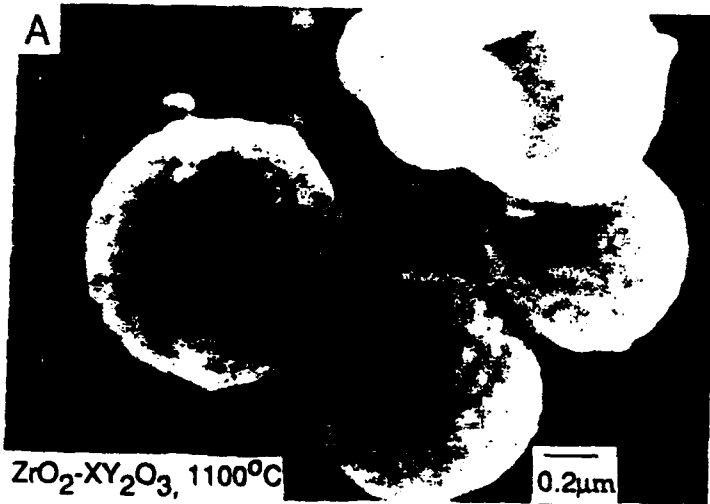
Fig. 2





Zr Acetate Fibers

2µm



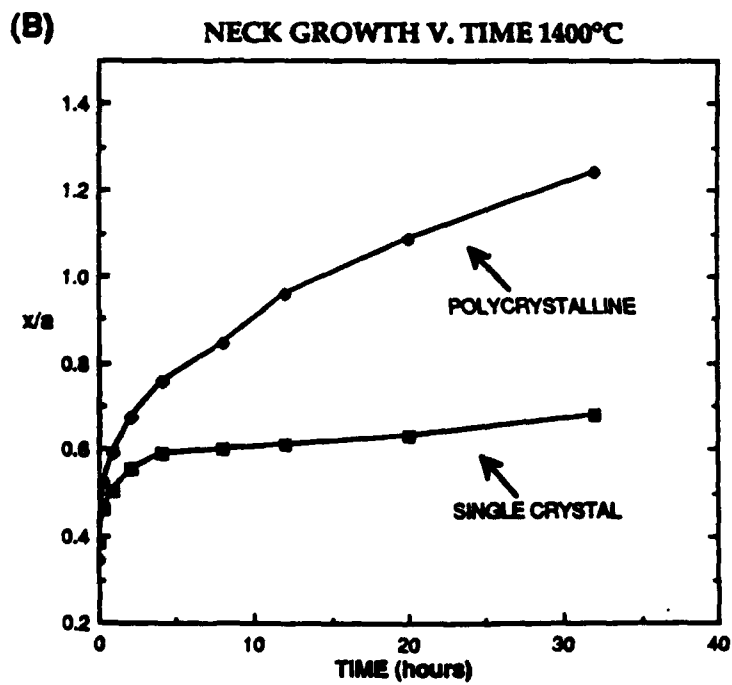
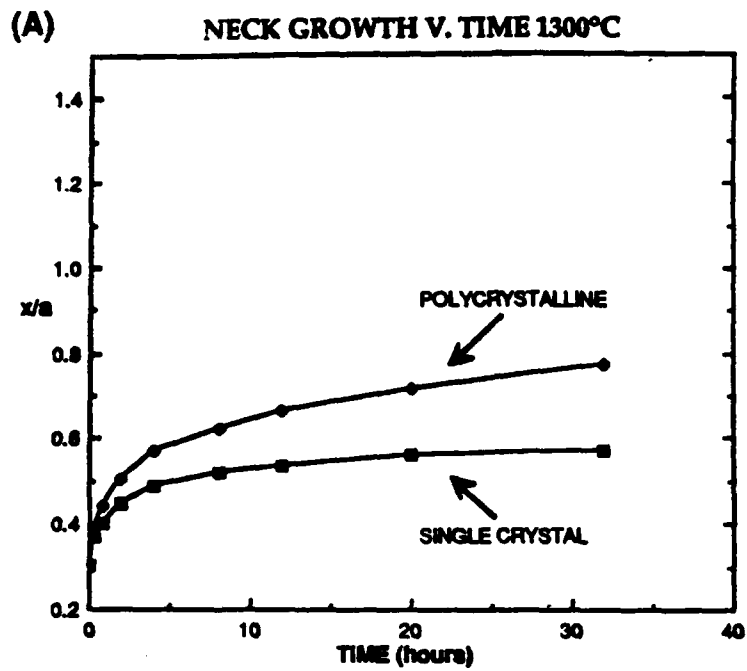
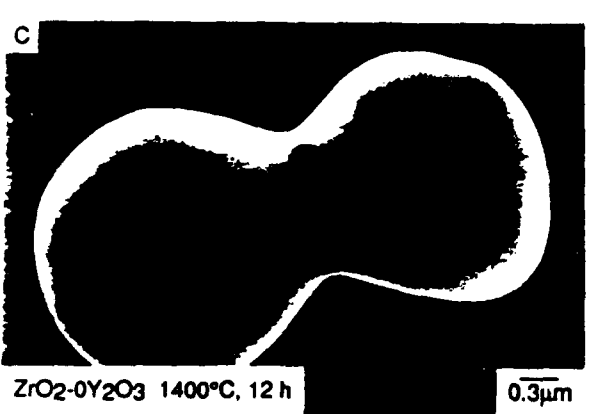
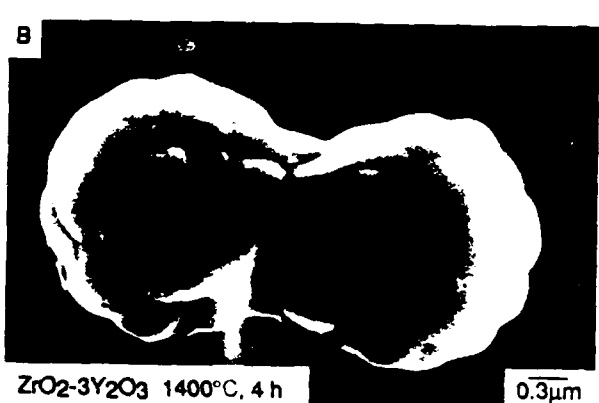
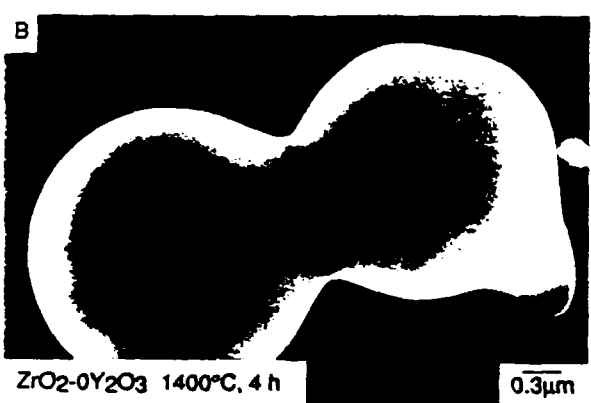
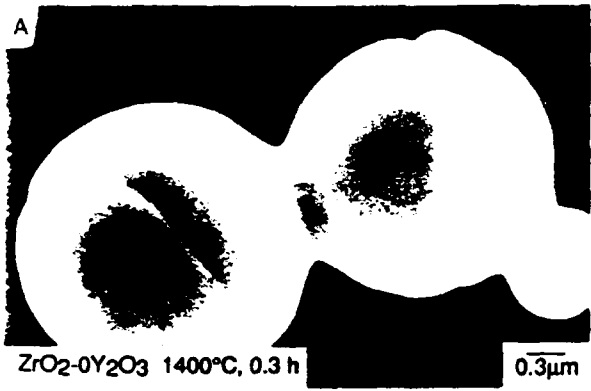
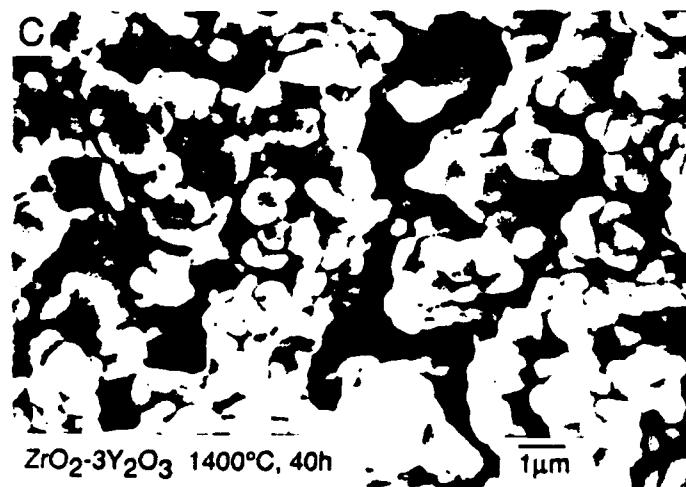
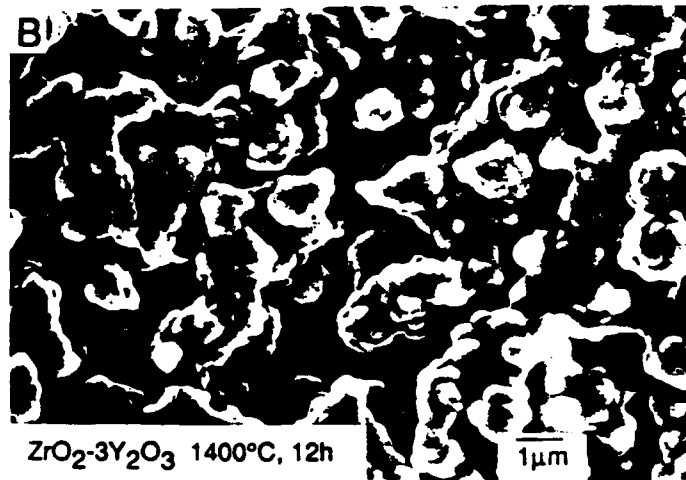
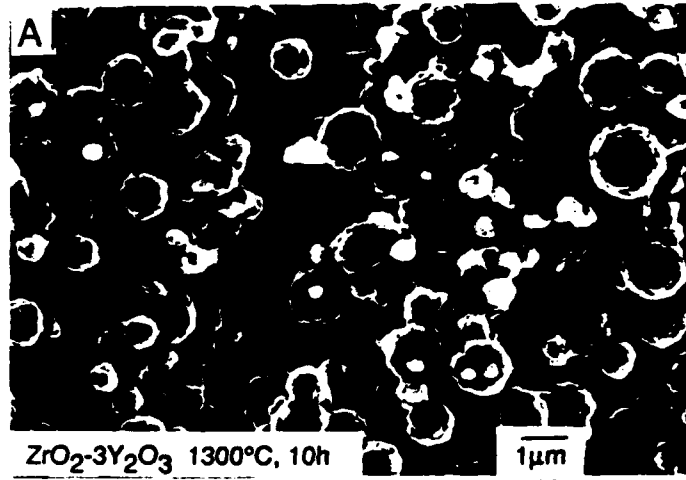
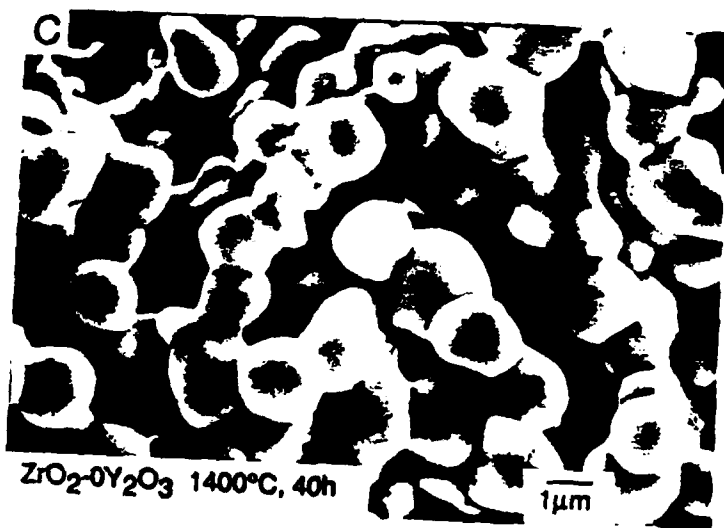
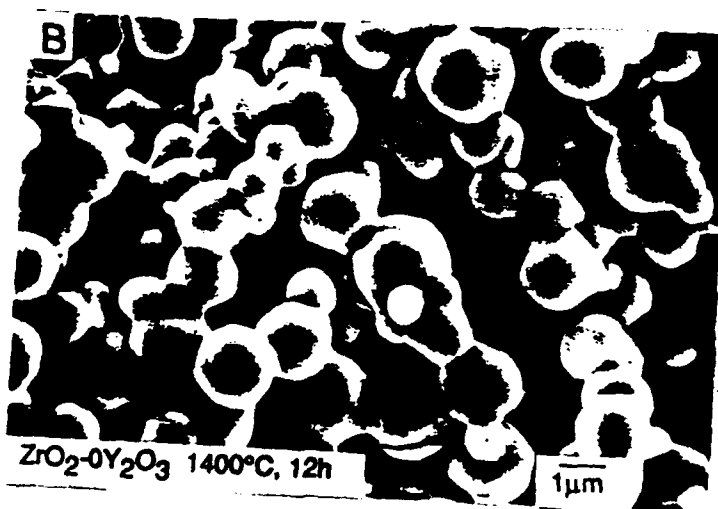
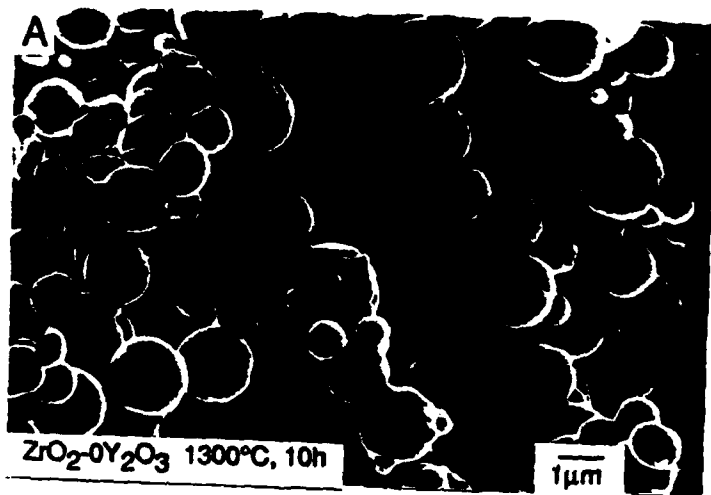
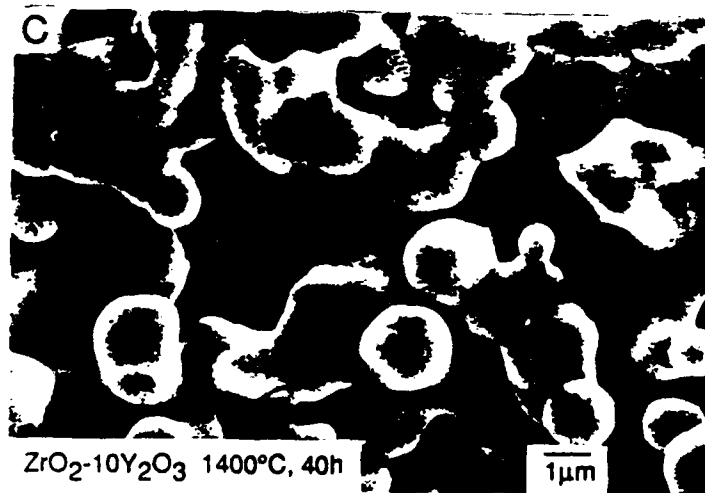
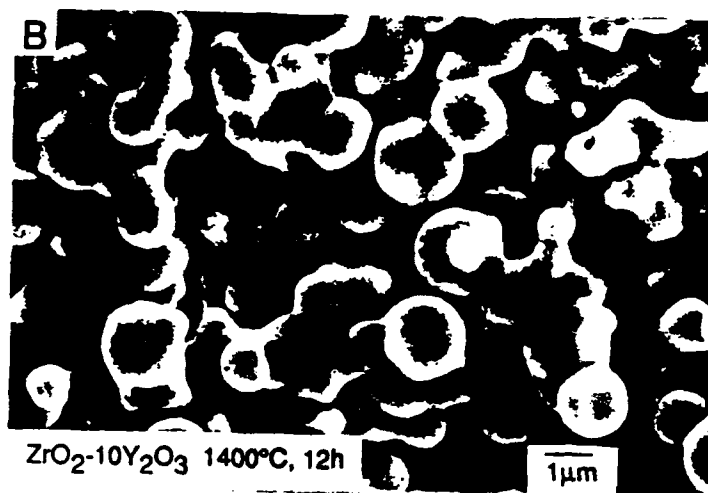
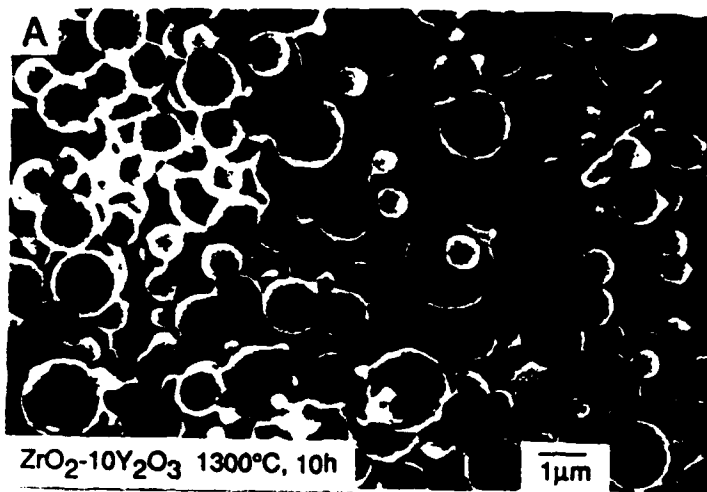


Fig. 6

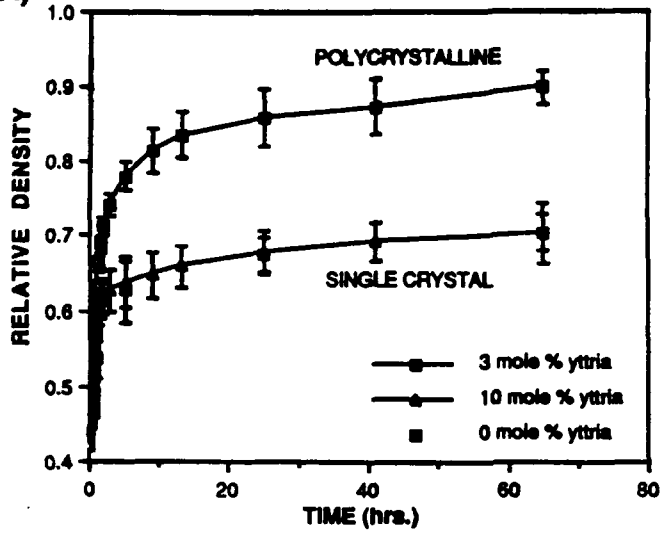








(A) DENSIFICATION OF ZIRCONIA POWDER



(B) CONSTANT HEATING RATE TO 1400°C

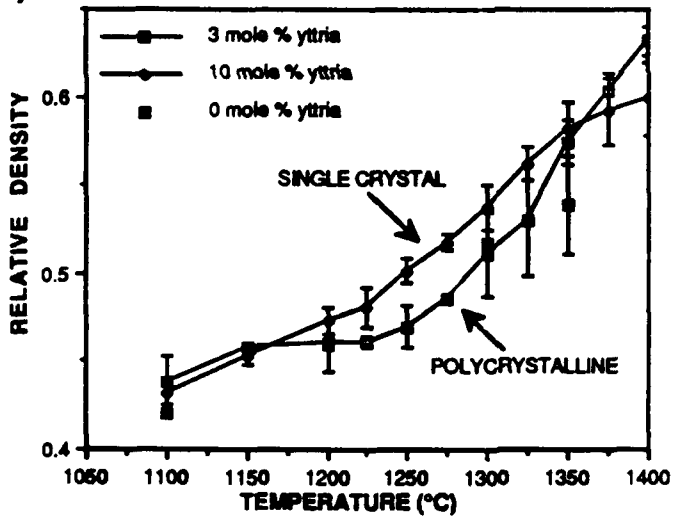
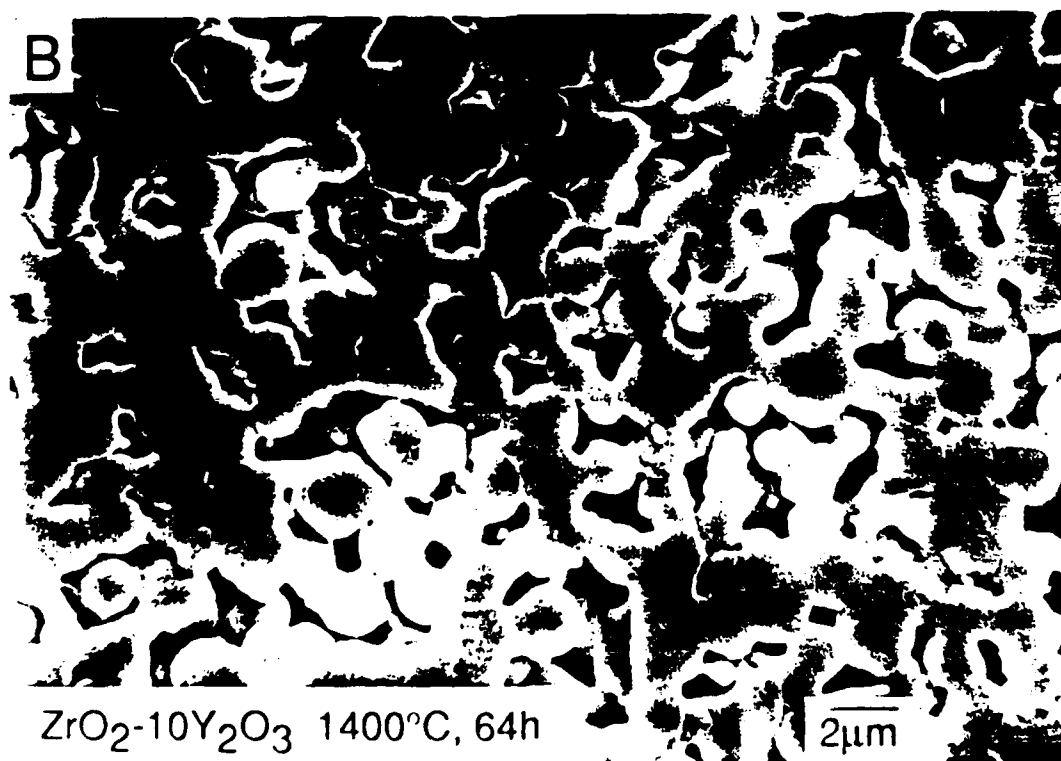
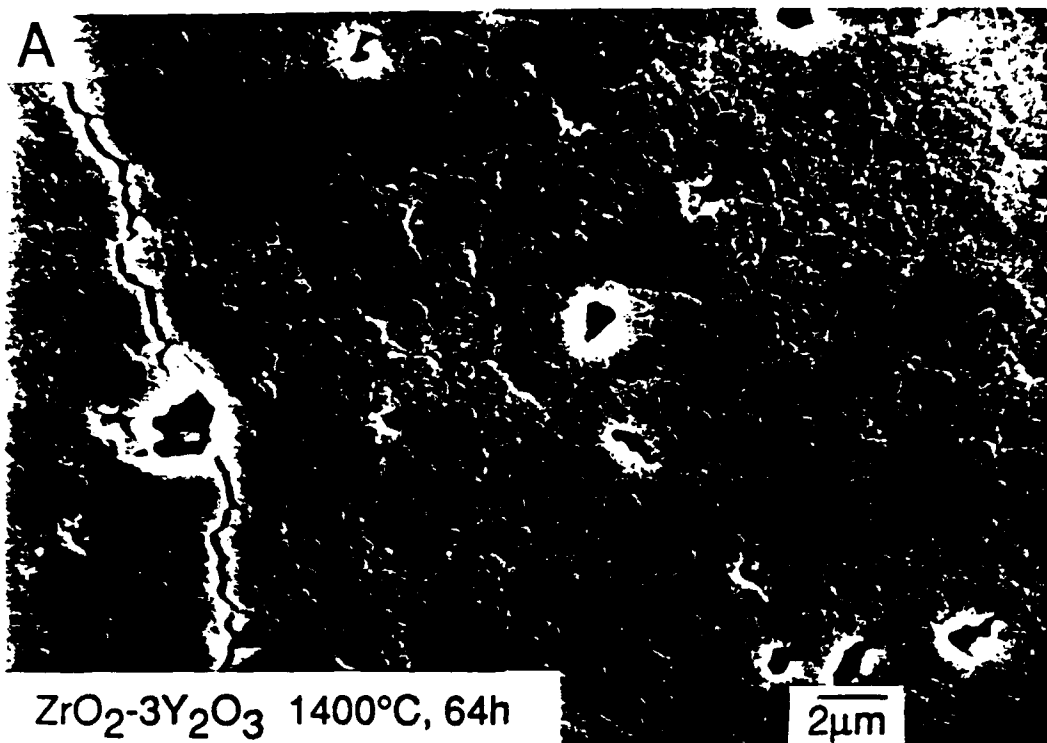
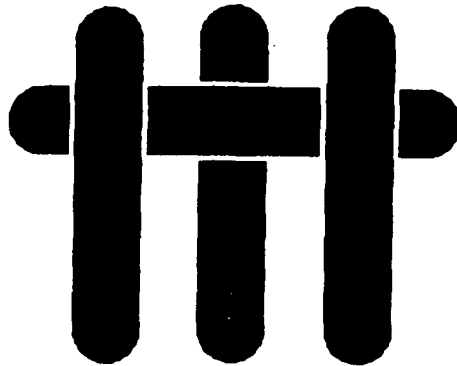


Fig. 11



M A T E R I A L S



Powder Processing and Densification of Ceramic Composites

Fred F. Lange, David C. C. Lam, and Olivier Sudre

**Materials Department
College of Engineering
University of California, Santa Barbara
Santa Barbara, CA 93106**

Presented at:

**Materials Research Society Meeting
San Diego, April, 1989**

POWDER PROCESSING AND DENSIFICATION OF CERAMIC COMPOSITES

FRED F. LANGE, DAVID C. C. LAM AND OLIVIER SUDRE

Materials Department, College of Engineering, University of California, Santa Barbara, Santa Barbara, CA 93106

ABSTRACT

Two issues, packing powder/reinforcement systems and constrained densification, are reviewed. It is shown that pressure filtration has the greatest potential for packing powders containing reinforcements and packing powders within reinforcement preforms. High particle packing is achieved with repulsive interparticle potentials, and for a very small particle to reinforcement diameter ratio. It is now clear that individual reinforcements do not constrain the densification of powders. Shrinkage constraint is caused by a network of either non-touching or touching reinforcements. Network shrinkage (and thus composite shrinkage) caused by powder densification leads to the development of a denser interconnected matrix material surrounding lower density regions. Densification of the lower density regions requires the creep deformation of the denser continuum. As detailed elsewhere in this proceedings, grain growth causes this denser continuum to become more resistant to creep and coarsening within the lower density regions causes desintering and the dissipation of sintering 'stresses'. These phenomena do not occur during the densification of glass powders and explains the different densification behavior of crystalline powder matrices relative to glass powder matrices.

INTRODUCTION

Reinforcements are incorporated into ceramics in an attempt to increase the fracture toughness of the ceramic matrix, impart R-Curve behavior (toughness increases as the crack grows) and to produce a material which can gracefully fail at high strains. To realize these properties, the reinforcements must act as bridges behind an extending crack. The extending crack must somehow by-pass the reinforcement and the bridging reinforcement must somehow dissipate work as it acts as a bridge. Analytical fracture models are relatively well developed, but processing methods to make useful composites are lacking.

Non-powder processing methods for making ceramic matrix composites, based on forming ceramic matrixes via infiltration into reinforcement preforms, has been reviewed by Jamet et al. ¹ and Naslain ². They include cyclic chemical vapor infiltration/deposition, cyclic sol-gel infiltration/heat treatment, and cyclic organometallic infiltration/pyrolysis. Molten metals are also infiltrated into partially sintered powder compacts. ³ In addition, several different ceramic matrixes can be 'grown' within fiber preforms via an environmental reaction method (e.g., the oxidation of certain aluminium alloys ⁴) under development by the Lanxide Corporation. These methods can be synergistically used with powder methods.

Powder processing of composites involves three critical issues: 1) incorporating and consolidating powder-reinforcement systems, 2) making the powder matrix strong, and 3) controlling the matrix/reinforcement interface toughness and frictional characteristics. This review will focus on the first two of these issues.

PACKING PARTICLES AND REINFORCEMENTS

Powder Packing

Particle morphology, interparticle forces and particle size distribution are the major factors controlling the density to which mass can be consolidated in the form of powders.

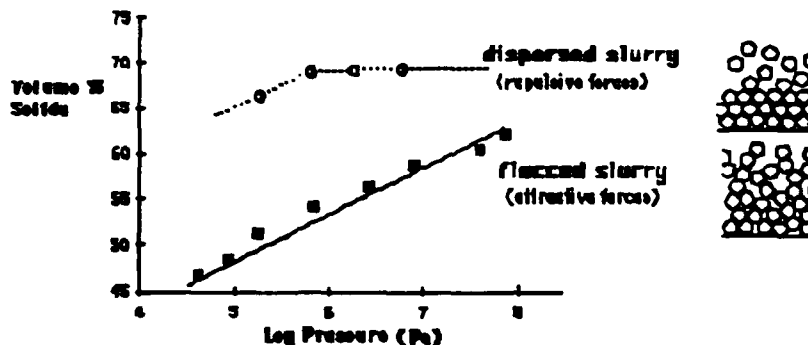


Figure 1 Packing density of Al_2O_3 powder compacts produced by pressure filtration. Graph and schematic show that repulsive interparticle forces allow particles to pack as individuals to produce high packing density which is relatively insensitive to applied pressure.

Interparticle forces have the greatest effect on particle packing. The effect of interparticle forces is best illustrated when powder is packed from the slurry state, e.g., by pressure filtration, where the interparticle forces are controlled by surface-chemical methods (charge site density through pH control, polyelectrolytes, etc.). Figure 1 illustrates the particle packing density of aqueous dispersed (pH = 2) and flocced (pH = 8) slurries of Al_2O_3 powder as a function of filtration pressure. As shown in the schematic, the repulsive interparticle forces within the dispersed slurry allows the particles to flow and pack as individuals, find their lowest free energy position as they are added to the consolidation layer, and produce a very high, pressure insensitive, packing density. The packing density produced from flocced slurries is much lower and pressure sensitive. For this case, the attractive interparticle forces produce a connective network within the slurry before they are packed. This network itself must be consolidated to form the consolidated layer by particle rearrangement. Particle rearrangement also continues within the consolidation layer. Dry powders behave much like the flocced slurry, i.e., the packing density is very pressure sensitive and they pack to a lower density relative to dispersed slurries. Thus, roundish, dispersed particles which are packed, e.g., by pressure filtration, are required to achieve high packing densities.

Packing of Mixed Powder/Whisker (Chopped Fiber) Systems

As shown in Fig. 2 mixed powder/whisker (or chopped fiber) systems can be consolidated by pressure filtration.

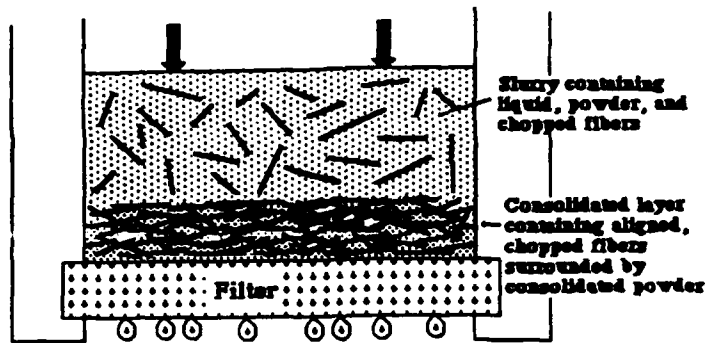


Figure 2 Pressure filtration of mixed whisker (or chopped fiber)-powder system.

The question of how whiskers influence the packing of powders and vice versa has been addressed with recent experiments⁵ where several different manufactured SiC whiskers and chopped carbon fibers (whisker and fiber aspect ratios between 10 and 20). The reinforcements were mixed with either alumina or silicon powder to form 5 different composite systems where the particle to whisker diameter ratio (R) was different for each system (between 0.02 and 4). Both powders packed to a relative density of 0.60 without reinforcements. Within each composite system, different mixtures were prepared with different volume fractions of reinforcements. After consolidation, one measures the bulk density of the composite and then calculates the packing density of both the powder and the reinforcement. Figure 3 illustrates the relative packing density of matrix powder (either alumina or silicon) as a function of the particle to fiber diameter ratio consolidated by pressure filtration at 58 MPa. Each curve represents results for a given volume fraction of reinforcement (based on solid volume). As shown, reinforcements can significantly reduce the powder packing density. Not shown in Fig. 3 is that the powder reduced the packing density of the reinforcement network. The greater R , the lower the packing density of both the powder and the reinforcement.

The reasons for the decrease in packing density of both the powder matrix and whisker network with increasing particle/whisker diameter ratio might be visualized in Fig. 4. With regard to powder packing, the whisker network defines irregular polyhedra into which powder must be packed. For a given whisker aspect ratio and packing density, the volume of the average polyhedron is proportional to the fiber diameter. When the particle volume is much smaller ($R \rightarrow 0$), the particles might be expected to pack to the same density as if the reinforcement was not present. When the volume of any given polyhedron is smaller than the particle volume ($R > 1$), the particle must be excluded. Between these two limits, the particle packing density should exhibit fractal behavior (the measured volume of a polyhedron should decrease with the increasing size of the particle used to measure volume), i.e., their packing density should decrease.

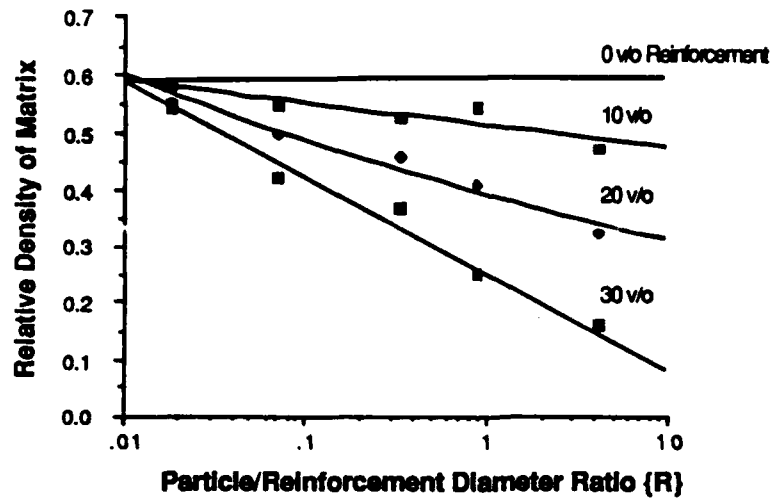


Figure 3 The packing density of the powder matrix in mixed, dispersed powder/reinforcement systems significantly decreases with increasing particle to reinforcement diameter ratio.

With regard to the packing density of the whisker network, it might be recognized that only four whiskers can be brought together to touch at a nodal point. Whisker packing density is proportional to the density of nodal points. The void volume at each nodal point is proportional to the whisker diameter. Particles larger than the nodal point volume will cause the whiskers to separate and thus decrease their packing efficiency. With this concept, it can be seen that the highest packing density for both the powder and the whisker network is achieved when $R \rightarrow 0$. The data in Fig. 3 suggests that R should be < 0.02 .

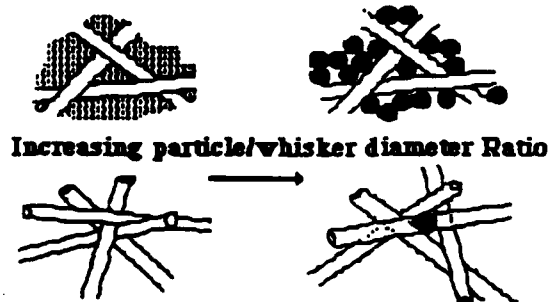


Figure 4 Particle packing within a whisker network should be greatest when the particles are much smaller ($R \rightarrow 0$) than the size of voids defined by the network. Particles that expand the nodal points of four touching whiskers will lower the packing density of the whisker network.

Packing Powders Within Reinforcement Preforms

Three dimensional preforms can be produced by either felting or weaving continuous fibers or matting chopped fibers. The problem of packing powders within preforms was solved by Jamet et al. ⁶ by pressure filtration. Our adaptation is shown in Fig. 5a. In this process the consolidated layer builds up within the preform which is fixed to the filter. The preform is not subjected to differential stresses if filled with a liquid or slurry prior to filtration; it is only subjected to the hydrostatic pressure exerted by the slurry. Our studies ⁷ show that powders can be packed within the preform provided that three conditions are satisfied. First, the

particles must be small enough to flow through the preform channels and smaller yet ($R < 0.05$) to achieve high packing densities. Second, the particles in the slurry must repel one another (flocced slurries clog the channels). And, third, repulsive surface forces must exist between the preform material and the particles. These last two requirements can more than double the colloidal requirements for processing.

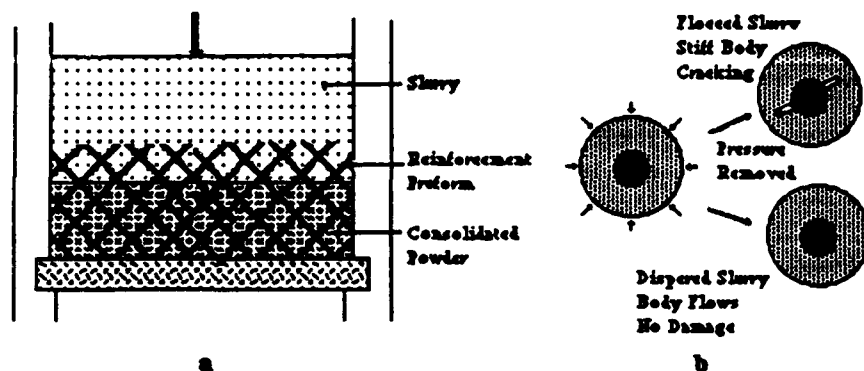


Figure 5 Powder can be packed within reinforcement preforms by pressure filtration (a). When the pressure is removed, the reinforcement material can recover either more or less strain than the powder compact. Differential strain can induce damage (b) in the powder compact unless stresses are dissipated by body flow.

High pressures are desirable because of the parabolic rate kinetics of pressure filtration and the low permeability of highly packed, sub-micron powders. During filtration, both the reinforcement material and surrounding powder are compressed. Both relieve their stored strain when the pressure is removed. Since both have different strain recoveries, stresses can arise due to differential strain recovery. Bodies formed from flocced slurries are stiff after consolidation; stresses produced by differential strain recovery can damage these bodies as shown in Fig. 5b. Bodies formed from dispersed slurries, on the other hand, still flow after consolidation and appear to dissipate stresses arising from differential strain recovery.⁷ Studies have also shown that the strain recovery is time dependent⁸. Thus, the rheology of the consolidated body must be understood and controlled to avoid damage induced by the reinforcement during processing.

STRENGTHENING THE POWDER MATRIX

After packing powders into the desired shape, powder compacts are conventionally strengthened by a heat treatment that allows mass transport to first form necks between touching particles via sintering and then eliminate the void phase. That is, conventional strengthening produces densification and thus, shrinkage.

It is now widely recognized that the densification behavior of a crystalline powder can be dramatically influenced by an inert, second phase. The phenomena associated with this effect limits the pressureless processing of many composite systems and causes the composite processor to resort to deformation processing, viz. hot-pressing and HIPing. Deformation processing certainly must be avoided if composites are to be engineered with reinforcements architecturally situated along principal stress trajectories.

De Jonghe and coworkers ⁹ were the first to systematically characterize constrained densification. They demonstrate that a very small volume fraction (0.03) of an inert (non-densifying) inclusion phase would significantly limit the densification behavior of a composite powder compact. Their isothermal data for ZnO powder compacts containing SiC inclusions show that the densification rate at any time decreases with increasing volume fraction of the SiC phase. Bordia and Raj ¹⁰ have reported similar data for TiO₂ powder compacts containing Al₂O₃ inclusions. Brook et al. ¹¹, reporting similar data for Al₂O₃ powder containing dense Al₂O₃ inclusions, indicate that the inclusion phase also produces a less than theoretical end-point density. None of these observations are predicted by a model developed by Onoda and Messing ¹² which suggested that inclusions would not affect densification until they were about to form a connective network at larger volume fractions.

Models to explain the densification behavior of mixed powder-reinforcement systems are based on the fact that the densifying powder shrinks and must place the inert particles in a state of compression. Hsueh, Evans, and McMeeking ¹³ argue that if the inert particles are placed in compression, the powder itself must be in a state of mean hydrostatic tension. Raj and Bordia ¹⁴ had previously reached identical conclusions by modeling the composite system with a spherical inert inclusion surrounded by a concentric spherical shell of powder. Both groups suggested that the mean hydrostatic tensile stress within the powder would be relaxed by creep within the densifying powder. Both explain the lower densification rate of the composite by superimposing the hydrostatic tensile stress on the compressive sintering 'stress' commonly used to represent the driving potential for powder densification. Although these models are mathematically appealing, Scherer ¹⁵ has pointed out that the parameters needed to fit data are unreasonable with respect to the mechanics of the problem and also indicated that the mean hydrostatic stress that might develop within the powder is much smaller than required by the models. In addition, neither model predicts the densification behavior at higher inclusion fractions (either closely spaced or touching), nor do they predict an end point density less than theoretical.

In recent experiments, Lange ¹⁶ slip cast alumina powder rings around dense alumina discs. These specimens are a two dimensional analog of that modeled by Raj and Bordia with an equivalent inclusion volume fraction of 0.35. After slow drying, they were heated with controlled heating rates to 1550 °C. Most specimens developed hair-line, radial cracks that would span the ring. These cracks developed either during drying (differential shrinkage < 1 %) or, if not present after drying, during heating to 800 °C (densification shrinkage = 0.3 %). This catastrophic cracking phenomena, which appeared to initiate from agglomerates, occurred when the ring was weakest, i.e., when the critical stress intensity factor of the consolidated powder was small. Upon heating to 1550 °C, the hair-line cracks underwent a large crack opening displacement consistent with the shrinkage produced during densification. Constrained ring specimens that did not develop hair-line cracks (about 20 %, i.e. those that survived the 800 °C treatment) could be heated without macrocracking at any heating rate to achieve the same relative density at 1550 °C as unconstrained rings subjected to an identical heating schedule. This observation strongly suggested that a single inclusion would not alter the densification behavior of a surrounding compact provided catastrophic fracture was avoided prior to and during the formation of sintering necks between particles. This conclusion suggests that the mean hydrostatic stress, thought to decrease the driving potential for

densification in previous models, plays little role in constrained densification of single inclusions.

Experiments ¹⁷ with alumina powders containing high volume fractions of silicon carbide whiskers showed that the powder within the whisker network did shrink and densify onto the whisker network but the whisker network itself did not shrink. That is, the relatively rigid whisker network constrains composite shrinkage, but does not prevent the powder within the network from shrinking. Namely, as voids within portions of the densifying powder disappear their volume is conserved by the opening displacement of other voids (e.g., incipient crack-like voids) created within the powder during packing and/or initial heating when the powder is weak. From outside the composite, the powder appears to be completely constrained from densifying, but from within, damage in the powder grows as portions of the powder undergo complete densification.

In the above experimental example the densifying powder was completely constrained and the reason for the constraint of shrinkage is easily visualized, viz., by the high density SiC whisker network. The question of how shrinkage is constrained within a composite compact where inert inclusions do not form a touching network was addressed by Lange. ¹⁸ As shown in Fig. 6a, the inert inclusions can be placed on lattice sites. In order to fit together with neighbors, each unit cell must retain its shape as the powder shrinks during densification.

The amount of powder between pairs of inclusions relative to the distance between their lattice sites will govern the amount of powder densification for a given amount of composite shrinkage.

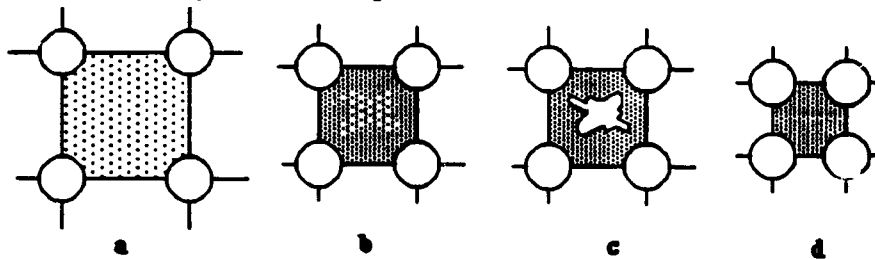


Figure 6 Schematic illustrating a) inclusions on sites of simple cubic lattice, b) uniform composite shrinkage causes powder to densify more between more closely spaced inclusions (cell edges) and prevents the same densification between inclusions of larger spacing (between diagonal sites), c) coarsening of lower density regions causes desintering and larger pore formation (pore volume conserved) and d) deformation of the denser matrix would be required to eliminate lower density region in (b) or larger void in (d). - 7

Since the relative amount of powder (i.e., ratio of distance between inclusions to distance between lattice sites) between cell edge sites is less than the diagonal sites, a uniform cell (or composite) shrinkage will produce a different matrix density between edge and diagonal sites. Powder between site pairs forming cell edges will densify more relative to powder between diagonal pairs as shown in Fig. 6b. That is, the condition that the unit cell must retain its shape requires that the cell diagonals (or powder within the center of the cell) be constrained from shrinking to the same density as the powder between site pairs defining cell edges. If connected voids within the lower density regions can grow, then larger voids will develop to dissipate any shrinkage potential as shown in Fig. 6c. If, on the other hand, the densification potential of the lower density, constrained material can compress and deform the material along connecting cell edges (or pull the inclusions into the cell), then the matrix within the cell will fully densify without distorting the cell's shape

as shown in Fig. 6d. These concepts can be applied to a random distribution of inclusions, viz., for the same amount of composite shrinkage, the powder between more closely spaced inclusions will densify more than the powder between inclusions with larger than average spacings.

As detailed elsewhere in this proceedings ¹⁹, microstructure observations have shown that during composite densification, a network of denser material is observed surrounding lower density regions. Although this observation is consistent with the constraining network model discussed above, it was difficult to unambiguously conclude that the denser network was associated with more closely spaced inclusions. Two phenomena were observed as the composite was further heat treated to increase composite density. First, grain growth occurred within the dense network material due to grain boundary motion. Second, voids within the lower density regions grew larger by a desintering process (i.e., the separation of previously sintered grains) associated with grain coarsening. These larger voids were thermodynamically more stable with regard to densification than the low density microstructure from which they developed.

These microstructure observations have lead to a model of composite densification consistent with the constraining effect of the inclusion network: As the composite shrinks a network of denser material develops (expected to be associated with more closely spaced inclusions). The sintering 'stress' exerted by the lower density regions is small relative to the stress needed to deform the denser network. During this shrinkage process, the denser network becomes more resistant to deformation through grain growth, and the lower density regions dissipate their shrinkage potential via desintering. This model does not apply to glass powders which do not develop grain boundaries (viz., desintering can not occur between glass particles) and do not increase their creep resistance due to grain growth. Thus, this model not only explains the effect of a network of inert inclusion on the densification of a crystalline powder, but also explains why the densification of glass powders is less affected by this network.

AVOIDING DIFFERENTIAL DENSIFICATION: INNOVATIVE APPROACHES

Several studies ^{5,20} have now shown that mixed powder/reinforcement systems can be pressureless sintered to much higher densities than previously expected provided the powder can be packed to a high density. Although further gains are expected, pressureless sintering will be limited to either lower volume fractions of reinforcement or less than theoretical matrix densities. It is certainly obvious that powders packed within relatively stiff preforms will densify onto the preforms to produce extensive matrix damage. The need to avoid constrained densification leaves room for innovation. Many innovative routes can be imagined.

One innovative route is to densify the ceramic before adding the reinforcement. This route, which first appeared either very silly or too simple, has lead to two new processing methods. In the first ⁷, powder is packed within a preform (see Fig 5a) made from either an organic material or carbon. During the initial stages of heating, the preform is pyrolyzed leaving a powder compact with channels remnant of the preform. Heating to higher temperatures densifies the powder; channels shrink, but do not disappear. Metal can then be intruded into these connective channels to form a metal reinforced ceramic composite. The reinforcement architecture, 'fiber' diameter, and volume fraction is dictated by the

preform. Other advantages, e.g., different ceramic/metal combinations, etc. are obvious.

In the second 21, the ceramic is first made by a powder method as thin sheets via tape casting. After the ceramic is densified, it is made into a laminar composite by sandwiching fiber prepreps between ceramic sheets and hot pressing. Epoxy/carbon prepreps have been used to demonstrate this processing method. Properties are impressive.

ACKNOWLEDGEMENTS

This work was supported by a DARPA/ONR contract, No. N00014-86-K-0753, and is part of a larger multi-investigator, multi-institutional research program concerned with high temperature structural materials led by A. G. Evans and R. Mehrabian.

REFERENCES

1. J.-F. Jamet, L. Anquez, M. Parlier, M.-H. Ritti, P. Peres, and L. Gateau, "Composite Céramique: Relations Entre Microstructure et Rupture," *L'Aéronautique et l'Astronautique*, No. 123/124, 128-42 (1987).
2. R. Naslain, "Fibrous Ceramic-Ceramic Composite Materials Processing and Properties," *J. de Phys. Colloque C1, sup. au no. 2, vol. 47, C1-703-715* (1986).
3. A. J. Pyzik, A. A. Aksay and M. Sarikaya, "Microdesigning of Ceramic-Metal Composites," in *Ceramics Microstructures '86, Role of Interfaces*, pp 45-54, Ed. by J. A. Pask and A. G. Evans, Plenum Press, N.Y. (1987).
4. M. S. Newkirk, A. W. Urquhart, H. R. Zwicker, and E. Breval, "Formation of Lanxide Ceramic Materials," *J. Mater. Res.* 1 [1] 81-9 (1986).
5. D. Lam and F. F. Lange, to be published.
6. J. Jamet, D. Damange and J. Loubeau, "Nouveaux Matériaux Composites Alumine-Alumine à Rupture Fortement Dissipative et Leur Préparation," French Patent No. 2,526,785, Nov. 18, 1983.
7. F. F. Lange, B. V. Velamakanni, and A. G. Evans "A New Method for Processing Metal Reinforced Ceramic Composites," (to be published).
8. F. F. Lange and K. T. Miller, "Pressure Filtration: Kinetics and Mechanics," *Bul. Am. Ceram. Soc.* 66 [10], 1498-1504 (1987).
9. L. C. De Jonghe, M. N. Rahaman and C. H. Hsueh, "Transient Stresses in Bimodal Compacts During Sintering," *Acta. Metall.* 34 [7] 1467-71 (1986).
10. R. K. Bordia and R. Raj, "Sintering of $TiO_2-Al_2O_3$ Composites-A Model Experimental Investigation," *J. Am. Ceram. Soc.* 71 [4] 302-10 (1988).
11. R. J. Brook, W. H. Tuan, and L. A. Xue, "Critical Issues and Future Directions in Sintering Science," *Ceram. Trans., V 1, Ceramic Powder Science*, Ed. by G. L. Messing, E. R. Fuller, and H. Hausner, 811-21, Am. Ceram. Soc. (1988).
12. G. Y. Onoda and G. L. Messing, "Packing and Sintering Relations for Binary Powders," in *Processing of Crystalline Ceramics, Materials Science Research Vol 11*, ed by H. Palmour III, R. F. Davis and T. M. Hare, pp 99-112, Plenum Press, 1978.
13. C.-H. Hsueh, A. G. Evans, and R. M. McMeeking, "Influence of Multiple Heterogeneities on Sintering Rates," *J. Am Ceram. Soc.* 69 [4] C64-6 (1986).
14. R. Raj and R. K. Bordia, "Sintering Behavior of Bi-modal Powder Compacts," *Acta Met.* 32 [7] 1003-20 (1984).
15. G. W. Scherer, "Sintering with Rigid Inclusions," *J. Am. Ceram. Soc.*, 70 [10] 719-25 (1987).

16. F. F. Lange, "Densification of Powder Rings Constrained by Dense Cylindrical Cores," *Acta Met.* 37 [2] 697-704 (1989).
17. J. R. Porter and F. F. Lange, unpublished work.
18. F. F. Lange, "Constrained Network Model for Predicting Densification Behavior of Composite Powder," *J. Mater. Res.* 2 [1] 59-65, 1987.
19. O. Sudre, D. C. C. Lam, and F. F. Lange, "Densification Behavior of ZrO_2 Reinforced Al_2O_3 Composites," *This Proceedings*.
20. M. D. Sacks, H.-W. Lee, and O. E. Rojas, "Suspension Processing of Al_2O_3/SiC Whisker Composites," *J. Am. Ceram. Soc.* 71 [5], 370-9 (1988).
21. F. F. Lange, D. B. Marshall, and C. Folsom, "Fiber Reinforced Laminated Ceramic Composite," Patent under application.